nuclear fusion

fusion nucléaire

ядерный синтез

fusión nuclear

ATOMIC AND PLASMA–MATERIAL INTERACTION DATA FOR FUSION

(Supplement to the journal Nuclear Fusion)

VOLUME 1

INTERNATIONAL ATOMIC ENERGY AGENCY, VIENNA, 1991
AGENCE INTERNATIONALE DE L'ENERGIE ATOMIQUE, VIENNE, 1991
МЕЖДУНАРОДНОЕ АГЕНТСТВО ПО АТОМНОЙ ЭНЕРГИИ, ВЕНА, 1991
ORGANISMO INTERNACIONAL DE ENERGIA ATOMICA, VIENA, 1991

The following States are Members of the International Atomic Energy Agency:

AFGHANISTAN
ALBANIA
ALGERIA
ARGENTINA
AUSTRALIA
AUSTRIA
BANGLADESH
BELGIUM
BOLIVIA
BRAZIL
BULGARIA
BYELORUSSIAN SOVIET SOCIALIST REPUBLIC
CAMEROON
CANADA
CHILE
CHINA
COLOMBIA
COSTA RICA
COTE D'IVOIRE
CUBA
CYPRUS
CZECHOSLOVAKIA
DEMOCRATIC KAMPUCHEA
DEMOCRATIC PEOPLE'S REPUBLIC OF KOREA
DENMARK
DOMINICAN REPUBLIC
ECUADOR
EGYPT
EL SALVADOR
ETHIOPIA
FINLAND
FRANCE
GABON
GERMANY
GHANA
GREECE
GUATEMALA
HAITI
HOLY SEE
HUNGARY
ICELAND
INDIA
INDONESIA
IRAN, ISLAMIC REPUBLIC OF
IRAQ
IRELAND
ISRAEL
ITALY
JAMAICA
JAPAN
JORDAN
KENYA
KOREA, REPUBLIC OF
KUWAIT
LEBANON
LIBERIA
LIBYAN ARAB JAMAHIRIYA
LIECHTENSTEIN
LUXEMBOURG
MADAGASCAR
MALAYSIA
MALI
MAURITIUS
MEXICO
MONACO
MONGOLIA
MOROCCO
MYANMAR
NAMIBIA
NETHERLANDS
NEW ZEALAND
NICARAGUA
NIGER
NIGERIA
NORWAY
PAKISTAN
PANAMA
PARAGUAY
PERU
PHILIPPINES
POLAND
PORTUGAL
QATAR
ROMANIA
SAUDI ARABIA
SENEGAL
SIERRA LEONE
SINGAPORE
SOUTH AFRICA
SPAIN
SRI LANKA
SUDAN
SWEDEN
SWITZERLAND
SYRIAN ARAB REPUBLIC
THAILAND
TUNISIA
TURKEY
UGANDA
UKRAINIAN SOVIET SOCIALIST REPUBLIC
UNION OF SOVIET SOCIALIST REPUBLICS
UNITED ARAB EMIRATES
UNITED KINGDOM OF GREAT BRITAIN AND NORTHERN IRELAND
UNITED REPUBLIC OF TANZANIA
UNITED STATES OF AMERICA
URUGUAY
VENEZUELA
VIET NAM
YUGOSLAVIA
ZAIRE
ZAMBIA
ZIMBABWE

The Agency's Statute was approved on 23 October 1956 by the Conference on the Statute of the IAEA held at United Nations Headquarters, New York; it entered into force on 29 July 1957. The Headquarters of the Agency are situated in Vienna. Its principal objective is "to accelerate and enlarge the contribution of atomic energy to peace, health and prosperity throughout the world".

Printed by the IAEA in Austria
September 1991

ATOMIC AND PLASMA–MATERIAL INTERACTION DATA FOR FUSION

(Supplement to the journal Nuclear Fusion)

VOLUME 1

INTERNATIONAL ATOMIC ENERGY AGENCY, VIENNA, 1991

The volumes of ATOMIC AND PLASMA-MATERIAL INTERACTION DATA FOR FUSION are published by the International Atomic Energy Agency as supplements of the journal NUCLEAR FUSION.

For these supplements, papers, letters and reviews are accepted which deal with the following topics:

- Elementary collision processes in fusion plasmas involving photons, electrons, ions, atoms and molecules;
- Collision processes of plasma particles with surfaces of fusion relevant materials;
- Plasma-material interaction phenomena, including the thermophysical response of materials.

Each submitted contribution should contain fusion relevant data and information in either of the above areas. Original contributions should provide new data, using well established methods. Review articles should give a critical analysis or evaluation of a wider range of data. They are normally prepared on the invitation of the Scientific Editor or on prior mutual consent. Each submitted contribution is assessed by two independent referees.

Every manuscript submitted must be accompanied by a *disclaimer* stating that the paper has not been published and is not being considered for publication elsewhere. If no copyright is claimed by the authors, the IAEA automatically owns the copyright of the paper.

Guidelines for the preparation of manuscripts are given on the inside back cover. Manuscripts and correspondence should be addressed to: The Editor, NUCLEAR FUSION, International Atomic Energy Agency, Wagramerstrasse 5, P.O. Box 100, A-1400 Vienna, Austria.

Publisher: International Atomic Energy Agency, Wagramerstrasse 5, P.O. Box 100, A-1400 Vienna, Austria

Scientific Editor: R.K. Janev, Atomic and Molecular Data Unit, Division of Physical and Chemical Sciences

Editor: C. Bobeldijk, Division of Scientific and Technical Information

Manuscript Editors: J.W. Weil, Division of Publications
Maria Demir, Division of Publications

Annual subscription price (one issue): Austrian Schillings 300,—
Airmail delivery (optional): Austrian Schillings 40,— to any destination

---

ATOMIC AND PLASMA-MATERIAL INTERACTION DATA FOR FUSION, VOLUME 1
IAEA, VIENNA, 1991
STI/PUB/23/APID/1

FOREWORD

Atomic and plasma-wall interaction processes have an important impact on the energy balance, confinement and stability of a thermonuclear plasma. Fusion research areas in which these processes play a prominent part are: plasma radiation losses, impurity control, particle transport, thermal power and helium exhaust, neutral beam plasma heating and fuelling, edge plasma physics and plasma diagnostics. With the progress of fusion research towards the engineering reactor stage, plasma-material interaction processes related to the gross thermophysical response and the thermo-mechanical behaviour of plasma facing components to plasma particle and heat fluxes are also becoming increasingly important. Information on all of these processes is essential for both fusion plasma research and fusion reactor design.

The International Atomic Energy Agency, through its Atomic and Molecular Data Unit, co-ordinates a wide spectrum of programmes for the compilation, evaluation and generation of atomic, molecular and plasma-material interaction data for fusion. The purpose of these programmes, which were initiated more than fifteen years ago, is to provide the fusion community with consistent and expert assessed information on atomic and plasma-material interaction processes as required in fusion research. Recognizing the need for a more direct exchange of information on these processes between the atomic/material physics community and the fusion community, the Subcommittee on Atomic and Molecular Data for Fusion of the International Fusion Research Council has suggested that the Agency establish an annual publication on the subject of atomic and plasma-material interaction data for fusion as a supplement to the journal Nuclear Fusion. The content of scientific contributions in this journal-level publication should be strongly data oriented and highly fusion relevant. The contributions should be original in character and should either provide new (or improved) data or evaluate a broader class (or classes) of data or processes (review). While submission of individual contributions corresponding to the scope of the journal is strongly encouraged, it is expected that some contributions will result also from presentations at scientific meetings organized by the Agency in the framework of its co-ordinated data generation and evaluation programmes.

The present, first volume of Atomic and Plasma-Material Interaction Data for Fusion contains extended versions of the reviews presented at the IAEA Advisory Group Meeting on Particle-Surface Interaction Data for Fusion, held on 19-21 April 1989 at the IAEA Headquarters in Vienna. The review articles incorporate the original contributions presented at the meeting, as well as the most recent information on the specific subjects covered.

The plasma-wall interaction processes considered are the ones which are most important in a reactor level magnetic fusion device and have a strong impact on its operational performance. Apart from the processes induced by particle impact, plasma-material interaction effects related to off-normal plasma events (disruptions, runaway electron bombardment) are covered. A summary of the status of data information for all of these processes from the point of view of fusion reactor design needs is also provided.

To a certain extent, this volume can be considered as an updated and complementary source of information to the Data Compendium for Plasma-Surface Interactions published in 1984 as a Special Issue of Nuclear Fusion.

Vienna, September 1991

R.K. Janev
Scientific Editor

CONTENTS

PARTICLE BOMBARDMENT AND ENERGY FLUXES TO THE VESSEL WALLS IN CONTROLLED THERMONUCLEAR FUSION DEVICES

R. BEHRISCH
Max-Planck-Institut für Plasmaphysik,
Euratom-IPP Association,
Garching bei München,
Germany

ABSTRACT. For an ignited, continuously burning fusion plasma the energy and particle confinement must be appropriate to sustain the plasma at the burn temperature and at sufficient density, and to permit exhaust of the energy and of the ^{4}He ash produced by the fusion reactions as well as the supply of new fuel. In present plasma experiments with plasma confinement in a strong magnetic field the energy confinement is not yet sufficient for a D-T fusion plasma to ignite and to burn. Improvement of this confinement is still one of the major tasks in fusion research. For a continuously burning fusion plasma the necessary removal of the ^{4}He energy and the ^{4}He particles allows the power and particle fluxes to the vessel walls to be estimated. These fluxes initiate several processes, leading to a major modification of the plasma and of the vessel walls. For an understanding and a quantitative modelling of these plasma-solid interaction phenomena, it is necessary to know the atomic data for the different processes taking place at the vessel walls.

1. MAGNETIC CONFINEMENT OF A FUSION PLASMA

In the research of controlled thermonuclear fusion the most promising scheme for the confinement of the hot hydrogen plasma is a strong toroidal magnetic field with closed nested magnetic surfaces, as in a tokamak or a stellarator [1]. However, the confinement of a plasma in a magnetic field is limited. Besides freely moving and gyrating along the magnetic field lines, the plasma particles also diffuse and drift perpendicular to the magnetic surfaces. The plasma thus expands and comes in contact with the surrounding vessel walls which protect the plasma from the outer atmosphere. Neutral atoms in the plasma, neutrons and electromagnetic radiation are not confined by the magnetic field.

The first area of contact of the expanding plasma at the vessel walls is generally a limiter, being a solid which must be designed to withstand the large heat flux and particle bombardment from the plasma. The limiter determines the last closed magnetic surface (LCMS). Such an LCMS — the separatrix — may also be created by a special shape of the confining magnetic field, as in a stellarator or a divertor tokamak. Plasma particles which diffuse and drift from the central plasma across the separatrix form the scrape-off layer (SOL) plasma in the volume outside the separatrix. Magnetic field lines from that volume finally intersect the sides of the limiters and/or the divertor plates. Because of the free movement of particles along the magnetic field lines, these areas are in direct contact with and bombarded by the SOL plasma.

The other areas of the vessel walls, which are at some distance from the LCMS, are mostly oriented nearly parallel to the magnetic field lines. These areas are hit by much smaller plasma fluxes which diffuse from the SOL plasma to the vessel walls instead of hitting a divertor plate or the sides of a limiter.

Finally, the electromagnetic radiation, i.e. the bremsstrahlung and the recombination synchrotron and line radiation, from the plasma is nearly uniformly distributed on the vessel walls. The vessel walls are further bombarded with energetic neutral atoms, which are created in charge exchange collisions between neutral atoms entering the plasma and ions in the plasma, and with 14 MeV neutrons for a D-T fusion plasma.

The D-T reaction is the most promising fusion reaction with the largest cross-section at the lowest energy [1]:

$$D + T \rightarrow {}^4He\ (3.5\ MeV) + n\ (14.1\ MeV)$$

The cross-section has a maximum at energies of about 100 keV. For a Maxwellian velocity distribution, a plasma temperature of 10–15 keV permits sufficient fusion reactions between the ions in the high energy part of the velocity distribution for the plasma to burn.

2. PARTICLE AND POWER EXHAUST

2.1. Particle confinement

In a burning D–T fusion plasma the 3.5 MeV alpha particles from the fusion reaction must be confined for a sufficiently long time to transfer their energy to the plasma in order to balance the energy losses. However, the confinement of the alpha particles should not be too good. The upper limit for the alpha particle confinement time is given by the exhaust of the ^{4}He particles (representing the ash of the D–T fusion process) necessary to prevent poisoning of the plasma by ^{4}He. This has been expressed by the exhaust criterion [2–5]. The D and T lost by fusion processes must be refuelled, for example by D–T gas puffing and/or by injection of D and T pellets.

2.2. Energy confinement

The energy confinement time in a burning fusion plasma must be sufficient for the ^{4}He energy and any additional power deposited in the plasma to sustain the plasma at the burn temperature and heat the new fuel. This is expressed by the Lawson criterion and/or the ignition criterion [6, 7] which represent a minimum criterion for the product of the D–T density and the energy confinement time. However, the energy confinement must also be limited in order to prevent overheating of the plasma. This means that the ignition criterion [7] actually represents also a maximum condition for the product of the D–T density and the energy confinement time.

In present large plasma experiments the best values obtained for the product of plasma density, energy confinement time and plasma temperature is still a factor of about eight lower than the values needed for a burning fusion plasma, and further improvement of the energy confinement is one of the major tasks in fusion research [8].

For the necessary exhaust of energy and particles from a burning fusion plasma, a continuous flux of energy and particles has to leave the plasma. The energy confinement and the particle confinement of the plasma in the magnetic field, which are determined by the energy diffusion coefficient $\chi_\perp$ and the particle diffusion coefficient $D_\perp$ perpendicular to the magnetic surfaces as well as by the temperature and density gradients, have to be effectively controlled since otherwise the plasma will not burn properly. Regarding the necessary energy and particle exhaust, the limited plasma confinement in a magnetic field is very appropriate if the required confinement of both the energy and the ^{4}He particles can just be achieved and controlled.

Besides reaching the necessary energy and particle confinement, there are further boundary conditions which represent limits for a magnetically confined plasma, i.e. the density limit [9–11] and the limit for the plasma pressure relative to the confining magnetic field strength called the beta limit [11, 12]. Above these limits, the energy balance and/or the pressure balance are violated and in a tokamak the plasma disrupts [11].

3. VESSEL WALL LOAD AND PLASMA–SOLID TRANSITION

The particles and the energy leaving the plasma are deposited on the vessel wall structures. To remove the energy, very effective cooling, especially of the divertor tiles and the limiters, is needed. The particles will finally be thermalized and especially the helium has to be pumped away [13].

The intensities of the energy and particle fluxes leaving the plasma are given by the nuclear power and the tolerable ^{4}He concentration f. They do not directly depend on the details of the plasma confinement. However, the spatial distributions of the fluxes which impinge on the different areas of the vessel walls are determined by the shape of the confining magnetic field and the vessel wall structures.

The particle fluxes and the deposition of energy from the plasma on the different parts of the vessel wall depend on the parameters of the SOL plasma, especially in front of the vessel wall structures bombarded by the plasma, such as the limiters and divertor plates [14]. These plasma parameters finally adjust according to the fluxes from the central plasma and the fluxes of particles recycling from the different parts of the vessel walls, which depend also on the wall material and its state.

In the transition region between the hot plasma and the solid a local thermal equilibrium is generally not possible. Because of the higher velocity of the electrons the solid is negatively charged with respect to the plasma and a sheath develops [14, 39]. For understanding and modelling the interaction of the plasma with the surrounding vessel walls and the formation of the sheath, a detailed and reliable database is needed for the different atomic processes taking place when the hot plasma comes in contact with the surface of a solid.

4. ENERGY AND PARTICLE FLUXES

The values of the wall fluxes from a magnetically confined continuously burning D-T fusion plasma to the different parts of the vessel walls which are given here have been obtained from the energy and particle exhaust conditions for a fusion reactor such as the International Thermonuclear Experimental Reactor (ITER), which is designed by an international team working at the Max-Planck-Institut für Plasmaphysik, Garching [15–19] (see Fig. 1). The estimated values are in reasonable agreement with the more detailed values calculated for ITER with two-dimensional boundary plasma simulation codes [18]. For other planned fusion reactors the values are similar and they generally scale with the fusion power. The particle fluxes to the vessel walls have a broad energy and angular distribution and they are different in the different wall areas. Thus, the data for atomic interactions at the solid surfaces have to be known for a large range of parameters.

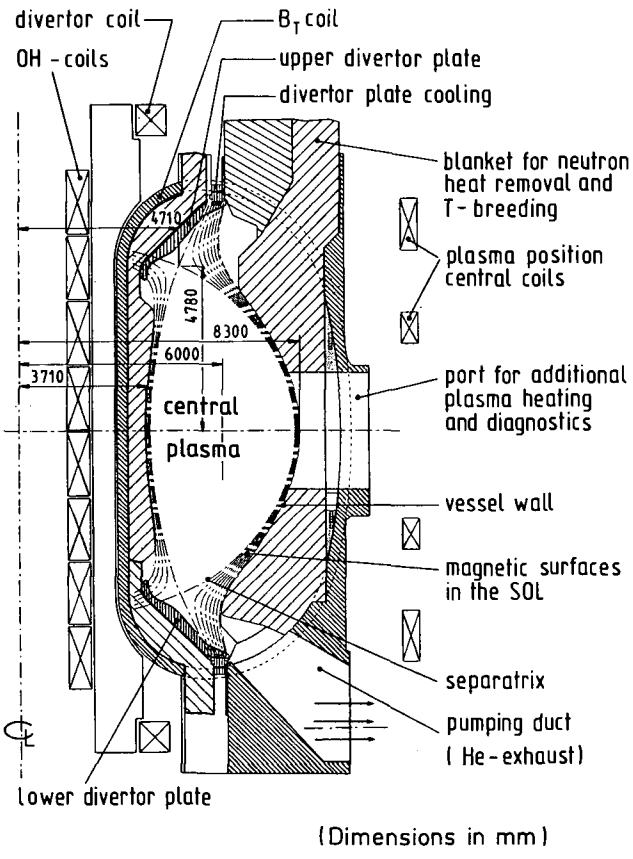

FIG. 1. Cross-section of the ITER torus. The cuts through the magnetic flux surfaces are shown by dash dotted lines.

4.1. Energy fluxes to the vessel walls and divertor plates

The energy fluxes which have to leave a continuously burning fusion plasma are determined by the fusion power and any additional power such as that required for heating and current drive. The additional power, however, can be only a small fraction of the fusion power (typically 10%) and will mostly be neglected in the following. For ITER, the total fusion power is planned to be P_{tot} = 1 GW, with P_n = 800 MW for the 14.1 MeV neutrons and P_α = 200 MW for the 3.5 MeV alpha particles. This corresponds to a total neutron and ^{4}He production rate $dN_n/dt = dN_\alpha/dt = 3.5 \times 10^{20}\ s^{-1}$. The He ions must be confined for some time and transfer their energy to the plasma in order to balance the energy losses. The neutrons will immediately leave the plasma and penetrate into the vessel walls. Here they will be slowed down by collisions with the atoms of the wall structure material and deposit their energy in an about 1 m thick layer called the blanket. In ITER, the first wall, which faces the plasma, will have an area A_w of about 800 m^2, i.e. an average power flux P_n/A_w = 1 MW/m^2 will be deposited on the blanket, and the average source flux of 14 MeV neutrons leaving the plasma, $\Gamma_n = dN_n/dtA_w$, will be $\Gamma_n = 4.4 \times 10^{17}\ m^{-2}\cdot s^{-1}$. Owing to scattering and nuclear reactions in the blanket, the actual neutron flux may finally be up to a factor of ten larger than the source flux [20]. Radiation damage and transmutations in the wall material due to the neutron bombardment and the necessary tritium breeding in reactions with lithium in the blanket structure are important and critical problems for fusion reactor design and for material selection.

4.1.1. Fluxes to the vessel walls

It is generally assumed that approximately half of the energy of the alpha particles P_α and of any additional power P_{add} will be lost from the plasma to the vessel walls by electromagnetic radiation, i.e. $P_{rad}/(P_\alpha + P_{add}) \approx 0.5$. The rest, which for ITER is of the order of about 100 MW, is conducted to the SOL plasma. The radiation losses P_{rad} from the plasma provide a nearly uniform power flux to the surface area of the vessel walls, $\Gamma_{E,rad} = P_{rad}/A_w$; for ITER, we have $\Gamma_{E,rad}$ = 100/800 MW/m^2, giving $\Gamma_{E,rad}$ = 125 kW/m^2. The power deposition on the vessel walls from the SOL plasma by ions and electrons is assumed to be small compared to the deposition by radiation.

4.1.2. Fluxes to the divertor plates

The non-radiated power, $P_\alpha + P_{add} - P_{rad}$, of about 100 MW, diffusing perpendicular to the magnetic surfaces into the SOL plasma, is conducted further along the magnetic field lines and is deposited predominantly in a narrow region around the intersection of the separatrix on the divertor plates (see Fig. 1).

The power flux density at the divertor plates depends on the width of the SOL plasma and on the splitting of the power flux between the outer and inner parts of the divertor plates as well as between the top and bottom plates. This flux density can be reduced by an inclination of the divertor tile surfaces (see Fig. 1).

For ITER it is expected that about 80% of the non-radiated power of 100 MW, i.e. 80 MW, will be conducted to the outer SOL plasma and thus distributed in the outer part of the top and bottom divertor plates, while 20 MW will be conducted to the inner part of the divertor plates [18, 19]. The outer part of the divertor plates will be inclined at an angle of 1.7° with respect to the magnetic field lines; this results in a calculated reduction of the power load density by a factor of about 34 compared with the flux parallel to the magnetic field lines. For ITER it is further predicted that about half of the power load, i.e. 40 MW, will be concentrated around the intersection of the separatrix with the inclined outer parts of the top and bottom divertor plates on two strips, each of about 0.08 m × 30 m, i.e. in an area of about two times 2.4 m^2, i.e. about 5 m^2. This means that about 25% of the alpha energy will be concentrated in an area less than 1% of the vessel wall area.

The magnetic flux tubes have each a cross-section of $2.4 \times \sin 1.7 = 0.07$ m^2. This gives a maximum power flux density along the field lines in the direction of the divertor plates of $Q \approx 20/0.07$, giving $Q = 280$ MW/m^2, and a peak power flux density on each of the inclined outer parts of the divertor plates of $\Gamma_{E,div} = 8$ MW/m^2. In calculating this power load it is assumed that the divertor plates will be very well aligned. Any misalignment will cause the power flux to increase locally. Especially the edges of the divertor plates, which are oriented normal to the magnetic field lines, may receive the full power load of 280 MW/m^2 flowing along the magnetic field lines. The divertor plates of ITER are being designed for a maximum power load of 20–40 MW/m^2 [19].

Finally, in tokamaks the plasma may disrupt in times of microseconds to milliseconds, depending on the size of the machine. During a disruption, the full plasma energy (thermal and magnetic) is deposited on the vessel walls, with peak energy depositions by ions of 2–20 MJ/m^2 and by runaway electrons (having energies up to the 100 MeV range) of 50–500 MJ/m^2 [16–19].

5. PLASMA TEMPERATURE IN FRONT OF THE DIVERTOR PLATES

The power deposition from a plasma at a temperature kT and a density n on a solid surface, for the case of no net electrical current, is given [14, 21, 22] by $Q = g\Gamma_p kT$, with $g \approx 7$ being the power transmission factor [14] and with the ion flux Γ_p being equal to the electron flux, $\Gamma_p = nc_s$, with c_s being the ion acoustic speed, $c_s = [(kT_e + kT_i)/m_i]^{1/2}$ or $c_s = (2kT/m_i)^{1/2}$ for $T_i = T_e = T$, and n being the plasma density in front of the divertor plates. For the power flux to the divertor plates we then obtain $Q = gn(2/m_i)^{1/2}(kT)^{3/2}$. For a given power flux Q along the magnetic flux tubes and a plasma density n in front of the divertor plates we can calculate the plasma temperature in front of the plates required for transferring the power flux Q onto the divertor plate. This gives $kT = (m_i/2)^{1/3}(Q/gn)^{2/3}$. For a deuterium plasma with $Q = 280$ MW/m^2 and $n = 2 \times 10^{20}$ m^{-3}, we obtain kT = 25 eV. For a lower density SOL plasma the temperature in front of the divertor plates will be accordingly higher and vice versa.

6. PARTICLE FLUXES FROM THE PLASMA TO THE VESSEL WALLS AND THE DIVERTOR PLATES

The total alpha particle flux which has to leave a D–T fusion plasma under steady state conditions is equal to the ^{4}He production rate $dN_\alpha/dt = P_\alpha/E_\alpha$. For 1 GW of nuclear power this gives $dN_\alpha/dt = 3.5 \times 10^{20}$ ^{4}He/s. The maximum helium concentration f, which is about equal to the fractional burnup of the plasma, is assumed to be typically 10%.

The confinement of higher Z impurities in a magnetically confined quiescent hydrogen plasma has been found to be better than the confinement of hydrogen ions, in agreement with theoretical predictions [23]. The impurity confinement is reduced to values close to those for hydrogen confinement if plasma instabilities such as sawtooth oscillations occur. In the following, we assume the same confinement time for the D–T ions and the ^{4}He ions, and we thus obtain a lower limit for the D–T flux across the separatrix. This flux is larger by a factor

of 1/f than the ^{4}He flux, i.e. about 4×10^{21} D–T/s. Actually, the D–T fluxes from the plasma to the vessel walls will be even larger. The ^{4}He particles are created and deposited preferentially in the plasma centre. The D–T fuel will probably also be deposited close to the plasma centre if pellets with sufficiently high velocities are used for refuelling. However, there will in addition be a comparable deposition of D and T in the boundary plasma by recycling of D and T neutrals from the vessel walls. These particles will have a shorter average confinement time [13].

6.1. Global ^{4}He particle and energy confinement

The global ^{4}He particle confinement time can be defined as $\langle\tau_{p(He)}\rangle = fN/(dN_\alpha/dt)$, with $N = nV$ being the number of D and T particles in the plasma, n the average plasma density and V the plasma volume. For a fusion reactor of the size of ITER, with a plasma volume $V = 1000$ m^3, an average plasma density $n = 10^{20}$ m^{-3} and a fractional burnup $f = 0.1$, this gives a global ^{4}He particle confinement time $\langle\tau_{p(He)}\rangle \approx 28$ s.

For describing the power flux leaving the plasma by diffusion, generally a global energy confinement time $\langle\tau_E\rangle$ is introduced. It is defined as $\langle\tau_E\rangle = E_{pl}/(P_\alpha + P_{add} - P_{rad})$, with $E_{pl} = 3NkT$ being the energy content in the plasma and kT the average plasma temperature. Here the contributions of helium and of other impurities and their electrons to the plasma energy are neglected. For a fusion reactor of the size of ITER, with a plasma temperature of 10 keV, we obtain $E_{pl} = 480$ MJ, giving a necessary global energy confinement time $\langle\tau_E\rangle \approx 4.8$ s.

We can further calculate the necessary ratio between the global particle confinement time and the energy confinement time:

$$\langle\tau_{p(He)}\rangle/\langle\tau_E\rangle = (fE_\alpha/3kT)[1 + (P_{add}/P_\alpha) - (P_{rad}/P_\alpha)]$$

For $P_{add} \ll P_\alpha$ and $P_{rad}/P_\alpha = 0.5$, we obtain $\langle\tau_{p(He)}\rangle/\langle\tau_E\rangle = fE_\alpha/6kT$. For a fusion plasma this gives values of the order of three to six, depending on the plasma temperature, the fractional burnup and the fraction of energy lost from the plasma by electromagnetic radiation. However, this ratio does not directly depend on the size, the plasma density and the confinement scheme of the fusion reactor.

6.2. Ion fluxes to the divertor plates

The major part of the plasma flux diffusing across the separatrix will be conducted along the magnetic field lines and reach the divertor plates. As for the energy fluxes, we assume that about 80% of the particles will reach the outer SOL and will diffuse to the outer inclined part of the divertor plates, along the magnetic flux tubes having cross-sections of about 0.07 m^2 each. The ion flux density along the magnetic field lines can be calculated from $\Gamma_p = n(2kT/m_i)^{1/2}$ [14, 21]. For the expected parameters of the plasma in front of the outer part of the divertor plates, $kT = 25$ eV and $n = 2 \times 10^{20}$ D–T/m^3, this gives a flux density along the magnetic field lines of $\Gamma_p \approx 10^{25}$ D–T/m^2·s within an area of about 0.07 m^2, corresponding to a total flux of about 7×10^{23} D–T/s. This flux is a factor of about 200 larger than the expected total particle exhaust flux of $dN/dt = 3.5 \times 10^{21}$ D–T/s from the plasma. The calculated large fluxes are a consequence of the high plasma density in front of the divertor plates used for ITER in order to attain a low plasma temperature. These high densities and fluxes in the vicinity of the divertor plates are expected to be achieved by strong recycling, i.e. strong reflection and re-emission of the hydrogen ions bombarding the divertor plates. The reflected and re-emitted particles will be ionized in the plasma close to the divertor plates and will cause an increase of the plasma density and thus of the particle flux back to the divertor plates. Compared with the average energy of the ions leaving the central plasma, the average energy of the ions close to the divertor plates will be reduced to the range of 20 eV, i.e. by a factor of about 10^2 to 10^3, in order to reduce the sputtering effects at the divertor plate.

For the outer inclined part of the divertor plates, having a total area of about two times 2.4 m^2, we obtain a flux density of $\Gamma_{p,div} \approx 1 \times 10^{25} \sin 1.7$, giving $\Gamma_{p,div} = 3 \times 10^{23}$ D–T/m^2·s at an average plasma temperature of about 25 eV. The particle and power fluxes to the inner parts of the divertor plates are expected to be lower by about a factor of five; however, it is planned that these parts will be less inclined with respect to the magnetic field lines, resulting in particle and energy flux densities similar to those on the outer parts of the divertor plates [18, 19].

The energy and angular distributions of ions impinging on a solid exposed to a plasma with temperature T, with a magnetic field and without a magnetic field, are still little investigated [21, 22, 24, 25]. For a plasma with $T_i = 0$, the ions enter the sheath potential in front of the divertor plates with the ion acoustic speed c_s and are subsequently accelerated in the sheath potential, which is $3kT_e$ for a hydrogen plasma. For a plasma with $T_i > 0$, the ions are mostly assumed to enter the sheath

TABLE I. EXPECTED FLUXES TO DIFFERENT AREAS OF THE VESSEL WALLS[a]

	Energy (peak)				Particles (peak)			
	14 MeV neutrons (MW/m^2)	Electrom. radiation (MW/m^2)	He, D, T ions (MW/m^2)	D,T(CX) neutrals (MW/m^2)	14 MeV neutrons ($m^{-2}\cdot s^{-1}$)	D,T(CX) neutrals ($m^{-2}\cdot s^{-1}$)	He ions ($m^{-2}\cdot s^{-1}$)	D, T ions ($m^{-2}\cdot s^{-1}$)
Vessel wall	1	0.125	—	0.03	4.5×10^{17}	5×10^{18}	—	—
Divertor plate	1	0.125	8 (20 to 40)		4.5×10^{17}	5×10^{18}	3.5×10^{22}	3.5×10^{23}

[a] For a fusion reactor such as ITER, with a nuclear power of 1 GW and a vessel wall area of 800 m^2.

with a Maxwellian velocity distribution before being further accelerated in the sheath potential. However, the shifted Maxwellian distribution resulting from this model does not fulfil the Bohm criterion [21, 26]. Nevertheless, this distribution has been used for calculating both the ion implanation profiles [27] and sputtering [28, 29] at the vessel walls in fusion devices. It is especially important to know the high energy tail of the energy distribution because these ions will still cause sputtering when the average plasma temperature is below the threshold energy for sputtering. The electrons from the plasma will be slowed down in the sheath potential and low energy electrons will be repelled, so that the total flux of electrons is equal to the ion flux.

6.3. Fluxes of energetic neutrals to the vessel walls

When the surface layers of the divertor plates and vessel walls become saturated with hydrogen, neutral hydrogen molecules and atoms will be re-emitted at a rate which makes the reflected and re-emitted flux about equal to the incident flux, being about 4×10^{21} D-T/s. Because of the large cross-section for charge exchange collisions, the flux of neutrals entering the plasma will cause a flux of energetic neutral atoms from the plasma back to the vessel walls. The energy distribution of the neutral flux leaving the plasma corresponds to the plasma temperature and thus the flux of energetic neutrals is routinely used to measure the plasma temperature [30–32]. The total flux of energetic charge exchange D and T neutrals is of the same order of magnitude as the D–T ion flux leaving the plasma, i.e. about 4×10^{21} D-T/s.This flux is expected to be more uniformly distributed on the vessel walls than the ion flux. Increased fluxes have been measured around the areas which represent major sources of neutrals at the vessel walls, such as limiters and divertor plates [31]. If uniformly distributed, the flux density of the energetic neutrals will be about 5×10^{18} D-T/$m^2\cdot s$. The final sinks for the neutrals are ionization in the plasma by electron and ion impact, and permanent trapping in the surface layers of the vessel walls.

The expected energy and particle fluxes to the different parts of the vessel walls of a continuously burning fusion reactor are summarized in Table I.

7. WALL MATERIALS

The materials for the vessel walls, limiters and divertor tiles must be able to withstand the plasma load, i.e. the particle and power fluxes and the heat pulses during plasma discharges, without major erosion and destruction. There will be erosion at the vessel walls by sputtering, arcing and sublimation due to the load from the plasma, and the eroded atoms may partly enter the plasma. In the plasma they represent impurity atoms which cause a reduction of the fusion reactions that is due to the dilution of the D–T ions for a given plasma pressure and an extra energy loss by radiation. The tolerable concentrations of impurities in a burning fusion plasma depend on their atomic number Z, and they decrease proportionally to Z^n, with $2 < n < 6$ [33]. For low-Z impurities such as boron, beryllium and carbon, the tolerable concentrations are in the range of 10^{-2}, while for high-Z impurities these concentrations are in the range of 10^{-5} to 10^{-4}. Therefore, low-Z materials such as beryllium, boron, borides, carbides and in particular carbon are favoured for the plasma facing components [34–38].

Another important criterion for selecting the plasma facing material is its property to withstand the high thermal load from the plasma without melting and excessive cracking. Regarding this criterion, carbon has favourable properties because it does not melt,

except at extremely high pressures. In present plasma experiments the best plasma parameters have been achieved with the plasma facing components made of carbon and/or coated with carbon, boron and beryllium [34–38]. Such coatings are, however, eroded at limiters and divertor tiles after a short discharge time and they have to be frequently renewed.

For the planned ITER and for other fusion reactors, different forms of carbon (such as highly oriented pyrolytic graphite and carbon fibre enforced carbon) are primary candidates for plasma facing materials [19]. Further, different forms of boron enriched carbon, boron carbide, beryllium and beryllium carbide may be considered. If the plasma in front of the vessel walls can be kept at a very low temperature, i.e. well below the threshold energy for sputtering which is in the range of 5–20 eV, also a refractory metal such as tungsten or an Ir–W compound may be considered.

8. TOPICS OF PLASMA–SOLID INTERACTION

The source of plasma–solid interactions is the limited particle and energy confinement of the plasma in the magnetic field, which is, however, necessary for the exhaust of the ^{4}He ash and the alpha energy. For better understanding, control and prediction of the plasma–solid interactions and for the selection of plasma facing materials, a detailed and reliable atomic database is needed for the effects induced by particle and energy fluxes such as those from the fusion plasma to the different areas of the vessel wall. The problem areas of plasma–solid interaction for which atomic data are needed can be divided into several parts, which are, however, closely interrelated:

— *The electrical coupling between the plasma and the solid,* i.e. the buildup of an electric field between the plasma and the solid due to the different velocities of the electrons and ions leaving the plasma [39]. The electric field is reduced by emission of electrons from the surface of the solid [39–41]. The electric field leads to a modification of the energy deposition as well as the angular and energy distribution of the particle fluxes from the plasma to the vessel walls [14, 21, 22]. Furthermore, electric arcs may ignite between the plasma and the vessel wall [41, 42].

— *The energy deposition* from the plasma by charged particles, energetic neutrals and electromagnetic radiation in the different areas of the vessel walls causes modifications of the wall material and of its properties in these areas [43–47].

— *The plasma particle balance,* i.e. the loss of ions and neutral atoms from the plasma to the walls, and the recycling of these particles from the vessel walls back into the plasma.

— *The impurities in the plasma,* their release from the vessel walls caused by the plasma exposure, their ionization in the boundary plasma, and their diffusion into the plasma and back onto the vessel walls.

9. ATOMIC PROCESSES AND REQUIRED DATA

9.1. Electron emission yields and ignition of electric arcs

For determining the sheath potential between the plasma and a solid surface, the emission of electrons from the solid surface due to the impact of ions, electrons and photons must be taken into account [14, 21, 40]. The sheath potential determines the energy of the bombarding ions and the power deposition from the plasma. Thus, detailed data are needed for ion, electron and photon induced electron emission yields, especially for the materials and the surface conditions of limiters and divertor plates as well as for the wall fluxes in fusion experiments and in a fusion reactor. The ion fluxes to the vessel wall will be predominantly D, T and helium, but there will also be carbon and oxygen ions and all ions from the wall material, probably with higher charge states, resulting in larger acceleration in the sheath giving higher impact energies.

At the surfaces exposed to the plasma in present fusion experiments, traces of electric arcs are found [41, 42]. For these arcs the vessel walls are the cathode and the plasma is the anode. The ignition of the arcs is correlated with plasma instabilities and with a localized large electron emission, for example by field emission from needle-like protrusions or from local dielectric layers representing areas of low work function. For designing a fusion reactor it is important to understand the ignition conditions of the arcs and to find means to suppress their ignition. The electron emission during the burn of arcs reduces the sheath potential.

9.2. Energy deposition and thermal shocks

In a fusion reactor the energy deposition in the areas with the largest thermal load is expected to be in the range of 10–30 MW/m^2, with possible maxima of up to 280 MW/m^2 if the wall tiles are not well enough aligned and the edges receive the full power flux. This

load will be deposited during the pulse of the plasma discharge, which is 200–1000 s and even longer, depending on whether continuous burn can be achieved. During plasma disruption periods of 0.1–0.3 ms, a peak pulse load of 2–20 MJ/m^2 may be deposited by ions; during periods of 5–50 ms, up to 500 MJ/m^2 may be deposited by runaway electrons with energies in the range of a few hundred kiloelectronvolts to megaelectronvolts.

In designing a first fusion reactor, the major problem is to find a material with sufficiently high thermal conductivity to keep the plasma facing surface at a tolerably low temperature to prevent surface melting and massive evaporation. In addition, the material must be able to withstand the thermal shocks occurring during plasma buildup and shutdown, plasma instabilities and disruptions without major surface melting, sublimation and surface cracking. The properties of materials with respect to these demands are being widely investigated [42–46]; however, more specific investigations are needed, especially for new low-Z materials such as carbides and borides, including fibre enforced materials as well as refractory metals such as tungsten.

9.3. Ion reflection, implantation, trapping and re-emission

The ions leaving the plasma and impinging on the different parts of the vessel walls are lost from the plasma. A fraction of them may be recycled if they are reflected at the vessel walls. The other ions are implanted and may be permanently trapped in the surface layers of the vessel walls. During ion bombardment, previously implanted ions may be desorbed from the surface layers of the vessel walls, while the implanted ions may be trapped. The plasma has to be replenished with the ions permanently trapped in the surface layers of the vessel walls which did not cause the desorption of other hydrogen atoms, for example by gas puffing or pellet injection, which has to be applied also to replenish the fuel that has been lost by fusion reactions. For controlling and predicting the plasma density and composition, detailed atomic data for ion reflection (including the energy, angular and charge state distributions of the reflected atoms), and for implantation, diffusion, trapping, saturation, and bombardment induced and thermal release are needed for the materials considered for plasma facing components. The data should be provided for targets with different surface topographies and different temperatures, for the bombardment conditions at the different parts of the plasma facing components, with respect to ion masses (hydrogen isotopes, helium, carbon, oxygen and ions from the wall material), ion energies, angles of incidence and current densities. For simulations of the plasma–material interaction processes it is advantageous to approximate and represent the yields and distributions by algebraic formulas. For computer simulation codes for the plasma and the plasma–solid interaction processes, also a more complex representation can be used [48].

An area for which more information is needed is temporary and permanent trapping of hydrogen and helium in the vessel walls by implantation and codeposition (i.e. bombardment of a solid surface by a flux of carbon and/or metal ions in addition to the flux of hydrogen and helium ions). This phenomenon, also called 'matrix trapping', is being used in physics experiments to trap even fluxes of noble gas atoms on a solid surface. Both trapping by ion implantation and trapping by codeposition play a central role in the phenomenon of wall pumping, which is an important contribution to the control of the plasma density in present tokamaks [49–51].

9.4. Impurity release at the vessel walls

One of the most critical problems in fusion research and in designing a fusion reactor is the erosion at divertor plates, limiters and vessel walls due to the impact of energetic plasma particles and power deposition. This erosion causes a loss of material from different wall structures which is finally redeposited mostly on other wall areas, resulting in an undesired material transport along the vessel walls [52]. A fraction of the eroded wall material may enter the fusion plasma, where it represents impurities.

The major erosion processes at the vessel walls are physical sputtering, chemical sputtering, thermal sublimation and radiation enhanced sublimation due to ion and neutral particle bombardment and surface heating. Chemical sputtering and radiation induced sublimation have been observed only for carbon and for some carbides at elevated temperature [53–58]. The possible contribution of the large fluxes of 14 MeV and lower energy neutrons to sputtering/erosion at the vessel walls is predicted to be negligible compared with plasma erosion [59, 60].

In the last 15 years, a large amount of data for total erosion have been obtained with well defined ion beams in the energy range from a few tens of electronvolts to a few kiloectronvolts, mostly at normal incidence on several relevant wall materials [53–58]. However, for many important quantities there

are still only few measured values available, for example for the dependence of the sputtering yield on the angle of ion incidence with respect to the target normal, the possible dependence of the erosion yield on the ion current density, and the energy distribution of the sputtered particles for different ion bombardment parameters. Generally, the sputtering yield has been measured by weight loss after bombardment with large ion fluences, i.e. at a surface topography which is representative for some steady state topography of solids after high fluence ion bombardment. In a fusion device, however, several different ions will bombard the vessel walls and they will have a distribution in energy and angle of incidence. At the divertor surfaces, where the magnetic field lines intersect at nearly grazing incidence, large angles of incidence will prevail. In this case the surface topography may be different from that which develops during bombardment of ions with single mass, single energy and single angle of incidence. So far, there are only few experimental investigations on the dependence of the sputtering yield and the distribution of the sputtering material on the surface topography. Such dependences have been predicted by computer simulation studies [61, 62]. However, the necessary detailed characterization of the surface topography and its change during the sputtering process make such measurements very difficult.

10. CONCLUSIONS

To understand the phenomena taking place in the different parts of the vessel walls in present fusion experiments and to predict the behaviour and lifetime of the materials and of the burning plasma in a future fusion reactor, it is necessary to have a reliable, internationally accepted detailed database for the atomic processes taking place at the surface of the wall material during bombardment with low to medium energy ions and neutrals and during deposition of high fluxes of energy in times of milliseconds, seconds and up to a few thousand seconds. For selecting a proper plasma facing material, many investigations of new materials, both low-Z and high-Z alloys and compounds, will be needed. The most reliable and reproducible data have been obtained in measurements with beams of single energy mass ions. In some cases the sputtering yields are determined by exposing a probe to plasma for some time. However, for these conditions, only the energy and the angular distributions of the ions from the plasma are known but not their mass distribution, and reasonably defined yields cannot be obtained.

As for the ion backscattering data, it is desirable to have algebraic formulas for the sputtering yield and its dependence on the ion energy and the angle of incidence as well as for the distribution of the sputtered particles.

ACKNOWLEDGEMENTS

It is a great pleasure to thank M.F.A. Harrison and P. Stangeby for many discussions and helpful suggestions in preparing this manuscript. Thanks are also due to several collegues from the Max-Planck-Institut für Plasmaphysik, especially W. Feneberg, for helpful discussions, and to H. Wolff for carefully reading the manuscript.

REFERENCES

[1] ENGELMANN, F., in Physics of Plasma-Wall Interaction in Controlled Fusion (POST, D.E., BEHRISCH, R., Eds), Plenum Press, New York, London (1986) 15.
[2] BEHRISCH, R., PROZESKY, V., Nucl. Fusion **30** (1990) 2166.
[3] REITER, D., WOLF, G.H., KLEVER, H., Nucl. Fusion **30** (1990) 2141; J. Nucl. Mater. **176&177** (1990) 756.
[4] TAYLOR, R.J., FRIED, B.D., MORALES, G.J., Comments Plasma Phys. Control. Fusion **13** (1990) 227.
[5] REDI, M., COHEN, S.A., ITER Document, Princeton Plasma Physics Laboratory, Princeton, NJ (1990); J. Nucl. Mater. **176&177** (1990) 262.
[6] LAWSON, J.D., Proc. Phys. Soc. B **70** (1957) 6.
[7] MEADE, D.M., Nucl. Fusion **14** (1974) 289.
[8] KEILHACKER, M., and JET Team, Phys. Fluids B **2** (1990) 1291.
[9] MURAKAMI, M., CALLEN, J.D., BERRY, L.A., Nucl. Fusion **16** (1976) 347.
[10] FIELDING, S., HUGILL, J., McCRACKEN, G.M., PAUL, J.W.M., PRENTICE, R., STOTT, P.E., Nucl. Fusion **17** (1977) 1382.
[11] WESSON, J., Tokamaks, Oxford Science Publications, Calderon Press, Oxford (1987).
[12] TROYON, F., GRUBER, R., SAURENMANN, H., SEMENZATO, S., SUCCI, S., Plasma Phys. Control. Fusion **26** (1984) 209.
[13] KAUFMANN, M., LACKNER, K., NEUHAUSER, J., VERNICKEL, H., Nucl. Fusion **25** (1985) 89.
[14] STANGEBY, P.C., McCRACKEN, G.M., Nucl. Fusion **30** (1990) 1225.
[15] GRIEGER, G., and INTOR Group, in Plasma Physics and Controlled Nuclear Fusion Research 1988 (Proc. 12th Int. Conf. Nice, 1988), Vol. 3, IAEA, Vienna (1989) 203.
[16] TOMABECHI, K., ibid., p. 215.
[17] POST, D.E., ibid., p. 233.
[18] HARRISON, M.F.A., HOTSTON, E.S., NET Rep. No. 97, EUR-FU/80/90-97, CEC, Brussels (1990).

[19] VIEIDER, G., SHATALOV, G., ITER Divertor Engineering Design, Techn. Note ITER-TN-PC-8-9-1, Max-Planck-Institut für Plasmaphysik, Garching (1989).
[20] BEHRISCH, R., Nucl. Fusion **12** (1972) 695.
[21] STANGEBY, P., in Physics of Plasma-Wall Interaction in Controlled Fusion (POST, D.E., BEHRISCH, R., Eds), Plenum Press, New York, London (1986) 41.
[22] CHODURA, R., ibid., p. 99.
[23] TAYLOR, J.B., Phys. Fluids **4** (1961) 1142.
[24] MATTHEWS, G.F., McCRACKEN, G.M., SEWELL, P., et al., J. Nucl. Mater. **145–147** (1987) 225.
[25] BOGEN, P., RUSBÜLD, D., SAMM, U., in Controlled Fusion and Plasma Physics (Proc. 16th Eur. Conf. Venice, 1989), Vol. 13B, Part I, European Physical Society (1989) 971.
[26] BOHM, D., in The Characteristics of Electrical Discharges in Magnetic Fields (GUTHRIE, A., WAKERLING, R.K., Eds), McGraw Hill, New York (1949).
[27] ECKSTEIN, W., Calculated Trapping Curves of D in C and Si, Rep. IPP-9/30, Max-Planck-Institut für Plasmaphysik, Garching (1980).
[28] GUSEVA, M.I., MARTINENKO, Yu.V., Nucl. Instrum. Methods **63** (1976) 241.
[29] ECKSTEIN, W., LÁSZLÓ, J., to be published in J. Nucl. Mater.
[30] PETROV, M.W., Sov. Phys.-Tech. Phys. **13** (1968) 708.
[31] WAGNER, F., J. Vac. Sci. Technol. **20** (1982) 1211.
[32] VERBEEK, H., and the ASDEX Team, J. Nucl. Mater. **145–147** (1987) 523.
[33] CECCHI, J.L., J. Nucl. Mater. **93&94** (1980) 28.
[34] BOL, K., ARUNASALAM, V., BITTER, M., et al., in Plasma Physics and Controlled Nuclear Fusion Research 1978 (Proc. 7th Int. Conf. Innsbruck, 1978), Vol. 1, IAEA, Vienna (1979) 11.
[35] WINTER, J., J. Nucl. Mater. **176&177** (1990) 14.
[36] REBUT, P.H., LALLIA, P.P., in Fusion Technology (Proc. 15th Symp. Utrecht, 1988), Vol. 1, Elsevier, Amsterdam (1988) 1.
[37] WINTER, J., ESSER, H.G., KÖNEN, L., et al., J. Nucl. Mater. **162–164** (1989) 713.
[38] POSCHENRIEDER, W., FUSSMANN, G., von GIERKE, G., et al., in Controlled Fusion and Plasma Heating (Proc. 13th Eur. Conf. Schliersee, 1986), Vol. 10C, Part I, European Physical Society (1986) 169.
[39] LANGMUIR, I., Phys. Rev. **33** (1929) 954; **34** (1929) 876.
[40] ERTL, K., BEHRISCH, R., in Physics of Plasma-Wall Interaction in Controlled Fusion (POST, D.E., BEHRISCH, R., Eds), Plenum Press, New York, London (1986) 515.
[41] CRASTRON, J., HANCOX, R., ROBSON, A.E., et al., in Peaceful Uses of Atomic Energy (Proc. 2nd Int. Conf. Geneva, 1958), Vol. 32, UN, New York (1958) 414.
[42] BEHRISCH, R., in Physics of Plasma-Wall Interaction in Controlled Fusion (POST, D.E., BEHRISCH, R., Eds), Plenum Press, New York, London (1986) 495.
[43] BEHRISCH, R., J. Nucl. Mater. **93&94** (1980) 498.
[44] McGRATH, R.T., KROSKI, J.A., WATSON, R.D., et al., Design Considerations for ITER Plasma Facing Components, Rep. SAND-89-0901, UC-420, Sandia Laboratories, Albuquerque, NM (1989).
[45] WATSON, R.D., J. Nucl. Mater. **176&177** (1990) 110.
[46] BOLD, H., MIYAHARA, A., J. Nucl. Mater. **171** (1990) 8.
[47] CROESSMANN, C.D., GILBERTSON, N.B., WATSON, R.D., WHITLEY, J.B., Fusion Technol. **15** (1989) 127.
[48] ECKSTEIN, W., HEIFETZ, D.B., J. Nucl. Mater. **145–147** (1987) 332.
[49] COHEN, S.A., EHRENBERG, J., JONES, T.T.C., et al., Plasma Phys. Control. Fusion **29** (1987) 1250.
[50] EHRENBERG, J., J. Nucl. Mater. **162–164** (1989) 63.
[51] EHRENBERG, J., HARBOUR, P.J., Nucl. Fusion **31** (1991) 287.
[52] BEHRISCH, R., EHRENBERG, J., J. Nucl. Mater. **155–157** (1988) 95.
[53] BOHDANSKY, J., ROTH, J., OTTENBERGER, W., Data on Low Energy Light Ion Sputtering, Rep. IPP-9/26, Max-Planck-Institut für Plasmaphysik, Garching (1976).
[54] LANGLEY, R.A., BOHDANSKY, J., ECKSTEIN, W., et al. (Eds), Data Compendium for Plasma-Surface Interactions, Special Issue 1984, Nucl. Fusion (1984).
[55] MATSUNAMI, N., YAMAMURA, Y., ITIKAWA, Y., et al., Energy Dependence of the Yields of Ion Induced Sputtering of Monoatomic Solids, Rep. IPPJ-AM-32, Nagoya University (1983).
[56] YAMAMURA, Y., ITIKAWA, Y., ITOH, N., Angular Dependence of Sputtering Yields of Monoatomic Solids, Rep. IPPJ-AM-26, Nagoya University (1983).
[57] ROTH, J., in Physics of Plasma-Wall Interaction in Controlled Fusion (POST, D.E., BEHRISCH, R., Eds), Plenum Press, New York, London (1986) 351 and 389.
[58] ROTH, J., J. Nucl. Mater. **172&173** (1990) 132.
[59] BEHRISCH, R., HARLING, O.K., THOMAS, M.T., et al., J. Appl. Phys. **48** (1977) 3914.
[60] BEHRISCH, R., in Sputtering by Particle Bombardment (BEHRISCH, R., Ed.), Topics in Applied Physics, Springer-Verlag, Berlin (1983) 179.
[61] SOTNIKOV, V.M., Sov. J. Plasma Phys. **7** (1981) 236.
[62] RUZIC, D.N., Nucl. Instrum. Methods Phys. Res., Sect. B **47** (1990) 118.

REFLECTION

W. ECKSTEIN
Max-Planck-Institut für Plasmaphysik,
Euratom-IPP Association,
Garching bei München,
Germany

ABSTRACT. New information about reflection or backscattering in the field of plasma-wall interaction is reviewed. The paper is an extension of an earlier overview published in Nuclear Fusion (1984). The main new developments were in backscattering at low energies, of heavy projectiles (heavier than helium), compound targets such as hydrogen implanted carbon, the dependence of the reflection coefficients on the angle of incidence and the surface roughness. Data sets as input for plasma codes have been produced and empirical formulas developed to fit the available data. Most of the new information is due to results from experiments rather than calculations.

1. INTRODUCTION

Reflection or backscattering of projectiles from solid surfaces in connection with plasma-wall interaction is discussed in Refs [1, 2]. Since the last extensive survey published in Nuclear Fusion [1], new knowledge has been accumulated. Reference [1] gives the basic information and a collection of experimental and simulated data available at that time. The present review can be regarded as an extension of the former one and discusses recent developments.

First, we discuss briefly the main information of the earlier review. The definitions of the energy and particle reflection coefficients R_E and R_N are given, including the definitions of energy and angular distributions and the reduced energy ϵ (Eq. (2.8) in Ref. [1], page 13, should have M_2 in the numerator instead of M_1). The terminology and abbreviations introduced in Ref. [1] are also used in the present paper. It has been shown that the reflection coefficients scale approximately with the reduced energy; this is the reason for plotting the available data versus ϵ. The experimental data were compared with results from simulations and found to be in agreement within the absolute error limits. The data given in Ref. [1] were restricted to hydrogen and helium projectiles and to projectile energies above a few hundred electronvolts. Some data on energy and angular distributions were also provided as well as data on compound targets and charge state distributions of backscattered projectiles. Since all the information given in Ref. [1] is still valid, this paper will mainly concentrate on new developments and applications.

We discuss here the reflection of heavier projectiles in more detail because of the importance of the bombardment of walls and limiters by heavier impurities in today's plasma machines. Especially in this field, many new data are available. The other field for which more information has been obtained is the reflection of low energy (< 100 eV) projectiles and oblique incidence. Most of the new knowledge has come from computer simulations and only a minor but important fraction from experiments or analytical approaches. As the previous survey, the present review deals only with fast collisional processes; recombination processes at the surface and thermal emission are not included.

2. COMPUTER SIMULATION

2.1. Low energies

At low energies the reflection yield increases and, eventually, total reflection occurs. However, Baskes [3], using the Embedded Atom Method (EAM), showed that the hydrogen particle and energy reflection coefficients do not reach unity at very low energies. Instead, the reflection coefficients decrease again when the kinetic energy approaches the strength of chemical binding forces to surface atoms. The same effect was demonstrated earlier (with unrealistically high binding energies) [4] using the binary collision model and applying a planar surface potential for the hydrogen projectiles to simulate the chemical binding effect. More realistic binding energies (in the eV range) were assumed in

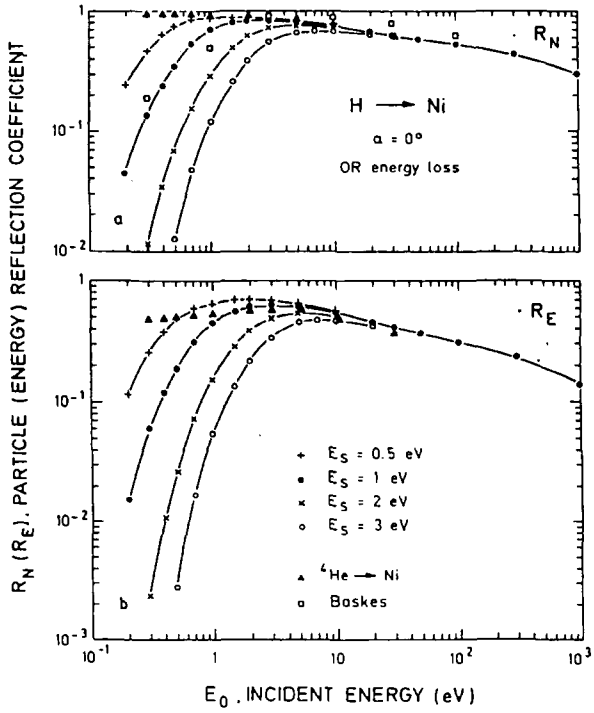

FIG. 1. Calculated particle and energy reflection coefficients, R_N and R_E, versus incident energy E_0. The parameter for the curves is the surface binding energy (planar potential) E_s. Nickel is bombarded at normal incidence, $\alpha = 0°$. For comparison, data for ^{4}He ($E_s = 0$ eV) and recent data by Baskes [3] are also given. (Fig. 2 of Ref. [5].)

Ref. [5] using the Monte Carlo program TRIM.SP. The decrease of the reflection coefficients for hydrogen bombardment of nickel is shown in Fig. 1. The decrease starts below 10 eV and depends strongly on the binding energy assumed for hydrogen. For a zero binding energy (as for helium) the reflection coefficients do not decrease. The effect seems to be stronger for smaller mass ratios M_2/M_1 (target mass to projectile mass), leading to an isotope effect. The decrease of the reflection coefficients occurs below $\epsilon = 10^{-2}$ (where $\epsilon = 0.032534E_0$ [eV] $M_2/[(M_1 + M_2)Z_1Z_2(Z_1^{2/3} + Z_2^{2/3})^{1/2}]$ is the reduced energy, and M_1, M_2 are the projectile and target mass, respectively), depending on the mass ratios M_2/M_1. This is also shown for other chemically active projectiles such as oxygen [6].

These calculations have been performed assuming clean surfaces. It should be noted, however, that in steady state conditions reflection coefficients smaller than unity lead to a buildup of large surface concentrations, which in turn may reduce the chemical binding force of impurity projectiles.

Furthermore, it is shown in Ref. [5] that the hydrogen reflection coefficients are not strongly dependent on the angle of incidence, that the energy distribution of the backscattered hydrogen becomes strongly dependent on the mass ratio and that the angular distributions of

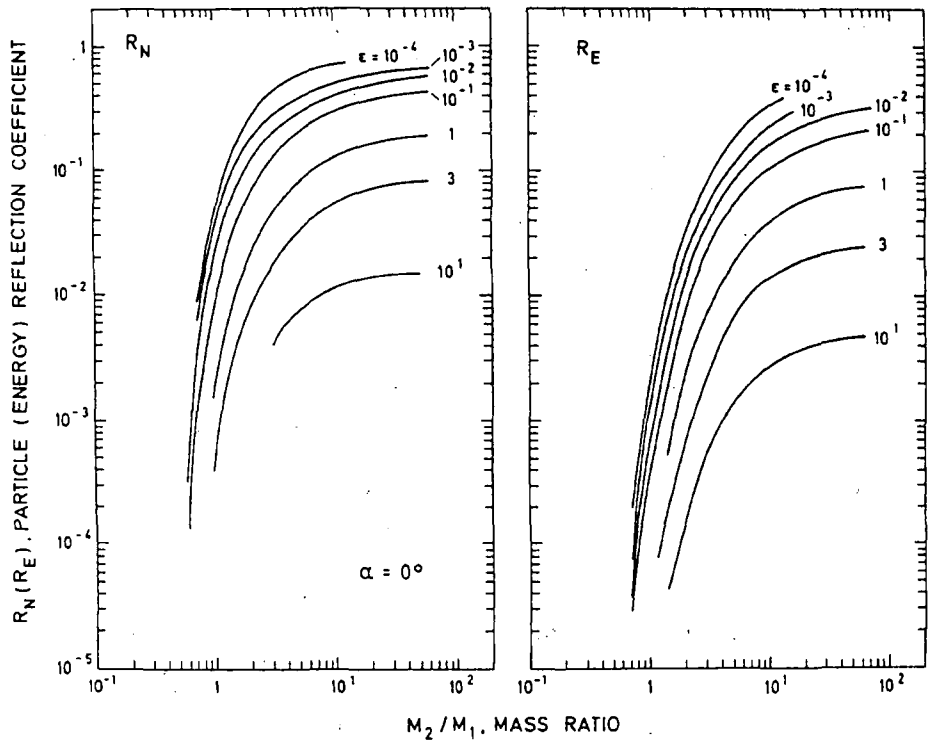

FIG. 2. Particle and energy reflection coefficients versus mass ratio M_2/M_1 for different reduced energies ϵ at normal incidence, $\alpha = 0°$. (Fig. 2 of Ref. [6].)

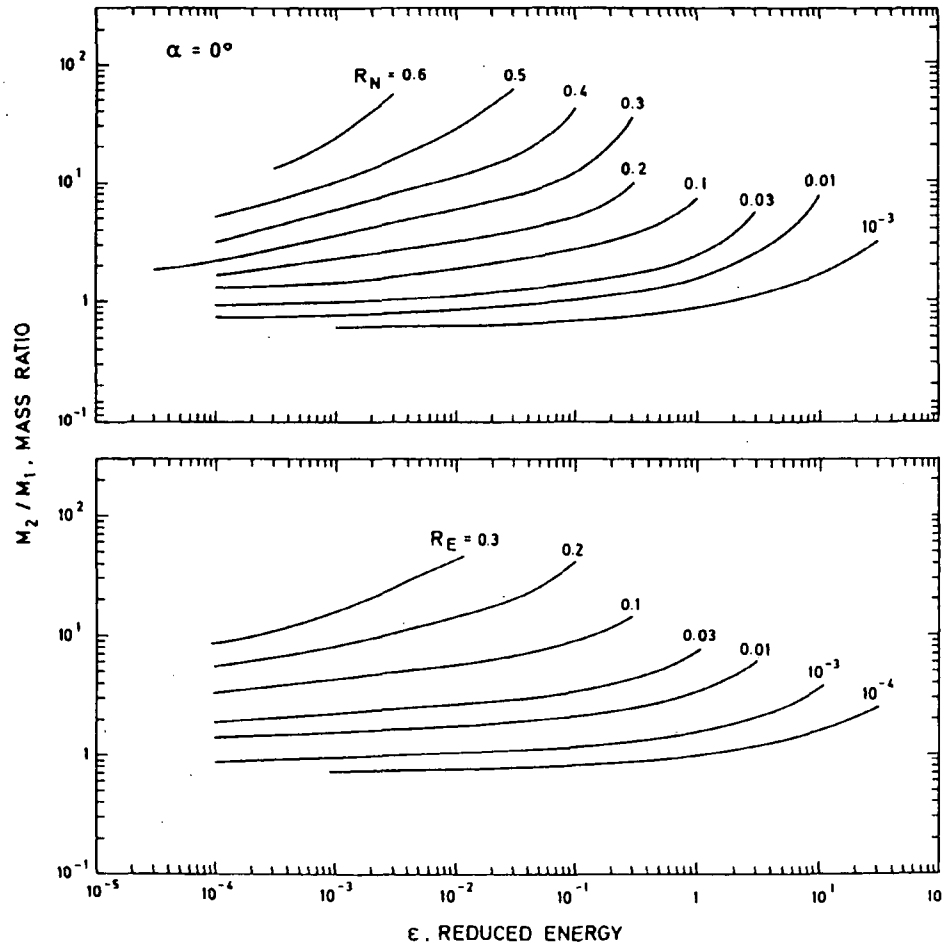

FIG. 3. Lines of equal particle (top) and energy (bottom) reflection coefficients versus reduced energy ϵ and mass ratio M_2/M_1. (Data below $\epsilon = 10^{-2}$ should be taken with care because of a possible binding energy of the projectiles to the surface). (Fig. 3 of Ref. [6].)

backscattered projectiles are closely cosine in the eV range but have a tendency to become overcosine at higher energies.

2.2. Reflection of heavy projectiles

Projectiles heavier than helium are regarded here as heavy projectiles. Many data [7, 8] have been calculated with the program TRIM.SP [9] and some with MARLOWE [10]. The general results for the reflection coefficients are given in Figs 2 and 3 for normal incidence, neglecting chemical interaction of the projectile with the surface and neglecting a change of the target by bombardment (low fluence). Both figures demonstrate that the reflection coefficients scale with the reduced energy ϵ for a fixed mass ratio. Figure 2 also shows that the reflection coefficients vanish for a mass ratio $M_2/M_1 < 0.5$. The reflection coefficients increase with increasing mass ratio M_2/M_1 and

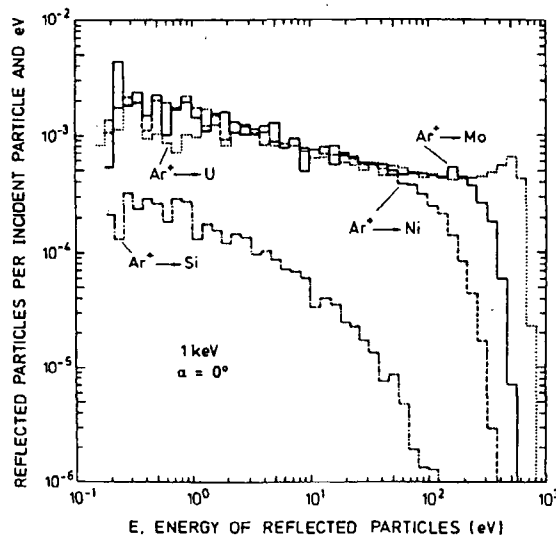

FIG. 4. Energy distributions of backscattered particles for a fixed incident energy, E_0 = 1 keV, and normal incidence, $\alpha = 0°$. The four examples are: Ar → Si: $M_2/M_1 = 0.703$; Ar → Ni: $M_2/M_1 = 1.47$; Ar → Mo: $M_2/M_1 = 2.40$; Ar → U: $M_2/M_1 = 5.96$.

with decreasing reduced energy ϵ. From Fig. 3 it is possible to obtain an approximate value for the reflection coefficients if the reduced energy ϵ and the mass ratio M_2/M_1 are given. The calculated reflection coefficients are in good agreement with those determined with different simulation programs [6, 7], with theoretical data [11] and with experimental results [12–14]. Older experimental data for alkaline ions on molybdenum must be wrong, at least partially (see Fig. 4 of Ref. [6]). From the computer simulations in Ref. [6] it can be concluded that the scaling of the reflection coefficients with the reduced energy ϵ and the mass ratio M_2/M_1 is well fulfilled for $\epsilon > 10^{-2}$. Below $\epsilon = 10^{-2}$ the reflection coefficients for the same mass ratio but for different projectile/target combinations diverge (see Fig. 7 of Ref. [6]). The scaling works also for the angular and energy distributions for $\epsilon > 10^{-2}$.

An example for the strong change in the energy distribution of backscattered projectiles with the mass ratio M_2/M_1 is given in Fig. 4. The angular distribution of backscattered projectiles at low reduced energies and $M_2/M_1 \approx 1$ becomes undercosine (less intensity at exit angles normal to the surface) [8]. In Refs [8, 15], backscattering coefficients and sputtering yields as well as energy and angular distributions are compared for $M_2/M_1 = 1$. More detailed information (as well as the numbers of the calculated reflection coefficients) than in Ref. [6] are given in Ref. [16]. Further data on particle reflection coefficients are given in Refs [9, 17] and detailed energy distributions in Ref. [18]. An interesting relation between the particle reflection coefficient and the skewness γ (3rd moment) of the depth distribution of implanted projectiles is given in Refs [19, 20]:

$$R_N = [1 + 10 \exp(-\gamma/0.3)]^{-1}$$

In this connection, the bombardment by cluster ions [21] should be mentioned. The paper by Yamamura [21] deals with argon clusters, but similar calculations might be of interest also for hydrogen clusters. The particle reflection coefficient seems to be rather high in these studies.

2.3. Data sets for particle transport codes

Reflection coefficients give only a global picture of the backscattering process. If one is interested in a more detailed description, including the known energy and angular distributions of backscattered projectiles, as is somewhat desirable in transport codes, it is not practicable to use the full simulated distributions. In Ref. [22] it is proposed to use the method of inverse cumulative distributions to reduce the simulated data sets for application as input in transport codes. The mathematical problem is the sampling of a one-dimensional distribution g with the assumption

$$\int_0^a g(y)\, dy = 1$$

The cumulative distribution G of g is defined by

$$G(x) = \int_0^x g(y)\, dy$$

Then the sampling is done by computing the inverse of G:

$$F(z) = G^{-1}(z)$$

Hence a random number, $\omega = G(x)$, between 0 and 1 corresponds to the point $x = F(\omega)$.

From the simulated distribution $f(E_0, \alpha; E, \beta, \varphi)dE \sin\beta\, d\beta\, d\varphi$, three one-dimensional distributions f^i are determined:

$$f^1_{E,\alpha}(E) = \int_0^{2\pi} \int_0^{\pi/2} f(E_0, \alpha; E, \beta, \varphi) \sin\beta\, d\beta\, d\varphi$$

With a given energy E', β' is obtained from

$$f^2_{E,\alpha;\,E'}(\beta) = \int_0^{2\pi} f(E_0, \alpha; E', \beta, \varphi)\, d\varphi$$

Finally, with the chosen values E' and β', φ' is selected from the distribution

$$f^3_{E,\alpha;\,E',\beta'}(\varphi) = f(E_0, \alpha; E', \beta', \varphi)$$

Suppose that $F^1(\xi)$, $F^2(\eta, \xi)$ and $F^3(\zeta, \eta, \xi)$ are the inverse cumulative distributions of f^1, f^2 and f^3, respectively. Choose three random numbers, ω_1, ω_2 and ω_3, between 0 and 1. Then the corresponding energy is $F^1(\omega_1)$, the polar emission angle is $F^2(\omega_2, \omega_1)$ and the azimuthal emission angle is $F^3(\omega_3, \omega_2, \omega_1)$.

The inverse distributions F^i have been tabulated for $\omega = 0.1, 0.3, 0.5, 0.7, 0.9$, which leads to five values for F^1, 25 values for F^2 and 125 values for F^3 [23, 24]. Other values may be approximated by linear interpolation. The data for the distributions F^i have been calculated for hydrogen and deuterium bombardment of carbon and iron. Twelve incident energies E_0 were

```
  1  2.01  26  55.85  0.20E+03  30.0  0.48E+00  0.28E+00    4.0  150000

                              E = F¹(ξ)
4.11621E+01  9.16650E+01  1.25388E+02  1.50845E+02  1.72264E+02
                          cos β = F²(η,ξ)
4.82512E-01  6.71025E-01  7.93261E-01  8.86497E-01  9.64969E-01
4.64730E-01  6.53370E-01  7.78114E-01  8.76673E-01  9.60974E-01
4.33166E-01  6.27778E-01  7.58580E-01  8.67415E-01  9.57185E-01
4.18912E-01  6.07695E-01  7.37668E-01  8.49384E-01  9.52098E-01
3.16181E-01  4.77127E-01  6.08052E-01  7.38092E-01  8.90093E-01
                          cos φ = F³(ζ,η,ξ)
-9.40744E-01 -5.56888E-01  6.39957E-02  6.32576E-01  9.56665E-01
-9.43654E-01 -5.83060E-01 -2.24479E-02  5.53254E-01  9.38340E-01
-9.42093E-01 -5.89996E-01 -3.12502E-02  5.86502E-01  9.51357E-01
-9.48138E-01 -5.63722E-01  3.37287E-03  6.00102E-01  9.56278E-01
-9.48829E-01 -5.67355E-01 -1.34341E-02  5.95892E-01  9.56689E-01
-9.39812E-01 -5.87232E-01 -2.29355E-02  5.59451E-01  9.44811E-01
-9.54797E-01 -5.73702E-01  3.88109E-02  5.87853E-01  9.49178E-01
-9.45895E-01 -5.85986E-01 -4.72025E-02  5.59331E-01  9.42824E-01
-9.46810E-01 -6.23763E-01 -4.98033E-02  5.61962E-01  9.39646E-01
-9.52464E-01 -5.42686E-01  5.07274E-02  6.15900E-01  9.60989E-01
-9.45583E-01 -5.56639E-01  2.38740E-02  6.11949E-01  9.62670E-01
-9.42630E-01 -5.42541E-01  3.99673E-02  6.07405E-01  9.51145E-01
-9.52148E-01 -5.53455E-01  4.96278E-02  6.20170E-01  9.55360E-01
-9.36373E-01 -5.59117E-01  2.80664E-02  6.24856E-01  9.44436E-01
-9.48415E-01 -5.61017E-01  3.99420E-03  5.94793E-01  9.49916E-01
-9.35363E-01 -4.59087E-01  1.55117E-01  6.70963E-01  9.52263E-01
-9.36900E-01 -4.98864E-01  1.52805E-01  6.60322E-01  9.60455E-01
-9.37112E-01 -5.15799E-01  1.07914E-01  6.31572E-01  9.61274E-01
-9.35616E-01 -5.13909E-01  1.37291E-01  6.88522E-01  9.63320E-01
-9.43480E-01 -5.41079E-01  7.34927E-02  6.16984E-01  9.47225E-01
-7.03645E-01 -2.60166E-02  4.62108E-01  8.07130E-01  9.81169E-01
-6.50592E-01 -7.77765E-04  5.20594E-01  8.27842E-01  9.80434E-01
-6.36706E-01 -3.04945E-02  4.52518E-01  7.94421E-01  9.75293E-01
-6.26121E-01 -5.22297E-02  4.84883E-01  8.20234E-01  9.78384E-01
-5.59808E-01 -7.71548E-02  3.96122E-01  7.88742E-01  9.76687E-01

 2.41242E-03
 1.12409E-02  3.03862E-02  4.48608E-02  5.48056E-02  6.40575E-02
 6.85487E-02  7.02169E-02  7.30784E-02  7.14487E-02  6.78814E-02
 6.47248E-02  5.92711E-02  5.38432E-02  4.79405E-02  4.23970E-02
 3.62376E-02  3.00269E-02  2.42397E-02  1.96202E-02  1.56679E-02
 1.27294E-02  1.00860E-02  7.60939E-03  5.33812E-03  3.73412E-03
 2.95137E-03  2.60180E-03  1.33453E-03  8.98242E-04  6.54433E-04
 3.59297E-04  2.56641E-04  1.02656E-04  8.98242E-05  5.13281E-05
 3.84961E-05  2.56641E-05  1.28320E-05  1.28320E-05  1.28320E-05
 0.00000E+00  0.00000E+00  0.00000E+00  0.00000E+00  0.00000E+00
 0.00000E+00  0.00000E+00  0.00000E+00  0.00000E+00  0.00000E+00
 0.00000E+00  0.00000E+00  0.00000E+00  0.00000E+00  0.00000E+00
 0.00000E+00  0.00000E+00  0.00000E+00  0.00000E+00  0.00000E+00
 0.00000E+00  0.00000E+00  0.00000E+00  0.00000E+00  0.00000E+00
 0.00000E+00  0.00000E+00  0.00000E+00  0.00000E+00  0.00000E+00
 0.00000E+00  0.00000E+00  0.00000E+00  0.00000E+00  0.00000E+00
 0.00000E+00  0.00000E+00  0.00000E+00  0.00000E+00  0.00000E+00
 0.00000E+00  0.00000E+00  0.00000E+00  0.00000E+00  0.00000E+00
 0.00000E+00  0.00000E+00  0.00000E+00  0.00000E+00  0.00000E+00
 0.00000E+00  0.00000E+00  0.00000E+00  0.00000E+00  0.00000E+00
```

FIG. 5. Data set of deuterium incident on iron, with E_0 = 200 eV and α = 30°. The first row in the set gives the atomic numbers and masses in amus of the incident particle and target species, in that order, the incident energy and polar angle, the particle and energy reflection coefficients, the length 1 of the depth division (in Å) used for the implantation distribution, and the number of Monte Carlo histories used in the TRIM calculation. The second row gives the five energy values F^1, the next five rows give the polar angle values F^2, and the following rows give the azimuthal angle values F^3. The bottom block gives the implanted particle distribution D(x). The first value is the fraction of adsorbed incident atoms, D(x = 0), and the following 20 rows give the implantation distribution, per implanted particle, in depth intervals of 1 (Å). (Fig. 2 of Ref. [24].)

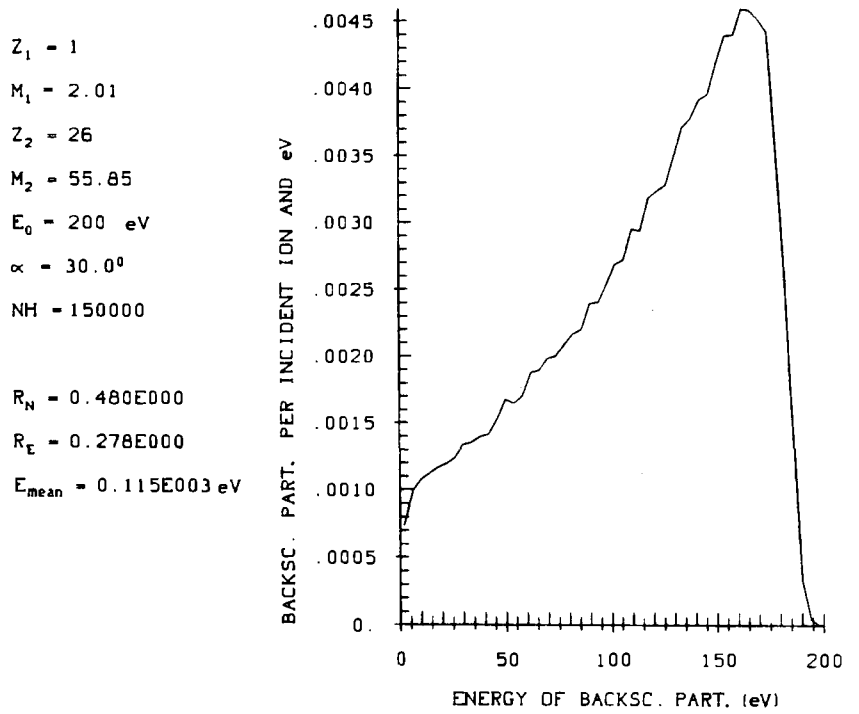

FIG. 6. Energy distribution of backscattered particles for deuterium on iron, with E_0 = 200 eV and α = 30°. The input data are for: Z_1 — the atomic number of the incident particle, M_1 — the mass of the incident particle in amu, Z_2 — the atomic number of the target element, M_2 — the mass of the target element in amu, and NH — the number of Monte Carlo histories used in the TRIM calculations. The output data are for: R_N — the particle reflections coefficient, R_E — the energy reflection coefficient and E_{mean} — the mean energy (in eV) of backscattered particles. (Fig. 3 of Ref. [24].)

chosen: 1, 2, 5, 10, ..., 5000 eV. For each value of E_0, seven incident angles α where used: 0°, 30°, 45°, 60°, 70°, 80° and 85°. Thus, for each projectile/target combination, 84 data sets were determined.

Figure 5 shows an example of a table for 200 eV deuterium bombardment of iron at an angle of incidence of 30°. The first line gives the input parameters for the simulation. In addition to the distributions F^i the depth distribution D(x) of the implanted deuterium is given, which may be used as an input for a diffusion calculation. All simulations have been performed with 150000 projectiles for all energies; this gives lower statistical errors for low energies owing to the larger reflection coefficients. Figure 6 gives the energy distribution of the backscattered projectiles for the same input conditions. The corresponding polar angular distributions are shown in Fig. 7.

The method described above is fast and economical in storage and does not use the rejection method for sampling from these distributions. The computer storage needed for each projectile/target combination is 13020 words. This is small enough to be stored directly in a transport program, rather than on a magnetic disk, so that access to the tables during a calculation can be made very quickly. It should be mentioned that the direct use of the TRIM program in the transport code to compute reflection data is approximately 200 times slower than the sampling method. In addition, the sampling data from the tables have a much better statistical relevance. The data sets for H, D → C and Fe have been calculated at the computer centre of IPP Garching; the data are also stored there and at the Magnetic Fusion Energy Computer Center at Livermore and at the Kernforschungszentrum Jülich. Further data sets can be generated if necessary.

2.4. New simulated data for elemental targets

Since the publication of reflection data [1], some new simulations have been performed. The data calculated with the ACAT program by Takeuchi and Yamamura [25] were not included in Ref. [1]. Their reflection coefficients and energy distribution for 0.01–10 keV hydrogen on copper and gold for normal

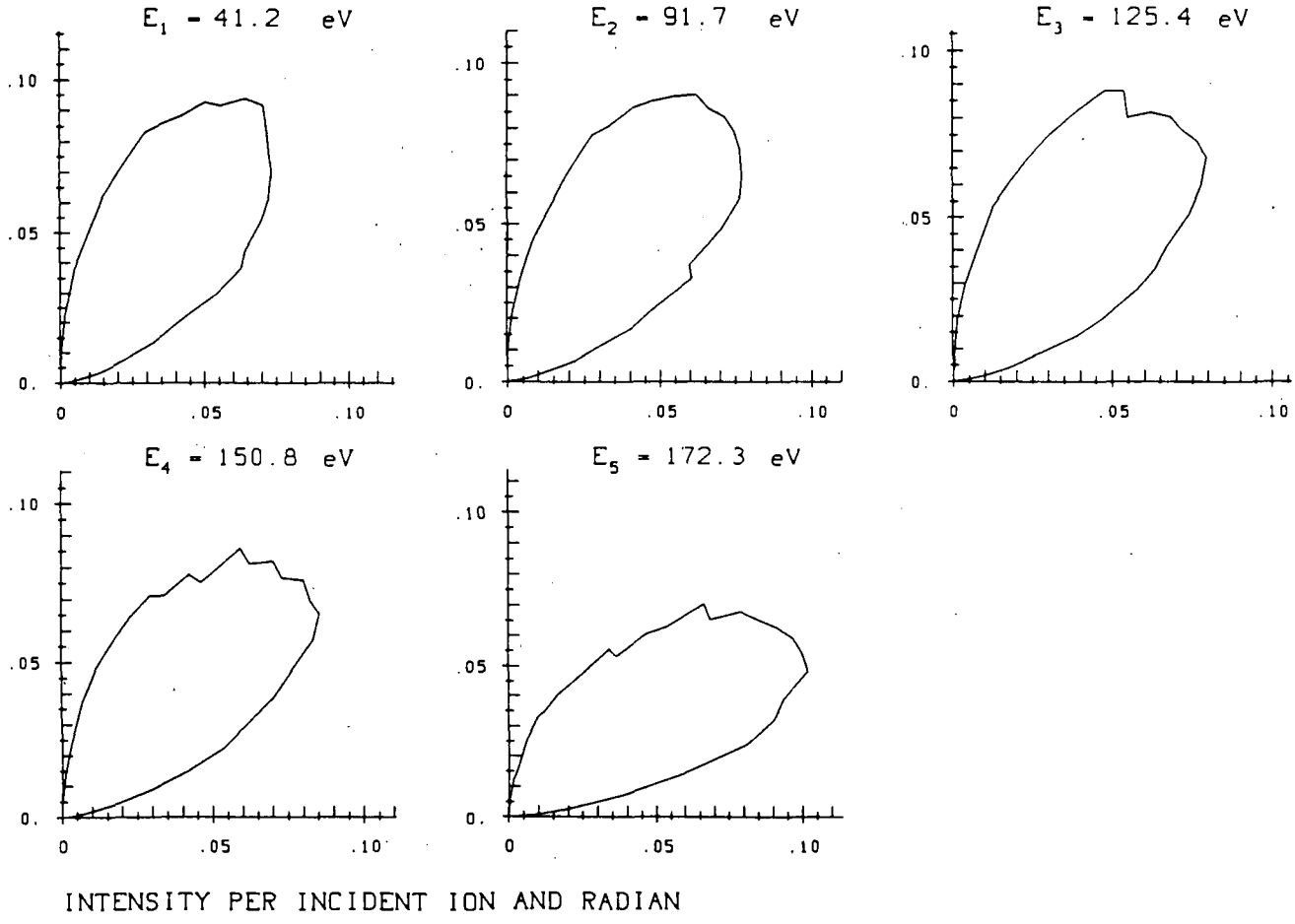

FIG. 7. Distributions of the polar angles of backscattered particles for the five energy regions, for the case of deuterium on iron, with E_0 = 200 eV and α = 30°. The values of E_i are given in Fig. 5 by F^1. (Fig. 4 of Ref. [24].)

incidence are in good agreement with earlier simulated data and experimental results.

Values for the particle reflection coefficients and the mean energy of backscattered projectiles calculated with the Monte Carlo program BABOUM for H and D bombardment of Be, C and Si are given in Ref. [26]. The energy range of the projectiles was between 0.2 and 2 keV and the bombardment was normal to the surface. A Maxwellian distribution of the projectile was investigated in order to simulate the interaction of a plasma with surfaces, but neglecting drift velocity and sheath potential [26]; this was studied earlier also in Ref. [27].

For higher incident energies, particle reflection coefficients are given in Ref. [28]. R_N was determined with the Monte Carlo program TRIM for 5–1500 keV ^{3}He bombardment of about 30 elemental targets at normal incidence.

Energy reflection coefficients for oblique incidence are provided in Ref. [29]. MARLOWE calculations were made for 10, 20 and 40 keV H bombardment of Al, Cu and Mo at angles of incidence α = 60°, 72.5° and 85°. The TRIM calculations were performed for 26.7, 40 and 80 keV H bombardment of Cu at α = 0°, 45°, 78° and 85°. In the range investigated, the data scale approximately as $\cos^2\alpha$, as proposed in Ref. [30]:

$$R_E = 0.66 \exp(-2.3 \sqrt{\epsilon} \cos\alpha)$$

More general expressions are given in Section 5.

2.5. Compound targets

In recent years, inner walls of nearly all plasma machines were, at least partially, covered with carbon, which has the ability to store hydrogen up to a composition of about $C_{0.7}H_{0.3}$. Higher hydrogen concentration for the titanium and iron hydrides have been investigated in Ref. [31]. The decrease of the reflection coefficients due to the incorporated hydrogen as

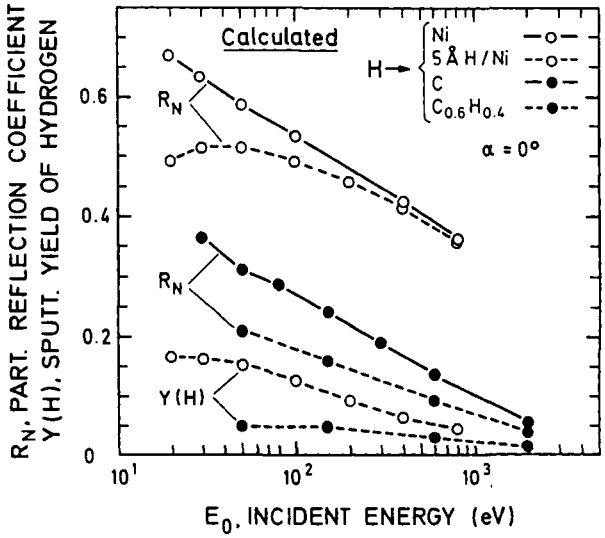

FIG. 8. Calculated particle reflection coefficient R_N and hydrogen sputtering coefficient Y(H) for pure nickel and hydrogen containing nickel and for carbon targets (program TRSPVMC). (Fig. 6 of Ref. [34].)

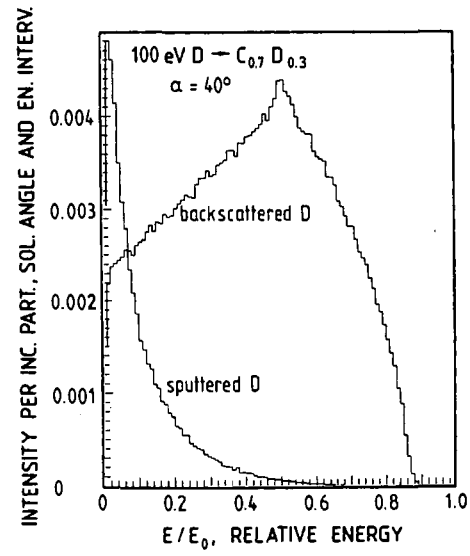

FIG. 9. Energy distributions of backscattered and sputtered deuterium due to the bombardment of deuterium implanted carbon, $C_{0.7}D_{0.3}$, by 100 eV D, as calculated with the Monte Carlo program TRIM.SP (version TRSPVMC).

predicted by simulations was found to be larger than observed experimentally. The energy distributions of backscattered and sputtered deuterium from TiD_2 by 0.5 keV D bombardment were compared in Ref. [32]. The reduction of the particle reflection coefficient of argon projectiles by the absorption of nitrogen on tungsten in the energy range from 20 eV to 1 keV at normal incidence was studied by Yamamura [33].

The systems C_xH_{1-x} and H/Ni were investigated with the Monte Carlo program TRIM.SP (version TRSPVMC) in the projectile energy range from 20 eV to 2 keV at normal incidence [34]. The decrease of the particle reflection coefficient due to the hydrogen content in the target becomes stronger at lower energies, as shown in Fig. 8. The sum of the sputtered and backscattered hydrogen gives approximately the same value as the reflection coefficient R_N for the pure material (see Fig. 8), but the energy distributions for backscattered and sputtered hydrogen and quite different. The sputtered hydrogen particles have lower energies than the backscattered ones as demonstrated in Fig. 9. Both contributions have energies much larger than the thermal ones.

Bombardment of surfaces with non-volatile species as, for example, the bombardment of tungsten with carbon may lead to reflection coefficients which depend on the projectile fluence. The backscattering of carbon from clean tungsten is large, but when a carbon layer is formed on tungsten (which occurs if the sputtering yield is smaller than unity) the reflection coefficients decrease to low values (bombardment of carbon by carbon), see Fig. 10. The reflection coefficients change by more than an order of magnitude in this example. The interplay of implantation and sputtering can lead to large changes in the reflection coefficients.

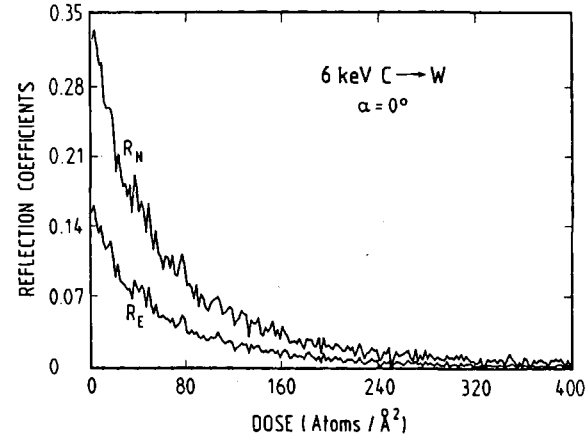

FIG. 10. Dependence of the reflection coefficients R_N and R_E on the dose of the incident projectiles, calculated with the dynamic Monte Carlo program TRIDYN (see Ref. [62]). Tungsten is bombarded by 6 keV carbon at normal incidence. The decrease of the reflection coefficients is due to the formation of a carbon layer at the surface.

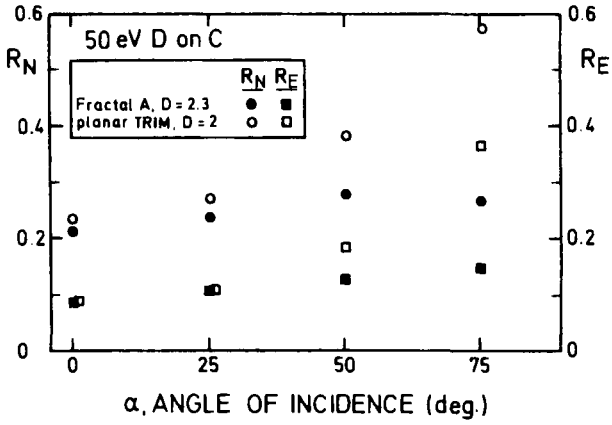

FIG. 11. R_N and R_E versus the angle of incidence α for 50 eV D on C, for a fractal surface A with D = 2.30 and a planar surface with D = 2.00. The error bars are of the size of the data points. At large angles, the planar and fractal results differ by more than a factor of two. The fractal surface A is generated by a one-dimensional trapezoidal line. (After Fig. 7 of Ref. [39].)

2.6. Surface roughness

The first attempt to introduce macroscopic surface structures into a computer simulation program was undertaken by Sotnikov [35]. One-dimensional structures were used in Ref. [35], two-dimensional structures (tetrahedral pyramides) in a later paper [36] and cylindrical structures recently [37]. Rectangular structures were applied in the ACAT program [38] as well as a random surface (with and without vacancies). The random surface is rough in atomic dimensions. The standard surface model in TRIM.SP [9] is also for such a surface. Ruzic and Chiu [39] used the fractal concept to describe surface roughness. The fractal dimension D is considered to be a measure for the roughness. A value of D between 2.05 and 2.3 can, for example, be attributed to different kinds of carbon [40]. The roughness increases with increasing D (D < 3). The fractal surface was introduced in a TRIM Monte Carlo program as well as in the EAM molecular dynamics code [41]. Special surface structures as in Refs [35–38] are model systems which are probably not very realistic. The random model (D ≈ 2) mentioned above as well as the fractal concept do not depend on special geometrical structures, but it is not clear whether they give a better description of reality. Nevertheless, all the models applied indicate a stronger influence of surface roughness at lower energies (a few hundred electronvolts) and especially at grazing incidence, whereas at normal incidence the effects are small. The main effect is a reduction of the reflection coefficients (up to a factor of two at grazing incidence), see Fig. 11, and a broader energy distribution of the backscattered projectiles.

It should be mentioned that the surface roughness may change during bombardment; even polishing may be possible under specific conditions. Experimental investigations of surface structures, especially below 10 nm, would be helpful to check the different models.

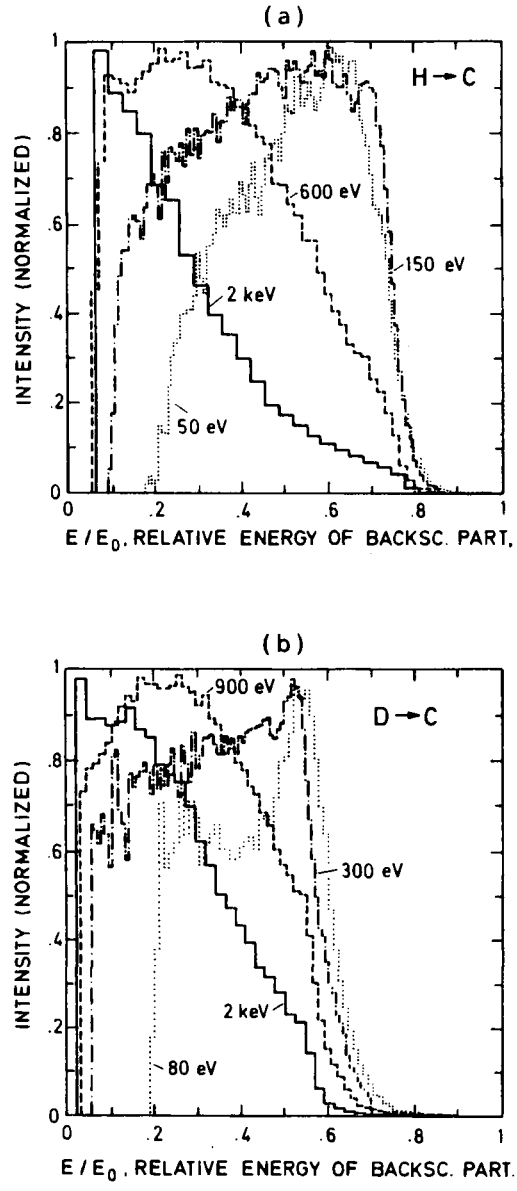

FIG. 12. Measured energy distributions of hydrogen backscattered from carbon. The distributions are normalized to the same maximum intensity: (a) 0.05, 0.15, 0.60, 2 keV H at normal incidence, and (b) 0.08, 0.3, 0.9, 2 keV D at normal incidence. (Fig. 2 of Ref. [43].)

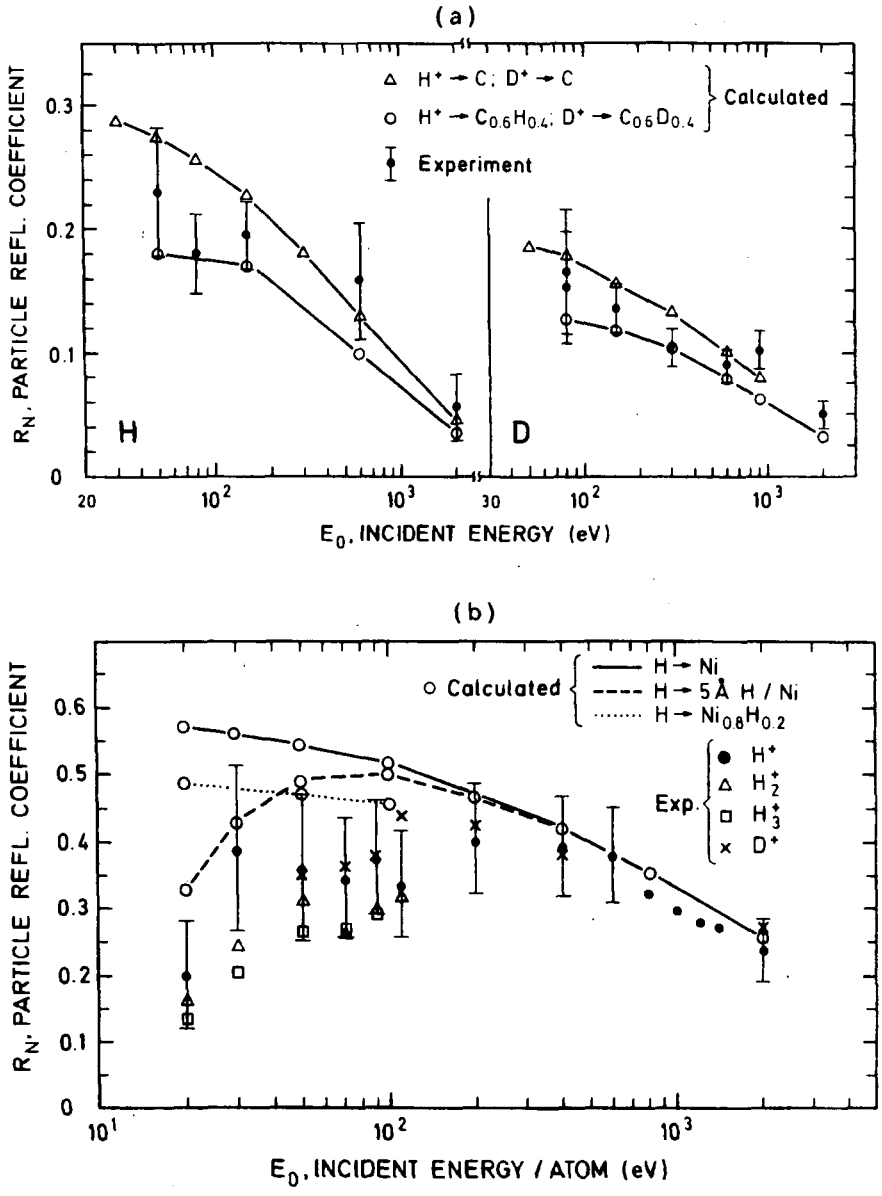

FIG. 13. Calculated and measured particle reflection coefficients for (a) H^+ and D^+ from carbon, and (b) H^+, H_2^+, H_3^+ and D^+ from nickel. The calculations account only for the reflected and sputtered hydrogen atoms with energies higher than the experimental 'cut-off' energy (≈ 10 eV). (Fig. 5 of Ref. [34].)

3. EXPERIMENTAL INVESTIGATIONS

Energy reflection coefficients have been measured by the heat flow from an irradiated target [29]. The experimental results for 10–80 keV bombardment of Al, Cu, Mo and W targets at angles of incidence $\alpha = 70°$, 80° and 85° show an approximate scaling with $\epsilon \cos^2 \alpha$, but they are systematically lower than the data determined by simulations with TRIM and MARLOWE. Different surface roughness may be responsible for the differences between the experimental and the calculated data. Values for R_E have also been determined with a very sensitive pyroelectric calorimeter for He, Ar and Xe bombardment of C, Si, Cu, Ag and Au at normal incidence in the energy range of 0.1–4 keV [42].

In another experiment, energy distributions of backscattered hydrogen atoms have been measured by a

time of flight method [34, 43] with a calibrated neutral hydrogen detector [44]. For the first time, hydrogen energy distributions down to an incident energy of 20 eV have been measured absolutely. Figure 12 clearly demonstrates the shift of the maximum in the energy distributions from low relative energies at high incident energy to high relative energies at low bombarding energy. The cut-off of the distribution at low energies (≈ 10 eV) is due to the sensitivity limit of the detector. The measured energy distributions show good agreement with data simulated by TRIM.SP (version TRSPVMC), taking into account the reduced reflection due to different hydrogen concentrations in carbon and due to the hydrogen adsorption on nickel.

From the integrations of the measured energy distributions, taking the azimuthal symmetry of the normal incidence into account, the particle reflection coefficients can be determined. A comparison of the R_N values determined in this way with simulated data is shown in Fig. 13. The overall good agreement gives additional confidence in the simulated data also for the low energy range.

4. ANALYTICAL APPROACHES

Wedell [45] used the single collision approximation, in combination with inelastic stopping proportional to the velocity, to derive simple formulas for the reflection coefficients at normal incidence:

$$R_N(\epsilon, \mu) = \frac{(1+\mu)^2}{\mu} \frac{f(\epsilon)\rho_T}{2\epsilon} \psi_0(m, \mu)$$

$$R_E(\epsilon, \mu) = \mu \frac{f(\epsilon)\rho_T}{2\epsilon} \chi_0(m, \delta)$$

where ρ_T is the reduced pathlength and $f(\epsilon)$ is Lindhard's potential function. The functions ψ_0 and χ_0 depend only on the mass ratio, $\mu = M_2/M_1 = \delta^{-1}$, and the power potential parameter m. For details see Ref. [45]. The mean reduced energy becomes proportional to the energy:

$$\frac{\bar{\epsilon}}{\epsilon} = \frac{R_E(\epsilon, \mu)}{R_N(\epsilon, \mu)} = \left(\frac{\mu}{1+\mu}\right)^2 \frac{\chi_0(m, \delta)}{\psi_0(m, \mu)}$$

The formulas are claimed to be as good as results from computer simulations in the limits

$$2 \leq \epsilon < \frac{a}{Z_1 Z_2 e^2} \frac{M_2}{M_1 + M_2} Z_1^{4/3} M_1 E_B$$

with $E_B = 25$ keV.

These formulas apply for normal incidence and for $M_2/M_1 > 1$. The ϵ-range of applicability becomes rather small for hydrogen and high-Z atoms. From trajectory calculations by simulation it seems rather doubtful that the single collision model is a good approach in the energy range given above [46].

Several papers investigate the backscattering at grazing incidence [47–49]. Small-angle scattering theory is used to determine energy distributions [47] which are highly peaked near the incident energy. The agreement with experimental data [50] and with simulated data is satisfactory. Small-angle multiple scattering theory was used in Refs [48, 49] to derive simple expressions for the reflection coefficients which are in reasonable agreement with the data calculated by TRIM. Again, surface roughness is not taken into account, which may be especially important for grazing incidence.

Another approach, the bipartition model originally used for electron transport, was applied by Luo and Wang [51] to determine particle reflection coefficients. This method is also based on the Boltzmann transport equation.

5. DATA COMPILATIONS AND EMPIRICAL FORMULAS

The most complete data compilation for values of the reflection coefficients has been performed jointly by the Radiation Centre of Osaka prefecture and the Data and Planning Centre of the National Institute for Fusion Science in Nagoya (former Institute of Plasma Physics of the Nagoya University). The procedures are described in several papers [52–54]. Normal incidence is treated in Refs [52, 53] and oblique incidence in Ref. [54]. Data of the reflection coefficients depending on the angle of incidence are collected in Ref. [55], together with plots for comparison of the data with the empirical formulas. Earlier data compilations [56] are revised in Ref. [57] and give the available data up to 1984. All the data provided are for H, D, T, ^{3}He and ^{4}He projectiles on 40 elemental targets and for H and ^{4}He projectiles on some compound targets. The data are stored in the computer centre of the National Institute for Fusion Science in Nagoya. Procedures are available to search for the reflection coefficients of

specific projectile/target combinations. The formulas used in Ref. [57] are as follows:

$$R_E = (0.705/f)/[1 + (\epsilon/0.047)^{0.597} + (\epsilon/0.619)^{1.5}]$$

$$r_E = 1/[1 + (\epsilon/0.133)^{0.285}] + 0.530/[1 + (\epsilon/85)^{-1.46}]$$

$$R_N = R_E/r_E$$

where

$$f = Z_1^{2/3} M_1^{-1/2} \left(\frac{M_1 + M_2}{M_2}\right)^{\frac{2\epsilon - 1}{\epsilon + 1}}$$

$$\frac{\rho_a}{\rho_t} = \{2\epsilon/\rho_n + [1/S_L + 1/(4 S_B)]^{-1}\}/S_a$$

ρ_a is the range of the projectile for which a stopping cross-section S_a is assumed. ρ_t is the pathlength of the projectile. ρ_n is the pathlength obtained by assuming only nuclear stopping, using the formula by Wilson et al. [58]:

$$\rho_n = \{\Gamma[0, (C - 1) \ln (B\epsilon)] - \Gamma[0, -2 \ln (B\epsilon)]\}/AB$$

$$\Gamma(v, x) = \int_x^\infty e^{-t} t^{v-1} dt$$

$$A = 0.56258, \quad B = 1.1776, \quad C = 0.62680$$

$$S_L = D \left(\frac{M_1 + M_2}{M_2 \zeta}\right)^{3/2} S_a$$

$$\zeta = (Z_1^{2/3} + Z_2^{2/3})^{1/2} Z_2^{-1/3}$$

where D is the correction factor for the low energy electronic stopping cross-section:

$$S_a = 0.0793 Z_1^{2/3} M_1^{-3/2} M_2 \epsilon^{1/2}$$

$$D = 0.2617 (1 + Z_2^{2/3})^{3/2} Z_2^{-1} A_1$$

where A_1 is the coefficient in the semi-empirical formula of Andersen and Ziegler [59] for the electronic stopping cross-section of hydrogen. S_B is the high energy stopping cross-section in LSS units:

$$S_B = 61.47 Z_1 Z_2^{-1} (Z_1^{2/3} + Z_2^{2/3})^{1/2} (M_1 + M_2) M_1^{-1}$$
$$\times \{\ln [\epsilon_B/(1 - \beta^2) + 1 + G/\epsilon_B] - \beta^2\}/I_0 \epsilon_B$$

with

$$\epsilon_B = 2 m_e c^2 \beta^2 / Z_2 I_0$$

$$I_0 = \begin{cases} 12 + 7 Z_2^{-1} & \text{for } Z_2 < 13 \\ 9.76 + 58.5 Z_2^{-1.19} & \text{for } Z_2 \geq 13 \end{cases}$$

$$G = \begin{cases} 100 Z_1/Z_2 & \text{for } Z_1 < 3 \\ 5 & \text{for } Z_1 \geq 3 \end{cases}$$

where $m_e c^2$ is the rest energy of the electron, $Z_2 I_0$ is the mean excitation energy of target atoms and β is the ratio of the projectile velocity to the velocity of light.

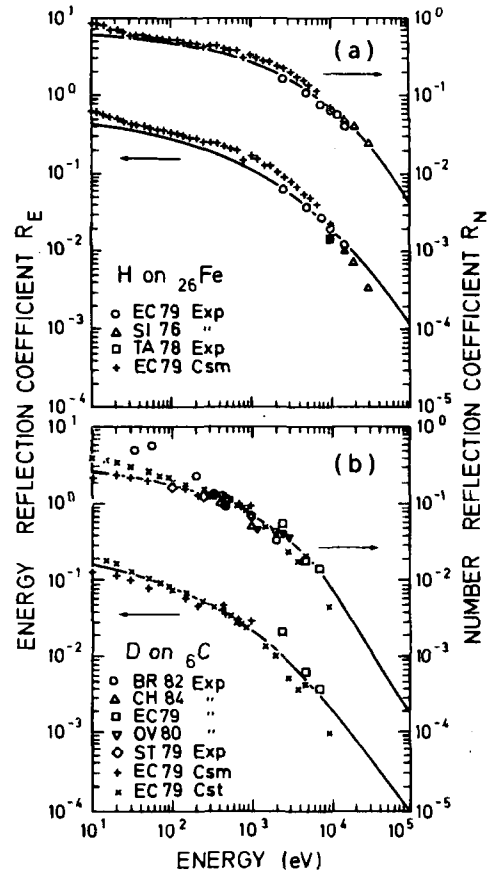

FIG. 14. Particle (or number) and energy reflection coefficients for (a) H on Fe, and (b) D on C, versus the reduced energy. The plots are taken from the data collection given in Ref. [57] (pages 46 and 62).

The above procedure is rather complicated; the ϵ-dependence of f is purely empirical (besides the range term) and may not be justified, taking the absolute errors of the available data into account.

Compound targets can be handled by the same formulas, but, instead of Z_2 and M_2, the values of Z_c and M_c have to be used. Z_c and M_c are the mean values of charge and mass of the target atoms with target composition X_mY_n ....

$$Z_c,\ M_c = (mX + nY + \ldots)/(m + n + \ldots)$$

The values of ϵ/ρ, S_L, S_B and S_A for the compound have to be determined by using Bragg's rule.

Figure 14 shows two examples, for D on C and H on Fe, for the fits from Ref. [57]. All earlier fit formulas were only valid in a limited energy range or for special projectile/target combinations. The fit formulas of Ref. [57] do not given the decrease of the reflection coefficients at very low energies for projectiles which bind chemically to the surface. The formulas fit data for heavy projectiles as long as $M_2/M_1 \geq 2$ [60]. Different formulas must be derived for $M_2/M_1 < 2$.

For the dependence of the reflection coefficients on the angle of incidence, the following formulas are given in Ref. [55]:

$$R(\alpha) = R(0) + [1 - R(0)]/(1 + a_1 \cot^{2a_2} \alpha)$$

where for R_N the values $a_1 = 7.38\ \epsilon^{0.359}$ and $a_2 = 0.836/\epsilon^{0.087}$, and for R_E the values $a_1 = 17.9\ \epsilon^{0.453}$ and $a_2 = 0.771/\epsilon^{0.014}$ apply.

6. CONCLUSIONS

All the data available before 1984 have been compiled in an earlier review [1]. The progress since then has been described in this paper. Important new experimental data have been determined for the low energy range down to 20 eV energy for incident hydrogen. Computer simulations brought many new data, especially for projectiles heavier than helium (see also Ref. [61]) — a field not covered in the last review. Heavy projectile (non-volatile) bombardment can drastically change the reflection coefficients because of implantation, which may lead to a strong dynamic behaviour. Other topics investigated in more detail are backscattering from hydrogen implanted targets with the contribution of sputtered hydrogen, and backscattering from rough surfaces using the fractal concept for describing these surfaces. The available computer generated data sets give information on the energy and angle of backscattered projectiles as well as on the reflection coefficients to be used as input in plasma codes dealing with the influence of surface facing the plasma. In some analytical approaches, backscattering for normal and grazing incidence have been investigated. The most complete collection of reflection coefficients are stored in the Data and Planning Centre of the National Institute for Fusion Science in Nagoya.

The available information from experimental and computed data gives a nearly complete picture of backscattering. Still missing are experimental results in the eV range and experimental information on surface roughness below 10 nm, down to atomic resolution, to check the models applied in computer simulations.

REFERENCES

[1] LANGLEY, R.A., BOHDANSKY, J., ECKSTEIN, W., MIODUSZEWSKI, P., ROTH, J., TAGLAUER, E., THOMAS, E.W., VERBEEK, H., WILSON, K.L., Data Compendium for Plasma-Surface Interactions, Nucl. Fusion, Special Issue 1984, IAEA, Vienna (1984).

[2] BEHRISCH, R., ECKSTEIN, W., in Physics of Plasma-Wall Interactions in Controlled Fusion (POST, D.E., BEHRISCH, R., Eds), Plenum Press, New York (1986).

[3] BASKES, M.I., J. Nucl. Mater. **128&129** (1984) 676.

[4] JACKSON, D.P., Radiat. Eff. **49** (1980) 233.

[5] ECKSTEIN, W., BIERSACK, J.P., Appl. Phys. A **38** (1985) 123.

[6] ECKSTEIN, W., BIERSACK, J.P., Z. Phys., B **63** (1986) 471.

[7] ROBINSON, M.T., J. Appl. Phys. **54** (1983) 2650.

[8] ECKSTEIN, W., BIERSACK, J.P., Z. Phys., B **63** (1986) 109.

[9] BIERSACK, J.P., ECKSTEIN, W., Appl. Phys. **34** (1984) 73.

[10] ROBINSON, M.T., TORRENS, I.M., Phys. Rev. **39** (1974) 5008.

[11] BØTTIGER, J., DAVIES, J.A., SIGMUND, P., WINTERBON, K.B., Radiat. Eff. **11** (1971) 69.

[12] BØTTIGER, J., DAVIES, J.A., Radiat Eff. **11** (1971) 61.

[13] BØTTIGER, J., WOLDER JÖRGENSEN, H., WINTERBON, K.B., Radiat. Eff. **11** (1971) 133.

[14] BØTTIGER, J., HOLCK, O., SIDENIUS, G., Nucl. Instrum. Methods **170** (1980) 499.

[15] ECKSTEIN, W., Self-Sputtering and Reflection, Rep. IPP-9/54, Max-Planck-Institut für Plasmaphysik, Garching (1986).

[16] ECKSTEIN, W., Data on Heavy Ion Reflection, Rep. IPP-9/61, Max-Planck-Institut für Plasmaphysik, Garching 1987).

[17] NIKIFOROV, V.I., PAVLENKO, V.I., SLABOSPITSKIJ, R.P., KHIRNOV, I.V., Simulation of Ion-Bombardment Sputtering for Multi-Component Solids. Attestation of the PERST Programming System, Preprint

KhFTI 87-58, Institute of Physics and Technology, Khar'kov (1987).
[18] LATTA, B.M., Nucl. Instrum. Methods **36** (1985) 479.
[19] FINK, D., BIERSACK, J.P., SANCHEZ, P.F., FICHTNER, P.F., Radiat. Eff. **103** (1987) 89.
[20] BIERSACK, J.P., Nucl. Instrum. Methods, Sect. B **19/20** (1987) 32.
[21] YAMAMURA, Y., Nucl. Instrum. Methods, Sect. B **33** (1988) 493.
[22] BATEMAN, G., Distribution of Neutrals Scattered off a Wall, Appl. Phys. Rep. No. 1, Princeton Plasma Physics Laboratory, Princeton, NJ (1980).
[23] ECKSTEIN, W., HEIFETZ, D.B., Data Sets for Hydrogen Reflection and their Use in Neutral Transport Calculations, Rep. IPP-9/59, Max-Planck-Institut für Plasmaphysik, Garching (1986).
[24] ECKSTEIN, W., HEIFETZ, D.B., J. Nucl. Mater. **145-147** (1987) 332.
[25] TAKEUCHI, W., YAMAMURA, Y., Radiat. Eff. **71** (1983) 53.
[26] BECERRA-ACEVEDO, R., TERREAULT, B., Nucl. Instrum. Methods, Sect. B **28** (1987) 1.
[27] SOTNIKOV, V.M., Zh. Tekh. Fiz. **51** (1981) 1045; Sov. Phys. — Tech. Phys. **26** (1981) 631.
[28] FINK, D., BIERSACK, J.P., STÄDELE, N., CHENG, V.K., Radiat. Eff. **104** (1987) 1.
[29] CHEN, C.K., BOHDANSKY, J., ECKSTEIN, W., ROBINSON, M.T., J. Nucl. Mater. **128&129** (1984) 687.
[30] KOBOROV, N., KURNAEV, V.A., TELKOVSKY, V.G., ZHABREV, G.I., Radiat. Eff. **69** (1983) 135.
[31] OEN, O.S., ROBINSON, M.T., J. Nucl. Mater **76&77** (1987) 370.
[32] ECKSTEIN, W., MÖLLER, W., Nucl. Instrum. Methods, Sect. B **7/8** (1985) 727.
[33] YAMAMURA, Y., Nucl. Instrum. Methods, Sect. B **33** (1988) 429.
[34] ARATARI, R., ECKSTEIN, W., Nucl. Instrum. Methods, Sect. B **42** (1989) 11.
[35] SOTNIKOV, V.M., Fiz. Plazmy **7** (1981) 431; Sov. J. Plasma Phys. **7** (1981) 236.
[36] KOBOROV, N.N., KARNAEV, V.A., SOTNIKOV, V.M., J. Nucl. Mater. **128&129** (1984) 691.
[37] PIGAROV, A.Yu., IGITKHANOV, Yu.L., Contrib. Plasma Phys. **30** (1990) 71.
[38] YAMAMURA, Y., MÖSSNER, C., OECHSNER, H., Radiat. Eff. **103** (1987) 25.
[39] RUZIC, D.N., CHIU, H.K., J. Nucl. Mater. **162-164** (1989) 904.
[40] AVNIR, D., FARIN, D., PFEIFER, P., J. Chem. Phys. **79** (1983) 3566.
[41] DAW, M.S., BASKES, M.I., Phys. Rev., B **29** (1984) 6443.
[42] WINTERS, H.F., COUFAL, H., RETTNER, C.T., BETHUME, C.S., Energy Transfer from Rare Gases to Surfaces: I. Collisions with Gold and Platinum in the Range 1-4000 eV, Int. Rep. IBM Research Division, San José, CA (1989).
[43] ARATARI, R., ECKSTEIN, W., J. Nucl. Mater. **162-164** (1989) 910.
[44] VERBEEK, H., ECKSTEIN, W., An Apparatus for the Production of a Neutral Hydrogen Beam in the Energy Range of 10 to 1000 eV, Rep. IPP-9/45, Max-Planck-Institut für Plasmaphysik, Garching (1983).
[45] WEDELL, R., Appl. Phys. A **35** (1984) 91.
[46] ECKSTEIN, W., Trajectories of Particles in a Solid and Moments of Depth Distributions, Rep. IPP-9/43, Max-Planck-Institut für Plasmaphysik, Garching (1983).
[47] VUKANIC, J.V., JANEV, R.K., Nucl. Instrum. Methods, Sect. B **16** (1986) 22.
[48] VUKANIC, J.V., JANEV, R.K., HEIFETZ, D.B., Nucl. Instrum. Methods, Sect. B **18** (1987) 131.
[49] VUKANIC, J.V., JANEV, R.K., MEYER, F.W., Phys. Lett., A **131** (1988) 294.
[50] HOU, M., ECKSTEIN, W., VERBEEK, H., Radiat. Eff. **39** (1978) 207.
[51] LUO, Z., WANG, S., Phys. Rev. B **36** (1987) 1885.
[52] MORITA, K., TABATA, T., ITO, R., J. Nucl. Mater. **128&129** (1984) 681.
[53] TABATA, T., ITO, R., MORITA, K., TAWARA, H., Nucl. Instrum. Methods, Sect. B **9** (1985) 113.
[54] TABATA, T., ITO, R., MORITA, K., TAWARA, H., Radiat. Eff. **85** (1985) 45.
[55] TABATA, T., ITO, R., ITIKAWA, Y., ITOH, W., MORITA, K., TAWARA, H., Dependence of the Backscattering Coefficients of Light Ions Upon Angle of Incidence, Rep. IPPJ-AM-34, Institute of Plasma Physics, Nagoya (1984).
[56] TABATA, T., ITO, R., ITIKAWA, Y., ITOH, N., MORITA, K., Data on the Backscattering Coefficients of Light Ions from Solids, Rep. IPPJ-AM-18, Institute of Plasma Physics, Nagoya (1981); At. Data Nucl. Data Tables **28** (1983) 493.
[57] ITO, R., TABATA, T., ITOH, N., MORITA, K., KATO, T., TAWARA, H., Data on the Backscattering Coefficients of Light Ions from Solids (A Revision), Rep. IPPJ-AM41, Institute of Plasma Physics, Nagoya (1985).
[58] WILSON, W.D., HAGGMARK, L.G., BIERSACK, J.P., Phys. Rev. B **15** (1977) 2458.
[59] ANDERSEN, H.H., ZIEGLER, J.F., Hydrogen Stopping Powers and Ranges in all Elements, Pergamon Press, New York (1977).
[60] TABATA, T., ITO, R., Present Status of Data Compilation on Ion Backscattering, Rep. IPPJ-AM-64, Institute of Plasma Physics, Nagoya (1989).
[61] ECKSTEIN, W., Computer Simulation of Ion-Solid Interactions, Springer-Verlag, Heidelberg (1991).
[62] MÖLLER, W., ECKSTEIN, W., BIERSACK, J.P., Comput. Phys. Commun. **51** (1988) 355.

TRAPPING, DETRAPPING AND RELEASE OF IMPLANTED HYDROGEN ISOTOPES

K.L. WILSON, R. BASTASZ, R.A. CAUSEY
Sandia National Laboratories,
Livermore, California,
United States of America

D.K. BRICE, B.L. DOYLE, W.R. WAMPLER
Sandia National Laboratories,
Albuquerque, New Mexico,
United States of America

W. MÖLLER, B.M.U. SCHERZER
Max-Planck-Institut für Plasmaphysik,
Garching bei München,
Germany

T. TANABE
Osaka University,
Osaka,
Japan

ABSTRACT. The paper gives a review of the theory and experimental data currently available for hydrogen isotope trapping and release in various plasma facing materials used in fusion reactor experiments. A transport formalism that includes bulk trap sites, surface barriers and thermal gradients is described. The behaviour of implanted hydrogen in beryllium, tungsten and molybdenum is discussed in detail. Because of the widespread usage of carbon materials in present day fusion experiments, the theory and database for carbon at elevated temperatures are also discussed.

1. INTRODUCTION

Hydrogen isotope trapping and release by plasma facing materials control predominantly fuel retention and recycling in magnetic confinement fusion devices. With the development of fusion technology, it became clear that plasma–wall interactions involving hydrogenic particles have a major influence not only on the lifetime of the first wall and other plasma facing components but also on the fundamental properties of heated plasmas. Consequently, an understanding of the particle and energy flow between materials and plasmas is necessary for optimizing plasma performance as well as for predicting the component lifetimes. In the next generation of fusion experiments, tritium fuel will be used extensively. The inventory of tritium that is retained when materials are exposed to tritium plasmas also causes concern. A knowledge of the trapping and release characteristics of plasma facing materials is essential to ensure safe radioactivity levels in such advanced fusion experiments.

Over the past decade, hydrogen trapping and release in fusion materials have been studied extensively in the laboratory and in large scale fusion experiments. In parallel, a phenomenological theory based on simple diffusion in the presence of bulk and surface defects has been developed to account for the transport of hydrogen isotopes in and out of materials during and after exposure to hydrogenic plasmas. This work has added much to our understanding of hydrogen behaviour in fusion materials and has enabled a realistic consideration of the consequences of hydrogen trapping and release in the design of fusion experiments.

In recent years, it has been endeavoured to reduce Z_{eff} in fusion experiments and, consequently, there has been increased use of low-Z refractory plasma facing materials such as carbon and beryllium. However, in the course of the ITER design process there has been a revival of the idea of using high-Z materials such as molybdenum or tungsten in cases where a low plasma edge electron temperature ($\simeq 10$ eV) can be maintained in a high recycle divertor. Therefore, we give first a

short summary of the theory of hydrogen trapping and release in metals, based on the 1984 Nuclear Fusion Data Compendium for Plasma-Surface Interactions [1], and discuss also the subsequent theoretical developments [2]. Then, we present a review of the experimental database for beryllium, tungsten and molybdenum. The paper concludes with a major section on theory and experiment for hydrogen behaviour in carbon materials.

2. TRAPPING AND RELEASE OF HYDROGEN IN METALS

2.1. Theory of hydrogen isotope retention/release

2.1.1. Formalism for metals

An implanted hydrogen atom that comes to rest in a metal at or above room temperature will begin to undergo thermally activated diffusion. It can become trapped in the lattice at radiation damage (e.g. a vacancy) or through an intrinsic defect (e.g. a grain boundary); it can enter a second phase (e.g. metal hydride) or it can reach the surface and be thermally desorbed as a molecule. (Non-thermal desorption by photons, electrons or ion impact is not considered here.) In the presence of a source (implanted flux) and sinks (traps), these thermally activated processes are described by a set of coupled differential transport equations

$$\frac{\partial C}{\partial t} = D\frac{\partial^2 C}{\partial x^2} + G - \frac{\partial C_T}{\partial t} \quad (1)$$

$$\frac{\partial C_T}{\partial t} = \frac{DC(C_T^0 - C_T)}{\lambda^2} - C_T \nu_{exp}(-E_T/kT) \quad (2)$$

Equation (1) is the diffusion equation for a mobile hydrogen concentration C, with a lattice diffusivity D, an implantation source term G, and the conversion of mobile hydrogen to trapped hydrogen C_T. Equation (2) describes the change in the concentration of trapped hydrogen C_T with time, where C_T^0 is the total concentration of saturable traps, E_T is the detrapping energy, and λ and ν are material constants.

The appropriate boundary condition for the release rate of hydrogen in the form of molecules J_{H_2} is generally assumed to be second-order, molecular recombination limited kinetics:

$$J_{H_2} = -D\frac{\partial C}{\partial x}\bigg|_{x=0} = K_r C(0)^2 \quad (3)$$

where K_r is the molecular recombination rate constant and C(0) is the bulk concentration of mobile hydrogen just beneath the surface.

Equations (1) to (3) are greatly simplified. For this discussion, it is important to highlight several parameters that control hydrogen trapping and release for materials.

The hydrogen diffusivity D is a measure of the hydrogen mobility in a perfect lattice. During a time t, hydrogen will migrate to a mean square radius $\overline{r^2}$ equal to 6Dt by a random-walk diffusion process [3]. The diffusivity D is generally of the form

$$D = D_0 \exp(-E_D/kT) \quad (4)$$

TABLE I. SELECTED VALUES OF HYDROGEN DIFFUSIVITY AND SOLUBILITY

Material	D_0 ($cm^2 \cdot s^{-1}$)	E_D (eV)	S_0 ($H/cm^3(atm)^{1/2}$)	E_S (eV)	Ref.
Aluminium	2.1×10^{-1}	0.47	3.1×10^{21}	0.84	[5]
Copper	1.1×10^{-2}	0.40	1.3×10^{20}	0.37	[5]
Inconel 718	1.0×10^{-2}	0.52	4.1×10^{19}	0.06	[6]
Nickel	6.9×10^{-3}	0.42	3.1×10^{20}	0.16	[7, 8]
Type 304 stainless steel	2.0×10^{-3}	0.54	7.7×10^{19}	0.11	[9]
Titanium	1.8×10^{-2}	0.54	1.5×10^{20}	-0.49	[10, 11]

TABLE II. ESTIMATES OF HYDROGEN TRAPPING CHARACTERISTICS

Material	C_T^0 ratio of H to host	E_T (eV)	Ref.
Aluminium	0.05	1.5	[12]
Stainless steel	0.01	0.8–1.0	[13]

where D_0 is a material constant, E_D is the migration energy, k is Boltzmann's constant and T is the absolute temperature.

The hydrogen solubility S is the concentration of hydrogen atoms in a solid that is in equilibrium with hydrogen gas at a pressure p:

$$S = S_0 p^{1/2} \exp(-E_S/kT) \quad (5)$$

where S_0 is a material constant and E_S is the heat of solution, which can be either positive (endothermic) or negative (exothermic), indicating that energy is either expended or liberated when hydrogen is absorbed into the material [4].

Table I summarizes the diffusivities and solubilities of hydrogen in various metals [5–11]. Isotopic differences between ^1H, ^2H and ^3H are small compared to uncertainties in other critical trapping parameters and therefore are not considered. The metals in Table I have comparable diffusivities and their solubilities can vary significantly.

Traps for hydrogen are generally characterized by a trap concentration C_T^0 (expressed as the ratio of hydrogen atoms to host atoms) and a detrapping energy E_T. Although hydrogen traps can have multiple occupancy, be virtually unsaturable (i.e. bubbles) or even represent the growth of a new phase (e.g. a metal hydride), a saturation of one hydrogen per trap is assumed in Eq. (2) for simplicity. Table II presents estimates of C_T^0 and E_T for hydrogen trapped within the projected range depth for hydrogen ions implanted in two typical metals [12, 13].

Since the release of hydrogen atoms from traps (C_T) into mobile hydrogen (C) follows first-order kinetics (Eq. (2)), the detrapping energy can easily be related to the temperature at which hydrogen is released from the traps. As a rule of thumb, trapped hydrogen with E_T = 1 eV will detrap at ≈400 K; with E_T = 2 eV at 800 K, etc. Hence, while trapping in stainless steels decreases rapidly for temperatures above ~400 K (1 eV), hydrogen is strongly trapped in aluminium at temperatures up to ~600 K (1.5 eV).

The molecular recombination rate constant K_r controls the thermal release of hydrogen molecules at the surface of the material under implantation. The nature of K_r has been the subject of numerous experimental and theoretical studies [14–34]. Suffice it to say that there is no general agreement either in the database or in the rate limiting steps that control molecular recombination. The parameter K_r can be directly inferred from Eq. (3) if the hydrogen flux J_{H_2} and the concentration of mobile hydrogen C(0) are measured. However, techniques to measure C(0) cannot easily distinguish mobile from trapped hydrogen and hence this approach has not been very successful. Recombination coefficients are also affected very strongly by surface impurities. Sub-monolayer coverages of oxygen on iron have been shown to decrease the recombination coefficient by orders of magnitude [3], and thicker surface oxides can also change the activation energy of K_r [33]. A meaningful comparison between theory and experiment thus requires careful consideration of the influence of surface impurities. Theoretical approaches generally assign the rate limiting step either to associative recombination of hydrogen atoms on the surface or to some step involving the transfer of an atom from a bulk site to a surface site. Both general approaches appear to have some validity within the parameter space dictated by the incident flux of hydrogen, the surface temperature and the material's other hydrogen transport parameters.

2.2. Models for hydrogen transport

2.2.1. Numerical models

A number of computer codes, such as PERI [35], TMAP [36], DIFFUSE [37] and PIDAT [38], have been developed to numerically solve the equations for hydrogen transport outlined in the previous section. These codes have the advantages of providing exact time dependent solutions for hydrogen behaviour in a material and can, in principle, include important non-linear effects such as position and concentration varying diffusivities, and mass diffusion from a temperature gradient. A disadvantage of the numerical approach is the inability to infer physical trends without resorting to a time consuming matrix of computer runs.

2.2.2. Analytical approximations

As an alternative to the numerical solution to the diffusion equation, Ali Khan et al. [17] and Doyle and Brice [39–43] have developed theories using simplified

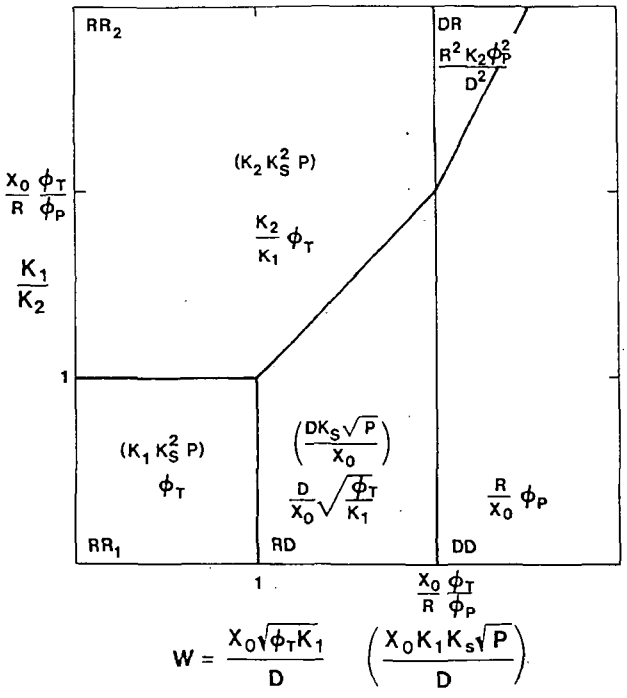

FIG. 1. Transport classification space for permeation of hydrogen isotopes through wall membranes [39].

solutions to the diffusion equation and dimensionless transport parameters. The transport parameter concept results in a natural classification of the transport behaviour of hydrogen in all materials for which the solutionized hydrogen is mobile. The analytical results provide physical insight into the processes governing hydrogen permeation and inventory and also permit simple checks on the accuracy of numerical calculations.

In the formalism of Doyle and Brice [39–43], the steady state hydrogen transport is characterized in terms of three dimensionless parameters, W, α and y^2. W is the ratio of a characteristic diffusion time and a characteristic surface recombination response time. Similarly, α is the ratio of the average depth of hydrogen injection into the material to the effective material thickness, while y^2 is the ratio of the recombination efficiency at the outer surface to that at the inner surface. These parameters are simple functions of the various parameters of the materials.

The equations developed for the transport parameter treatment provide a natural partition of the parameter space of (W,α,y^2) according to whether the hydrogen efflux at the two surfaces is diffusion limited (D) or recombination limited (R). For example, when the outer (e.g. plasma) side efflux at the two surfaces is recombination limited and the inner (e.g. coolant) side efflux is diffusion limited, we label the region RD, and the hydrogen permeation rate is given by the expression $J = \phi_T\alpha/W$ (ϕ_T being the injected hydrogen flux density). The five characteristic regions are RR_1, RR_2, RD, DR and DD, where the two RR regions differ in the surface recombination rate that governs the hydrogen efflux. Within each region a simple analytical formula, characteristic of that region, gives $J(W, \alpha, y^2)$.

Figure 1 illustrates the partition of a parameter space into the five regions, showing a W, y^2 plane for a particular value of α ($= R/X_0$). The expressions in the figure give the hydrogen permeation rate in terms of the various materials and plasma parameters. The dependence of W and y^2 on these parameters is also indicated. The results in Fig. 1 are for a two-component plasma, one component being a true plasma and the second component being a background gas. Expressions in parentheses give the permeation rate when only gas is present (i.e. the plasma flux ϕ_p is small), while the expressions for simultaneous injection of gas and plasma are not enclosed. The importance of gas driven permeation has also been discussed by Tanabe [44]. Gas driven permeation cannot occur in the DR and DD regions, and so no parenthetical expressions appear for these cases. Also, we note that in the RD region the gas driven and the plasma driven permeation exhibit an interference (synergistic) effect. That is, the net permeation is less than the sum of plasma permeation alone and gas permeation alone. Since this region represents the normal operating region of many reactor designs, the effect is beneficial since net permeation is reduced.

2.2.3. *MEASTRI code*

MEASTRI, a hybrid analytical/Monte Carlo code, has been developed by Brice [45] for evaluating particle transport in solids. The code provides for the simultaneous implantation of multiple atomic species and includes the buildup to saturation and isotope exchange. These effects have been shown to be important for hydrogen implantation. In the analytic portion of the code, both sputtering and diffusion are included in a natural way, and disparate time-scales for the various processes (implantation, sputtering, diffusion, etc.) are easily accommodated. The code is particularly useful for high fluence implantations.

Atomic concentrations in the near surface region of a solid exposed to energetic incident atomic projectiles, e.g. a tokamak plasma, are propagated in time by the code through the method of equivalent atomic stopping (MEAS). In MEAS, a spatially inhomogeneous target,

with atomic number densities for k-type atoms given by $N_k(x,t)$, is replaced by a spatially homogeneous target of a preselected standard for average atomic type. This is accomplished by replacing N_k atoms of type k by $\epsilon_k N_k$ standard atoms, where ϵ_k is a constant which may be regarded as the relative stopping power of k-type atoms for the incident projectiles. The standard target is then spatially homogeneous with atomic number density N_{std} by defining a new depth scale, z(x,t), where

$$z(x,t) = (N_{std})^{-1} \Sigma_k \epsilon_k(1) \int_{x_0(t)}^{x} N_x(x',t)dx \qquad (6)$$

Here, $x_0(t)$ gives the instantaneous location of the target surface which is uniformly eroded by sputtering.

In the inhomogeneous target the implantation source profiles are $\{P_k(x,t)\}$, where $P_k(x,t)dx$ is the probability that a k-type atom implanted at time t will come to rest in the intervals (x,s + dx). In the homogeneous target, $\{P_k\}$ becomes replaced by $\{Q_k\}$, where

$$Q_k(z)dz = P_k(x,t)dx \qquad (7)$$

and, as indicated, the transformation eliminates the time dependence in these source profiles, $\{Q_k\}$. It is this transformation which lies at the heart of the MEAS procedure and the MEASTRI code.

It should be noted that other codes also exist for dealing with this problem. Analytic codes [46, 47] are able to easily accommodate effects such as diffusion, sputtering, trapping, etc., but it is difficult with such procedures to deal with the time dependence of the $\{P_k\}$, which are normally obtained through an auxiliary (external) calculation. Similarly, Monte Carlo codes [48–52] can easily evaluate the evolution of $\{P_k(x,t)\}$ simultaneously with $\{N_k(x,t)\}$, but they are unable to effectively incorporate diffusion, etc. Hybrid codes, however, can overcome these difficulties through a transformation of co-ordinates. This transformation eliminates the time dependence of the $\{P_k\}$, which may then be evaluated by a typical Monte Carlo procedure (i.e. the $\{Q_k\}$ can be obtained in this way and the analytical procedures use this information to determine the $\{N_k(x,t)\}$). Although the analytic solution is obtained in the co-ordinate, the reverse of the transformation, Eq. (7), is easily accomplished to complete the solution.

The sputtering model built into MEASTRI assumes a uniform erosion of the target surface. The velocity of surface erosion, $v_0(t) = dx_0/dt$, is determined from the elemental target sputtering coefficients S_j,k (the sputtering coefficients for j-projectiles incident on k-targets) with an interpolation procedure to determine the effective sputtering coefficients for non-elemental targets. The weighting factors in the interpolation procedure are proportional to the surface atomic concentrations $\{N_k(x_0,t)\}$ and the equivalency factors $\{\epsilon_k\}$. This manner of weighing the elemental contributions to sputtering is consistent with the spirit of the Sigmund model of ballistic sputtering [53], although other sputtering mechanisms could also be included in the code.

3. HYDROGEN RETENTION AND RELEASE CHARACTERISTICS FOR BERYLLIUM

Recent success in the JET tokamak has revived the interest in beryllium as a plasma facing material. The hydrogen trapping characteristics of beryllium have been recently reviewed [54]. Hydrogen interactions with elemental beryllium are limited. While beryllium is known to form a covalent hydride that can be made by the decomposition of organo-metallic compounds, the crystalline hydride phase has never been synthesized directly from the elements [4]. The hydrogen solubility and diffusivity in pure beryllium are a matter

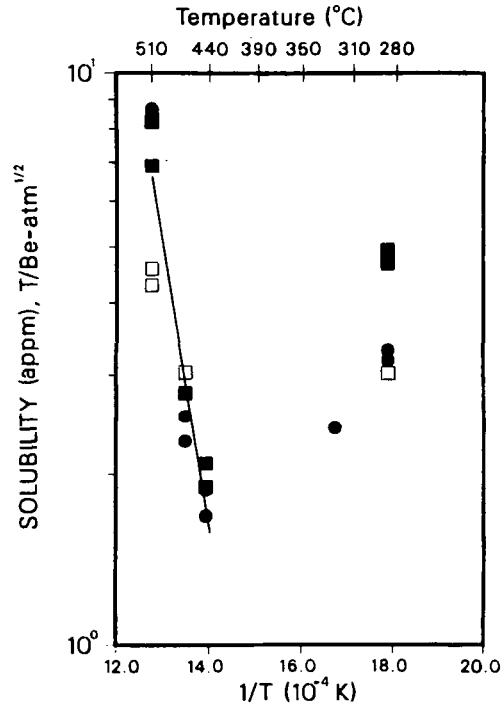

FIG. 2. Arrhenius plot of the solubility of tritium in beryllium for three sample configurations [58]: ■ 0.057–0.08 mm thick, 99.8% Be; ● 0.10–0.15 mm thick, 99.8% Be; □ 0.057–0.08 mm thick, 98.5% Be.

of controversy. Pemsler and Rapperport [55] inferred a minimum hydrogen diffusivity of 8×10^{-10} cm^2/s at 1025 K and a solubility 'limit' of 9×10^{14} H/cm^3 (7×10^{-9} atom fraction) over the temperature range 625–1325 K from proton implantations. In a detailed tritium charging/desorption experiment by Jones and Gibson [56] it was found that the solubility of tritium in beryllium was 6×10^{-6} atom fraction/atm$^{1/2}$, independent of temperature. They also determined the diffusivity to be 3×10^{-7} exp(-0.19 eV/kT) cm^2/s. Al'tovskij and Eremin [57] measured gas driven permeation through beryllium membranes and tubes, and reported large variations in permeability (the product of diffusivity and solubility), depending on the beryllium grain size. More recently, Swansiger [58] determined the tritium solubility in high purity beryllium, using tritium gas charging followed by tritium dissolution counting. As shown in Fig. 2, he found an intrinsic lattice solubility which is extremely endothermic, in marked contrast to the virtually athermal solubility reported by Jones and Gibson [56]. Swansiger also found evidence for strong extrinsic trapping of tritium at the $\approx$1–10 appm level for temperatures below 600 K. The temperature dependence of this intrinsic bulk trap suggests an activation energy for detrapping of $\approx$ 1–1.5 eV. The best values for hydrogen solubility and diffusivity in beryllium are:

$$S = 18.4 \exp(-1.0 \text{ eV/kT}) \text{ atom fraction/atm}^{1/2}$$

$$D = 3 \times 10^{-7} \exp(-0.19 \text{ eV/kT}) \text{ cm}^2\text{/s}$$

The nature of trapping of hydrogen isotopes in beryllium during energetic ion implantation has been studied by several investigators. After low fluence implantation, hydrogen is observed to accumulate in sites near the basal plane [59]. At higher fluences the precipitation of microscopic bubbles and more macroscopic blisters have been reported [55, 60]. As in the case of other low atomic number materials such as graphite and TiC, implantation of hydrogen isotopes can lead to significant saturation trapping in the near surface region of beryllium. Liu et al. [61] reported a saturation retention of 4×10^{17} D/cm^2 following 10 keV D$^+$ implantation at temperatures of $\lesssim$425 K. X-ray analysis of the samples after implantation did not show any evidence of crystalline beryllium hydride, although the possibility of an amorphous hydride state could not be ruled out. Langley [62] observed similar trapping of deuterium in a surface layer extending over the range of the implanted D$^+$ ions, although the magnitude of the reported retention was significantly higher than that found by other investigators. Pontau et al. [63] also observed that, unlike in the case of nickel, during simultaneous H$^+$/He$^+$ implantation the implanted hydrogen competes

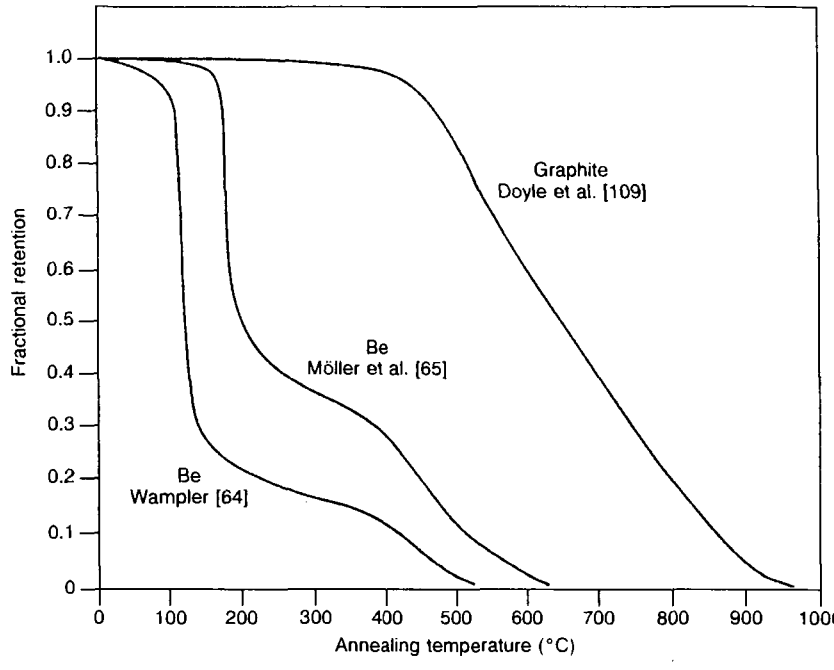

FIG. 3. Comparison of thermal annealing of beryllium and graphite that were implanted with deuterium at room temperature [54].

with the helium for trapping sites in beryllium. This observation is consistent with the stronger hydrogen trapping in beryllium compared to that in nickel.

The most systematic studies of the retention of implanted hydrogen isotopes in beryllium have been conducted by Wampler [64] and by Möller et al. [65]. In the experiments performed by Wampler [64], nuclear reaction analysis was used to determine the deuterium retention during irradiation and during post-irradiation annealing. Deuterium ion energies of 0.5, 1.5 and 3.0 keV were used in the experiments. At low fluences, virtually all of the deuterium was retained, but the retention saturated at higher fluences. At room temperature, the saturation concentration was determined to be 0.31 D/Be. A similar behaviour was reported for an experiment performed at 473 K, but a lower saturation value was found. An isochronal annealing programme showed the release of hydrogen to be characterized by a relatively narrow detrapping stage at 400 K, followed by a broad stage at approximately 675 K. For the saturated samples, most of the release occurred at the lower temperature. The release behaviour was described as being controlled by a 1 eV trap with a concentration of 0.25 atom fraction and a 1.8 eV trap with a concentration of 0.05 to 0.10 atom fraction. The higher energy traps must be filled before occupation of the lower energy traps.

Further hydrogen implantation experiments on beryllium were also performed by Möller et al. [65] over a range of implant energies and temperatures. Figure 3 compares the data of Möller et al. for the deuterium retention in beryllium as a function of temperature during post-irradiation annealing with those of Wampler [64]. The bombardments in both cases were carried to saturation at room temperature. The results have been changed to fractional retentions to account for the difference in implant energies. For beryllium, the 1 eV trap energy probably corresponds to amorphous beryllium hydride [66]. Beryllium hydride decomposes at 400 K [67], the same temperature as that found for the sharp release stage of the deuterium implanted beryllium. The 1.8 eV trap is probably due to trapping at point defect sites. In the work by Swansiger [58] on the solubility of tritium in beryllium, evidence of intrinsic trapping at temperatures in the range of 500–700 K was reported. This observation is consistent with the higher trap energy found in the implantation experiments.

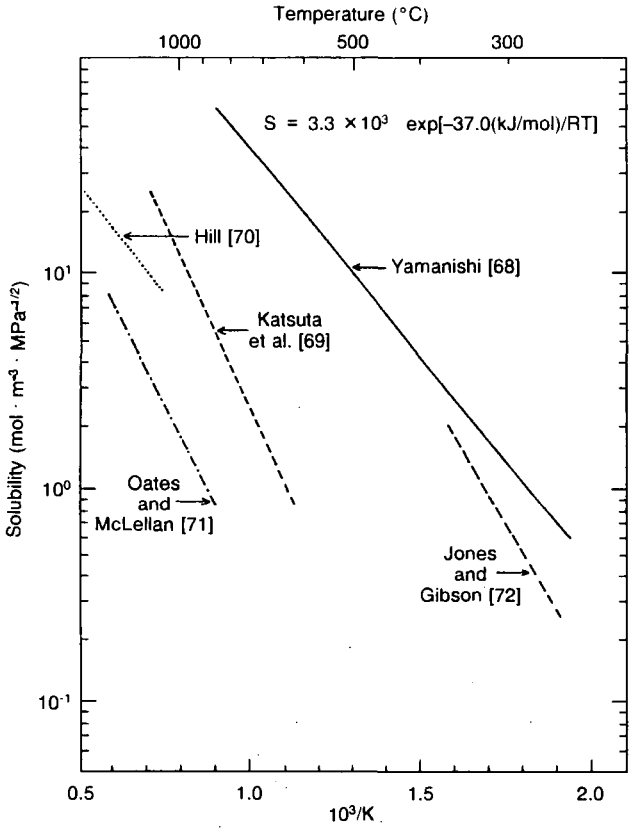

FIG. 4. Arrhenius plot of the solubility of hydrogen isotopes in molybdenum by various investigators. The analytic expression for S is due to Kanno [83].

4. HYDROGEN BEHAVIOUR IN MOLYBDENUM AND TUNGSTEN

4.1. Introduction

Because of their refractory nature and good thermal properties, molybdenum (Mo) and tungsten (W) are considered to be alternatives to graphite as plasma facing materials, especially for a divertor plate operated in the low edge temperature/high recycling plasma mode. In addition, the tritium inventory in these high-Z metals is expected to be much less than that in graphite.

Although various studies on hydrogen behaviour in Mo and W have been carried out, the literature data for the behaviour of hydrogen in Mo and W show some uncertainty and/or discrepancies which are probably due to their bcc nature and high melting point. Similar to bcc iron (Fe), in which significant hydrogen trapping occurs below 500 K and diffusion data are scattered by several orders of magnitude, earlier data for solubility (S), diffusivity (D) and permeability (Φ) of hydrogen in W and Mo could have

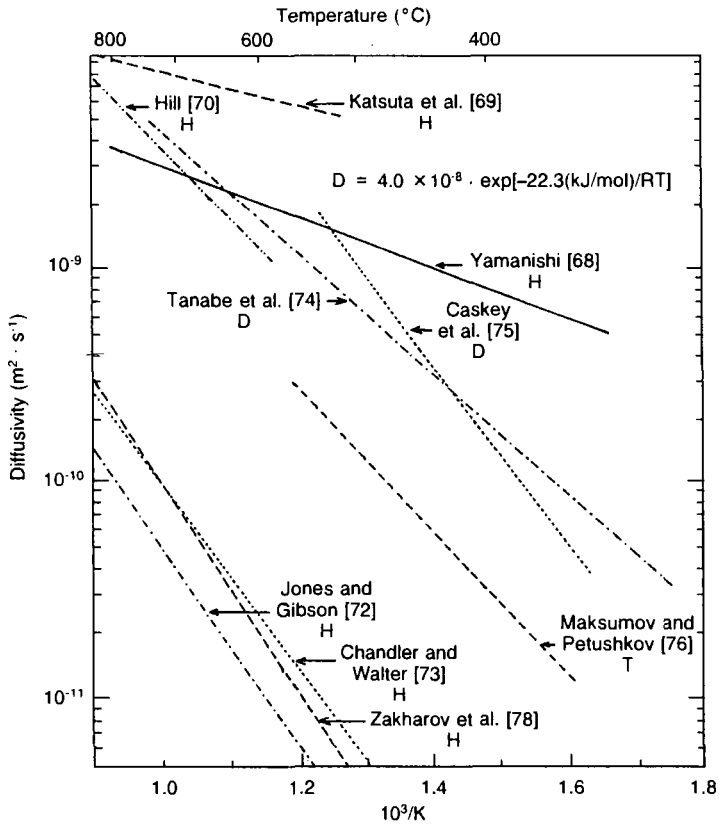

FIG. 5. Arrhenius plot of the measurements of the diffusivity of hydrogen isotopes in molybdenum [68-89]. The analytic expression for D is due to Kanno [83].

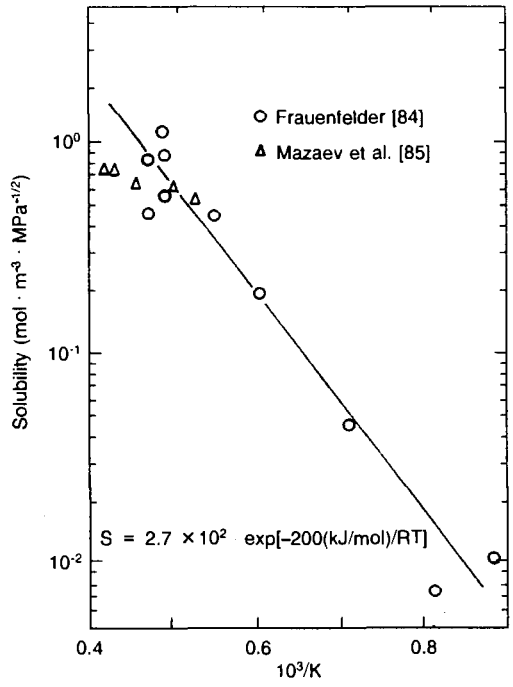

FIG. 6. Arrhenius plot of various measurements of hydrogen solubility in tungsten [83-85].

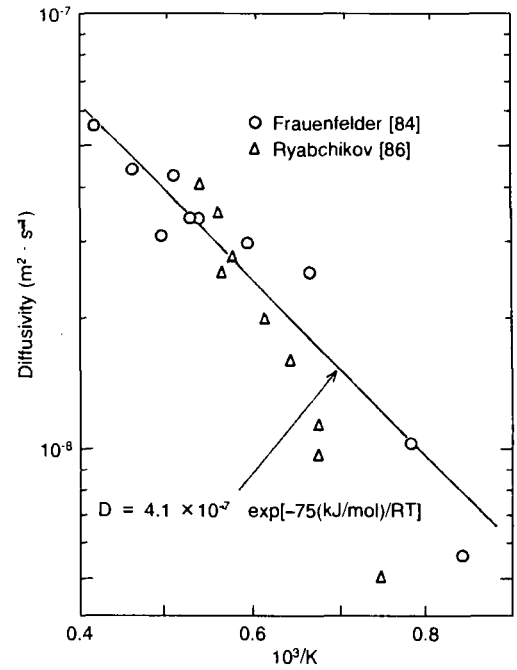

FIG. 7. Arrhenius plot of various measurements of hydrogen diffusivity in tungsten [83, 84, 86].

been influenced by the sample history and by impurites on the surface and in the bulk.

Here we first summarize the data for solubility and diffusivity of hydrogen in Mo and W, and then discuss the effects of implantation on hydrogen behaviour in these metals. Unfortunately, most data were taken more than a decade ago, and the specimens utilized at that time were made by powder sintering, which might have introduced some errors due to impurities and lattice imperfections.

4.2. Solubility, diffusivity and permeability in Mo and W

The hydrogen solubility (S) and diffusivity (D) in Mo and W are respectively given in Figs 4-7 [68-89]. The equations in the graphs are recommended values by Kanno [83]. Since solubility is determined in equilibrium or at steady state, the reported data are generally reliable. On the other hand, the diffusivity determined from time transient behaviour is influenced by bulk trapping and surface processes.

Owing to their high melting temperatures, both metals are usually produced by powder sintering, which introduces many impurities and lattice imperfections. Both work potentially as trapping sites, as in the

case of hydrogen trapping in bcc Fe [90]. Therefore, diffusion data may be influenced by the manufacturing process and the sample history.

Comparing various hydrogen diffusion coefficients in bcc metals, Katsuta et al. [91] have demonstrated that the activation energy for hydrogen diffusion in bcc metals is not very large; they have also reported the largest diffusion coefficient [69] with the smallest activation energy which is consistent with the results of Yamanishi [68], as shown in Fig. 4. Applying the ion driven permeation technique, which gives accurate diffusion coefficients in Ni and Cu, Tanabe et al. [74] have also obtained rather large diffusion coefficients and suggested that the large scatter in the data is due to trapping, as in the case of Fe [90].

Although the recommended equations in Figs 6 and 7 for W were made by Kanno [83] more than a decade ago, almost no new data have been added and no new recommendation is possible.

4.3. Effect of impurities and lattice imperfections

4.3.1. Impurities

Since the oxides of Mo and W are volatile, surface oxides are easily removed by high temperature annealing in vacuum. The effect of water vapour, included in H_2 gas as the main impurity, on hydrogen permeation in Mo is very small [92]. Therefore, it seems difficult to employ an oxide layer as a permeation barrier. Carbon and sulphur, the main impurities, are difficult to remove because of high temperature stability of the metal carbide and sulphide, but their impact on hydrogen properties is unknown.

4.3.2. Lattice imperfections

In their early re-emission measurements, McCracken and Erents [93] have shown that deuteron bombardment of Mo produces irradiation damage which traps large amounts of deuterium. Since then, several studies of re-emission, thermal desorption and depth profiling of H implanted in Mo have been performed and a significant concentration of H is found to be trapped by the H implantation near room temperature [94–98]. This trapping can, in turn, result in flaking and embrittlement of the subsurface region [93]. Lanford et al. [99] have also reported large trapping of H in W predamaged by He irradiation. In Mo, hydrogen is considered to be trapped at vacancies with a trapping energy as high as 1 eV [95]. Channelling techniques have determined the lattice location, as reviewed by Myers et al. [100].

Gorodetsky et al. [101] have reported an anomaly in the temperature dependence of plasma driven permeation of Mo, which was attributed to co-diffusion of H and vacancies, but it could not be reproduced by Scherzer and Børgesen [161]. Tanabe et al. [102] have observed a transient permeation 'spike' in ion driven permeation, which is interpreted as enhanced release of implanted H by the irradiation damage. Transient behaviour is influenced by trap formation or ion irradiation, but no quantitative estimation is possible at present and more data are needed, especially at elevated temperature. It should be noted, however, that the trapping may not significantly influence steady state permeation. Katsuta et al. [69] have shown that the effect of neutron irradiation of Mo on H permeation is very small.

In spite of large numbers of surface adsorption studies of H on W single crystals, few data have been reported on the behaviour of implanted H in W, except for depth profile data [57] and the study of ion driven permeation of Perkins and Noda [103]. It is not possible to develop a detailed model for the behaviour of H implanted in W using the existing database.

As described above, the sintered materials have been used in most of the earlier work, and the reported data are possibly influenced by impurities and/or lattice imperfections. Recently, e-beam melted very pure Mo, which can even be cold rolled, is available and a new technique to produce a large block of single crystalline Mo by sintering has been developed. Re-examination of H solution, diffusion and permeation utilizing new Mo and W materials is highly recommended.

Since the behaviour of hydrogen in metals is highly dependent on temperature, the operating temperature of plasma facing components plays a very important role in hydrogen recycling in a tokamak. It is important to note that hydrogen in solids cannot be controlled by electric or magnetic fields, but temperature variation can result in desorption or adsorption of huge amounts of hydrogen compared to that in the plasma. Therefore, hydrogen recycling studies must be done under controlled temperature conditions.

5. HYDROGEN RETENTION AND RELEASE CHARACTERISTICS FOR GRAPHITE

5.1. Modelling of hydrogen trapping and release in graphite

Hydrogen isotopes implanted into graphite show two well distinguished types of behaviour, one of which is

characterized by trapping in and re-emission from the kinetic range of the implanted ions, while the other is dominated by diffusion into the bulk of the material.

At low and moderate temperatures (up to 1300 K), implanted hydrogen atoms are trapped at the end of their kinetic range at low fluences [104–108]. With increasing fluence, a growing fraction of the incident flux is re-emitted until a stationary state is reached, at which incident and re-emitted flux are balanced. The stationary concentration of hydrogen in the implanted range depends *slightly* on depth [106, 107] but *strongly* on temperature [108, 109], decreasing by more than one order of magnitude between 300 and 900 K.

In addition to trapping within the ion range, diffusion occurs beyond the range above 500 K, probably along internal surfaces. Above 1000 K, transgranular diffusion is also observed, the diffusing hydrogen decorating high energy traps [110–112]. This diffusion and trapping beyond the kinetic ion range is discussed in Section 5.2.

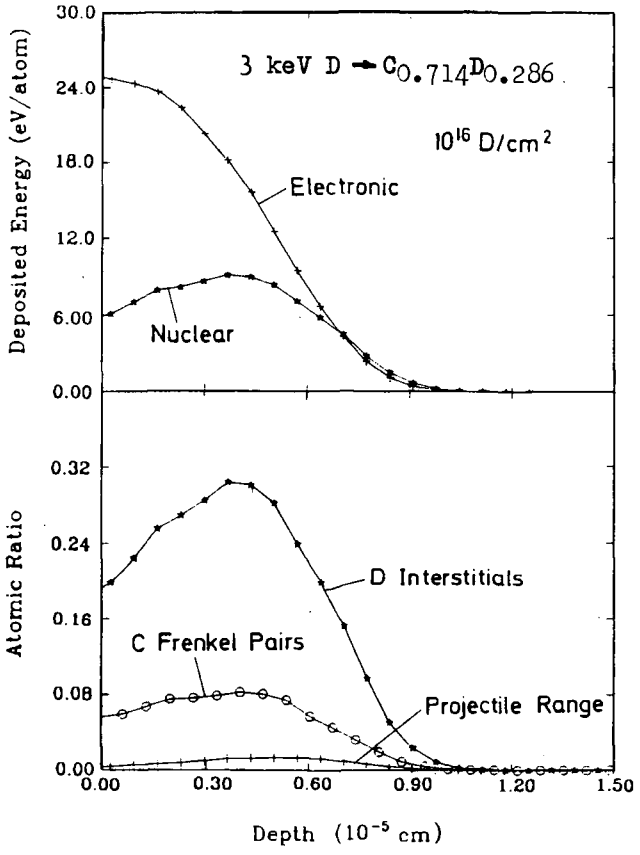

FIG. 8. Range, energy deposition and damage profiles as obtained from a TRIM computer simulation for deuterons incident on a saturated C:D target. A displacement threshold of 30 eV is assumed for the production of Frenkel pairs, whereas a binding energy of 2.7 eV is taken as a threshold for C–D bond breaking by nuclear knock-off (the formation of 'D interstitials'). Both the C Frenkel pair and the D interstitial distributions include secondary events taking place in collision cascades [121].

Room temperature implantation and release of hydrogen in graphite was empirically described satisfactorily by the local saturation model [113, 114] or, for the case of isotopic exchange, by the local mixing model [115]. The model of local saturation and mixing is based on the assumption of a maximum trap concentration, C_T, which the material can accommodate. C_T is assumed to be independent of depth. Temperature effects are not included. At low fluence, the fraction of the incident ion flux which is not reflected kinetically is completely retained with a depth distribution matching the range distribution of the ions. The implant concentration increases with fluence until C_T is reached. At any depth where this local saturation has been established, any additionally deposited ion will cause immediate release of trapped atoms through the surface. No retrapping of these released atoms in yet unsaturated areas is admitted. For an isotope mixture, the local ratio of trapped isotopes determines the ratio of the release rates.

This simple empirical model has proven successful in describing the trapping of monoenergetic hydrogen ions, with energies ranging from 50 eV to about 10 keV, implanted into various kinds of graphite [106, 115, 116, 122]. A saturation concentration $C_T = (0.4 \pm 0.06)$ H-atoms/C-atom has been established by a number of independent groups [106, 113, 116]. To be used with the model of local saturation and mixing, computations of ion range profiles are available from different analytical [117] or computer simulation [118, 119] codes. The range profiles of hydrogen isotopes implanted into graphite calculated by computer simulation (for example the most commonly used TRIM [119] code) are found to be in good agreement with experimental data with respect to the mean or most probable range. The predicted width of the distributions, however, appears too small, for unknown reasons [105, 107]. Hence, a mean correction factor of 1.7 has been applied to the width of the simulated profiles [120, 121], to be consistent with experimental observation. An example showing the range, damage and energy deposition profiles, which have been scaled in this way, is given in Fig. 8.

For an analytical approximation of the hydrogen deposition profile for monoenergetic implants, a Gaussian with its image Gaussian subtracted (to account for surface effects in kinetic reflection) has been proposed [107, 114]. The successful application

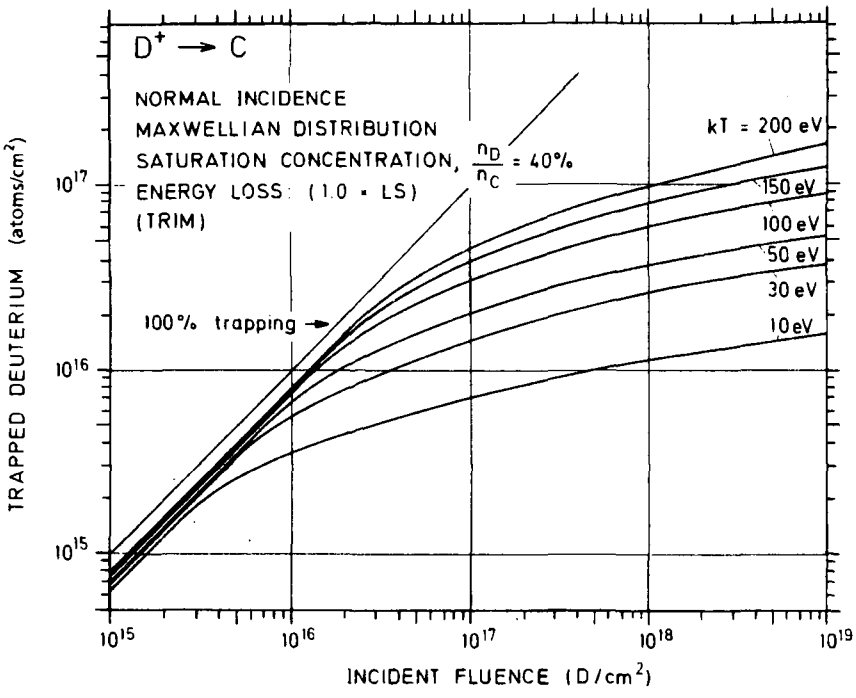

FIG. 9. Trapped deuterium versus the incident fluence for D in C, as obtained from the model of local saturation using TRIM range distributions. Trapping curves are shown for six plasma temperatures, for a Maxwellian energy distribution and an isotropic angular distribution of the incident particles. A saturation concentration C_T = 0.4 D atoms/C atom has been assumed [12].

of the local saturation model has encouraged several groups to calculate the trapped inventories for walls of plasma devices being exposed to hydrogen fluxes with a Maxwellian energy distribution and an isotropic or cosine distribution for the angles of incidence [137, 114, 122]. Figure 9 shows an example of such calculations.

A detailed comparison of depth profiles of H and D during isotopic exchange of 1.5 keV D implants by 1.5 keV H was made by Wampler and Magee [106]. They show that the local mixing model together with TRIM deposition profiles predicts the depth dependence of the H/D exchange with reasonable accuracy.

The dependence of C_T on temperature has been incorporated into the local mixing model in an empirical way by Möller and Roth [123] making use of experimental values of $C_T(T)$ [109]. An attempt to predict a temperature dependent saturation on physcial grounds was made by Brice et al. [124]. In their extended local mixing model, they introduced a term for thermal desorption and a beam enhanced redistribution of trapped atoms over trapping states with different activation energies E_t. Mean trap binding energies of 3.6 eV and 2.9 eV were assumed for high and low damage states, respectively. A maximum trap concentration of C_T – 0.44 traps/C-atom was taken, independent of depth. In addition to E_t and C_T, several free parameters enter the model which had to be determined by curve fitting. Doing this, an excellent fit was obtained for a temperature dependent isotopic mixing experiment in the temperature range 300 K $\leq$ T $\leq$ 900 K [109, 124].

Another approach to calculate the temperature dependence of trapping of D in C was chosen by Braun and Emmoth [108]. They assumed temperature dependent effective cross-sections σ_{eff} for ion induced detrapping. This, with the designation 'gas sputtering model', had been proposed already for previous room temperature isotope exchange experiments [125, 126]. This model, however, contradicts a linear increase of the trapped inventory at low fluences, which is observed experimentally [104, 113]. However, Braun and Emmoth [108] obtain a good reproduction of their experimental data by fitting best values of σ_{eff} for incident energies of 2–20 keV and temperatures of 300–1300 K. It should be mentioned here that the shapes of hydrogen trapping curves in graphite depend critically on the homogeneity of the flux distribution

across the beam spot during implantation. Some of the experimental data suffer from inhomogeneous beam distributions. This may be the reason for controversial conclusions from data taken in different experiments.

Although the local mixing model, including its high temperature extensions, and the 'gas sputtering' model provide good fits to special experimental data, the empirical choice of fitting parameters prohibits the application of these models to complex implantation conditions such as varying energy, or isotopic composition of the incident atoms, or changing target temperatures. Furthermore, these models only provide rough information on the inventory in the implanted layer. They cannot be expected to model correctly very small changes of this inventory, which may occur for varying discharge conditions in plasma machines. These changes, however, might have large consequences for the hydrogen recycling and its influence on the discharge, since only a small fraction of the saturated wall inventory corresponds to one initial gas fill of the device.

Both the local mixing model and the gas sputtering model neglect a possible retrapping of the detrapped hydrogen atoms. Further, the local mixing model cannot describe the ion induced release of hydrogen from graphite during bombardment with ions other than hydrogen [116, 127–129] or with high energy hydrogen ions, the range of which is large compared to the depth of the pre-implanted layer [120, 129, 130]. Wampler and Myers [129] suggested that the decrease of ion induced release at high fluences, which had been observed by Roth et al. [116], may be due to retrapping of the detrapped deuterium before it can leave the sample. They employed a McNabb–Foster [131] formalism for the diffusion of hydrogen in the presence of traps. The hydrogen inventory is split up into a solute fraction C_s and a trapped fraction C_t. The ion induced detrapping rate (acting on the trapped fraction) is proportional to a detrapping cross-section σ and the incident ion flux Φ. In addition to the concentration of saturation C_T, a new fitting parameter defining a characteristic length of retrapping, $L = (\alpha C_T)^{-1/2}$, is introduced, α being a trapping rate coefficient. As a best fit to the experimental data, $L \approx 1.5$ nm was found. The model calculations result in detrapping cross-sections which are considerably larger than the initial release cross-section, due to the fact that a large fraction of detrapped atoms is retrapped in empty traps. Comparing the values of σ with the mean energy deposited per carbon atom in the implanted region, the authors conclude that the detrapping is mainly caused by atomic collisions rather than by the electronic energy loss. This formalism has been extremely successful in the modelling of 'supershot' conditioning in TFTR [127]. Conditioning by low density helium/carbon plasmas has been the key to achieving improved performance in TFTR. The model for supershot conditioning based on ion induced release and retrapping can predict both the amount of deuterium removed and the rate at which the conditioning proceeds.

Model calculations of this kind were also used recently by Langley [128] to fit the release of hydrogen by helium in a plasma simulator. In addition, the author takes into account the recombinative release of hydrogen atoms which have been removed from their traps by irradiation effects.

This is consistent with the picture of the local formation of hydrogen molecules and their fast diffusion to the surface, which evolved from implantation and subsequent thermal annealing experiments by Möller et al. [132, 133]. In view of the similarity of saturated hydrogen implanted graphite with a-C:H layers formed by plasma enhanced chemical vapour deposition [134], this picture was also confirmed by thermal effusion experiments from a-C:H/a-C:D bilayers by Wild and Koidl [135] and the evidence of fast molecular hydrogen permeation through a-C:H found by Pillath et al. [136].

With the above knowledge on ion induced detrapping, retrapping and bulk molecule formation and diffusion, the phenomenon of local saturation during hydrogen implantation appears in a new light and can be understood as resulting from a balance between ion deposition and those effects. With the total local hydrogen concentration, as above, composed from a solute and a trapped fraction, Möller and Scherzer [121, 138] write the following rate equations:

$$\frac{\partial C_s}{\partial t}(x,t) = -k_{st}C_s(C_T - C_t) + k_tC_t + S_d(x)C_t - k_{ss}C_s^2 + S_r(x) \quad (8)$$

$$\frac{\partial C_t}{\partial t}(x,t) = k_{st}C_s(C_T - C_t) - k_tC_t - S_d(x)C_t \quad (9)$$

Equations (8) and (9) account for the deposition of ions according to their range distribution $S_r(x)$, a trapping at saturable traps, $C_T(x)$ denoting the trap concentration, a thermal detrapping, an ion induced detrapping due to an energy deposition function $S_d(x)$, and the local formation of molecules. Molecular diffusion towards the surface is assumed to proceed infinitely fast. Trapping, thermal detrapping and

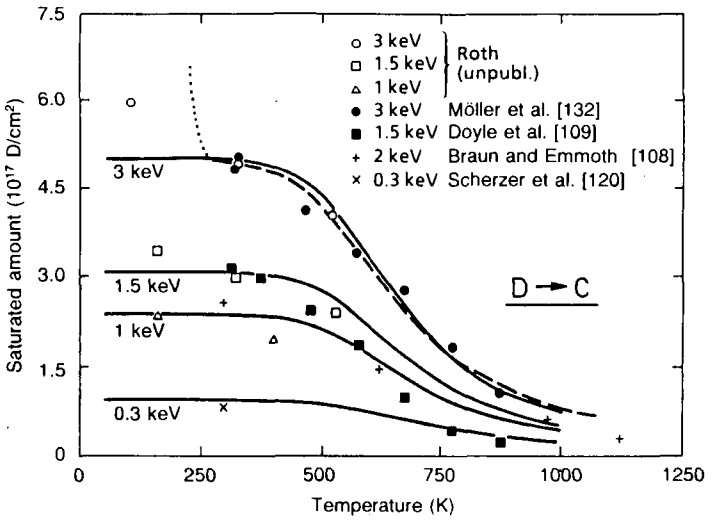

FIG. 10. Saturated retained amounts of deuterium implanted into graphite as a function of temperature and ion energy: Comparison of experimental data and model calculation. Solid lines: Analytical approximation (Eqs (3) and (4)), dashed line: numerical result. The dotted line indicates the increase of C_S at low temperatures. The calculations were performed for an ion flux of 10^{15} cm$^{-2}\cdot$s^{-1} and a trap concentration of $C_T = 0.42$. The experimental data are taken from Roth (unpublished data) and from Refs. 83, 84, 95 and 107 in Ref. [121].

recombination are subject to rate constants k_{st}, k_t and k_{ss}, respectively, each of which is composed of a pre-exponential factor and an activation term according to $k = k^0 \exp(-U/kT)$.

When thermal detrapping is neglected, an analytical solution can be given for the stationary state of the saturated layer under implantation, by

$$C_s^\infty = \sqrt{S_r/k_{ss}} \tag{10}$$

$$C_t^\infty = \frac{C_T}{1 + \sqrt{k_{ss}S_d^2/k_{st}^2 S_r}} \tag{11}$$

Since the solute concentration in the implanted layer appears to be negligible above room temperature, the depth profile at saturation is solely given by Eq. (11) and determined by the three parameters C_T, $\alpha_0 = \sqrt{k_{ss}^0}/k_{st}^0$ and $U_\alpha = \frac{1}{2}U_{ss} - U_{st}$. A nearly flat depth profile within the ion range requires $S_d^2(x)$ being proportional to $S_r(x)$. Therefore, it was argued [121] that the effects of the nuclear energy deposition should be suitably chosen for the damage function $S_d(x)$ (see Fig. 8). The authors chose the depth distribution of hydrogen released by nuclear knock-off. The effect of C Frenkel pair formation on the free hydrogen production can be neglected in view of the H:C ratio of less than about 0.4.

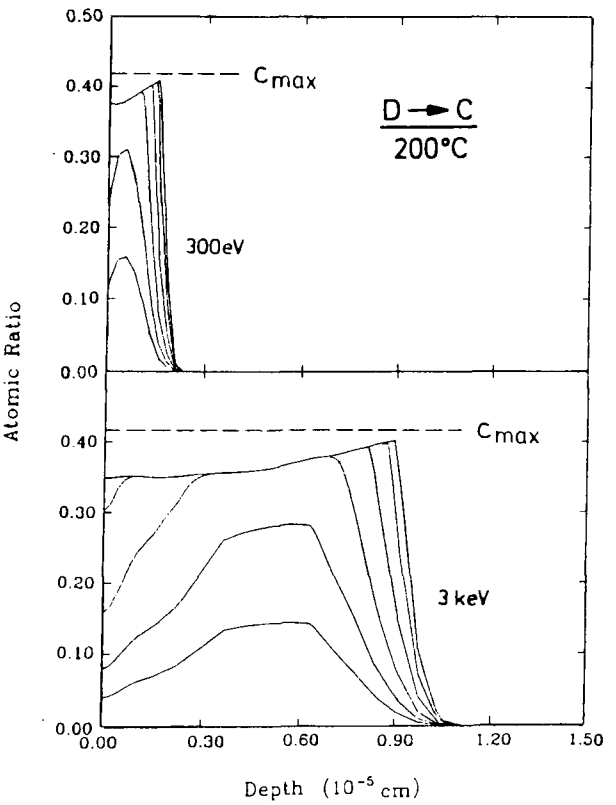

FIG. 11. Depth profiles obtained from the model calculations at different fluences of implantation (range of fluences 1×10^{17} cm^{-2} to 2×10^{18} cm^{-2} at 3 keV, 2×10^{16} cm^{-2} to 4×10^{17} cm^{-2} at 300 eV). The ion flux is 10^{15} cm$^{-2}\cdot$s^{-1} [121].

With the parameters $C_T = 0.42 \pm 0.02$, $\alpha_0 = 120 \pm 75\ s^{1/2}$, and $U_\alpha = 0.31 \pm 0.04$ eV, satisfactory fits were obtained for the retained amount of deuterium in saturation as a function of temperature and ion energy (see Fig. 10). Saturated depth profiles (Fig. 11) show a depletion towards the surface which has also been observed experimentally [106, 107]. The release during thermal diffusion is modelled to occur at the experimentally observed mean temperature, but in a temperature range which is considerably narrower than the experimental one [109]. This discrepancy can be explained by a broad spectrum of activation energies around the mean binding energy of 2.7 eV.

The calculations by Möller and Scherzer [121, 138] have all been performed using one identical set of parameters. In recent investigations [135], the model has also been applied to the release of deuterium from a thin saturated layer by large range protons, with merely qualitative success. Recently, the model (again using identical parameters) was applied by Pitcher [139] to the density behaviour in tokamaks with carbon limiters. Scaling relations between total power input, edge temperature, hydrogen and carbon fluxes, plasma density and effective charge were predicted on the basis of the above formalism. The results are in good agreement with experimental experience for certain conditions of operation at JET and TFTR [140].

Recently, Brice [141] proposed a similar model, assuming uniform solute and trapped concentrations within the ion range:

$$\frac{\partial C_s}{\partial t} = -k_{st}C_s(C_T - C_t) + k_t^* C_t + S_d C_t - k_{ss}^* \times \frac{C_S^2 C_s^2}{(C_S - C_s)^2} + S_r \qquad (12)$$

$$\frac{\partial C_t}{\partial t} = k_{st}C_s(C_T - C_t) - k_t^* C_t - S_d C_t \qquad (13)$$

These equations have been written in analogy to models being valid for hydrogen implantation into metals [123, 142]. Recombinative release is assumed to occur at the surface. Nevertheless, this difference with respect to the Möller/Scherzer [121, 138] formalism is merely semantic: The bulk recombination and fast molecular diffusion assumed for the latter may be interpreted as a recombination at inner surfaces. Consequently, Eqs (12) and (13) are identical to Eqs (8) and (9) except for terms which limit the solute concentration to a maximum value, C_S. This is only of significance for very high fluxes.

In the evaluation of Eqs (12) and (13), Brice [141] assumes relatively small recombination rate factors (a sufficiently high activation energy for recombination), which produces a relatively high solute fraction. Thereby, the broad thermal release spectrum which is observed experimentally [109, 143] can be reproduced with only one detrapping activation energy of about 0.1 eV. Satisfactory fits are obtained for both thermal release and implanted amounts. An example is given in Fig. 12. However, different sets of parameters had to be used in order to fit different experimental data sets.

The question of whether there is a significant amount (i.e. more than a few per cent) of a diffusing solute fraction of hydrogen during implantation into graphite has been a subject of controversy in recent literature. Whereas Scherzer et al. [144, 145] were not able to find a dynamic inventory during deuterium implantation in the keV range, Morita et al. [146] observed a significant decrease of the hydrogen inventory after terminating the implantation. Scherzer [145] argued that possible experimental problems could have affected the latter finding.

Pitcher [140] pointed out that the different parameter sets employed by Möller and Scherzer [121, 138] and by Brice [141] lead to an opposite flux dependence of the saturated amount. A conclusive experiment which could check the validity of the above formalisms and

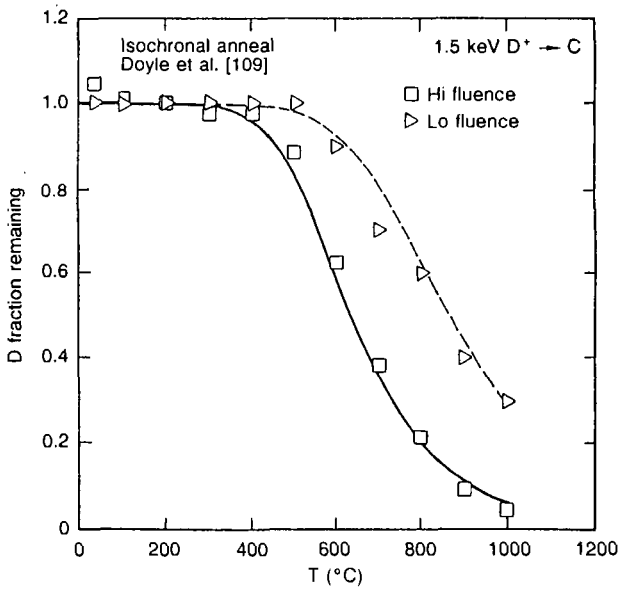

FIG. 12. Comparison of experimental isochronal anneal measurements with predictions from model calculations for D implanted into C. Experimental fluences were 10^{16} cm^{-2} (triangles) and 10^{18} cm^{-2} (squares) [141].

decide about the correct parameters would indeed be the study of this flux dependence. Such an experiment, however, would require very high hydrogen fluxes in a range covering several orders of magnitude above $\sim 10^{16}$ cm$^{-2}\cdot$s^{-1}, for which suitable experimental facilities are still not available.

In conclusion, the phenomenological model of local saturation and mixing may be employed to yield reasonable predictions on the hydrogen inventory. More detailed descriptions, which are sometimes necessary (for example to predict recycling transients), require more elaborate models. These have become available recently. However, they are still awaiting a conclusive confirmation by experiment.

5.2. Bulk diffusion, solubility and trapping of hydrogen and graphite at elevated temperatures

5.2.1. Diffusion

The high temperature behaviour of hydrogen in graphite has recently been reviewed by Causey [112]. There have been many attempts to measure the diffusion coefficient of the hydrogen isotopes in graphite, and the reported values have varied tremendously. The different experimental techniques used by the researchers are discussed here and the results for the diffusivities are shown in Fig. 13. Elleman [147] used pyrolytic carbon microspheres with internal cores of lithium aluminate enriched in the ^{6}Li isotope in his experiments. The particles were placed in a nuclear reactor at room temperature to generate tritium from the n–α reaction. Diffusivities were determined from breakthrough times during isothermal anneals. Elleman reported a diffusion coefficient of D = 700 exp (–3.25 eV/kT) cm^2/s over the temperature range 1073–1473 K. Rohrig et al. [148] used the release rate of tritium from nuclear graphites during isothermal anneals to determine the diffusivity of tritium in graphite. They reported the diffusion coefficient to be given by D = 0.04 exp(–2.78 eV/kT) cm^2/s. Causey et al. [149] used a recoil injection technique to measure the tritium diffusion coefficient in pyrolytic carbon. The diffusion coefficient for laminar pyrolytic carbon was reported to be D = 3.3 × 10^2 × exp (–4.3 eV/kT) cm^2/s. For silicon doped pyrolytic carbon, the coefficient was given D = 1.1 × 10^{-3} × exp(–2.3 eV/kT)cm^2/s. For low temperature isotropic pyrolytic carbon, two different diffusion coefficients were determined, depending on whether hydrogen was used in the gas sweeping over the samples during the isothermal anneals. The porosity in the isotropic

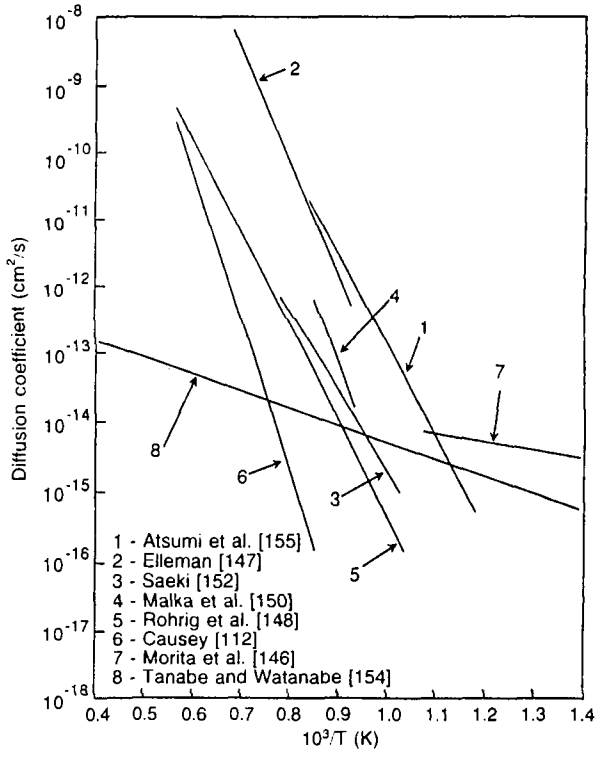

FIG. 13. Arrhenius plot of the diffusivity of tritium in graphite by various investigators [112, 146–154].

material was given as the cause for the larger apparent diffusion coefficient, and isotropic exchange with trapped tritium was suggested as a possible explanation for the enhanced release when hydrogen was used in the sweep gas. Malka et al. [150], in experiments similar to those performed by Rohrig et al. [148], used nuclear graphite, with the tritium production due to activation of lithium impurities in the graphite. Their diffusion coefficient of D = 8.3 × 10^3 exp(–3.8 eV/kT) cm^2/s is also shown in Fig. 13. Saeki [151] examined the effect of neutron irradiation on the release rate of tritium from different types of graphites. In a subsequent study [152] on the release of tritium from irradiated graphite, Saeki used isothermal anneals to determine the diffusivity of tritium in graphite. The graphite was ground to a powder to remove the effects of grain orientation. The curve shown in Fig. 13 is for natural graphite with relatively large powder size, and the equation is given by D = 3.8 × 10^{-4} exp(–2.22 eV/kT) cm^2/s. For the nuclear graphite, the activation energy for the diffusion was seen to increase with neutron fluence. In a third study [153], Saeki examined the effect of the degree of preferred orientation of the grains in pyrolytic carbon

on the tritium diffusion coefficient. He reported two different diffusion coefficients with very different activation energies. An activation energy of 2.7 eV was given for the highly oriented material and 1.1 eV for the isotropic carbon. This difference was proposed to be caused by radial pores in the isotropic material. Saeki proposed the difference to be due to a more rapid diffusion along the basal planes than that which is possible along the prism planes. The highly oriented material, with the basal planes aligned with the external surface, would require a greater diffusion distance before the tritium could be released from the carbon.

Morita et al. [146] recently used elastic recoil depth profile analysis to measure diffusion during hydrogen implantation into graphite at 300–1000 K. Tanabe and Watanabe [154] subsequently examined deuterium retention in graphite exposed to D^0 at 460–1323 K by means of re-emission and thermal desorption techniques. They obtained results similar to those of Morita et al. and determined a diffusion coefficient of $D = 2.1 \times 10^{-12} \exp(-0.45 \text{ eV/kT}) \text{ cm}^2/\text{s}$ for hydrogen saturated graphite. These results, also shown in Fig. 13, differ markedly from the other data and have not yet been fully explained. Differences in the various experimental methods used to obtain the data summarized in Fig. 13 may be primarily responsible for the differences in the reported hydrogen concentration in graphite, and variations in the sample materials and hydrogen loading methods may also be important.

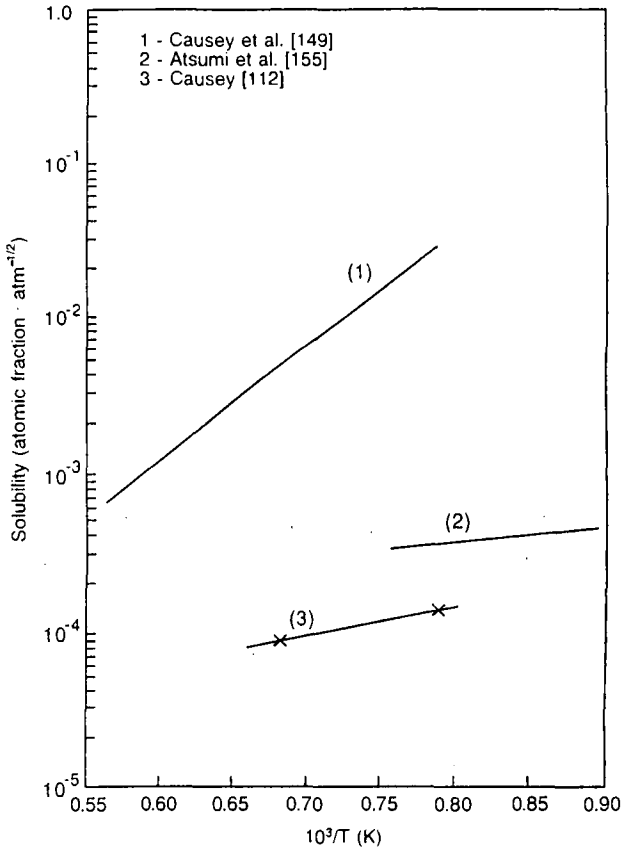

FIG. 14. Arrhenius plot of the solubility of hydrogen isotopes in graphite.

5.2.2. *Solubility*

An apparent deuterium solubility in pyrolytic carbon was reported by Causey et al. [149]. In this study, laminar pyrolytic carbon samples were exposed to tritium gas at different temperatures and pressures. The amount of absorbed deuterium was determined by subsequent outgassing through a calibrated mass spectrometer. Because of the slow inward diffusion and the large diffusion distance in this non-porous material, equilibrium saturation of the samples could not be reached. This non-equilibrium condition meant that the values determined for the solubility were based on the earlier measured diffusion coefficient, and any errors in that measurement would have carried over to the solubility. The solubility was reported to be $5.1 \times 10^{-8} \exp(+1.45 \text{ eV/kT})$ atom fraction/$\text{atm}^{1/2}$. An Arrhenius plot of these data and the other solubility results is shown in Fig. 14.

Atsumi et al. [155] recently measured the solubility of deuterium in ISO 88 graphite at temperatures between 1123 and 1323 K and pressures between 2.5×10^2 Pa and approximately 1.3×10^4 Pa. Although not stated in the paper, it appears that the solubility values were determined by pressure changes in a constant volume chamber measured by a capacitance manometer. The solubility was reported to be given by $S = 6.44 \times 10^{-5} \exp(+0.2 \text{ eV/kT})$ atom fraction per $\text{atm}^{1/2}$. As predicted by Sievert's law, the results were seen to scale linearly with the square root of pressure. The reported temperature dependence of the solubility is shown in Fig. 14, together with two additional data points determined in experiments at 1273 and 1473 K with 1 atm pressure. Deuterium containing 1% tritium was used in the experiments performed with POCO AXF-5Q graphite. Both data sets show a negative heat of solution, suggesting bonding of the hydrogen isotopes to the graphite.

The study by Atsumi et al. [155] appears to give the best estimate for the hydrogen isotope solubility in graphite. This expression is:

$S = 6.44 \times 10^{-5} \exp(+0.2 \text{ eV/kT})$ atom fraction/$\text{atm}^{1/2}$

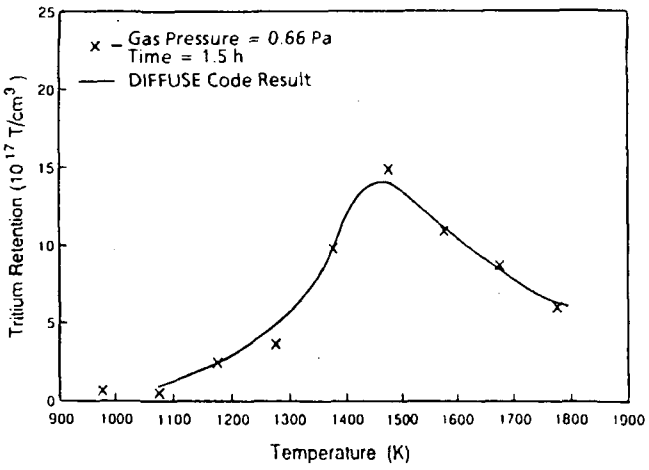

FIG. 15. Tritium retention in POCO AXF-5Q graphite as a function of temperature [156].

The best estimate for the diffusivity comes from the combination of the solubility results by Atsumi et al. [155] and the inward migration rates reported by Causey et al. [156] for POCO AXF-5Q graphite. In the latter study, the inward migration rate was analysed using the DIFFUSE [37] computer code to determine the product of diffusivity and solubility. The effect of trapping was included in this analysis. The diffusivity is given by

$$D = 0.93 \exp(-2.8 \text{ eV/kT}) \text{ cm}^2/\text{s}$$

5.2.3. *Trapping*

The review of the diffusion data for hydrogen isotopes in graphite and pyrolytic carbon reveals great disparities in the reported values, sometimes as great as four to five orders of magnitude. The primary reason for these measured differences is trapping. The magnitude of the effect of trapping on the apparent diffusion coefficient was demonstrated in the recent studies by Causey and co-workers [156, 157]. In these studies with Papyex and POCO AXF-5Q graphite, samples were exposed to 0.66 Pa neutral gas pressure. Results for the experiments performed at 0.66 Pa and a fixed time of 1.5 h are shown in Fig. 15. It can be seen that the tritium retention initially rises with increasing temperature, but then decreases with increasing temperature. Above 1500 K, the inward migration rate is not fast enough to replace the atoms that escape from the traps, and the net result is less than 100% filling of the traps. Below 1500 K, there was not sufficient time during the 1.5 h experiments for the tritium to diffuse completely into the 10 μm grains and fill the traps. The DIFFUSE computer [37] code was used to analyse these data, and it was determined that the trap energy was 4.3 eV with an intrinsic trap density of 17 appm for this graphite.

The trap energy of 4.3 eV is the same as that given for the bond energy between hydrogen and carbon in typical hydrocarbons [158]. These sites are thought to be on the prism planes along the crystalline edges [159, 160]. Neutron damage is thought to significantly increase the concentration of these trapping sites.

6. SUMMARY

The theory for hydrogen trapping and release in metals is quite well developed, although there is still some controversy regarding the form of the molecular recombination coefficient. However, there are large gaps in the database for the three most popular metallic plasma facing materials: beryllium, molybdenum and tungsten. A wealth of data and modelling have been generated over the last decade for interaction of hydrogen with carbon based materials. However, there are still major discrepancies between various measurements, and the modelling has reached only the phenomenological level.

ACKNOWLEDGEMENT

This work was supported in part by the United States Department of Energy, under Contract No. DE-AC04-76DP00789.

REFERENCES

[1] WILSON, K.L., in Data Compendium for Plasma-Surface Interactions, Nucl. Fusion, Special Issue 1984, IAEA, Vienna (1984) Ch. 3.
[2] MYERS, S.M., RICHARDS, P.M., WAMPLER, W.R., BESENBACHER, F., J. Nucl. Mater. **165** (1989) 9.
[3] SHEWMON, P.G., Diffusion in Solids, McGraw Hill, New York (1963) 52.
[4] MUELLER, W.M., BLACKLEDGE, J.P., LIBOWITZ, G.G., Metal Hydrides, Academic Press, New York (1968).
[5] EICHENAUER, W., PEBLER, A., Z. Metallkd. **48** (1957) 373.
[6] ROBERTSON, W.M., Metall. Trans., A **8** (1977) 1709.
[7] VOLKL, J., ALEFELD, G., in Diffusion in Solids (NOWICK, A.S., BURTON, J.J., Eds), Academic Press, New York (1975) Ch. 5.
[8] ROBERTSON, W.M., Z. Metallkd. **64** (1973) 436.
[9] LOUTHAN, M.R., Jr., DERRICK, R.D., Corros. Sci. **15** (1965) 287.

[10] WASILEWSKY, R.J., KEHL, G.M., Metallurgia **50** (1954) 225.
[11] MORTON, J.R., STARK, D.S., Trans. Faraday Soc. **56** (1960) 354.
[12] WILSON, K.L., HAGGMARK, L.G., Thin Solid Films **63** (1979) 283.
[13] WILSON, K.L., J. Nucl. Mater. **103 & 104** (1981) 453.
[14] HOTSTON, E.S., McCRACKEN, G.M., J. Nucl. Mater. **68** (1977) 277.
[15] LIVSHITS, A.I., Sov. Tech. Phys. Lett. **3** (1977) 6.
[16] PERKINS, H.K., NODA, T., J. Nucl. Mater. **71** (1978) 349.
[17] ALI-KHAN, I., DIETZ, K.J., WAELBROECK, F.G., WIENHOLD, P., J. Nucl. Mater. **76 & 77** (1978) 337.
[18] LIVSHITS, A.I., NOTKIN, M.E., YAKOVLEV, S.V., Sov. Tech. Phys. Lett. **4** (1978) 4.
[19] WAELBROECK, F.G., ALI-KHAN, I., DIETZ, K.J., WIENHOLD, P., J. Nucl. Mater. **85 & 86** (1979) 345.
[20] BASKES, M.I., J. Nucl. Mater. **92** (1980) 318.
[21] BRAUN, M., EMMOTH, B., WAELBROECK, F.G., WIENHOLD, P., J. Nucl. Mater. **93 & 94** (1980) 861.
[22] WAELBROECK, F.G., DIETZ, K.J., WIENHOLD, P., WINTER, J., ALI-KHAN, I., MERKENS, H., ROTA, E., J. Nucl. Mater. **93 & 94** (1980) 839.
[23] WAELBROECK, F.G., WIENHOLD, P., WINTER, J., ROTA, E., BANNO, E., Influence of Bulk and Surface Phenomena on the Hydrogen Permeation through Metals, Kernforschungsanlage Jülich (1966).
[24] MYERS, S.M., WAMPLER, W.R., BESENBACHER, F., J. Appl. Phys. **56** (1984) 1561.
[25] KERST, R.A., SWANSIGER, W.A., J. Nucl. Mater. **122 & 123** (1984) 1499.
[26] CAUSEY, R.A., KERST, R.A., MILLS, B.E., J. Nucl. Mater. **122 & 123** (1984) 1547.
[27] PICK, M.A., SONNENBERG, K., J. Nucl. Mater. **131** (1985) 208.
[28] WAMPLER, W.R., Appl. Phys. Lett. **48** (1986) 6.
[29] CAUSEY, R.A., BASKES, M.I., J. Nucl. Mater. **145–147** (1987) 284.
[30] WAMPLER, W.R., J. Nucl. Mater. **145–147** (1987) 313.
[31] RICHARDS, P.M., J. Nucl. Mater. **152** (1988) 246.
[32] BESENBACHER, F., J. Nucl. Mater. **165** (1989) 9.
[33] RICHARDS, P.M., MYERS, S.M., WAMPLER, W.R., FOLLSTAEDT, D.M., J. Appl. Phys. **65** (1989) 180.
[34] WAMPLER, W.R., RICHARDS, P.M., Phys. Rev., B **41** (1990) 7483.
[35] WIENHOLD, P., PROFANT, M., WAELBROECK, F., WINTER, J., J. Nucl. Mater. **93 & 94** (1980) 866.
[36] HOLLAND, D.F., MERRILL, B.J., in Engineering Problems of Fusion Research (Proc. 9th Symp. Chicago, 1981), IEEE, New York (1981) 1209.
[37] BASKES, M.I., DIFFUSE 83, Rep. SAND83-8231, Sandia National Laboratories, Albuquerque, NM (1983).
[38] MÖLLER, W., PIDAT-A Computer Program for Implant, Diffusion, and Trapping, Rep. IPP-9/44, Max-Planck-Institut für Plasmaphysik, Garching (1983).
[39] DOYLE, B.L., J. Nucl. Mater. **111–112** (1982) 628.
[40] BRICE, D.K., DOYLE, B.L., J. Nucl. Mater. **120** (1984) 230.
[41] DOYLE, B.L., BRICE, D.K., J. Nucl. Mater. **122 & 123** (1984) 1523.
[42] BRICE, D.K., J. Nucl. Mater. **122 & 123** (1984) 1531.
[43] BRICE, D.K., DOYLE, B.L., J. Vac. Sci. Technol., A **5** (1987) 2311.
[44] TANABE, T., Fusion Eng. Des. **10** (1989) 375.
[45] BRICE, D.K., J. Nucl. Mater. **162–164** (1989) 985.
[46] BIERSACK, J.P., Radiat. Eff. **19** (1973) 249.
[47] LAM, N.Q., LEAF, G.K., J. Mater. Res. **1** (1986) 251.
[48] BIERSACK, J.P., HAGGMARK, L.G., Nucl. Instrum. Methods **174** (1980) 257.
[49] HAUTALA, M., Radiat. Eff. **51** (1980) 35.
[50] ROUSCH, M.L., ANDREADIS, T.D., GOKTEPE, O.F., Radiat. Eff. **55** (1981) 119.
[51] MÖLLER, W., ECKSTEIN, W., Nucl. Instrum Methods, Sect. B **2** (1984) 814.
[52] DAVIDSON, C.M., Nucl. Instrum Methods, Sect. B **13** (1986) 421.
[53] SIGMUND, P., in Sputtering by Particle Bombardment I (BEHRISCH, R., Ed.), Springer-Verlag, Berlin (1981) Ch. 2.
[54] WILSON, K.L., CAUSEY, R.A., HSU, W.L., MILLS, B.E., SMITH, M.F., WHITLEY, J.B., J. Vac. Sci. Technol., A **8** (1990) 1750.
[55] PEMSLER, J.P., RAPPERPORT, E.J., Trans. Metall. Soc. AIME **230** (1964) 90.
[56] JONES, P.M.S., GIBSON, R., J. Nucl. Mater. **21** (1967) 353.
[57] AL'TOVSKIJ, R.M., EREMIN, A.A., EREMINA, L.F., et al., Izv. Akad. Nauk. SSSR, Met. **3** (1981) 73.
[58] SWANSIGER, W.A., J. Vac. Sci. Technol., A **4** (1986) 1216.
[59] VIANDEN, R., KAUFMANN, E.N., RODGERS, J.W., Phys. Rev. **22** (1980) 63.
[60] VERBEEK, H., ECKSTEIN, W., in Applications of Ion Beams to Metals, Plenum Press, New York (1974) 607.
[61] LIU, M.B., SHEFT, I., GRUEN, D.M., J. Nucl. Mater. **79** (1979) 267.
[62] LANGLEY, R.A., J. Nucl. Mater. **85 & 86** (1979) 1123.
[63] PONTAU, A.E., BAUER, W., CONN, R.W., J. Nucl. Mater. **93 & 94** (1980) 564.
[64] WAMPLER, W.R., J. Nucl. Mater. **122 & 123** (1984) 1598.
[65] MÖLLER, W., SCHERZER, B.M.U., BOHDANSKY, J., Retention and Release of Deuterium Implanted into Beryllium, IPP-JET Report No. 26, Max-Planck-Institut für Plasmaphysik, Garching (1986).
[66] SONNENBERG, K. (JET Joint Undertaking), personal communication, 1989.
[67] WEAST, R.W. (Ed.), Handbook of Chemistry and Physics, CRC Press, Cleveland, OH (1974) 72.
[68] YAMANISHI, Y., Hydrogen Permeation in Metals, PhD Thesis, Osaka University (1983) (in Japanese).
[69] KATSUTA, H., IWAI, T., OHNO, H., J. Nucl. Mater. **115** (1983) 208.
[70] HILL, M.L., J. Metals **12** (1960) 725.
[71] OATES, W.A., McLELLAN, R.B., Scr. Metall. **6** (1972) 349.

[72] JONES, P.M.S., GIBSON, R., J. Nucl. Mater. **21** (1967) 353.
[73] CHANDLER, W.T., WALTER, W.J., Refractory Metal Alloys, Plenum Press, New York (1966) 197.
[74] TANABE, T., FURUYAMA, Y., SAITOH, N., IMOTO, S., Trans. Jpn. Inst. Met. **28** (1987) 706.
[75] CASKEY, G.R., Jr., LOUTHAN, M.R., Jr., DERRICK, R.G., J. Nucl. Mater. **55** (1975) 279.
[76] MAKSUMOV, T.M., PETUSHKOV, E.E., Dokl. Akad. Nauk. SSSR **31** (1974) 32.
[77] FRAUENFELDER, R., J. Chem. Phys. **48** (1968) 3955.
[78] ZAKHAROV, A.P., GORDETSKY, A.E., SHARAPOV, V.M., Z. Phys. Chem., Neue Folge (Wiesbaden) **117** (1979) 245.
[79] SMITHELLS, C.J., RAMSLEY, C.E., Proc. R. Soc. **157** (1938) 157.
[80] HUFFINE, C.L., WILLIAMS, J.M., Corrosion **16** (1960) 430.
[81] GUTHRIE, J.W., BEAVIS, L.C., BEZEAL, D.R., PERKINS, W.G., J. Nucl. Mater. **53** (1974) 313.
[82] STEIGERWALD, E.A., The Permeation of Hydrogen through Materials for the Sunflower System, Final Report, Rep. E-5823, NASA CR-54004, TRW Electromechanical Division, Cleveland, OH (1963).
[83] KANNO, M. Shin Kinzoku Kogyo No. 4 (1975) 91; No. 6 (1975) 149 (in Japanese).
[84] FRAUENFELDER, R., J. Vac. Sci. Technol. **6** (1969) 388.
[85] MAZAEV, A.A., AVARBE, R.G., VILK, Yu.N., Izv. Akad. Nauk SSSR, Met. **6** (1968) 223.
[86] RYABCHIKOV, L.N., Ukr. Fiz. Zh. **9** (1964) 293.
[87] MOORE, G.E., UNTERWALD, F.C., J. Chem. Phys. **40** (1964) 2639.
[88] WEBB, R.W., Permeation of Hydrogen through Metals (Activation Energies for Permeation of Hydrogen through Metals for Use in the SNAP Reactor Program), Rep. NAA-SR-10462, Atomics International, Canoga Park, CA (1965).
[89] AITKEN, E.A., BRASSFIELD, H.C., CONN, P.K., DUDERSTADT, E.C., FRYXELL, R.E., Trans. Met. Soc. AIME **239** (1987) 1565.
[90] VOLKL, J., ALEFLED, G., in Diffusion in Solids, Academic Press, New York (1975) 232.
[91] KATSUTA, H., McLELLAN, R.B., FURUKAWA, K., J. Phys. Chem. Solids **43** (1982) 533.
[92] TANABE, T., Hydrogen permeation through Mo, to be published in J. Nucl. Mater.
[93] McCRACKEN, G.M., ERENTS, S.K., in Application of Ion Beams to Metals, Plenum Press, New York (1974) 585.
[94] BAUER, W., THOMAS, G.J., J. Nucl. Mater. **53** (1974) 127.
[95] BRAGANZA, C., CARTER, G., FARRELL, G., Nucl. Instrum. Methods **132** (1976) 679.
[96] SCHULTZ, R., BEHRISCH, R., SCHERZER, B.M.U., J. Nucl. Mater. **93&94** (1980) 608.
[97] HANSEN, A.L., VINCENT, D.H., DAVIS, C.N., J. Nucl. Mater. **98** (1981) 259.
[98] OKUDA, S., IMOTO, S., Jpn. J. Appl. Phys. **19** (1980) 87.
[99] LANFORD, W.A., TRAUTREITTER, H.P., ZIEGLER, J.F., KELLER, J., Appl. Phys. Lett. **28** (1976) 566.
[100] MYERS, S.M., RICHARDS, P.M., WAMPLER, W.R., BESENBACHER, F., J. Nucl. Mater. **165** (1989) 9.
[101] GORODETSKY, A.E., ZAKHAROV, A.O., SHARAPOV, V.M., ALIMOV, V.Kh., J. Nucl. Mater. **93&94** (1980) 588.
[102] TANABE, T., SAITO, N., ETOH, Y., IMOTO, S., J. Nucl. Mater. **103&104** (1981) 483.
[103] PERKINS, H.K., NODA, T., J. Nucl. Mater. **71** (1978) 349.
[104] LANGLEY, R.A., BLEWER, R.S., ROTH, J., J. Nucl. Mater. **76&77** (1978) 313.
[105] BORGESEN, P., BOTTIGER, J., MÖLLER, W., J. Appl. Phys. **49** (1978) 4401.
[106] WAMPLER, W.R., MAGEE, C.W., J. Nucl. Mater. **103&104** (1981) 509.
[107] WAMPLER, W.R., BRICE, D.K., MAGEE, C.W., J. Nucl. Mater. **102** (1981) 304.
[108] BRAUN, M., EMMOTH, B., J. Nucl. Mater. **128&129** (1984) 657.
[109] DOYLE, B.L., WAMPLER, W.R., BRICE, D.K., J. Nucl. Mater. **103&104** (1981) 513.
[110] WILSON, K.L., HSU, W.L., J. Nucl. Mater. **145–147** (1987) 121.
[111] CAUSEY, R.A., BASKES, M.I., WILSON, K.L., J. Vac. Sci. Technol., A **4** (1986) 1189.
[112] CAUSEY, R.A., J. Nucl. Mater. **162–164** (1989) 151.
[113] STAUDENMAUER, G., ROTH, J., BEHRISCH, R., et al., J. Nucl. Mater. **84** (1979) 149.
[114] COHEN, S.A., McCRACKEN, G.M., J. Nucl. Mater. **84** (1979) 157.
[115] DOYLE, B.L., WAMPLER, W.R., BRICE, D.K., PICRAUX, S.T., J. Nucl. Mater. **93&94** (1980) 551.
[116] ROTH, J., SCHERZER, B.M.U., BLEWER, R.S., BRICE, D.K., PICRAUX, S.T., WAMPLER, W.R., J. Nucl. Mater. **93&94** (1980) 601.
[117] SCHIOTT, H.E., K. Dan. Vidensk. Selsk., Mat.-Fys. Medd. **35** (1986) No. 9.
[118] ROBINSON, M.T., TORRENS, I.M., Phys. Rev., B **9** (1974) 5008.
[119] BIERSACK, J.P., HAGGMARK, L.G., Nucl. Instrum. Methods **174** (1980) 257.
[120] SCHERZER, B.M.U., WIELUNSKI, M., MÖLLER, W., TUROS, A., ROTH, J., Nucl. Instrum. Methods, Sect. B **33** (1988) 714.
[121] MÖLLER, W., SCHERZER, B.M.U., J. Appl. Phys. **64** (1988) 4860.
[122] ECKSTEIN, W., Calculated Trapping Curves of D in C and Si, Rep. IPP 9/33, Max-Planck-Institut für Plasmaphysik, Garching (1980).
[123] MÖLLER, W., ROTH, J., in Physics of Plasma-Wall Interactions in Controlled Fusion (POST, D.E., BEHRISCH, R., Eds), Plenum Press, New York (1986).
[124] BRICE, D.K., DOYLE, B.L., WAMPLER, W.R., J. Nucl. Mater. **111&112** (1982) 598.
[125] ERENTS, S.K., Nucl. Instrum. Methods **70** (1980) 455.
[126] UNDERWOOD, M.C., ERENTS, S.K., HOTSTON, E.S., J. Nucl. Mater. **93&94** (1980) 575.
[127] WAMPLER, W.R., DOYLE, B.L., J. Nucl. Mater. **162–164** (1989) 1025.
[128] LANGLEY, R.A., J. Nucl. Mater. **162–164** (1989) 1030.
[129] WAMPLER, W.R., MYERS, S.M., J. Nucl. Mater. **111&112** (1982) 616.

[130] SCHERZER, B.M.U., WANG, J., MÖLLER, W., J. Nucl. Mater. **162–164** (1989) 1013.
[131] McNABB, A., FOSTER, P.K., Trans. Metall. Soc. AIME **227** (1963) 618.
[132] MÖLLER, W., BORGESEN, P., SCHERZER, B.M.U., Nucl. Instrum. Methods, Sect. B **19&20** (1987) 826.
[133] MÖLLER, W., SCHERZER, B.M.U., Appl. Phys. Lett. **50** (1987) 1870.
[134] VIETZKE, E., PHILIPPS, V., Nucl. Instrum. Methods, Sect. B **23** (1987) 449.
[135] WILD, C.H., KOIDL, P., Appl. Phys. Lett. **51** (1987) 1870.
[136] PILLATH, J., WINTER, J., WAELBROECK, F., J. Nucl. Mater. **162–164** (1989) 1046.
[137] BRICE, D.K., DOYLE, B.L., WAMPLER, W.R., PICRAUX, S.T., HAGGMARK, L.G., J. Nucl. Mater. **114** (1983) 277.
[138] MÖLLER, W., J. Nucl. Mater. **162–164** (1989) 138.
[139] PITCHER, C.S., Fusion Eng. Des. **12** (1990) 63.
[140] PITCHER, C.S. (Culham Laboratory, Abingdon), personal communication, 1990.
[141] BRICE, D.K., Nucl. Instrum. Methods, Sect. B **44** (1990) 302.
[142] BRICE, D.K., DOYLE, B.L., J. Nucl. Mater. **130** (1984) 330.
[143] SAWICKI, J.A., ROTH, J., HOWE, L.M., J. Nucl. Mater. **162–164** (1989) 1019.
[144] SCHERZER, B.M.U., BØRGESEN, P., MÖLLER, W., Reemission, Trapping, and Desorption of Implanted Deuterium from JET Samples, IPP-JET Rep. No. 32, Max-Planck-Institut für Plasmaphysik, Garching (1986).
[145] SCHERZER, B.M.U., J. Nucl. Mater. **168** (1989) 121.
[146] MORITA, K., OHTSUKA, K., HASEBE, Y., J. Nucl. Mater. **162–164** (1989) 990.
[147] ELLEMAN, T.S. (General Atomics, San Diego, CA), unpublished work.
[148] ROHRIG, H.D., FISCHER, P.G., HECKER, R., J. Am. Ceram. Soc. **59** (1976) 316.
[149] CAUSEY, R.A., ELLEMAN, T.S., VERGHESE, K., Carbon **17** (1979) 323.
[150] MALKA, V., ROHRIG, H.D., HECKER, R., in Tritium Technology in Fission, Fusion, and Isotope Application (Proc. Conf. Dayton, OH, 1980), American Nuclear Society (1980) 102.
[151] SAEKI, M., J. Nucl. Mater. **99** (1981) 100.
[152] SAEKI, M., Int. J. Appl. Radiat. Isot. **43** (1983) 739.
[153] SAEKI, M., J. Nucl. Mater. **131** (1985) 32.
[154] TANABE, T., WATANABE, Y., J. Nucl. Mater. **176** (1990) (in press).
[155] ATSUMI, H., TOKURA, S., MIYAKE, M., J. Nucl. Mater. **155–157** (1988) 241.
[156] CAUSEY, R.A., BASKES, M.I., WILSON, K.L., J. Vac. Sci. Technol., A **4** (1986) 1189.
[157] CAUSEY, R.A., WILSON, K.L., J. Nucl. Mater. **138** (1986) 57.
[158] PAULING, L., The Nature of the Chemical Bond, 2nd edn, McGraw Hill, New York (1940).
[159] BRADBURN, H., COULSON, C.A., RUSHBROOKE, G.S., Proc. R. Soc. (Edinburgh) **62** (1984) 336.
[160] DIGONSKI, V.V., KRYLOV, V.N., J. Appl. Chem. USSR **33** (1964) 725.
[161] SCHERZER, B.M.U., BØRGESEN, P., Radiat. Eff. Lett. **76** (1980) 169.

PHYSICAL SPUTTERING

W. ECKSTEIN, J. BOHDANSKY, J. ROTH
Max-Planck-Institut für Plasmaphysik,
Euratom-IPP Association,
Garching bei München,
Germany

ABSTRACT. The paper reviews empirical formulas used to describe the dependence of the sputtering yield on the projectile energy and the angle of incidence. Values of the parameters of plasma relevant materials are given in a table. New information on the dependence of the sputtering yield on Maxwellian bombardment and on the surface roughness is described, as well as new results on energy and angular distributions of sputtered atoms. Finally, the sputtering of compounds and alloys is discussed as well as the bombardment of elements by non-volatile species.

The paper reviews first some of the semi-empirical formulas for the sputtering yield for light and heavy ions as presented in Ref. [1]; these are based on a more fundamental investigation of the sputtering process by Sigmund [2] limited to heavy ion sputtering. Then, recent developments are discussed in greater detail. A more recent overview on physical sputtering with special regard to the fusion reactor technology is given by Roth [3].

1. SPUTTERING YIELD

The sputtering yield determines the collisional removal of target atoms by projectiles and is defined as removed surface atoms per incident projectile. As explained in Ref. [1], the yield depends on the type of projectile, its angle of incidence and its energy. The yield is also a specific function of the bombarded material. More detailed information, for example on the energy and angular distributions of the ejected surface atoms, is given by the 'differential yield'.

1.1. Normal incidence

The most widely used formula for the sputtering yield was given by Bohdansky [4]. This formula describes the yield for all projectile-target combinations from threshold energies to about 100 keV. Other fitting formulas [5, 6] are restricted to light projectiles [5] or are less accurate [6]. The Bohdansky formula is

$$Y(E_0, \alpha = 0) = Q\, S_n(\epsilon) g(E_0/E_{th}) \qquad (1.1)$$

where $Q = 0.042\, h(M_2/M_1)/U$ is the 'yield factor' given by analytical theory [2]. Q depends on the surface binding energy U and the projectile and target masses, M_1 and M_2, respectively (see Eq. (12) and Fig. 4 of Ref. [4]). However, best agreement with experimental data is found when Q is used as a fitting parameter. The analytic expression [5] for the nuclear stopping cross-section $S_n(\epsilon)$, which is based on the Thomas-Fermi potential, is given by

$$S_n(\epsilon) = \frac{3.441\sqrt{\epsilon}\ln(\epsilon + 2.718)}{1 + 6.355\sqrt{\epsilon} + \epsilon(6.882\sqrt{\epsilon} - 1.708)} \qquad (1.2)$$

ϵ is the reduced energy defined by

$$\epsilon = E_0/E_{TF} = E_0 \frac{M_2}{M_1 + M_2} \cdot \frac{a_L}{Z_1 Z_2 e^2}$$

$$E_{TF}\,(eV) = 30.74 \frac{M_1 + M_2}{M_2} Z_1 Z_2 (Z_1^{2/3} + Z_2^{2/3})^{1/2} \qquad (1.3)$$

Z_1 and Z_2 are the nuclear charges of the projectile and the target atom, respectively, E_0 is the projectile energy and a_L is the screening length defined by Lindhard:

$$a_L = 0.468503\,(Z_1^{2/3} + Z_2^{2/3})^{-1/2} \qquad (1.4)$$

The function g in Eq. (1.1) takes into account threshold effects. It is given in Ref. [1] by

$$g(\delta) = (1 - \delta^{2/3})(1 - \delta)^2 \qquad (1.5)$$

with $\delta = E_{th}/E_0$.

The parameters E_{TF}, E_{th} and Q are given for the most important materials involved in plasma-wall interaction in Table I, where some values have been slightly changed from those given in Table 6.1 of Ref. [1] (page 65). For other materials the threshold

TABLE I. PARAMETERS FOR THE SPUTTERING YIELD

Target	H	D	T	^{4}He	C	O	Self-sputtering
Beryllium							
E_{th} (eV)	20	9	21	30	40	70	25
E_{TF} (eV)	256	282	308	780	4152	6970	2208
Q (atoms/ion)	0.1	0.3	0.24	0.59	1.6	1.3	1.4
f	1.69	1.70	1.71	1.71			
η (rad)	0.141	0.171	0.191	0.281			
Boron							
E_{th} (eV)	20	20	21	30	40		35
E_{TF} (eV)	333	361	389	895	4857	8023	3716
Q (atoms/ion)	0.1	0.15	0.24	0.59	1.6		0.94
f	2.22	2.24	2.25	2.25			
η (rad)	0.131	0.161	0.171	0.251			
Graphite							
E_{th} (eV)	35	30	30	29	42		42
E_{TF} (eV)	415	447	479	1087	5687	9298	5687
Q (atoms/ion)	0.035	0.10	0.20	0.32	1.5		1.5
f	2.51	2.53	2.54	2.54			
η (rad)	0.121	0.151	0.161	0.241			
Aluminium							
E_{th} (eV)	53	24	22	20			25
E_{TF} (eV)	1059	1097	1135	2448	10295	15718	34545
Q (atoms/ion)	0.043	0.093	0.2	0.34			5.4
f	1.67	1.70	1.71	1.71			
η (rad)	0.131	0.161	0.171	0.261			
Titanium							
E_{th} (eV)	80	50	40	25	35		40
E_{TF} (eV)	2054	2096	2138	4502	16947	24843	117898
Q (atoms/ion)	0.017	0.055	0.10	0.125	1		3.7
f	1.93	2.00	2.02	2.04			
η (rad)	0.121	0.151	0.161	0.241			
Iron							
E_{th} (eV)	64	44	40	33	35		40
E_{TF} (eV)	2544	2589	2634	5514	20247	29839	174096
Q (atoms/ion)	0.042	0.13	0.21	0.44	3.2		13
f	1.79	1.87	1.89	1.91			
η (rad)	0.151	0.181	0.201	0.291			
Nickel							
E_{th} (eV)	50	31	25	22	28	48	34.4
E_{TF} (eV)	2799	2846	2893	6044	22011	31856	206960
Q (atoms/ion)	0.041	0.115	0.22	0.45	2.5	1.55	11.7
f	1.82	1.90	1.93	1.94			
η (rad)	0.151	0.181	0.201	0.301			
Copper							
E_{th} (eV)	55	34	30	19			36
E_{TF} (eV)	2926	2971	3017	6292	22696	32723	224619
Q (atoms/ion)	0.1	0.23	0.35	0.81			17
f	1.60	1.68	1.70	1.72			
η (rad)	0.151	0.191	0.211	0.311			

TABLE I (cont.)

Target	H	D	T	^{4}He	C	O	Self-sputtering
Molybdenum							
E_{th} (eV)	199	90	70	46	55		64
E_{TF} (eV)	4718	4767	4816	9944	34183	48322	533048
Q (atoms/ion)	0.007	0.023	0.045	0.12	0.93		18
f	2.12	2.29	2.34	2.37			
η (rad)	0.121	0.151	0.161	0.251			
Tungsten							
E_{th} (eV)	443	220	140	110	80	40	65
E_{TF} (eV)	9870	9923	9977	20373	66507	91979	1998599
Q (atoms/ion)	0.007	0.019	0.038	0.106	0.93	2.2	20
f	2.08	2.44	2.56	2.62			
η (rad)	0.121	0.141	0.161	0.241			
Stainless steel							
E_{th} (eV)	65	50	40	30		65	
E_{TF} (eV)	2518	2564	2608	5463	20084	29175	
Q (atoms/ion)	0.033	0.090	0.15	0.36		1.2	
f	1.81	1.89	1.92	1.93			
η (rad)	0.151	0.181	0.201	0.298			
Silicon carbide							
E_{th} (eV)	38	25	22	18		90	
E_{TF} (eV)	767	803	840	1841	8311	12997	
Q (atoms/ion)	0.039	0.11	0.18	0.36		1.3	
f	3.0	2.6		3.0			
η (rad)	0.272	0.247		0.309			
Titanium carbide							
E_{th} (eV)	65	31	29	18		90	
E_{TF} (eV)	1161	1198	1236	2653	10917	16540	
Q (atoms/ion)	0.025	0.040	0.096	0.36		1.3	
f	1.4	2.5		3.3			
η (rad)	0.309	0.383		0.321			

energy E_{th}, which is a function of M_1 and M_2 and of the surface binding energy U, can be taken from Fig. 5 of Ref. [3] as a guideline. Equation (1.1) gives good adjustment in the low keV range, but exhibits deviations at higher energies. In many cases the accuracy of the formula is better than 30%, but in special cases differences of more than 50% are possible. The original data have an accuracy of about $\pm 30\%$, but the reproducibility is sometimes not better than a factor of two.

It should be mentioned that different formulas for S_n are given in the literature. The values of the fitting parameters Q and g depend on the choice of the formula for S_n. The importance of self-sputtering in fusion devices has led to new experimental and computational investigations of the yields, especially for Be, C and W [7–10]. Also, calculations of the sputtering yield for tritium (see Fig. 1) and ^{3}He have been performed [11] after the publication of the Data Compendium [1], leading to some corrections of the estimated parameters in Table 6.1 of Ref. [1].

1.2. Oblique incidence

The sputtering yield for oblique incidence is especially important at limiter plates and at parts which are close to the main plasma, where the magnetic field lines cross these parts at oblique angles. According to Chodura [12], in such situations the mean angle of particle incidence, α, is about 65°, taking the sheath potential into account. For grazing particle incidence the sputtering yield can increase with the incident angle by an order of magnitude above the values at normal incidence for

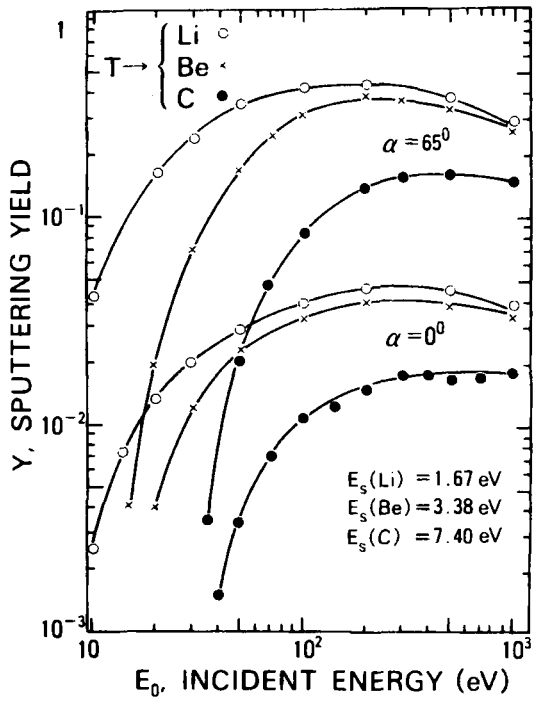

FIG. 1. Sputtering yield versus incident energy E_0 for normal incidence, $\alpha = 0°$, and for oblique incidence, $\alpha = 65°$. Lithium, beryllium and carbon are bombarded by tritium. For the corresponding surface binding energies E_s, the heats of sublimation are indicated (from Fig. 7 of Ref. [9]). Calculations were performed with the program TRIM.SP.

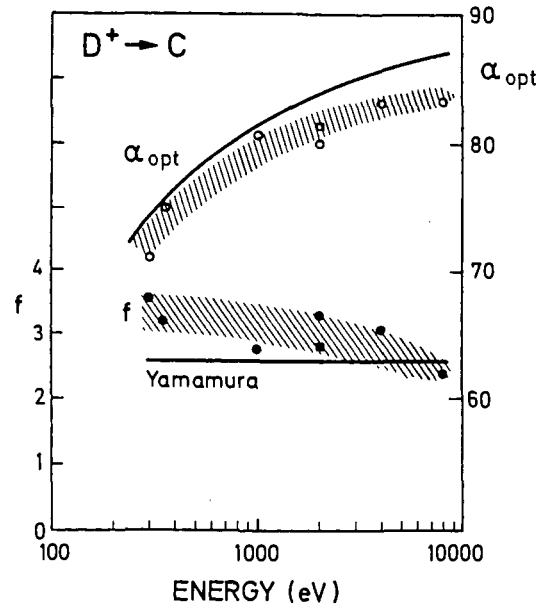

FIG. 2. Individual fitted values for the parameters f and α_{opt}, for the sputtering of carbon by deuterium, are given by the open (α_{opt}) and full points (f) and the shaded areas. The solid lines represent the fitting formulas (1.7) given by Yamamura et al. [13].

the light projectiles such as hydrogen. The maximum of the yield versus the incident angle decreases and shifts to smaller angles with decreasing projectile energy. The enhancement of the sputtering yield disappears in the case of bombardment of heavy targets by light ions and at energies below about 300 eV. However, for light targets such as carbon the enhancement is still appreciable for energies as low as 50 eV (see Fig. 1). This is demonstrated by computer simulations [11].

According to Yamamura et al. [13], the angular dependence of the sputtering yield for light ions can be described by

$$Y(E_0, \alpha)/Y(E_0, 0) = (\cos\alpha)^{-f} \times \exp\{f[1 - (\cos\alpha)^{-1}] \sin\eta\} \quad (1.6)$$

Yamamura et al. [13] give empirical formulas for f and η:

$$f = U(0.94 - 1.33 \times 10^{-3} M_2/M_1)$$

$$\eta = a_L n^{-1/3} (2\epsilon \sqrt{U/\gamma E_0})^{-1/2} \quad (1.7)$$

where for U the heat of sublimation is taken, n is the density of the target material (in atoms/Å^3) and γ is the energy transfer factor, $\gamma = 4 \cdot M_1 M_2/(M_1 + M_2)^2$. Table I gives values for f and η, partly taken from Ref. [13]. η is given in the table for 1 keV; for other incident energies E_0, η can be determined by

$$\eta(E_0) = \eta(1 \text{ keV}) \, (1000/E_0(\text{eV}))^{1/2} \quad (1.8)$$

The maximum of the sputtering yield versus the incident angle is reached [12] at

$$\alpha_{opt} = \pi/2 - \eta \quad (1.9)$$

It has to be mentioned that these empirical formulas for f and α_{opt} do not always give good agreement with experimental and simulated values. An individual fit for f and α_{opt} gives a more satisfactory picture. For light projectiles it seems that f is only weakly dependent on the energy E_0, as shown in Fig. 2. Therefore, wherever no recent experimental values exist, Yamamura's values are given in Table I independent of energy. For heavy projectiles, however, the values for f are energy dependent and an individual fit has to be applied. Equation (1.6) implies that the threshold energy E_{th} is independent of the angle of incidence, which is a good approximation for a large mass ratio M_2/M_1. For $M_2/M_1 \approx 1$, the threshold energy decreases

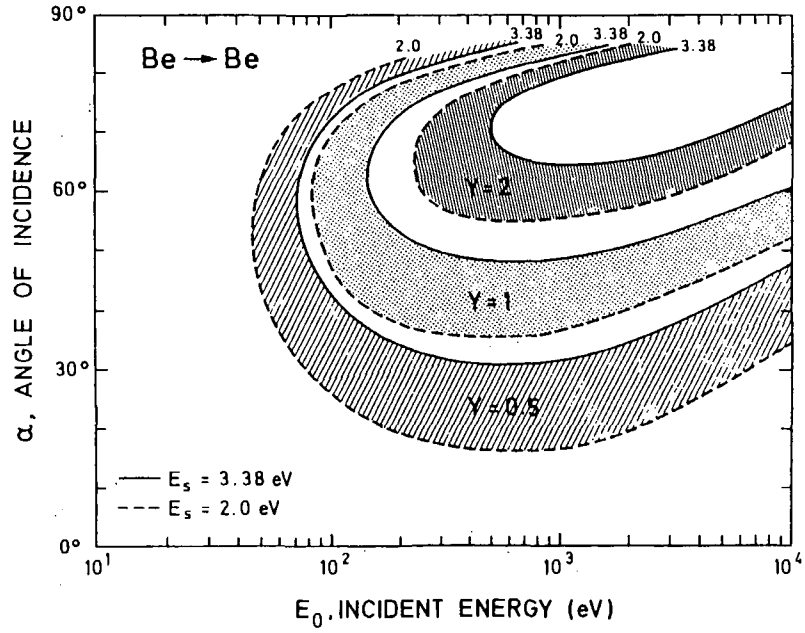

FIG. 3. Curves for constant beryllium self-sputtering yield, Y = 0.5, 1 and 2, at the angle of incidence versus the incident energy. The shaded areas are limited by calculations using surface binding energies E_s of 3.38 eV (heat of sublimation) and 2 eV (Fig. 6 of Ref. [7]). These two binding energies give approximately the range in which agreement with the experimental data for other projectiles has been achieved.

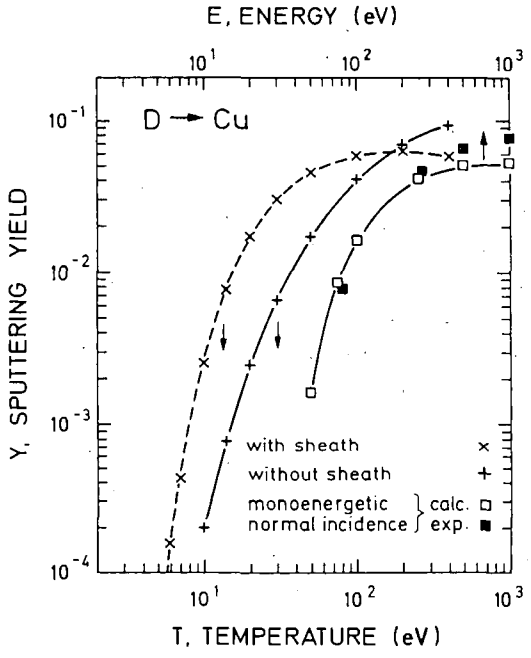

FIG. 4. Comparison of the sputtering yield data for an isotropic Maxwellian incident flux and for a monoenergetic bombardment at normal incidence. A Maxwellian distribution with a sheath potential of 3 kT and without a sheath potential has been used. Copper is bombarded by deuterium; the data were calculated with the program TRIM.SP. The experimental data (monoenergetic, normal incidence) are from Ref. [38].

with increasing angle of incidence. Newer experimental and simulated data on the angular dependence of the sputtering yield can be found in Refs [7–11].

Of special importance to plasma machines is the parameter range in which the self-sputtering yield is above unity because a dramatic increase in the impurity production occurs in this range. Self-sputtering yields larger than unity occur especially at oblique incidence. As an example, values of the self-sputtering yield of beryllium of Y = 0.5, 1 and 2 are presented in Fig. 3 in a plot of the angle of incidence versus the incident energy. The shaded areas give the limits for calculations with different surface binding energies (2 and 3.38 eV) for which agreement with experimental data for other incident particles has been achieved [7]. Other examples are the dependence of the sputtering yield on the angle of incidence for tungsten self-sputtering [9] and for the bombardment of BeO by O [10].

1.3. Isotropic Maxwellian bombardment

There are a few calculations for the bombardment of solid targets by a Maxwellian energy distribution characterized by a temperature which includes an

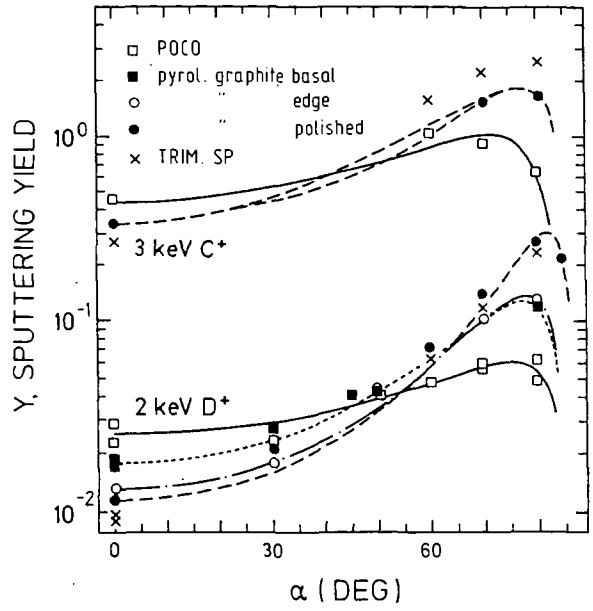

FIG. 5. Sputtering yield versus angle of incidence for graphites with different degrees of surface roughness. The roughness increases from polished pyrolytic graphite to pyrolytic graphite (edge plane), to pyrolytic graphite (basal plane), to POCO. Carbon is bombarded by 2 keV deuterium and 3 keV carbon. The crosses indicate data computed with the program TRIM.SP [16]. Curves are fits to the data points using Eqs (1.6) and (1.7).

isotropic incidence angle distribution. An example for the bombardment of Cu by D is shown in Fig. 4. Because of the high energy tail of the Maxwellian distribution the sputtering yield reaches typical values of about 10^{-2} already at plasma temperatures of about 20 eV. For monoenergetic bombardment at normal incidence such a yield is reached only at 80 eV. This example may demonstrate that threshold effects are less important for a Maxwellian distribution compared to a monoenergetic distribution. A sheath potential (in the calculation usually 3 kT) has two effects: (1) it increases the energy of the bombarding species, which increases the yield, and (2) it decreases the angle of incidence, leading to a decrease of the sputtering yield. As one can see from Fig. 2, effect (1) dominates below 200 eV owing to the steep increase of the sputtering yield near the threshold; at larger temperature the effect of the angle of incidence is more important. Similar calculations have been performed also for Ti and W [14]. These calculations indicate that the advantage of the high threshold energy of high-Z materials is strongly reduced in the case of a Maxwellian distribution of the incident particles.

1.4. Surface roughness

The surface structure certainly influences the sputtering of surface atoms. As discussed in the paper on reflection (this issue, page 17), a quantitative description of the influence on the sputtering data is being developed. The difficulty is that structures below about 100 Å may be important. These structures can now be studied with the tunnelling microscope, but no systematic study of ion bombarded surfaces has been performed so far. Experimental data [15] for D and C bombardment of C with different roughnesses are shown in Fig. 5. The values for the best polished targets are in resonable agreement with the simulated data: with increasing roughness, the yield at normal incidence increases, whereas at large angles of incidence the yield increases less. This qualitative statement is in agreement with new simulations based on the TRIM.SP program [16] including a fractal surface [17] and based on the ACAT program [18] using special surface structures [19]. In another paper the influence of these surface structures on the angular distributions is discussed [20]. It should be mentioned that in the TRIM.SP program a random roughness of the order of a monolayer is always included. The question remains which surface structures give a good description of ion bombarded surfaces. For specially prepared surface structures, even a reduction of the sputtering yield by a factor of three could be obtained for W [21].

1.5. Threshold effects and cluster bombardment

Threshold effects have been investigated in several papers [22–24] by a few-collision model. The results are in qualitative agreement with computer simulations for the angular distributions of sputtered atoms [24]. The threshold energy depends on the mass ratio and the angle of incidence [22]. Computer simulations do not seem to support the dependence of the sputtering yield near the threshold [25].

The sputtering by cluster ions was studied by Yamamura [26], who showed that non-linear effects can increase the sputtering yield by more than an order of magnitude for the case of argon clusters (up to 200 atoms) bombarding carbon.

2. ENERGY DISTRIBUTIONS

From analytical theory [2] the energy (angular) distribution of sputtered atoms is given by

$$\frac{dY}{dE\, d\beta} \sim S_n(E) \frac{E}{(E+U)^3} \cos\beta \qquad (2.1)$$

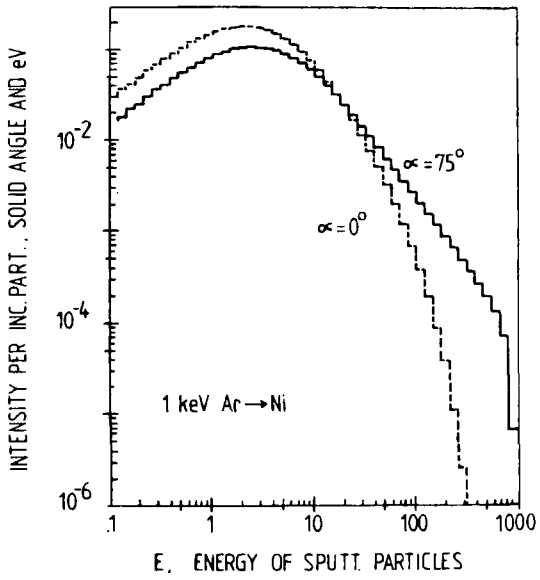

FIG. 6. Energy distributions of sputtered nickel atoms by 1 keV argon bombardment for normal incidence, α = 0, and oblique incidence, α = 75° (α is counted from the surface normal). The energy distributions are integrated over all emission directions, calculated by TRIM. SP (Fig. 2 of Ref. [29]).

This distribution has a maximum at $E_{max} = U/2$ and it decreases at high energies E with E^{-n}, where n = 2. The energy distribution cannot extend beyond the maximum transferable energy, $T_m = E_0$. Computer simulations have shown that E_{max} can be slightly higher than U/2 [16], but is usually remains below U even for oblique incidence [13]. For very low incident energies the maximum of the energy distribution may be at energies lower than U/2 [27]. At oblique incidence the energy distribution shows a slower decrease towards high energies because of direct recoil sputtering (see Fig. 6). Directly sputtered recoil atoms are created in a single collision at grazing incidence and thus they can have relatively high energies. The change in the energy distribution is much more pronounced in the forward direction compared to a distribution integrated over all emission directions, as shown in Fig. 4. Looking in specific directions the energy distributions can be quite different, especially in the incident plane for oblique angles of incidence. Because of direct recoils, a second maximum can develop in the incident plane [28]. Even for normal incidence the energy distribution depends on the polar emission angle in a more difficult way [29] than given by Eq. (2.1). The influence of the direct recoils can also be seen in the mean energy of sputtered atoms, where the effect is most important for mass ratios around $M_2/M_1 = 1$ [29].

Velocity distributions of sputtered chromium atoms have been measured by Husinsky et al. [30], those of sputtered hydrogen from metal hydrides by Mertens and Bogen [31], and those of sputtered carbon by Bogen et al. [32]. These laser induced fluorescence experiments measure the low energy part of the distribution (<50 eV) so that the direct recoil part is not included. The other limitation is that only a small number of excited states is considered.

Changes of the energy distribution at specific emission angles are not important if the angular distribution of incident particles is isotropic or has rotational symmetry with respect to the surface normal.

3. ANGULAR DISTRIBUTIONS

Equation (2.1) assumes a cosine distribution of all sputtered atoms. This is also found to be true by computer simulations; it applies even for oblique incidence if the distribution is integrated over the azimuthal angle [8]. Only at low incident energies (lower than a

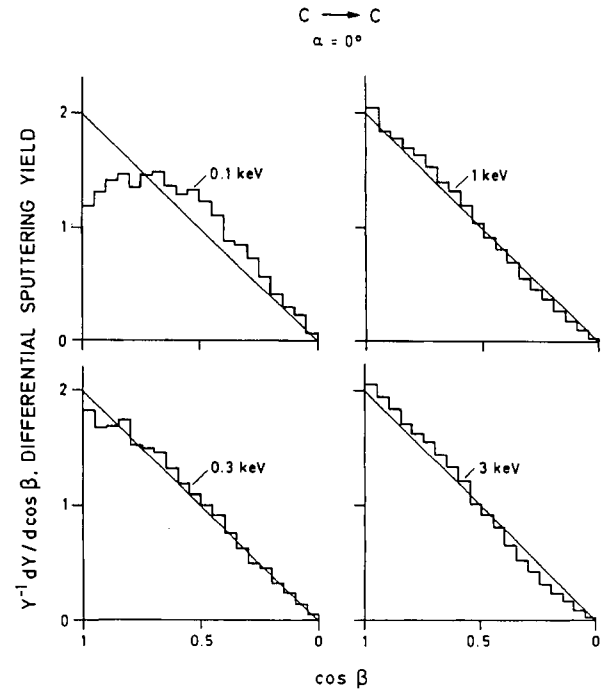

FIG. 7. Angular distributions of carbon sputtered by carbon at normal incidence and for four incident energies. Because of the presentation versus the cosine of the polar emission angle β, a cosine distribution is represented by the straight line. The differential sputtering yield is integrated over the azimuthal angle. The histograms have been calculated by TRIM.SP [8].

few hundred eV) the distribution becomes undercosine (less intensity at normal exit directions), see Fig. 7. At higher energies an overcosine distribution is sometimes observed. The polar angular energy distributions are not cosine for oblique incidence and specific azimuthal emission directions; in this case a preferred emission in the forward direction is found [1, 16]. However, if the projectiles have a broad distribution of incident angles, preferred emission in specific directions becomes less significant [3]. There is also evidence that the surface roughness or specific surface structures change the angular distributions of sputtered atoms [33]. Angular distributions near the threshold for light to heavy projectiles are studied with a few-collision model and with the ACAT program in Ref. [24].

The same algorithm as for backscattered particles can be used to produce a data set as input for plasma edge codes, to describe not only the total yields but also energy and angular distributions (see paper on backscattering, page 17).

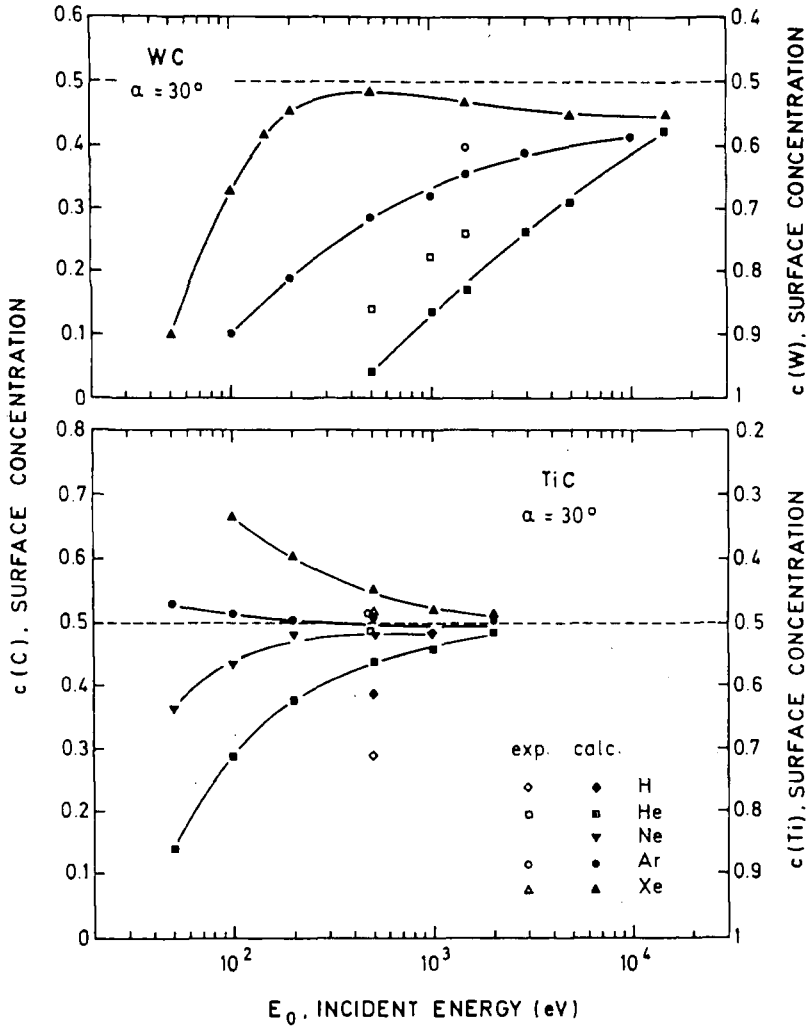

FIG. 8. Surface concentrations at equilibrium conditions (stoichiometric sputtering) versus the incident energy. WC and TiC are bombarded by H, ^{4}He, Ne, Ar and Xe at an incident angle, α = 30° (Fig. 6 of Ref. [34]). The experimental data are from Refs [39, 40].

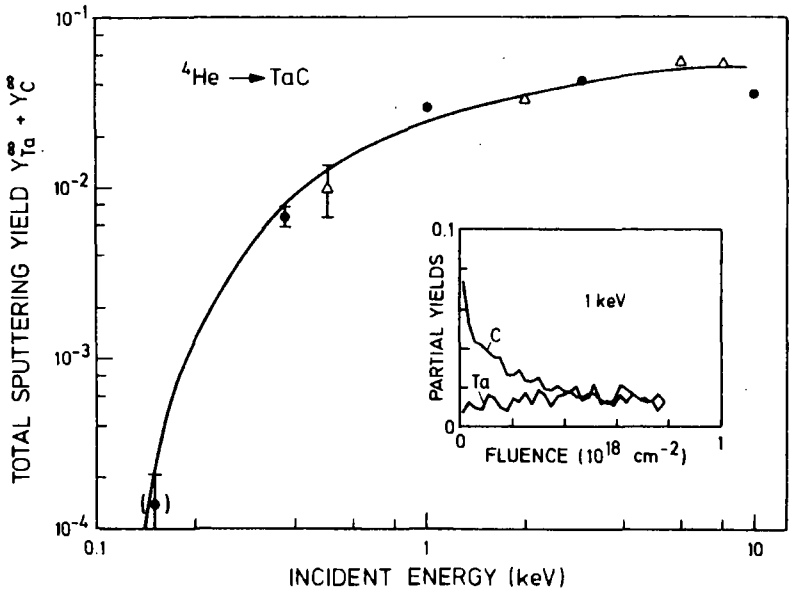

FIG. 9. Total sputtering yield at equilibrium of TaC due to bombardment with ^{4}He at normal incidence versus the incident energy. The full points represent results from dynamic calculations, the open points are experimental data [41] and the solid line is a semi-empirical fit [41]. The insert shows the partial sputtering yields of C and Ta versus the He fluence (Fig. 2 of Ref. [42]).

4. SPUTTERING OF COMPOUNDS AND ALLOYS

The main differences with regard to elemental sputtering arise from the fact that the projectile transfers different energies to the components and that the surface binding of the components may be different. For the partial sputtering yields Y_i of the two components the linear cascade theory [2] predicts

$$\frac{Y_1}{Y_2} = \frac{c_1}{c_2}\left(\frac{M_1}{M_2}\right)^{2m}\left(\frac{U_1}{U_2}\right)^{1-2m} \qquad (4.1)$$

where c_i are the bulk concentrations, M_i are the masses, U_i are the binding energies of the two components and m is the exponent in the power potential. Equation (4.1) states that the yield ratio depends only weakly on the mass and energy of the projectile, since the potential constant m is of the order of 0.1 for the energies of sputtered atoms. Preferential sputtering is expected for the lightest component and for the least bound species. Therefore, the surface composition will change with fluence until the sputtering yield ratios reflect the bulk composition. The surface at equilibrium will then be

$$\left(\frac{c_1}{c_2}\right)_{surf} = \left(\frac{c_1}{c_2}\right)_{balk}\left(\frac{M_1}{M_2}\right)^{2m}\left(\frac{U_1}{U_2}\right)^{1-2m} \qquad (4.2)$$

Computer simulation shows a more complicated picture [34, 35]. The surface concentration depends indeed on the projectile, i.e. its mass and energy (see Fig. 8), in agreement with experimental data. Dynamical simulation programs such as TRIDYN [36] allow us also to determine the development of the surface concentration and the partial sputtering yields with fluence (see Fig. 9). Steady state conditions are usually reached at a fluence of about 10^{18} cm^{-2}, depending on the projectile energy. Many experimental details can be well described by such simulation programs, for example the changes in the surface composition by the change of the projectile energy (see Fig. 6 of Ref. [34]). Additional effects such as diffusion and segregation may complicate the situation, but there are many systems which seem to be dominated by collisional effects, for example the carbides.

If a solid is bombarded by non-volatile projectiles, these atoms are implanted and therefore change the composition in the implantation range. This change of composition depends on the sputtering yield; a yield below unity will lead to a buildup of the projectile species on the substrate. In weight loss measurements the weight gain of the target by the implantation of the projectiles is taken into account. The reflection of heavy projectiles at normal incidence can usually be neglected. As an example, the buildup of layers of non-volatile projectile species on top of a substrate has been inves-

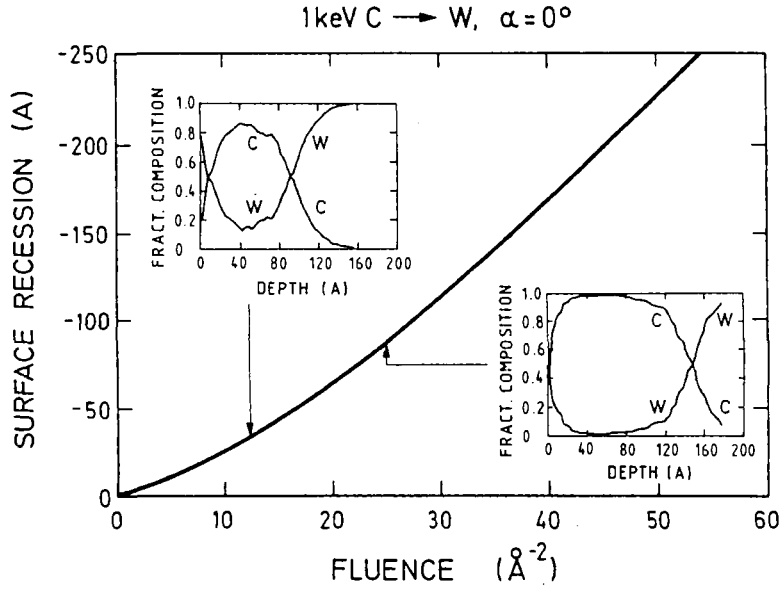

FIG. 10. Surface recession of tungsten bombarded by 1 keV carbon at normal incidence. The negative sign of the recession represents a carbon built up on tungsten. The inserts give the depth distributions of C and W at two fluences, 12.5 A^{-2} and 25 A^{-2}. Calculations with the dynamic program TRIDYN [36].

tigated by computer simulations, as shown in Fig. 10 for the bombardment of tungsten by carbon. For a sputtering yield smaller than unity, a carbon layer forms (the recession is negative), which is possible if the projectile energy is low enough. There might still be small concentrations of tungsten on the surface until a large fluence is reached. The carbon and tungsten yields versus the fluence are shown in Fig. 11. The buildup of a carbon layer depends also on the angle of incidence. Comparison with experimental weight loss measurements versus carbon fluence shows good agreement with the simulations [37]. This coverage of heavy materials such as iron and nickel by light projectiles such as beryllium, boron and carbon is an important process in plasma machines, where the low energies of the projectiles favour the buildup of layers rather than erosion. This well known formation of new layers in plasma machines is a severe difficulty for the calculation of impurity influx from yield data of elements and compounds; actually, a surface analysis of the inner wall is necessary in order to properly predict erosion from measured yield data.

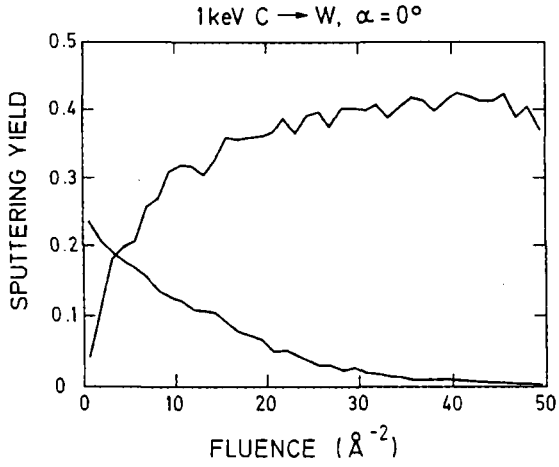

FIG. 11. Sputtering yield of tungsten bombarded by 1 keV carbon at normal incidence versus the fluence of the incident carbon. Steady state conditions are reached at a fluence of about 5 × 10^{17} atoms/cm^2. Calculations with the dynamic program TRIDYN [36].

5. SUMMARY

The sputtering of monoatomic targets is well understood. Many experimental data are available for sputtering by light projectiles. Because of the reasonable agreement with experimental values, computer simulation can produce data which are difficult to obtain experimentally, such as differential sputtering yields and multi-energy bombardment (Maxwellian distribution). The data set for self-sputtering is far less complete owing to experimental difficulties, but simulations can fill this gap. The influence of surface roughness,

which is especially important for oblique incidence, has been recognized recently in experiments, and first simulation approaches have been started. However, a realistic quantitative analysis is not at hand.

A further field which attracts increasing attention is the sputtering of compounds and their erosion and redeposition [43]. It seems that dynamical computer simulation programs can support experimental investigations if diffusion and segregation processes can be neglected; this means that the effects at high target (wall) temperatures must be studied experimentally. It should, however, be pointed out that redeposited layers may have a different structure and therefore a sputtering behaviour which is not thoroughly investigated. It will be necessary to pay more attention to the sputtering of compounds and composites by impurity ions in order to meet the requirements of future plasma machines.

REFERENCES

[1] LANGLEY, R.A., BOHDANSKY, J., ECKSTEIN, W., MIODUSZEWSKI, P., ROTH, J., TAGLAUER, E., THOMAS, E.W., VERBEEK, H., WILSON, K.L., Data Compendium for Plasma–Surface Interactions, Nucl. Fusion, Special Issue 1984, IAEA, Vienna (1984).

[2] SIGMUND, P., in Sputtering by Particle Bombardment, Vol. 1 (BEHRISCH, R., Ed.), Springer-Verlag, Berlin, Plenum Press, New York (1981) 9.

[3] ROTH, J., in Physics of Plasma–Wall Interactions in Controlled Fusion (POST, D.E., BEHRISCH, R., Eds), Plenum Press, New York (1986) 351.

[4] BOHDANSKY, J., Nucl. Instrum. Methods, Sect. B **2** (1984) 587.

[5] MATSUNAMI, N., YAMAMURA, Y., ITIKAWA, Y., et al., At. Data Nucl. Data Tables **31** (1984) 1.

[6] SMITH, D.L., BROOKS, J.N., POST, D.E., HEIFETZ, D., in Engineering Problems of Fusion Research (Proc. 9th Symp. Chicago, 1981), Institute of Electrical and Electronics Engineers, New York (1982) 719.

[7] ROTH, J., ECKSTEIN, W., BOHDANSKY, J., J. Nucl. Mater. **165** (1989) 199.

[8] ECKSTEIN, W., BIERSACK, J.P., Z. Phys. B **63** (1986) 109.

[9] HECHTL, E., YANG, H.R., WU, C.H., ECKSTEIN, W., An experimental study of tungsten selfsputtering, to be published in J. Nucl. Mater.

[10] WU, C.H., HECHTL, E., YANG, H.R., ECKSTEIN, W., Erosion of beryllium by oxygen, to be published in J. Nucl. Mater.

[11] ECKSTEIN, W., SAGARA, A., KAMADA, K., J. Nucl. Mater. **150** (1987) 266.

[12] CHODURA, R., J. Nucl. Mater. **111/112** (1982) 420.

[13] YAMAMURA, Y., ITIKAWA, Y., ITOH, N., Angular Dependence of Sputtering Yields of Monoatomic Solids, Rep. IPPJ-AM-26, Institute of Plasma Physics, Nagoya Univ. (1983).

[14] ECKSTEIN, W., unpublished results.

[15] ROTH, J., GAUTHIER, E., LASZLO, J., ECKSTEIN, W., Sputtering of low-Z materials, J. Nucl. Mater., in press.

[16] BIERSACK, J.P., ECKSTEIN, W., Appl. Phys. **34** (1984) 73.

[17] RUZIC, D., Nucl. Instrum. Methods, Sect. B **47** (1990) 118.

[18] TAKEUCHI, W., YAMAMURA, Y., Radiat. Eff. **71** (1983) 53.

[19] YAMAMURA, Y., MÖSSNER, C., OECHSNER, H., Radiat. Eff. **103** (1987) 25.

[20] YAMAMURA, Y., MÖSSBAUER, C., OECHSNER, H., Radiat. Eff. **105** (1987) 31.

[21] ZIEGLER, J.F., CUOMO, J.J., ROTH, J., Appl. Phys. Lett. **30** (1977) 268.

[22] YAMAMURA, Y., MIZUNO, Y., J. Nucl. Mater. **128&129** (1984) 559.

[23] YAMAMURA, Y., BOHDANSKY, J., Vacuum **35** (1985) 561.

[24] YAMAMURA, Y., MIZUNO, Y., KIMURA, H., Nucl. Instrum. Methods, Sect. B **13** (1986) 393.

[25] ROTH, J., ECKSTEIN, W., Sputtering Data, Rep. IPP-9/82, Max-Planck-Institute für Plasmaphysik, Garching (1990).

[26] YAMAMURA, Y., Nucl. Instrum. Methods, Sect. B **33** (1988) 493.

[27] BAY, H.L., Nucl. Instrum. Methods, Sect. B **18** (1987) 430.

[28] ECKSTEIN, W., Nucl. Instrum. Methods, Sect. B **27** (1987) 78.

[29] ECKSTEIN W., Nucl. Instrum. Methods, Sect. B. **18** (1987) 344.

[30] HUSINSKY, W., BETZ, G., GRIGIS, I., VIEHBÖCK, F., BAY, H.L., J. Nucl. Mater. **128&129** (1984) 577.

[31] MERTENS, P., BOGEN, P., J. Nucl. Mater. **128&129** (1984) 551.

[32] BOGEN, P., DÖBELE, H.J., MERTENS, P., J. Nucl. Mater. **145&147** (1987) 434.

[33] HUCKS, P., STÖCKLIN, G., VIETZKE, E., VOGELBRUCH, K., J. Nucl. Mater. **76&77** (1978) 727.

[34] ECKSTEIN, W., MÖLLER, W., Nucl. Instrum. Methods, Sect. B **7/8** (1985) 727.

[35] ECKSTEIN, W., BIERSACK, J.P., Appl. Phys., A **37** (1985) 95.

[36] MÖLLER, W., ECKSTEIN, J., BIERSACK, J.P., Comput. Phys. Commun. **51** (1988) 355.

[37] ECKSTEIN, W., ROTH, J., Sputtering of tungsten by carbon, to be published in J. Nucl. Mater.

[38] BOHDANSKY, J., J. Nucl. Mater. **93&94** (1980) 44.

[39] TAGLAUER, E., HEILAND, W., in Sputtering (Proc. Symp. Vienna, 1980), Institut für Allgemeine Physik, Technische Universität, Vienna (1980) 423.

[40] VARGA, P., TAGLAUER, E., J. Nucl. Mater. **111&112** (1982) 726.

[41] ROTH, J., BOHDANSKY, J., MARTINELLI, A.P., Radiat. Eff. **48** (1980) 213.

[42] MÖLLER, W., ECKSTEIN, W., Nucl. Instrum. Methods, Sect. B **2** (1984) 814.

[43] BROOKS, J.N., BRICE, D.K., DeWOLD, A.B., McGRATH, R.T., J. Nucl. Mater. **162–164** (1989) 363.

EROSION OF GRAPHITE DUE TO PARTICLE IMPACT

J. ROTH
Max-Planck-Institut für Plasmaphysik,
Euratom-IPP Association,
Garching bei München,
Germany

E. VIETZKE
Institut für Plasmaphysik,
Forschungszentrum Jülich,
Association Euratom-KFA,
Jülich,
Germany

A.A. HAASZ
Institute for Aerospace Studies,
Fusion Research Group,
University of Toronto,
Downsview, Ontario,
Canada

ABSTRACT. An outline is given on the present understanding of the erosion processes of graphite by particle impact, with emphasis on the use in fusion devices. There are three different ion induced erosion mechanisms: physical sputtering, radiation enhanced sublimation and chemical sputtering. The use in fusion devices determines the choice of the ion species, hydrogen, deuterium, helium, oxygen and self-ions, as well as the energy range from thermal energies to several keV. Additionally, the paper presents empirical analytic formulas for which comprehensive theories do not exist. Finally, the influence of doping of graphite on the erosion processes is discussed.

1. INTRODUCTION

For most materials, the dominant mechanism of erosion of materials due to ion bombardment is physical sputtering.[1] For graphite, several additional erosion mechanisms have been found, such as the chemical interaction of graphite with hydrogen ions and atoms, and enhanced sublimation due to ion irradiation. It is, therefore, reasonable to devote one paper of this issue exclusively to carbon based materials, including a brief discussion on physical sputtering. Erosion processes for graphite due to high heat load rather than to ion impact are included in the following papers.

In the previous data compendium [1] the emphasis was on chemical sputtering of graphite by hydrogen isotopes and oxygen. In this field, a large number of new investigations have been conducted since then and simplified models had to be discarded. Recent data will be reviewed here, with emphasis on the simultaneous interactions of graphite with thermal atomic hydrogen and energetic ions. Radiation enhanced sublimation was only briefly discussed in Ref. [1]. In the last six years, this erosion process has been found to be very important in tokamak experiments and we will therefore discuss it here in more detail. We will also review several attempts to reduce chemical sputtering and radiation enhanced sublimation of graphite by additions of dopants. Erosion measurements of hydrogenated carbon layers on surfaces of tokamak plasma facing components will also be included.

The atomic mechanisms governing the different erosion processes have been discussed in separate reviews [2-8] and it is clearly beyond the scope of this paper to repeat the discussion of models. The emphasis will be on the presentation of data and empirical formulas to estimate sputtering yields.

[1] For a review on physical sputtering see paper by W. Eckstein, J. Bohdansky, J. Roth, this issue, page 51.

2. PHYSICAL SPUTTERING OF GRAPHITE

Physical sputtering is the ejection of surface atoms which receive sufficient kinetic energy through collisions with incident projectile ions to overcome the surface binding energy of the solid. Physical sputtering of fusion relevant materials is reviewed in detail in the paper by Eckstein et al.; only carbon related results will be discussed here.

Figures 1 and 2 give examples of the dependence of the sputtering yield of graphite on the energy and the angle of incidence for various light ions and carbon ions. Compared with heavier elements, carbon as a target exhibits for these ions a lower threshold energy for sputtering, E_{th}, of about 30 eV. The self-sputtering yield, which is smaller than unity at normal incidence, exceeds one at angles of incidence above 70° [9].

In general, the physical sputtering yield can be expressed as a function of incident energy, $Y(E_0)$, and also as a function of incident angle, $Y(\alpha)$:

$$Y(E_0) = Q\, S_n \left(1 - \left(\frac{E_{th}}{E_0}\right)^{2/3}\right)\left(1 - \frac{E_{th}}{E_0}\right)^2 \qquad (1)$$

with

$$S_n = \frac{3.44\sqrt{\frac{E_0}{E_{TF}}}\ln\left(\frac{E_0}{E_{TF}} + 2.72\right)}{1 + 6.36\sqrt{\frac{E_0}{E_{TF}}} + \frac{E_0}{E_{TF}}\left(6.88\sqrt{\frac{E_0}{E_{TF}}} - 1.71\right)}$$

and

$$Y(\alpha) = Y(\alpha = 0)\,(\cos\alpha)^{-f} \exp\left[f\left(1 - (\cos\alpha)^{-1}\right)\cos\alpha_{opt}\right] \qquad (2)$$

The parameters E_{th}, E_{TF}, Q, f and $\eta = \pi/2 - \alpha_{opt}$ are listed in Table I; the energy dependence of f and α_{opt} is shown in Fig. 2 of the paper by Eckstein et al. The analytical expressions (2) for f and α_{opt} given by Yamamura et al. [10] are reasonable approximations, although the predicted energy dependence differs somewhat from the experimental data. However, data obtained for highly polished surfaces may deviate rather strongly from those for unpolished, technical surfaces [9, 11]. In Fig. 3, the angular dependence of the sputtering yield of graphites with various degrees of surface roughness is compared.

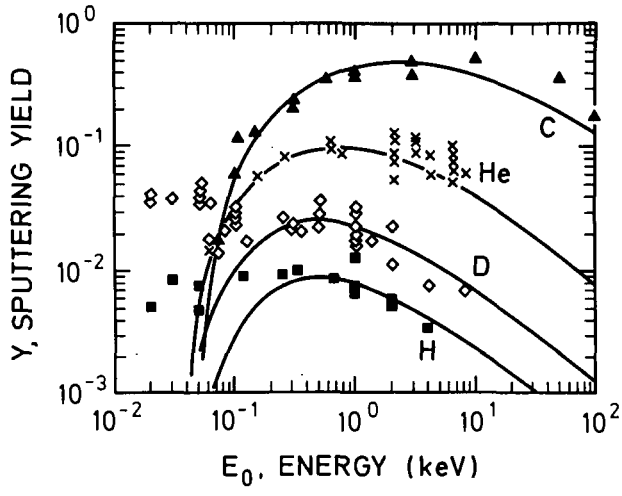

FIG. 1. Dependence of the sputtering yield of graphite on energy for H, D, He and C ions at normal incidence. The variation of the data points represents the reproducibility of measurements as well as the dependence on the surface preparation of different types of graphite. The solid curves are given by Eq. (1).

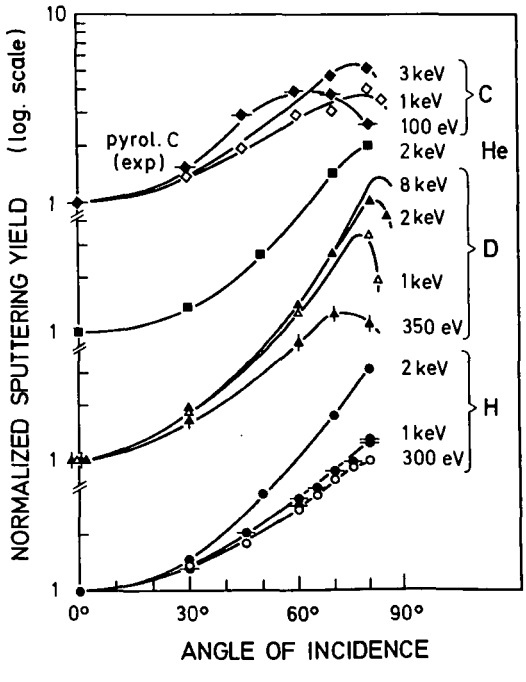

FIG. 2. Dependence of the sputtering yield of graphite on the angle of incidence for H, D and C ions for highly polished pyrolytic graphite. The curves are least-mean-square fits to the data using Eq. (2) with the fitting parameters f and α_{opt}. Data for C [9], for He, D and 2 keV H [3], and for 0.3 and 1 keV H [11].

TABLE I. PARAMETERS FOR THE SPUTTERING YIELD

	H	D	T	^{4}He	C
E_{th} (eV)	35	30	30	29	42
E_{TF} (eV)	415	447	449	1087	5687
Q	0.035	0.1	0.2	0.32	1.5
f	2.51	2.53	2.54	2.54	
η	0.121	0.151	0.161	0.241	
Y_{low}	8×10^{-3}	4×10^{-2}	10^{-1}		

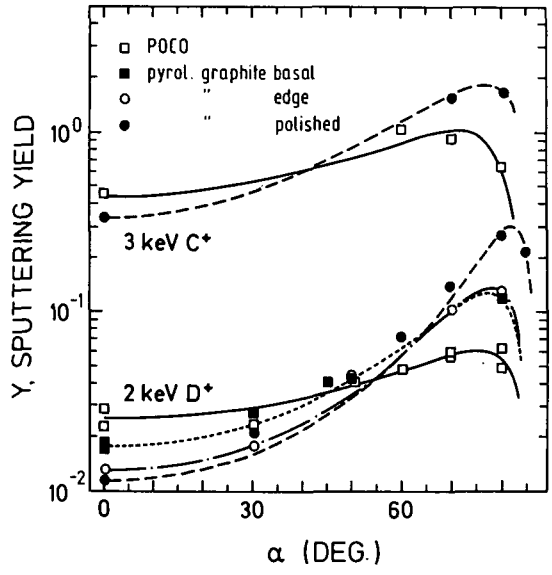

FIG. 3. Angular dependence of the sputtering yield for various types of graphite exhibiting different degrees of surface roughness [12]. The curves are best fits using Eq. (2).

Porous graphites with larger degrees of surface roughness have been found to exhibit higher sputtering yields for normal incidence [12]. For grazing angles of incidence, however, the increase in sputtering yield is less for porous materials than for polished surfaces [12, 11]. In view of these variations the precision of the empirical fit by Yamamura et al. [10] appears adequate and their values of f and η are given in Table I for the case of 1 keV; f is considered to be independent of energy, while

$$\eta \propto 1/\sqrt{E_0} \qquad (3)$$

for E_0 in keV.

For evaluating the impurity transport and the redeposition in plasma devices, the angular and energy distributions of sputtered atoms are also important. This is discussed in detail in Ref. [3] for fusion applications, and graphite is expected to be similar to other materials. It is shown that for ions with a broad range of incidence angles the angular distribution of sputtering atoms can reasonably well be approximated by

$$dY/d\vartheta = Y(0) \cos\vartheta \qquad (4)$$

For the energy distribution of sputtered particles the well known Thompson equation [13] can be modified owing to the small amounts of energy transferred to surface atoms for fusion applications (see Ref. [3]):

$$dY/dE_1 = [E_1/(E_1 + U_0/3)^4]^{2/3} \qquad (5)$$

where U_0 is the surface binding energy, which can be taken to be 7.4 eV for carbon [14].

If these distributions need to be treated in more detail for special applications, differential sputtering yields should be interpolated from experimental data or calculated by computer simulations [15] in a way similar to the treatment of ion reflection[2].

3. RADIATION ENHANCED SUBLIMATION

Physical sputtering as outlined above is independent of the temperature of the surface. For graphite, however, the sputtering yields are observed to increase as the temperature varies from 300 K to > 2000 K. The temperature dependence of the sputtering yield of graphite irradiated by Ar^+, O^+, C^+ and D^+ is shown in Fig. 4. Above 1200 K, ion bombardment of carbon materials results in anomalous temperature dependent erosion, referred to as radiation enhanced sublimation (RES). This appears to be effective only for carbon and carbon based materials. The yield increases monotonically with increasing temperature and the effect is independent of the species of incoming particles [16]. Thus, the chemical affinity between the incoming ions and the target atoms cannot be responsible for RES. The eroded particles are predominantly monatomic [17], in contrast to thermal sublimation for which nearly equal amounts of C, C_2 and C_3 are observed above 2000 K. Thermal spike models are ruled out by this observation. Carbon atoms are emitted with an

[2] For a review on reflection see paper by W. Eckstein, this issue, page 17.

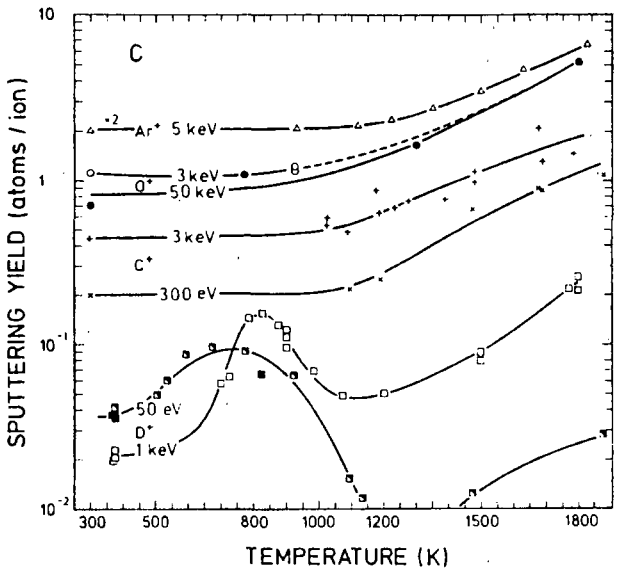

FIG. 4. Temperature dependence of the sputtering yield of graphite irradiated by Ar^+ [19], O^+ [31, 32], C^+ [9, 32, 34] and D^+ [26, 52] at different energies. The Ar yields have been normalized at room temperature to TRIM calculations which give a value of 1 for 5 keV Ar^+.

isotropic angular distribution even for grazing ion incidence [16] and with an energy distribution equivalent to the surface temperature [18]. This is in contrast to physical sputtering, where grazing angles of incidence result in an anisotropic emission of sputtered atoms and an energy distribution in the eV range (see Eq. (5)).

Most of the experimental features can be predicted by a proposed model [4, 7, 19, 20] which describes the process as the sublimation of radiation induced interstitials. Vacancy-interstitial pairs are created via nuclear collisions. Diffusing interstitials which reach the surface have a binding energy of only 0.15 eV [21] to the surface and sublimate thermally. It is assumed that the annihilation of interstitials is dominated by diffusion controlled recombination with vacancies. At temperatures above 1200 K, where vacancies become mobile and diffuse to sinks, the erosion yield due to RES increases and exceeds that due to physical sputtering. At low temperatures the process is less effective than physical sputtering because of recombination of interstitials with vacancies.

On the basis of this model, computer simulations were performed [4]. It was possible to reproduce the temperature dependence as well as the absolute RES yields using reasonable values [22] of the displacement energy (25 eV) and of interstitial and vacancy activation energies for diffusion (0.3 and 3.5 eV, respectively). Figure 5 [4, 16] shows the excellent agreement of the temperature dependence of the RES yield above 1000 K for H, D and He ions with model calculations (solid lines). There are, however, experimental findings which are not adequately described by the model. The predicted dependence of the RES yield on the ion flux is larger than experimentally determined [19, 23, 24] (see below). Also, the model predicts a transient yield enhancement at the commencement of irradiation. This transient enhancement, however, is only observed after annealing the sample to temperatures higher than 2000 K [20], which indicates that it is not only single vacancies which have to be considered as the sink for interstitials but also more stable defect clusters.

3.1. RES by light ions

The temperature dependence of the RES yield above 1000 K for H, D and He is shown in Fig. 5 [4, 16]. It is seen that the sputtering yield increases with increasing temperature and reaches values close to 1 for He at 2000 K. According to the above model, the yield must eventually reach saturation when all of the created interstitials sublimate from the surface.

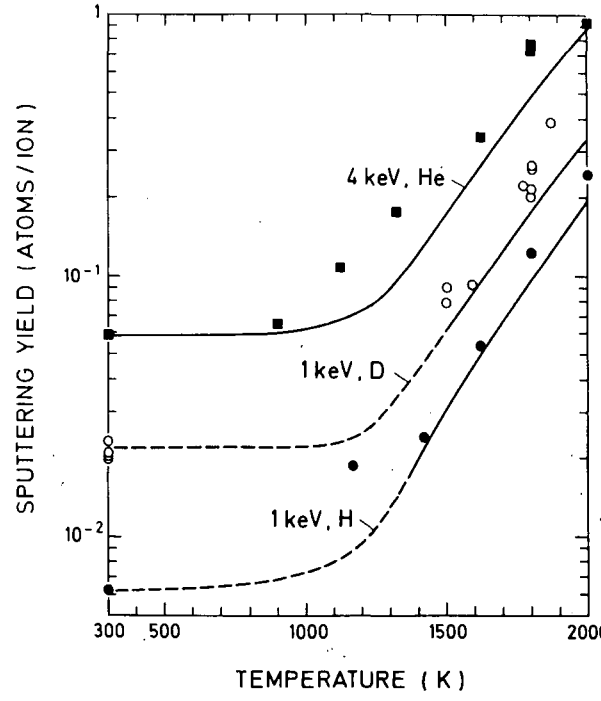

FIG. 5. Temperature dependence of the RES yield for H, D and He ions at different energies compared with model calculations (solid curves) [4].

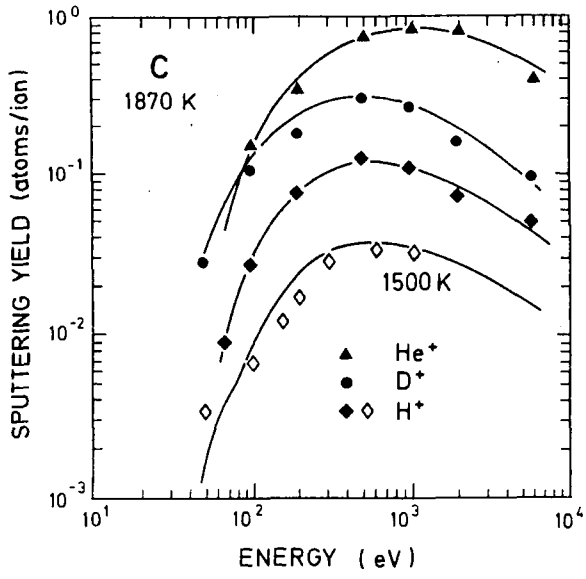

FIG. 6. Energy dependence of the RES yield for H, D and He ions at 1870 K [25] and for H at 1500 K [23]. The curves are obtained from Eqs (1) and (6).

However, at temperatures above 2000 K, thermal sublimation dominates the erosion for ion fluxes below 10^{16} cm$^{-2}\cdot$s^{-1}.

RES is observed even at hydrogen ion energies as low as 50 eV [23, 25, 26] (see Fig. 6). This indicates that the displacement energy, which is taken to be 25 eV in the bulk, may have lower values close to the surface [27]. On the basis of experimental data for Ge surface displacement, energies of 12.5 eV for graphite and 27.5 eV for diamonds [28] have been estimated. The energy dependence as shown in Fig. 6 for H, D and He at 1870 K [25] and H^+ at 1500 K [23] actually indicates that the RES yield drops towards a threshold energy for this process. As the temperature decreases, the yield becomes lower and is eventually dominated by the temperature independent physical sputtering yield [23]. The shoulder seen in the data for H^+ at 1500 K [23] may indicate a slightly lower threshold energy for physical sputtering than for RES.

The atomistic model [4] indicates a complex process which cannot be described by a single activation energy or a single threshold energy. However, the experimental data can be fitted reasonably well in this way. In fact, it could be shown [25] that the energy dependence of physical sputtering (Eq. (1)) could also be applied for RES, using the same threshold energy and a modified yield parameter given by

$$Q_{tot} = Q + 54\, M_i^{1.18} \exp[-0.78\ \text{eV/kT}]\, (\Gamma/10^{16})^{-0.1} \quad (6)$$

where M_i is the mass of incident ions in atomic mass units. The last term in this equation represents an attempt to include the ion flux dependence. The model [4, 19] would result in a decrease of the yield with ion flux as $Y \propto \Gamma^{-0.25}$, whereas experiments for Ar^+ [19] and H^+ [23, 29] in the flux range of 10^{13} to 10^{17} cm$^{-2}\cdot$s^{-1} show a more linear flux dependence. Results for the flux dependence of RES and chemical sputtering for 1 keV H^+ impact are shown in Fig. 7, where data from different experiments are collected [16, 23, 29]. (This figure also contains chemical erosion data which will be discussed in the next section.) For lower ion energies, data for high flux from the PISCES plasma simulator [24, 30] show only a moderate decrease of the RES yield compared to ion beam experiments at low flux. Clearly, the extrapolation to fusion relevant fluxes of 10^{18} cm$^{-2}\cdot$s^{-1} and higher is still not certain and requires further investigations. However, on the basis of the limited experimental data, a flux dependence given by $(\Gamma/10^{16})^{-0.1}$, with Γ in ions$\cdot$cm$^{-2}\cdot$s^{-1}, seems adequate.

3.2. RES due to oxygen and self-sputtering

RES occurs also for heavier ions and has been investigated for Ar^+ [17, 19], O^+ [31–33] and C^+

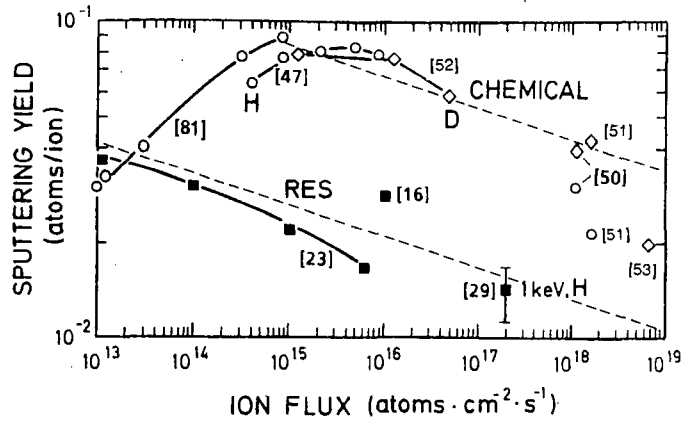

FIG. 7. Flux dependence of RES and chemical sputtering at T_{max} from different experiments. The RES data are for 1 keV H^+ at 1500 K (■). Chemical sputtering data are for H (○) and D (◇) at energies between 250 and 2000 eV. The curves extrapolating the high fluxes are taken from Eqs (6) and (8).

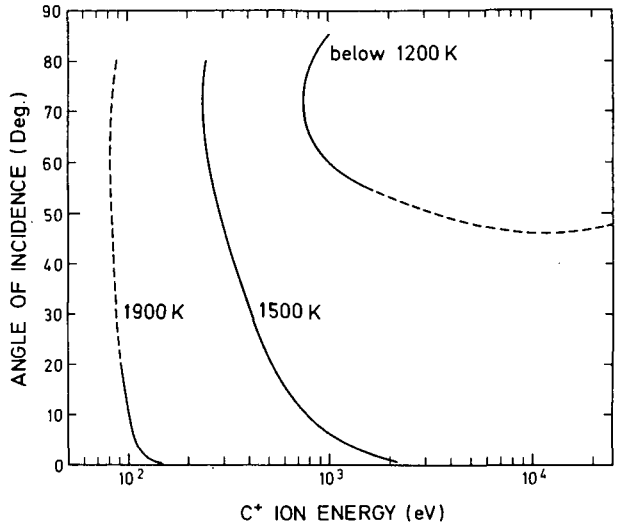

FIG. 8. Conditions for the self-sputtering yield of unity in the energy versus angle of incidence plane for different surface temperatures of graphite [9].

[9, 30, 32, 34] (see Fig. 4). Atomistic modelling of heavy ion bombardment faces the additional difficulty that the model predicts unreasonably large radiation damage concentrations because it is assumed that the only annealing process is recombination of single vacancies and interstitials [4]. The empirical formula presented in Eq. (6) holds, however, also for heavy ion bombardment. For oxygen, the erosion yield below 1000 K is of the order of unity, independent of energy due to chemical sputtering (see below). With increasing temperature (above 1200 K) the yield increases further and reaches a value of 5 at 1800 K.

Values of the self-sputtering yield Y_c higher than unity are detrimental in fusion devices owing to an avalanche effect. The effective erosion yield due to plasma induced sputtering, taking self-sputtering into account, has often been approximated by

$$Y_{eff} = Y_{D,T}/(1 - Y_c) \quad (7)$$

Although the derivation of Eq. (7) is valid only for a one-dimensional plasma description, it clearly shows a singularity as Y_c approaches unity.

In Section 2 it is shown that self-sputtering yields of one can be obtained for physical sputtering at grazing angles of incidence. The RES yield is not expected to depend as strongly on the ion angle of incidence as physical sputtering does, since, in the case of RES, not only the defects created in a shallow surface layer are involved in atom ejection but defects from the entire ion range diffuse to the surface. Indeed, both the model predictions and experimental data show only a weak dependence on the ion angle of incidence [9]. Taking into account the energy and angular dependence of RES, Roth et al. [9] have obtained regions in the energy versus angle of incidence space for different temperatures where the total self-sputtering yield exceeds unity (Fig. 8).

Figure 8 demonstrates that at temperatures below 1200 K, sputtering yields of unity are only obtained at high energies and grazing angles of incidence, while, at 1900 K, the yields are above unity for all angles of incidence and energies higher than 100 eV. Thus, RES poses strict limits on the usable temperature range of pure graphite.

4. CHEMICAL EROSION

In contrast to physical sputtering and RES, the chemical erosion of carbon depends strongly on the system of the implanted particle and the target material. Chemical sputtering has been observed only in systems where volatile molecules such as CO, CO_2 or C_xH_y are formed owing to interactions of projectile ions and carbon atoms. Desorption of molecules with thermal energies was recently confirmed by Vietzke et al. [35] for the case of CD_3 molecule formation under simultaneous D^0 and Ar^+ impact.

However, for the mechanism of molecule formation, no comprehensive model exists which can describe all experimental data. For the interaction of hydrogen isotopes with graphite, a model was proposed [36] which explains the occurrence of a peak in the erosion yield as a function of temperature. The release of hydrogen under steady state conditions competes with surface reactions for the formation of CH_4 molecules and H_2 recombination. This model predicts a flux dependence of the yield as $1/\Gamma$ at high incident fluxes. It has been modified on several occasions to include the strong effect on the incident ion energy [37] or the simultaneous erosion due to energetic hydrogen ions and thermal hydrogen atoms [8, 38]. The semi-empirical model for synergistic methane formation [8] leads to a reasonably good prediction of the temperature dependence and the flux dependence (including a shift in T_m for different fluxes) for the impact of H^0 only and H^+ only, for fluxes of $< 3 \times 10^{15}$ cm^{-2}·s^{-1}. A reasonably good prediction of the synergistic factor (see below) was also obtained for the case of combined H^0–H^+ impact. However, none of the models takes into account that it is not only CH_4 which is formed

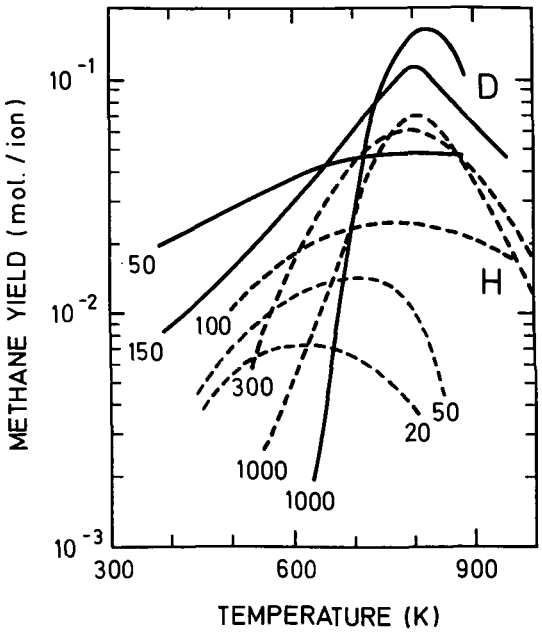

FIG. 9. Yields of CH_4 and CD_4 as a function of the surface temperature for different ion energies. The data for D (solid lines) are from Ref. [42] and those for H (dashed lines) are from Refs [47, 49].

but that also heavier hydrocarbon molecules are formed, which even dominate at ion energies below 300 eV [39–41]. No model describes the broadening of the temperature dependence at low ion energies, which leads to chemical erosion already at room temperature for energies below 100 eV [42]. It has been shown that H_2 recombination [43, 44], CH_4 formation [44, 45] and even formation of heavier hydrocarbons [46] occur at the end of the ion range rather than at the surface. The low energy yield at room temperature points to a possible diffusive release of volatile molecules. Further, the chemical reaction yield is not proportional to $1/\Gamma$, and no model describes the observed maximum yield at fluxes around 1×10^{15} atoms·cm^{-2}·s^{-1} and the slow decrease towards higher fluxes [8, 47, 48] (see Fig. 7). Thus, no model is available at present for reliable extrapolation of laboratory data to fusion reactor relevant fluxes higher than 10^{18} atoms·cm^{-2}·s^{-1}.

However, an extensive database exists for most of these reactions in certain parameter ranges. The main problem in the past was to extrapolate these data to the plasma edge conditions of a fusion device, i.e. the erosion yield of carbon under high hydrogen fluxes around 10^{18} H atoms·cm^{-2}·s^{-1}, at impact energies below 100 eV. Furthermore, the erosion due to simultaneous impact of carbon, oxygen and hydrogen may lead to combined effects.

For the most part, these questions have been answered. Here, we discuss only those results which are important for application in the field of plasma-wall interactions and which have not been included in the earlier compendium [1].

4.1. Carbon erosion by hydrogen

A typical set of graphs of the temperature dependence of methane formation on graphite at medium fluxes (10^{16} H$^+$·cm^{-2}·s^{-1}) is shown in Fig. 9 [42,47,49]. The temperature dependence of the formation of other hydrocarbons is in most cases very similar to that of methane formation (see below). The methane yield has a maximum around 800 K. For 300 eV ions, it reaches a value of nearly 0.1 CH_4/H and 0.15 CD_4/D. With decreasing energy, the maximum yields decrease and the temperature dependence becomes broader. A similar broadening of the temperature dependence at low energies (< 100 eV) and high fluxes (10^{18} D$^+$·cm^{-2}·s^{-1}) was also observed in plasma experiments in TEXTOR [50] and in PISCES [51]. While there is no clear threshold for chemical sputtering as a function of H$^+$ ion energy, it appears that there are changes in the dominating reaction mechanisms for energies near and below 100 eV/H$^+$ [47]. From the model proposing that methane formation occurs at the end of the ion implan-

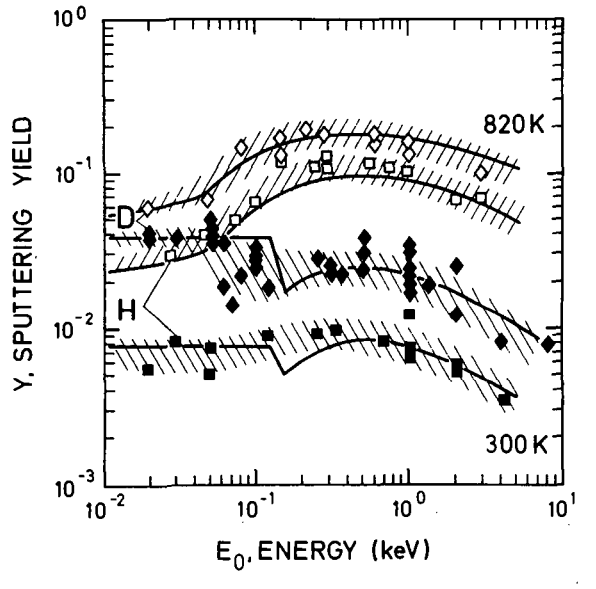

FIG. 10. Energy dependence of the total sputtering yield of graphite. The data are from mass loss measurements at room temperature and the maximum temperature for chemical sputtering for H (■, □) and D (◆, ◇) ions [52, 83]. The curves show the analytic fit obtained with Eqs (7) to (9).

tation zone [43–45, 50] we conclude that for the high energy cases the rate at which CH_4 leaves the surface may be controlled by molecular diffusion.

Roth and Bohdansky [42, 52] have investigated the total erosion process down to hydrogen energies of 20 eV, in an ion beam experiment at medium fluxes, as shown in Fig. 10. The energy dependence at the maximum of chemical sputtering is very similar for H and D ions and indicates a dependence on the energy which the projectile ions deposit near the surface in the form of broken C–C bonds [6, 37]. This might also explain the difference in the absolute yields due to H and D ions.

Because of the increased broadening of the temperature dependence of carbon erosion at low ion energies, an almost energy independent erosion yield dominated by hydrocarbon formation is obtained at room temperature and for ion energies in the range below 80 eV [42]. Therefore, a decrease of the ion impact energy in the range below 100 eV has only a minor effect on the total erosion yield. At high ion fluxes the broadening of the temperature dependence is enhanced and an energy independent yield is obtained below 200 eV [48]. In addition, a remarkable isotope effect is observed in the chemical yields for hydrogen and deuterium impact; this effect is not yet understood.

The flux dependence of the chemical sputtering yield, collected from various ion beam and plasma experiments, is given in Fig. 7, which also includes the RES data discussed in Section 3. An extrapolation of the data for fluxes of $> 10^{16}$ H·cm^{-2}·s^{-1} indicates a gradual decrease for higher ion fluxes. It has been suggested [36] that the chemical erosion of graphite is drastically suppressed at high ion fluxes. This is not observed in the PISCES facility [30, 48, 51], where the erosion of graphite by hydrogen plasma was investigated at low energies and high fluxes (100 eV, 10^{18} H·cm^{-2}·s^{-1}). The temperature dependence of the total yield is similar to that for lower fluxes as obtained with ion beams. The total yield is reduced only by a factor of two to three at high fluxes (10^{18} H·cm^{-2}·s^{-1}) compared to medium fluxes (10^{16} H·cm^{-2}·s^{-1}) (see Fig. 7).

Similar results were also obtained by in situ measurements at high fluxes (10^{18} cm^{-2}·s^{-1}) in DITE [53] and TEXTOR [50]. The yields were also reduced by a factor of about two to three relative to the yields at medium flux densities. In the TEXTOR sniffer probe experiments, at room temperature the erosion yield of hydrogen plasma on graphite decreased with increasing ion energy (75–275 eV), whereas at the peak temperature the yield increased with increasing energy. An isotope effect similar to that shown in Fig. 10 was also observed in these experiments.

The dependence of chemical erosion on ion energy, surface temperature and ion flux is tentatively described [54] by the following equations:

$$Y_{chem}(E_0, T) = \frac{6\times10^{19}\exp(-1\ \text{eV/kT})}{1\times10^{15} + 3\times10^{27}\exp(-2\ \text{eV/kT})} \times (200\ QS_n + 1000\ Y(E_0)) \left(\frac{\Gamma}{10^{16}}\right)^{-0.1} \quad (8)$$

where Q, S_n and $Y(E_0)$ are taken from physical sputtering (Eq. (1)) and Γ is given in ions·cm^{-2}·s^{-1}. To limit Y_{chem} to values below 0.25, which cannot be exceeded if methane formation dominates, the additional rule

$$Y'_{chem} = \frac{Y_{chem}}{(1 + Y_{chem}/0.25)} \quad (9)$$

applies. The broadening of the temperature dependence at low energies has been taken into account rather crudely by the additional condition for $T < 900$ K and $E_0 < 100$ eV:

$$Y''_{chem} = \max\{Y'_{chem}, Y_{low}\} \quad (10)$$

The values of Y_{low} for H and D as well as the estimated value for T are given in Table I.

The predicted results from this formula are introduced in Figs 7 and 10 for the flux and energy dependences of graphite erosion, respectively.

The chemical erosion yield is only partly due to the formation of methane molecules. Systematic studies of heavier hydrocarbons due to H^+ impact [39–41] and H^0 impact [41, 55] on carbon have been published recently. Figure 11 shows the energy dependence of the contribution of CH_x, $\Sigma\ C_2H_i$ and $\Sigma\ C_3H_i$ to the total chemical erosion as a function of the impinging hydrogen ion energy at the peak temperature. The energy dependence of the product formation exhibits a similar tendency; with decreasing energy, the ratios $\Sigma\ C_2H_i/CH_4$ and $\Sigma\ C_3H_i/CH_4$ increase. The absolute yields obtained by different authors agree reasonably well, with the exception of the $\Sigma\ C_2H_i$ formation, especially the C_2H_2 component; this is the main reason for the indicated uncertainty in the total chemical erosion yield. The reason for the discrepancy is unknown, since all data were obtained for

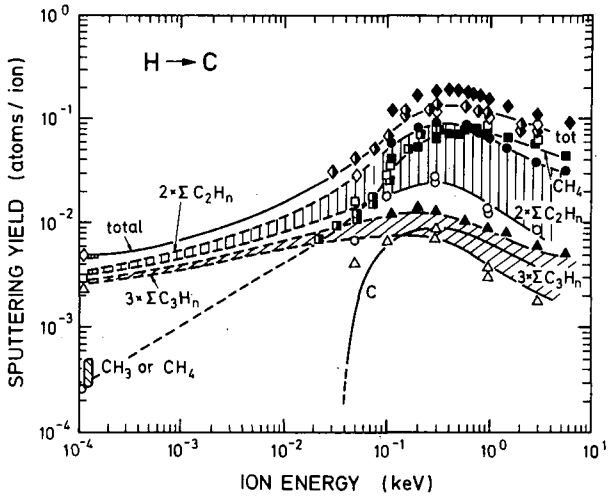

FIG. 11. Energy dependence of the contribution of different hydrocarbon molecules to the total erosion of graphite at the maximum temperature for chemical sputtering. Open points [41, 102], half filled points [39], solid points [40]. Data for thermal energies: Open points [41, 102], boxes [55].

pyrolytic graphite at similar ion fluxes of about 10^{15} to 10^{16} atoms·cm^{-2}·s^{-1}. Recently, the studies on the distribution of molecular species have been extended over a wide range of H^+ fluences [56], indicating that the C_2H_2 contribution increases with increasing ion fluence. This gives the first hint for the origin of the wide range of the C_2H_2 contribution reported. In all studies, the energy at which the maximum erosion yield occurs decreases with increasing carbon content of the hydrocarbon molecule.

Here again, we have some evidence of the existence of different controlling mechanisms for low and high energies. This observation appears to be consistent with the model discussed in Ref. [50]. If we assume that the implanted energetic hydrogen reacts only after thermalization, hydrocarbon formation should be independent of the H^+ ion impact energy. Only the depth at which the reaction occurs is different. Therefore, for high energy impact, the larger hydrocarbons formed in deeper subsurface layers (compared with CH_4) may be prevented from penetrating to the outer surface. For relatively low energy bombardment, on the other hand, the implantation zone is very near the outer surface and, thus, heavy hydrocarbons formed there are more readily released [50].

While molecular hydrogen does not react with graphite, the chemical reaction between atomic hydrogen and graphite occurs also at thermal hydrogen energies in the absence of radiation induced displacements. The formation of hydrocarbons due to thermal H^0 impact on different types of graphite has been studied extensively [8, 44, 57–59].

Thermal atomic hydrogen reacts with carbon materials, forming the radical CH_3 and a wide spectrum of higher volatile hydrocarbons. At temperatures up to 500 K, the hydrocarbon spectrum (not the yield) depends only slightly on the temperature. Above 500 K, the lighter hydrocarbons dominate [41, 55]. Balooch and Olander [60] reported a special branch of C_2H_2 production above 1200 K. This result has not been reproduced by other investigators. The different results on heavier hydrocarbon formation due to the reaction of thermal atomic hydrogen are included in Fig. 11 [41, 55]; see also Ref. [102]. Since for carbon erosion the number of carbon atoms in each molecule has to be taken into account, the chemical erosion of carbon by H^0 is dominated by formation of C_2H_x and C_3H_x molecules. The total sputtering yield shown in Fig. 11, which is about two orders of magnitude smaller than that for energetic ions, is the yield for annealed graphite. The sputtering yield from a surface activated by prebombardment or from deposited a-C:H layers is increased and approaches the yield for energetic ions [61–63]. Using thermal tritium and protium atoms, no isotopic effects were observed in the temperature dependence of hydrocarbon formation [64].

4.2. Carbon erosion by oxygen

Apart from its application in fusion, carbon is widely used in other high temperature applications, for example by the aerospace industry. Typically, the atmosphere of interest is that of air, and the primary reactions involve oxygen. Therefore, the literature gives extensive data on the erosion of graphite due to oxidation; results for the reaction of carbon with molecular and thermal atomic oxygen have been published in Ref. [1].

Relatively low reaction rates are observed for molecular oxygen at temperatures below 1000 K, and the measured sputtering yields depend on the type of graphite or on the surface orientation of pyrolytic graphite. The main reaction product is CO; the CO_2 yields are about two orders of magnitude lower. The reactivity of atomic oxygen with graphite is much higher, even at lower temperatures [33, 65].

Since the publication of the previous data compendium [1] in 1984, carbon erosion due to energetic oxygen ion impact has been studied in some detail [31, 33, 66–70]. In general, no pronounced temperature dependence of the erosion yield is observed. The

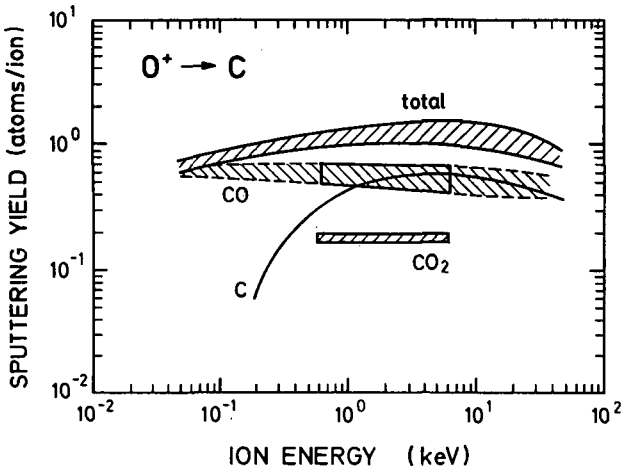

FIG. 12. Energy dependence of the total sputtering yield of graphite at room temperature bombarded with oxygen ions and of the reaction yield for various molecular species. The data are taken from Refs [31, 33, 66–69].

energy dependence of the reaction yield and of the released molecular species is shown in Fig. 12 for measurements at room temperature. When energetic oxygen impinges on carbon, the implanted oxygen is retained in the carbon until the oxygen concentration saturates. The saturation concentration decreases with increasing carbon temperature and decreasing impact energy, similar to the results for hydrogen impact [33, 71]. When saturation is reached, all the implanted oxygen reacts to form CO or CO_2. The total yield is about unity, independent of the incident energy, as can be seen in Fig. 12. The energies of the released molecules can be assumed to be thermal, while the sputtered carbon atoms have energies in the 5 eV range [14].

5. SYNERGISTIC EFFECTS IN THE CHEMICAL EROSION OF CARBON

In a tokamak fusion reactor, the plasma facing components are subjected to the simultaneous impact by energetic ions (H^+, He^+), charge exchange neutrals, Franck–Condon neutrals, impurity ions (e.g. metals, C, O), electrons, photons and neutrons. Multispecies impact on materials could lead to interactive processes, with the effect of the interaction differing from that obtained by a simple linear superposition of the effects caused by the impacting species acting separately. Such non-linear effects are normally referred to as synergistic effects. While a broad range of synergisms might occur during the complex interactions between the fusion plasma and the plasma facing materials, we restrict our discussion here to synergistic effects in the chemical erosion of carbon when exposed to combinations of energetic particles, including oxygen and carbon ions, thermal hydrogen atoms and electrons. We present data obtained in laboratory experiments, with emphasis on the results obtained since the publication of the previous data compendium [1] in 1984. Other reviews which appeared at about the same time include those by Roth [3, 6], Vietzke et al. [5] and Auciello et al. [72]. A more recent review was published by Vietzke and Philipps [50].

We examine first the data on hydrocarbon formation due to combined thermal H^0 atoms and energetic ions. This includes an increase of the self-sputtering yields by carbon ions owing to simultaneous impact of H^0 and C^+. Then we discuss the special case of a combination of thermal H^0 atoms and energetic O^+ ions. Finally, we consider the effect of electrons on the chemical erosion of carbon for simultaneous bombardment by hydrogen ions/atoms and electrons.

5.1. Energetic ions and thermal H^0 atoms

In the previous sections we have shown that the chemical sputtering yield of carbon due to the impact of energetic H^+ ions is about two orders of magnitude higher than that due to H^0 atoms. The generally accepted mechanism responsible for this effect is the deposition of energy into sites of nuclear damage in the surface layer [3] by energetic ions, which creates sites available for subsequent reactions with hydrogen. Because of their low energies, no collisional processes are associated with thermal H^0 atoms and, therefore, only inherent carbon bonds are available for reactions with hydrogen. If, however, thermal H^0 atoms impinge on a carbon surface that is simultaneously damaged by energetic ions, reaction probabilities enhanced over those for H^0 only could be expected.

In fact, clear evidence of such a synergistic enhancement of chemical erosion was found by Vietzke et al. [73] for experiments involving simultaneous bombardment of pyrolytic graphite by Ar^+ (5 keV) ions and sub-eV H^0 atoms. Pre-irradiation with Ar^+ alone also modifies the graphite, resulting in enhanced reactivity during subsequent H^0 exposure, after an initial transient period [62].

With a detection technique using a direct-line-of-sight quadrupole mass spectrometer, the CH_3 radical was found to be the dominant hydrocarbon produced during simultaneous Ar^+/H^0 impact on carbon [73, 44], as was found in the case of sub-eV H^0

irradiation alone. In addition, C_2 hydrocarbon compounds were observed [73].

The probabilities of reaction product formation as a function of temperature are characterized by maxima at about 800 K [73], similar to the case of H^+ impact alone (see above). Furthermore, a comparison of the reaction probabilites for CH_3 formation showed very similar results for different types of graphites under simultaneous irradiation by H^0 atoms and 5 keV Ar^+ ions [59]. This is in agreement with erosion data for H^+ only, for different forms of graphite [72, 74], and is probably due to the fact that radiation induced amorphization [72, 74, 75] may lead, at high fluences, to similar surface structures, thus diminishing or eliminating initial structural differences. At fluences higher than 10^{20} cm^{-2}, which are easily obtainable in the PISCES device [48], there are no structural effects. In this connection, it should be mentioned that the stronger diamond structure is more resistant to amorphization and chemical reactivity [76, 77].

For the case of simultaneously impinging energetic hydrogen ions and thermal H^0 atoms [44, 78–81], the difference between the hydrocarbon formation rates for the H^+/H^0 case is attributed to a synergistic chemical erosion effect. The additional erosion efficiency of thermal H^0 atoms was found to depend critically on the H^0 flux or, more precisely, on the H^0/H^+ flux ratio. The temperature dependence of hydrocarbon formation was found to be similar to that of the H^+-only case [41, 81].

For tokamak applications, where the H^+ fluxes are known quite accurately and only the order of magnitude of the H^0 fluxes is available, a useful indicator for the synergistic effect is the synergistic hydrocarbon formation rate divided by the H^+ flux, as a function of the H^0/H^+ flux ratio [41, 81] (Fig. 13). Up to flux ratios of $\Gamma_H^0/\Gamma_H^+ = 1$, the erosion yield per ion does not show a strong enhancement. Data from the plasma simulation device PISCES [48, 51], which are obtained for $\Gamma_H^0 \approx \Gamma_H^+$, also show no enhancement of the synergistic yield, in agreement with ion beam results. For higher Γ_H^0/Γ_H^+ ratios, the total hydrocarbon yield per H^+ ion increases with increasing H^0 flux. For flux ratios $\Gamma_H^0/\Gamma_H^+ > 100$, however, the erosion efficiency of an H^0 atom decreases again to the low non-synergistic level, such that the combined yield also decreases. (This is not apparent in Fig. 13; see Ref. [81].) For thermal atom fluxes much higher than energetic ion fluxes ($\Gamma_H^0/\Gamma_H^+ > 1000$) the definition of a yield per H^+ ion is no longer useful.
A comparison of the synergistic erosion rates for different ion energies is given in Fig. 13. The data

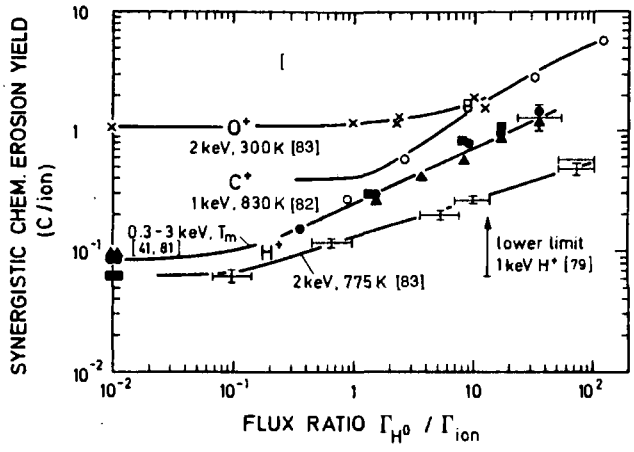

FIG. 13. Dependence of the synergistic chemical erosion yield of graphite for bombardment by H, O or C ions and thermal H atoms. The erosion rate is related to the incident ion flux and plotted versus the flux ratios H^0/O^+, H^0/C^+ and H^0/H^+. The data are taken from Refs [41, 79, 81–83].

have been obtained by four different laboratories, using analysis methods such as quadrupole residual gas analysis [79, 81, 82] and weight loss measurements [83]. The agreement is generally good; the differences are, at least partially, due to uncertainties in the determination of the H^0 fluxes [81].

The total chemical erosion yields shown in Fig. 13 include contributions from methane as well as from heavier hydrocarbons. There appears to be a reasonably smooth transition from the ions-only extreme, where C_2H_x and C_3H_y species are not very important, to the sub-eV H^0 extreme, where these species are dominant, especially because of the production of C_3H_6 and C_3H_8. This is not evident from Fig. 13; the reader is referred to Ref. [41]. For ion energies of > 300 eV/H^+, the proportion of heavy hydrocarbons appears to be independent of the ion energy for the case of combined H^+/H^0 impact. However, decreasing the ion energy to 100 eV or below results in an increasing fraction of heavier hydrocarbons; this is very similar to the case of H^+ bombardment alone [41]. In the range of interest for fusion applications, where simultaneous bombardment by 2 eV Franck–Condon atoms and low energy (< 300 eV) H^+ ions occurs at a ratio of $\Gamma_H^0/\Gamma_H^+ = 1$, the total erosion yield may be as much as two to three times higher than the methane yield [41]. For these conditions, the combined erosion yield at $T_m = 775$ K is of the order of 0.2.

Similar to the case of inert gas ions, the sputtering yield for carbon bombardment is also expected to be enhanced by simultaneous atomic hydrogen impact.

Very recently, such experiments have been performed [82], and the results are included in Fig. 13. It can be seen that for ratios of $\Gamma_H^0/\Gamma_C > 3$, the erosion yield increases. An erosion yield, related to the incident carbon ions, which is larger than unity is observed for $\Gamma_H^0/\Gamma_C = 5$. Since the carbon ion fluxes to limiters or divertor plates are expected to be small compared with atomic or energetic hydrogen fluxes, this yield enhancement may be of dramatic importance for erosion and impurity production.

5.2. Energetic oxygen and hydrogen

Very little is known about the complex reactions occurring when oxygen and hydrogen species impinge simultaneously on carbon. Recently, it was shown in a deuterium beam (5 keV D_2^+) experiment with 5% oxygen impurity (using ^{18}O isotopes) that, in addition to methane, CO and CO_2, also D_2O is formed [84]. The D_2O formation exhibits the same temperature dependence as the methane formation, peaked at 800 K. The D_2O formation at the peak temperature reaches the same values as the CO formation, which is nearly temperature independent.

Release of CO was also observed during the erosion of oxygen saturated carbon by atomic hydrogen of thermal energy. In this experiment, pyrolytic carbon was first implanted with a beam of 2.5 keV ^{18}O ions, up to saturation, and subsequently eroded by thermal atomic hydrogen. It was found that the stored oxygen leaves the carbon predominantly in the form of CO (temperature dependent), with a contribution of CO_2 and H_2O [84].

The total erosion of simultaneously incident 2 keV oxygen ions and thermal hydrogen [83] is shown in Fig. 13. If the yield is plotted versus the oxygen ion flux alone, a further increase is observed, with the erosion efficiency of the incident thermal hydrogen atoms being of the same order as that obtained during Ar^+ bombardment [73]. No reduction of the carbon erosion due to H_2O formation is seen. Recent results, involving combined energetic H^+ and thermal O_2 impact on pyrolytic graphite, also show that the production of CO and H_2O does not affect the yield and the temperature dependence of hydrocarbon formation [85].

5.3. Effect of electrons on erosion

The published data for synergistic erosion of carbon due to energetic ions and thermal H^0 atoms are in reasonably good agreement (see above). On the other hand, the data for the effect of electrons, in combination with H^0 atoms or H^+ ions, do not agree very well. For the case of simultaneous bombardment of graphites with thermal H^0 atoms and electrons, earlier results obtained at KFA Jülich [73] and at the University of Toronto [86] show relatively small enhancements (typically less than a factor of two), while the results of Ashby et al. [87] indicate a 20-fold enhancement over the H^0-only case. No new data have been published since the early 1980s, and the present explanation of the observed discrepancy is the same as that given in previous reviews [1, 72].

Similarly, in the case of simultaneous bombardment of carbon by energetic H^+ ions and electrons, the data obtained at Jülich and Toronto show that the presence of electrons has essentially no effect on hydrocarbon formation for temperatures of 800–2000 K [88], while Guseva et al. [89, 90] report strong synergistic enhancements. For fine grain MPg-8 graphite, bombarded by 10 keV H^+ and 400 eV electrons, the erosion yield, measured by weight loss, was found to increase by about an order of magnitude at 400 K, in comparison with the H^+-only case. The enhancement was found to decrease with increasing temperature, and at the location of the chemical erosion peak (800 K) it was 2.5 times the H^+ induced erosion [90]. Furthermore, an enhancement of four to five times the H^+ erosion yield was also observed in the RES temperature regime, 1100–1900 K [90]. For a sintered carbon sample containing 15% boron (USB-15), no low temperature enhancement was observed; however, at the location of the chemical erosion peak, a factor of five increase over the H^+-only case was observed [89]. By comparison, the Toronto and Jülich studies [88] show a negligible increase in the methane signals due to the addition of e^- to the hydrogen bombardment. In addition to methane, heavy hydrocarbon signals from a quadrupole mass spectrometer were also monitored, again indicating negligibly small enhancements [88]. At the present time, the discrepancy between the results of Guseva et al. [89, 90] and those given in Ref. [88] remains unresolved.

6. EROSION OF GRAPHITE BASED COMPOUNDS

The chemical reactivity as well as the mobility and sublimation of radiation induced interstitials (RES) originate from the specific electronic and structural properties of graphite and were observed to be strongly

suppressed for compounds such as carbides [7]. It was therefore attempted to reduce or suppress these regimes of enhanced erosion by slight modifications of the graphite structure by introducing small amounts of dopants into the lattice. Since these efforts were not systematically investigated and no comprehensive picture has evolved, the results are only summarized here and the reader is referred to the original literature.

6.1. Influence on chemical sputtering

Experiments were performed by covering the graphite surface with evaporated atoms (Ti, Ni, Si or Mo) in the monolayer range or by adding small concentrations of impurities to the bulk graphite (SiC, B, B_4C). A coverage of the surface with monolayers of evaporated Ti, Ni, Si or Mo resulted in a factor of about two smaller CH_4 formation for energetic hydrogen ions [91] and for atomic hydrogen [59]. A much stronger reduction could be obtained by adding small amounts of impurities to the bulk graphite [91, 92]. This supports the hypothesis that the chemical reaction does not occur at the surface but at the end of the ion range. Figure 14 shows the influence of the bulk boron concentration in graphite on chemical sputtering [91, 12]. For energetic 1 keV hydrogen or deuterium bombardment of boron doped carbon

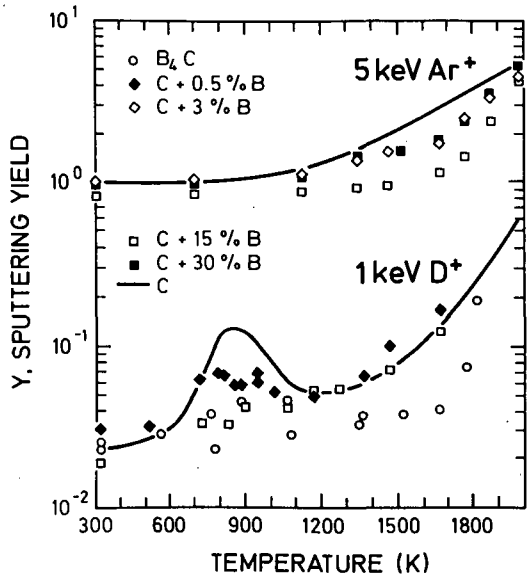

FIG. 14. Temperature dependence of the sputtering yield of pyrolytic graphite and of graphite modified by doping with various amounts of boron, for 1 keV D^+ [96] and 5 keV Ar^+ [98] bombardment. For comparison, the yield for B_4C is also shown [96, 99].

(3–15% B) the chemical erosion yield is reduced by factors of four to six [12, 59, 89] compared to that of pure graphite. The erosion yield peaks around 900 K. Hirooka et al. [30, 93] report only a 30% reduction for bulk boronized graphite (3% B) irradiated by 300 eV H^+ ions at temperatures between 500 and 1200 K in the PISCES-B facility. Reductions by a factor of three were observed for higher boron concentrations (10–20%) [93]. Similar results were obtained for the synergistic reaction of D^0/2.5 keV D^+ (flux ratio $D^0/D^+ = 20$) with bulk boronized graphite (3% B) [84]. For this material, there was no difference in the temperature dependence of the erosion yield due to thermal atomic hydrogen impact and there was a slight reduction of the yield (by about a factor of 1.5) compared with graphite [84].

When a boron containing hydrogenated carbon film (a-C/B:A) is exposed to thermal hydrogen atoms, mainly BH_3, CH_4 and C_2H_x volatile molecules are formed [84, 94]. No B_2H_x compounds are observed. The peak temperature of the yield depends on the boron content. With increasing boron content the maximum yields of all reaction channels are shifted to lower temperatures. For B/C = 0.5, the total erosion yield has a maximum value of 6×10^{-3} (B+C)/H at temperatures of 480 K. This value is more than a factor of six smaller than the erosion yield for thermal H^0 on a-C:H at the same temperature. The same behaviour is observed in the synergistic reaction of thermal D^0/2.5 keV D^+ (flux ratio $D^0/D^+ = 20$) on a-C/B:H (B/C = 2). The total chemical erosion peaks at 400 K and the yield is reduced by a factor of seven compared with the peak value for an a-C:H film at 800 K. The same trends are also observed for energetic hydrogen ions on a-C/B:H. The erosion yield for 1 keV H^+ irradiation peaks at 600 K and the yield is reduced by a factor of 5–18 compared with graphite. With 2.5 keV H^+ irradiation, no clear temperature dependence of the hydrocarbon formation could be observed, i.e. the erosion seems to be dominated by physical sputtering [84].

In comparison, chemical erosion of B_4C due to energetic H^+ impact is dominated by the formation of CH_4 [95], and the yield at T_m (650 K) is about two orders of magnitude lower than that for graphite. Similar to the results of bombardment of boronated graphite (3% B) in PISCES-B [30], no B–H compounds were observed with residual gas analysis [95]. The chemical erosion of the carbon component is small compared with physical sputtering and in fact may be rate limited by physical sputtering of the boron component [95, 96].

All these results show that doping of graphite with impurities such as boron and silicon can strongly reduce its reactivity with hydrogen isotopes. Recent investigations indicate that the dominating factor may be enhanced recombinative release of H_2 molecules instead of CH_4 formation [91, 97].

6.2. Influence on RES

As can be seen from Fig. 14, the addition of boron has only a small effect on the erosion yield for D^+ ions at temperatures above 1500 K, i.e. for RES. However, recent results from PISCES-B for 250 eV D^+ bombardment show a reduction of the RES yield by a factor of three for boron concentrations of 10% and more in graphite [93]. For doping with SiC, where a reduction of chemical erosion similar to that obtained with boron doping was found [91, 92], the depth distribution of silicon in the C/SiC alloy showed a depletion of silicon at temperatures above 1300 K, while around 900 K preferential removal of carbon occurs until silicon enrichment suppresses further methane formation. At high temperatures (> 1300 K), silicon is evaporated from the C/SiC alloy and erosion proceeds as for pure graphite.

In Fig. 14, a slightly different result is shown for RES on boronated graphite [98] during 5 keV Ar^+ bombardment. Clearly, RES is not suppressed. However, the onset of RES of all boronated materials investigated is shifted to higher temperatures, depending on the boron content and the structure of the material. Above 1800 K, boron sublimates and leads to a recovery of the RES emission of carbon, with values close to those for pure carbon. For comparison, the total erosion yield of B_4C [99] is also shown. Boron containing carbon films [20, 100] exhibit the same behaviour as boronated graphites.

Simultaneous evaporation of titanium during argon ion bombardment proved to be successful in reducing the radiation induced sublimation process [32]. Titanium is distributed over about 1500 Å, with a long tail into the bulk which is of the order of the cascade extension due to ion bombardment. The thickness of a layer of titanium evaporated without argon bombardment and subsequently annealed to 1800 K did not exceed the 400 Å depth resolution found in this measurement. No clustering of titanium could be observed by scanning electron microscopy [32]. The titanium concentration has a strong effect on the ion enhanced sublimation yield of carbon atoms. Small concentrations of titanium initially increase the erosion yield, while a concentration of about 10 at.% in the surface layer leads to an almost complete suppression of RES [32].

Considering the suppression of methane formation at 900 K due to silicon additions and the influece of titanium on RES, it has been proposed [91] that a small concentration of TiC should be alloyed into graphite in order to reduce both chemical sputtering and RES. This was recently demonstrated for carbon fibre reinforced graphite (C–C composite) (KUP-Vm) modified by small additions of titanium and silicon [101]. The chemical erosion yield of undoped C–C composites is very similar to that of other forms of pure graphite [102]. A component of the sputtered atom flux with low energies has been identified as sublimated atoms during helium irradiation, and this component could be drastically reduced for titanium and silicon doped materials compared with pure KUP-Vm. Although the details of the experiment as well as the titanium plus silicon modification remain unclear, this result shows encouraging properties for titanium doped graphite.

7. CONCLUSIONS

There are three different erosion mechanisms for graphite under ion irradiation: physical sputtering, radiation enhanced sublimation and chemical sputtering.

While physical sputtering is fairly well understood and an adequate analytical description is available, for the other two processes there is still considerable uncertainty regarding the extrapolation of existing data to fusion reactor conditions, such as lower energies, higher fluxes and variable surface temperatures. For RES, most data can be explained by a proposed model, except for the flux dependence, which is weaker than predicted. For chemical sputtering with hydrogen and oxygen ions, no unique model exists and there is still uncertainty regarding the composition of the molecular species as well as the extrapolation to ion fluxes higher than 10^{18} $cm^{-2} \cdot s^{-1}$.

For all three processes, conditions are identified where the erosion yield under carbon ion bombardment exceeds unity. For physical sputtering, this occurs at grazing ion incidence. However, since the yields exceed unity only marginally and depend strongly on surface roughness, it is possible that physical sputtering alone does not lead to runaway sputtering conditions in fusion reactors with graphite [103]. The erosion due to carbon ion impact may be further enhanced owing to chemical reactions of simultane-

ously incident thermal atomic hydrogen and may result in yields higher than unity even for normal incidence. Chemical effects, however, can be successfully suppressed by the addition of small amounts of dopants, such as 3% boron.

At elevated temperatures, RES enhances the self-sputtering yield and values higher than unity are reached for 1 keV C^+ at 1400 K. Examination of different graphites with different dopants shows that there are considerable variations, depending on the structure of the material. There is hope that further studies will result in the selection of graphite materials suitable for plasma facing components during operation at temperatures of up to 1900 K and more.

REFERENCES

[1] LANGLEY, R.A., BOHDANSKY, J., ECKSTEIN, W., MIODUSZEWSKI, P.,, ROTH, J., TAGLAUER, E., THOMAS, E.W., VERBEEK, H., WILSON, K.L., Data Compendium for Plasma-Surface Interactions, Special Issue 1984, Nucl. Fusion (1984).

[2] BEHRISCH, R. (Ed.), Sputtering by Particle Bombardment, Topics in Applied Physics, Vol. 47 (1981), Vol. 52 (1983), Springer Verlag, Berlin.

[3] ROTH, J., in Physics of Plasma-Wall Interactions in Controlled Fusion (POST, D.E., BEHRISCH, R., Eds), NATO ASI Series, Ser. B: Physics, Vol. 131, Plenum Press, New York (1986) 351.

[4] ROTH, J., MÖLLER, W., Nucl. Instrum. Methods B **7/8** (1985) 788.

[5] VIETZKE, E., ERDWEG, M., FLASKAMP, F., PHILIPPS, V., in Proc. 9th Int. Vacuum Congress and 5th Int. Conf. on Solid Surfaces, Madrid, 1983, Imprenta Moderna, Madrid (1983) 627.

[6] ROTH, J., in Sputtering by Particle Bombardment, Topics in Applied Physics, Vol. 52, Springer Verlag, Berlin (1983) 91.

[7] ROTH, J., in Physics of Plasma-Wall Interactions in Controlled Fusion, NATO ASI Series, Ser. B: Physics, Vol. 131, Plenum Press, New York (1986) 389.

[8] HAASZ, A.A., DAVIS, J.W., J. Chem. Phys. **85** (1986) 3293.

[9] ROTH, J., BOHDANSKY, J., OTTENBERGER, W., J. Nucl. Mater. **165** (1989) 193.

[10] YAMAMURA, Y., ITIKAWA, Y., ITOH, N., Angular Dependence of Sputtering Yields of Monoatomic Solids, Rep. IPPJ-AM-26, Institute of Plasma Physics, Nagoya University, Nagoya (1983).

[11] HAASZ, A.A., DAVIS, J.W., WU, C.H., J. Nucl. Mater. **162–164** (1989) 915.

[12] ROTH, J., ECKSTEIN, W., GAUTHIER, E., LASZLO, J., J. Nucl. Mater. **179–181** (1991) 34.

[13] THOMPSON, M.W., Philos. Mag. **18** (1968) 377.

[14] PASCH, E., BOGEN, P., MERTENS, Ph., J. Nucl. Mater. **166** (1990) 33.

[15] BIERSACK, J.P., ECKSTEIN, W., Appl. Phys. **34** (1984) 37.

[16] ROTH, J., BOHDANSKY, J., WILSON, K.L., J. Nucl. Mater. **111&112** (1982) 775.

[17] PHILIPPS, V., FLASKAMP, K., VIETZKE, E., J. Nucl. Mater. **111&112** (1982) 781.

[18] VIETZKE, E., FLASKAMP, K., HENNES, M., PHILIPPS, V., Nucl. Instrum. Methods B **2** (1984) 617.

[19] PHILIPPS, V., VIETZKE, E., SCHORN, R.P., TRINKAUS, H., J. Nucl. Mater. **155–157** (1988) 319.

[20] PHILIPPS, V., VIETZKE, E., TRINKAUS, H., J. Nucl. Mater. **179–181** (1991) 25.

[21] PHILIPPS, V., VIETZKE, E., FLASKAMP, K., Surf. Sci. **178** (1986) 806.

[22] KELLY, B.T., Physics of Graphite, Applied Science Publ., London (1981).

[23] HAASZ, A.A., DAVIS, J.W., J. Nucl. Mater. **151** (1987) 77.

[24] NYGREN, R.E., BOHDANSKY, J., POSPIESZCZYK, A., et al., J. Nucl. Mater. **166** (1990) 31.

[25] BOHDANSKY, J., ROTH, J., Fusion Technol. (1988) 889.

[26] ROTH, J., FRANZEN, P., unpublished data, 1990.

[27] PICRAUX, S.T., BRICE, D.K., HORN, K.M., TSAO, J.Y., CHASON, E., Nucl. Instrum. Methods B **48** (1990) 414.

[28] BRICE, D.K., TSAO, J.Y., PICRAUX, S.T., Nucl. Instrum. Methods B **44** (1989) 68.

[29] HAASZ, A.A., DAVIS, J.W., CROESSMANN, C.D., et al., J. Nucl. Mater. **173** (1990) 108.

[30] HIROOKA, Y., CONN, R.W., SKETCHLEY, T., et al., J. Vac. Sci. Technol. A **8** (1990) 1790.

[31] HECHTL, E., BOHDANSKY, J., J. Nucl. Mater. **122&123** (1984) 1431.

[32] ROTH, J., ROBERTO, J.B., WILSON, K.L., J. Nucl. Mater. **122&123** (1984) 1447.

[33] VIETZKE, E., TANABE, T., PHILIPPS, V., et al., J. Nucl. Mater. **145–147** (1987) 425.

[34] MAYERHOFER, U., Untersuchung zur strahlungs-induzierten Sublimation von Graphit, Dipl. Thesis, Technical University, Munich (1986).

[35] VIETZKE, E., PHILIPPS, V., FLASKAMP, K., et al., unpublished results, 1990.

[36] ERENTS, S.K., BRAGANZA, C.M., McCRACKEN, G.M., J. Nucl. Mater. **63** (1976) 399.

[37] YAMADA, R., SONE, K., J. Nucl. Mater. **116** (1983) 200.

[38] ITOH, N., MORITA, K., J. Nucl. Mater. **155–157** (1988) 58.

[39] ROTH, J., BOHDANSKY, J., Graphite in High Power Fusion Reactors, IEA Workshop Rep., Federal Institute for Reactor Research, Würenlingen (1983).

[40] YAMADA, R., J. Nucl. Mater. **145–147** (1987) 359.

[41] DAVIS, J.W., HAASZ, A.A., STANGEBY, P.C., J. Nucl. Mater. **155–157** (1988) 234.

[42] ROTH, J., BOHDANSKY, J., Nucl. Instrum. Methods B **23** (1987) 549.

[43] MÖLLER, W., SCHERZER, B.M.U., Appl. Phys. Lett. **50** (1987) 1870.

[44] VIETZKE, E., FLASKAMP, K., PHILIPPS, V., J. Nucl. Mater. **128/129** (1984) 545.

[45] ROTH, J., BOHDANSKY, J., Appl. Phys. Lett. **51** (1987) 964.

[46] YAMADA, R., J. Appl. Phys. **67** (1990) 4118.
[47] DAVIS, J.W., HAASZ, A.A., STANGEBY, P.C., J. Nucl. Mater. **145–147** (1987) 417.
[48] GOEBEL, D.M., BOHDANSKY, J., CONN, R.W., et al., Nucl. Fusion **28** (1988) 1041.
[49] WU, C.H., DAVIS, J.W., HAASZ, A.A., in Controlled Fusion and Plasma Heating (Proc. 15th Eur. Conf. Dubrovnik, 1988), Vol. 12B, Part II, European Physical Society (1988) 691.
[50] VIETZKE, E., PHILIPPS, V., Fusion Technol. **15** (1989) 108; PHILIPPS, V., VIETZKE, E., ERDWEG, M., J. Nucl. Mater. **162–164** (1989) 550.
[51] GOEBEL, D.M., BOHDANSKY, J., CONN, R.W., et al., Fusion Technol. **15** (1989) 102.
[52] ROTH, J., J. Nucl. Mater. **145–147** (1987) 87.
[53] PITCHER, C.S., McCRACKEN, G.M., GOODALL, D.H.J., HAASZ, A.A., MATTHEWS, G.F., STANGEBY, P.C., Nucl. Fusion **26** (1986) 1641.
[54] HARRISON, M.F.A., HOTSTON, E.S., Modelling of the Edge Plasma and Divertors of ITER, NET Team, NET Rep. EUR-FU/80/90-97, Max-Planck-Institut für Plasmaphysik, Garching (1989).
[55] VIETZKE, E., PHILIPPS, V., FLASKAMP, K., WILD, Ch., in Amorphous Hydrogen Films (Proc. Symp. Mat. Res. Soc. Strasbourg, 1987), Les Editions de Physique, Paris (1987) 351.
[56] YAMADA, R., J. Nucl. Mater. **174** (1990) 118.
[57] HAASZ, A.A., AUCIELLO, O., STANGEBY, P.C., J. Vac. Sci. Technol. A **4** (1986) 1179.
[58] PITCHER, C.S., AUCIELLO, O., HAASZ, A.A., STANGEBY, P.C., J. Nucl. Mater. **128/129** (1984) 597.
[59] PHILIPPS, V., FLASKAMP, K., VIETZKE, E., J. Nucl. Mater. **122/123** (1984) 1440.
[60] BALOOCH, M., OLANDER, D.P., J. Chem. Phys. **63** (1975) 4372.
[61] VIETZKE, E., PHILIPPS, V., Nucl. Instrum. Methods B **23** (1987) 449; J. Nucl. Mater. **145–147** (1987) 443.
[62] VIETZKE, E., PHILIPPS, V., FLASKAMP, K., J. Nucl. Mater. **162–164** (1989) 898.
[63] DAVIS, J., HAASZ, A.A., J. Nucl. Mater. **149** (1987) 349.
[64] HAASZ, A.A., YOULE, I.S., Comparison of chemical erosion of carbon due to sub-eV H^0 and T^0 atoms, to be published in J. Nucl. Mater.
[65] ROSNER, D.E., ALLENDORF, H.D., in Heterogeneous Kinetics at Elevated Temperatures (Proc. Int. Conf. Univ. Pennsylvania, 1969), Plenum Press, New York (1970) 231.
[66] HECHTL, E., BOHDANSKY, J., J. Nucl. Mater. **141–143** (1986) 139.
[67] HECHTL, E., BOHDANSKY, J., ROTH, J., J. Nucl. Mater. **103&104** (1981) 333.
[68] HECHTL, E., BOHDANSKY, J., J. Nucl. Mater. **154** (1988) 201.
[69] NAGATA, S., BERGSAKER, H., EMMOTH, B., ILYNSKY, L., Nucl. Instrum. Methods B **18** (1987) 515.
[70] HOLLAND, L., OJHA, S.M., Vacuum **26** (1976) 53.
[71] WAMPLER, W.R., BRICE, O.K., J. Vac. Sci. Technol. A **4** (1986) 1186.
[72] AUCIELLO, O., HAASZ, A.A., STANGEBY, P.C., Radiat. Eff. **89** (1985) 63.
[73] VIETZKE, E., FLASKAMP, K., PHILIPPS, V., J. Nucl. Mater. **111&112** (1982) 763.
[74] YAMADA, R., NAKAMURA, K., SONE, K., SAIDOH, M., J. Nucl. Mater. **95** (1980) 278.
[75] NIWASE, K., SUGIMOTO, M., TANABE, T., FUJITA, F.E., J. Nucl. Mater. **155–157** (1988) 303.
[76] YAMADA, R., J. Vac. Sci. Technol. A **5** (1987) 2222.
[77] HSU, W.L., J. Vac. Sci. Technol. A **6** (1988) 1803.
[78] YAMADA, R., NAKAMURA, K., SAIDOH, M., J. Nucl. Mater. **98** (1981) 167.
[79] YAMADA, R., SONE, K., J. Nucl. Mater. **120** (1984) 119.
[80] HAASZ, A.A., AUCIELLO, O., STANGEBY, P.C., YOULE, I.S., J. Nucl. Mater. **128&129** (1984) 593.
[81] HAASZ, A.A., DAVIS, J.W., AUCIELLO, O., et al., J. Nucl. Mater. **145–147** (1987) 412.
[82] DAVIS, J.W., HAASZ, A.A., Appl. Phys. Lett. **57** (1990) 1976.
[83] ROTH, J., OTTENBERGER, W. (Max-Planck-Institut für Plasmaphysik, Garching), unpublished results, 1990.
[84] VIETZKE, E. (Forschungszentrum Jülich), unpublished results, 1990.
[85] HAASZ, A.A., DAVIS, J.W. (Univ. of Toronto), unpublished results, 1990.
[86] HAASZ, A.A., STANGEBY, P.C., AUCIELLO, O., J. Nucl. Mater. **111&112** (1982) 757.
[87] ASHBY, C.I.H., RYE, R.R., J. Nucl. Mater. **92** (1980) 141.
[88] HAASZ, A.A., VIETZKE, E., DAVIS, J.W., PHILIPPS, V., J. Nucl. Mater. **176&177** (1990) 841.
[89] GUSEVA, M.I., IVANOV, S.M., MANSUROVA, A.N., At. Ehnerg. **55** 6 (1983) 366 (in Russian); Sov.J. At. Energy **55** (1983) 806.
[90] GUSEVA, M.I., MARTYNENKO, Yu.V., J. Nucl. Mater. **128/129** (1984) 798.
[91] ROTH, J., BOHDANSKY, J., ROBERTO, J.B., J. Nucl. Mater. **128&129** (1984) 534.
[92] PONTAU, A.E., WILSON, K.L., J. Vac. Sci. Technol. **20** (1982) 1322.
[93] HIROOKA, Y., CONN, R.W., CAUSEY, R., et al., J. Nucl. Mater. **176&177** (1990) 473.
[94] WINTER, J., ESSER, H.G., KÖNEN, L., et al., J. Nucl. Mater. **162–164** (1989) 713.
[95] DAVIS, J.W., HAASZ, A.A., J. Nucl. Mater. **175** (1990) 117.
[96] GAUTHIER, E., ECKSTEIN, W., LASZLO, J., ROTH, J., J. Nucl. Mater. **176&177** (1990) 438.
[97] SCHWÖRER, R., SCHERZER, B.M.U., ROTH, J., unpublished results, 1990.
[98] VIETZKE, E., PHILIPPS, V., FLASKAMP, K., WINTER, J., VEPREK, S., J. Nucl. Mater. **176&177** (1990) 481.
[99] BOHDANSKY, J., ROTH, J., J. Nucl. Mater. **122&123** (1984) 1417.
[100] PHILIPPS, V., Plasma Phys. Control. Fusion **31** (1989) 1685.
[101] BEGRAMBEKOV, L.B., BUZHINSKIJ, O.I., KOKUSHKIN, B.Ya., et al., J. Nucl. Mater. **170** (1989) 101.
[102] HAASZ, A.A., DAVIS, J.W., J. Nucl. Mater. **175** (1990) 84.
[103] ROTH, J., J. Nucl. Mater. **176&177** (1990) 132.

PARTICLE INDUCED ELECTRON EMISSION

E.W. THOMAS
School of Physics,
Georgia Institute of Technology,
Atlanta, Georgia,
United States of America

ABSTRACT. Particle induced electron emission from the wall of a plasma device alters the sheath potential and plasma transport in the scrape-off layer. Incident electrons eject electrons from a solid by a kinetic process. The ejected electrons cannot be distinguished from the reflected electrons and so the total yield is the sum of the two processes. Heavy particles eject electrons by the kinetic mechanism; when the projectile is ionized or excited, there may also be a contribution from potential ejection processes. Available data on electron ejection and electron reflection are reviewed, the most reliable data selected and, where appropriate, formulas are proposed that represent the functional dependence of the yield on the impact energy and impact angle.

1. INTRODUCTION

Particle induced electron emission from the walls of a plasma device has its major impact through altering the sheath potential adjacent to the walls; this in turn alters plasma transport in the scrape-off layer. Harbour and Harrison [1] showed that electron emission from the target of a collisionless divertor reduces both the plasma temperature and the sheath potential. The latter effect also lowers the energy of ions incident on the target and hence the sputtering yield and impurity production. Fuchs and Nicolai [2] demonstrated that the sheath potential drops to zero if the secondary electron emission exceeds unity. Brooks [3] showed how the sputtering yield is influenced by secondary electron ejection. Matthews et al. [4], included electron ejection in the theoretical modelling of the sheath potential and compared such models with experimental measurements on DITE. In most of these studies it is assumed that only secondary electron ejection by incident electrons is significant, but recently Mandrekas et al. [5] separated the influence of photo ejected and electron ejected secondary electrons. They predict that electron ejection causes a reduction of the electron and ion temperatures in the scrape-off layer, a rise in the centre and a reduced neutral density throughout the machine. The photoelectric ejection of electrons is a relatively minor contributor and most of the effect arises from the electron induced secondary electrons. Ejected electron flux is likely to be dominated by electron impact in the limiter regions and by photon impact on the wall. None of these studies appear to have specifically considered the electron flux induced by heavy particles.

Particle induced electron ejection from surfaces for situations relevant to plasma fusion machines has been reviewed previously by Thomas [6] and by Ertl and Behrisch [7]. The most important factor is the coefficient for total electron ejection from the surface, defined as the number of electrons ejected per incident particle. This coefficient is needed as a function of particle energy and as a function of incidence angle. For sophisticated predictions, one might also require the energy distribution of these electrons and their distribution in the ejection angles. While there is currently considerable research activity in studies of secondary electron emission, most of this research concentrates on recording the energy spectroscopy and the angular distributions to assist with elucidating energy band and crystallographic structures of single crystal solids. There are few active projects to study the total emission coefficients from polycrystalline materials, and there is very little information on 'technical' materials that would be found in a real fusion device, such as carbon and metals that have been heavily implanted with hydrogen, alloys or materials with overlayers of contaminants.

The experimental techniques are straightforward. Potential bias on an electrode collects all secondary electrons emitted into the 2π solid angle in front of the target. By use of spherical collectors and modulated bias potentials, it is possible to map out the complete energy distribution. The ratio of the collected electron current to the incident particle current is the coefficient for secondary electron emission; since the measurement is for a ratio of two signals, the result should be relatively free of systematic errors and measurement accuracies of a few per cent are anticipated. Poor

surface definition, contaminations and inherent differences between structures of different polycrystalline samples are major causes of discrepancies between independent measurements. We should note that much of the data published before the 1970s involved poor vacuum techniques and should be treated with caution; in general, the most recently published data are to be preferred.

2. BASIC PROCESSES

There are three types of processes whereby particles, incident on a surface, give rise to electrons ejected from that surface. The most general is the kinetic process whereby an incident species, electron or heavy particle, transfers part of its kinetic energy to electrons in the target, and some of these electrons have a direction and energy which permit them to escape into free space. The second process is potential ejection, a process where an electron from the solid transfers its kinetic energy to a lower energy state of the incoming projectile and the excess energy is transferred by an Auger process to a second target electron which escapes. Potential ejection processes are obviously restricted to incident heavy particles which are ionized or excited. The third process that we recognize as contributing to electron ejection is the reflection of incident electrons. Strictly speaking, this is not an ejection process at all, but it is backscattering. Since a backscattered electron cannot be inherently distinguished from a true secondary electron, there is a tradition of including the process together with other aspects of secondary electron emission.

Electron emission by the kinetic process is likely to be the dominant ejection mechanism for most circumstances. At relatively high projectile impact velocities it may be thought of [8] as split into three stages:

(1) Projectile interaction with the target excites target electrons to continuum states, creating a flux by primary excitation. Some secondary excitation may also be created by the more energetic excited electrons.
(2) A fraction of the excited electrons migrate to the surface.
(3) Electrons escape through the potential barrier at the surface and may be detected as 'secondary electrons'.

This three-step process is independent of whether the incident projectile is an ion or an electron. The secondary electrons will have a relatively low energy, peaking generally in the region of a few electronvolts. Schou [8] suggests that the secondary electron emission coefficient δ (the secondary emission coefficient is conventionally given the symbol δ for electron impact and γ for ion impact) may be written as the product of two components:

$$\delta\,(\text{or } \gamma) = D(E, 0, \cos\Theta)\Lambda \qquad (1)$$

Here, $D(E, x, \cos\Theta)\,dx$ is the energy deposited in electron excitation in the depth interval $x \rightarrow x + dx$ by a primary particle of energy E, incident on the surface at an angle Θ with respect to the surface normal; it represents the excitation of electrons. Λ is a material dependent parameter related to the probability that an excited electron will escape; it must include multiple scattering of the secondary electrons and the question of overcoming the potential barrier at the surface. The mean free path for slow electrons in a solid ranges from 100 A at 5 eV to 5 A at 100 eV [9]; thus, secondary electrons will escape from only a very small region close to the surface and this will generally be independent of whether the original projectile was an electron or an ion. Thus, Λ is often independent of the projectile and related only to the target. The factor D of Eq. (1) representing excitation should be directly proportional to the electronic stopping power and, because of the small escape depth of secondary electrons, the stopping power at the point of entry (i.e. $x = 0$) will suffice. The stopping power for electrons and that for protons are the same at high velocities, and the escape parameter is dependent only on the target. Therefore, the coefficients for proton and electron induced secondary electron emission should be the same as a function of velocity and should be directly proportional to the electronic stopping power. The general form of Eq. (1) may provide a valuable scaling relation. It should be borne in mind, however, that this picture is valid only at high velocities; at low velocities the excitation and escape parameters may not be decoupled as implied by Eq. (1) and the stopping powers are neither equal for different incident species nor are they reliably known. Regrettably, it is these low energies which are most important for fusion problems.

The potential ejection process involves electron transfer to vacant states of the incident projectile, followed by an Auger decay process; this process is described rather completely by Hagstrum [10]. Being related to vacant states of the projectile, it will occur only for ionized or excited incoming heavy species. The contribution to the coefficient will be independent

of energy, and the process will occur down to zero impact velocity. The ejected electrons will have specific energies related to the juxtaposition of energy levels in the projectile and the target. Apart from very low impact energies, the potential ejection process is relatively unimportant and total electron ejection is likely to be dominated by the kinetic ejection process. Exceptions are processes caused by the impact of highly ionized heavy ions where potential ejection is now recognized as making a very large contribution to electron ejection.

Finally, we must recognize that incident electrons may be reflected and thereby may contribute to ejection of electrons from a surface. The majority of reflected electrons have energies close to that of the incident projectile electron; by comparison, true secondary electrons have energies that peak in the region of a few electronvolts. The distributions do, however, overlap and there is no way of distinguishing reflected electrons from ejected electrons. Electron reflection occurs at vanishingly low incident energies and declines slowly with increasing projectile electron energy. At most energies of interest to fusion, electron reflection is a small contributor to the total ejected electron flux.

This paper is organized pragmatically, in terms of the observation of phenomena rather than the basic understanding or mechanism. First, we consider electron ejection by impact of electrons, including both true secondary electrons from the solid and reflection of the incident electrons themselves. Secondly we review electron ejection by ion impact through kinetic and potential ejection processes.

3. EJECTION OF ELECTRONS BY ELECTRON IMPACT

A typical energy spectrum of electrons ejected by the impact of electrons on a solid is shown in Fig. 1. At the energy of the incident electrons there is a peak which represents reflection of the incident electrons from the near surface region with little energy loss. Towards decreasing (ejected) electron energies there is a tail which represents backscattered electrons from some depth in the solid; these electrons have lost energy by multiple collisions. True secondary electrons are responsible for the major peak at an energy of a few electronvolts; the shape of this peak represents the excitation function of the valence band electrons modified by any losses due to multiple scattering as the electrons emerge. Towards higher energies there is a tail which represents the decreasing probability of transferring to the target electrons a large fraction of the projectile's energy. Structure may be observed in the reflected peak (due to excitation of plasmons and other discrete states) and also in the ejected electron distribution (due to Auger decays). These structures represent small contributions to the total electron flux and are of little importance in the behaviour of a fusion device; they will not be discussed here. Complete separation of incident and reflected electrons is impossible since both distributions have tails that overlap. It is the tradition to divide the two processes at an energy of 50 eV. Any electron with higher energy is considered to be reflected and any electron with lower energy is considered to be a true secondary electron from the solid. This is a satisfactory division for projectiles of incidence energy well in excess of 50 eV. For lower energies the division is quite arbitrary, and for incidence below 50 eV the division obviously cannot be used and only a sum of reflected and secondary electron coefficients can be specified.

The total yield ξ of emitted electrons per primary electron is expressed as

$$\xi = \delta + \eta \qquad (2)$$

where δ represents the true secondary electrons and η the reflected or backscattered electrons. Figure 2 gives the representative behaviour of these two coefficients; the reflected electron coefficient δ is fairly invariant with incident energy, and the true secondary electrons exhibit a peak in the coefficient around 800 eV; the

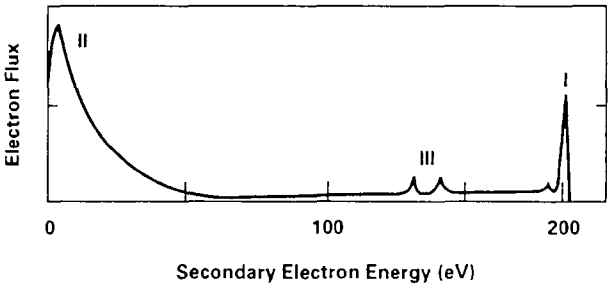

FIG. 1. Representative energy distribution of electrons emerging from a solid as a result of electron bombardment at a primary energy E (200 eV). Peak I is the main reflected peak with structure at slightly lower energies due to specific energy loss processes. Peak II is the main secondary electron peak. The minor peaks at III would be from Auger transitions. The secondary emission coefficient δ includes all electrons ejected at energies below 50 eV. The reflection coefficient η is taken as including all electrons ejected at energies above 50 eV.

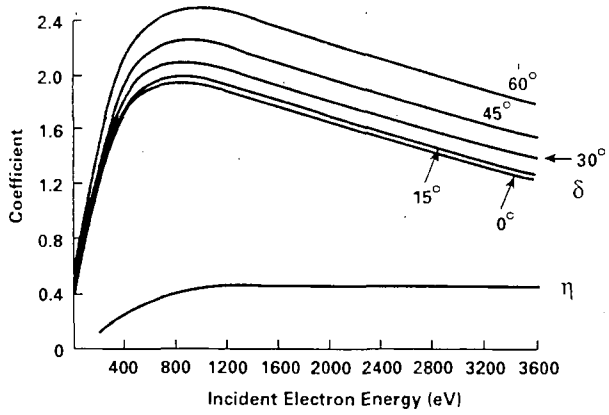

FIG. 2. Dependence of the secondary electron emission coefficient δ and the reflection coefficient η for electrons incident on W. δ is shown as a function of the angle of incidence (measured from the surface normal); η is shown for normal incidence only. Adapted from Bronshtein and Segal [11].

total yield is the sum of the two. The total yield is dominated by true secondary emission, except perhaps at very high energies. Backscattering is related to the interaction potentials between the electron and target nuclei so that it generally increases with target Z. Secondary electron ejection is related to the band structure of the solid and might be expected to exhibit a complex dependence on Z related to the shell structure of the target.

The practical separation of the two processes, reflection and secondary emission, is to first use a collector bias of +50 V to collect all ejected electrons and to measure ξ, and then to use a bias of -50 V to collect scattered electrons alone and to obtain η; the difference between ξ and η is the secondary emission coefficient δ (Eq. (1)).

Regrettably, there are no recent comprehensive reviews of this subject. One must refer to works of Kollath [12], Dekker [13], Hachenberg and Brauer [14] dating from the 1950s. These do, however, contain a wealth of information and a bibliography on data for elemental materials. A valuable statement of the theoretical situation with an extensive bibliography is provided by Schou [8].

The most useful data are those in sets for a variety of materials; from these, one may develop general algebraic representations that are valuable for modelling. As far as possible, we concentrate on such complete data sets. In addition, there are some very valuable studies of individual materials relevant to fusion device walls.

3.1. Electron reflection

Table I lists the sources of published data on electron reflection coefficient for elemental (generally metal) targets and certain carbides. The coverage is comprehensive, but much of the data is at impact energies above 4 keV, which is of little value for fusion device modelling. The largest data set is that of Hunger and Kuchler [15] for energies from 4 to 40 keV; it is said to be accurate to within ±2% and includes 27 elements from B to U. Other data sets listed here sometimes differ in magnitude by up to 10–20% but exhibit similar behaviour in terms of dependence on incidence energy and target atomic number Z. We would suggest that the various data sets referenced in Table I can be normalized together to provide a comprehensive picture, perhaps using the data by Hunger and Kuchler [15] as a standard. There are also data by Bronshtein [24, 25] at energies below 50 eV where the reliability of the separation of reflected electrons from true secondary electrons is questionable.

TABLE I. SOURCES OF PUBLISHED DATA ON ELECTRON REFLECTION COEFFICIENTS

Target	Z	Energy range (keV)	Comments	Refs
Be	4	0.1-100	(a)	[11, 16, 17]
C	6	0.2-40	(a)	[15, 18, 19, 20, 21]
Al	13	0.5-100	(a)	[16, 17, 18, 20, 21, 22]
Ti	22	4-40		[15]
Fe	26	0.2-40		[15, 19, 21]
Ni	28	4-40		[15, 21]
Cu	29	0.2-100	(a)	[15, 16, 17, 18, 19, 20]
Mo	42	0.2-4		[19, 21]
W	74	0.1-40	(a)	[11, 15, 21]
Au	79	4-100	(a)	[15, 16, 17, 22]
TaC		0.1-1.2	(b)	[23]
TiC		0.1-1.2	(b)	[23]
ZrC		0.1-1.2	(b)	[23]

(a) Data are available as a function of incidence angle [11, 16, 17].
(b) Data are available as a function of incidence angle [23].

Note that the majority of published data are for normal incidence. For an extensive coverage of most of the periodic table, see Hunger and Kuchler [15].

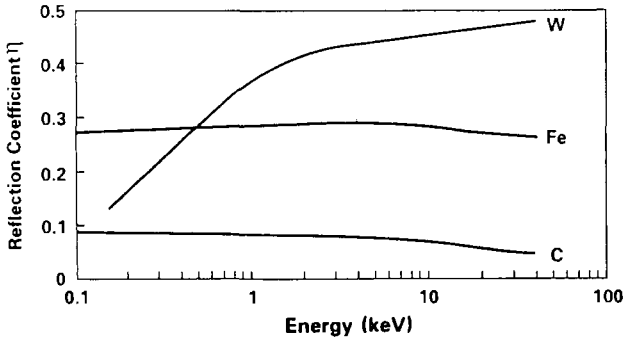

FIG. 3. Reflection coefficient as a function of incident electron energy. Composite of data from Hunger and Kruchler [15], Sternglass [19] and Bronshtein and Segal [11].

To provide a general picture, we show in Fig. 3 reflection coefficients from C, Fe and W targets over a wide energy range, obtained by normalizing together data from three sources [15, 19, 21]. For targets with $6 < Z < 29$, the coefficient increases monotonically from 0.09 (for C) to 0.28 (for Fe) and is almost invariant with energy from 0.1 to 10 keV. For higher Z targets, the behaviour is similar to that for W and the coefficient increases slowly with energy; above about 4 keV the coefficient has become almost invariant with energy and increases monotonically with Z. Data for the important case of Be are limited [11]; the value of η decreases from 0.08 at 0.3 keV to 0.06 at 3.6 keV, a little below that for C.

Data on relevant compounds are limited to the work of Thomas and Pattison [23] on TaC, TiC and ZrC. A representative data set is shown in Fig. 4; this also gives the true secondary emission coefficient δ.

The behaviour of the coefficient for reflection as a function of incidence angle Θ has been studied for a few of the elemental cases listed in Table I [11, 16, 17]. Figure 4 shows such data for the TiC case [23]; the coefficient increases only slowly with angle up to about 45°.

There are only limited data on the variation of backscattering with surface cleanliness. Studies on the carbides [23] show a small decrease (5%) after prolonged degassing of TiC. By contrast, the same work shows as much as 30% decrease in the secondary emission coefficient δ. It is argued that the primary influence of an adsorbed layer is on the (relatively slow) true secondary electrons and that the reflected primaries are not much influenced by surface contaminants.

It is, of course, preferrable to use original data for modelling purposes, but there are certain empirical fits to data that might be useful. Hunger and Kuchler [15] show that for energies above 4 keV, all data may be represented as a function of energy E (in keV) and target atomic number Z by the equation

$$\eta(E, Z) = E^{m(Z)} \exp(C(Z)) \tag{3}$$

where

$$m(Z) = 0.1382 - 0.9211\, Z^{0.5} \tag{4}$$

and

$$\exp(C(Z)) = 0.1904 - 0.2236 \ln Z + 0.1292 \ln^2 Z - 0.01491 \ln^3 Z \tag{5}$$

Also, Darlington and Cosslett [18], analysing the work of Orescher et al. [16] (for $E > 10$ keV), show that the variation of η with incidence angle Θ (measured from the surface normal) is reliably represented by

$$\eta(\Theta) = 0.891 \left(\frac{\eta(\Theta = 0)}{0.891} \right)^{\cos \Theta} \tag{6}$$

Since reflection is governed primarily by the atomic number of the target, the reflection coefficient for an alloy or compound may be estimated as the sum of the coefficients for the constitutent species, each weighted according to the proportion of the species present.

The various data referenced here are generally for 'flat' surfaces and normal incidence. When the surface

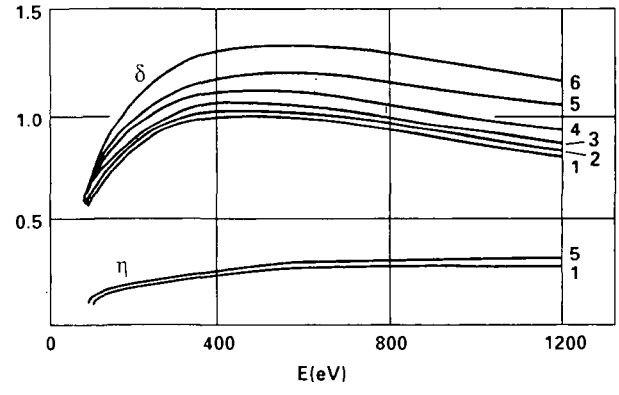

FIG. 4. Variation of the reflection coefficient η and the secondary emission coefficient δ for TiC with incident electron energy E for various angles of projectile incidence Θ. Line 1 for $\Theta = 0°$; 2 for 10°; 3 for 20°; 4 for 30°; 5 for 45°; 6 for 55°; all values are measured from the surface normal. From Thomas and Pattison [23].

TABLE II. MAXIMUM OF THE SECONDARY ELECTRON EMISSION YIELD, δ_{max}, AND PROJECTILE ENERGY AT WHICH IT OCCURS, E_{max}, FOR SELECTED ELEMENTAL METALS AND CERTAIN OTHER MATERIALS

Target	Z	δ_{max}	E_{max}	Refs
Be	4	0.5	200	[28]
C (graphite)	6	1.0	300	[28]
C (pocographite)	6	0.55	500	[32]
Al	13	1.0	300	[28]
Ti	22	0.9	280	[28]
Fe	26	1.3	400	[28]
Ni	28	1.35	550	[28]
Mo	42	1.25	375	[28]
W	74	1.4	650	[28]
TiC		1.0	460	[22]
TaC		0.84	270	[22]
ZrC		1.25	340	[22]
TiN		0.95	350	[34]
Stainless steel		1.22	400	[33]

Data are for normal incidence. For a more extensive listing, see Ref. [28].

is irregular or 'textured', the local angle of incidence may be very high, leading to a high reflection coefficient. Wintucky et al. [26] undertook a systematic study of reflection from pocographite textured by various sputtering procedures. The reflection coefficient varied from the 'normal' (graphite) value of about 0.06 to as much as 0.45; under some conditions, reflection and secondary emission were quite comparable. We must conclude that the reflection coefficient for a technical material exposed to a plasma may differ significantly from the results quoted in the publications referenced by us.

3.2. Secondary electron ejection by electrons

Secondary electrons result from excitation processes induced by the incoming projectile; somewhat arbitrarily, one defines secondary electrons as the emerging electrons with energies below 50 eV. The energy distribution represents an excitation function and peaks at low energies in the electronvolt region. Recall that such electrons emerge from only a small depth close to the surface, perhaps 5–100 A. The process is therefore very surface sensitive, and the data may be significantly influenced by surface contaminants and topography. Through Eq. (1) we have indicated how the process of excitation and the process of escape may be

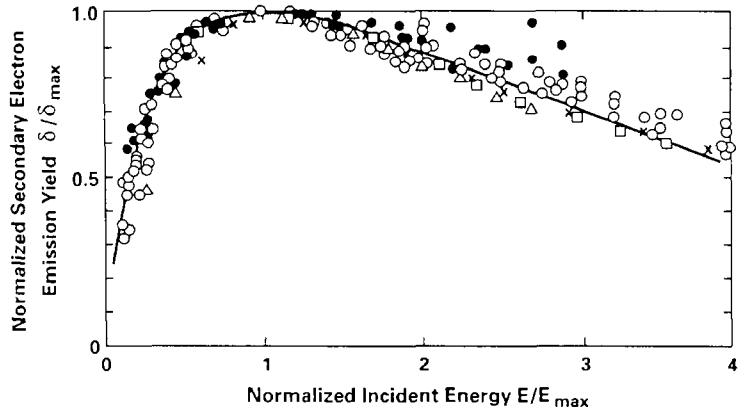

FIG. 5. Normalized secondary electron emission coefficient δ/δ_{max} as a function of normalized energy E/E_{max}. The circles are data for Li, Mg, Al, Si, Ti, Fe, Cu, Ni, Ga, Ge, Rb, Nb reproduced from the review of Kollath [12]. The other data points are for TaC (×), TiC (△) and ZrC (□) drawn from the work of Thomas and Pattison [22]. The line is the semi-emprirical curve of Eq. (7).

separated. This equation indicates that for high energies the coefficient for secondary electron emission should be directly related to electronic stopping, thus providing an opportunity to estimate coefficients by scaling.

We have already shown representative values of δ in Fig. 2 for W and in Fig. 4 for TiC. Experimentally, one observes that the dependence of the emission coefficient on the incident energy has a shape that is similar for most materials and can be characterized in terms of the maximum value of the coefficient, δ_{max}, and the energy at which this maximum occurs, E_{max}. In terms of these two parameters, Kollath [12], following the work of Sternglass [27], shows that the coefficients for almost all materials may be expressed in the form

$$\frac{\delta}{\delta_{max}} = (2.72)^2 \frac{E}{E_{max}} \exp\left[-2\left(\frac{E}{E_{max}}\right)^{1/2}\right] \qquad (7)$$

Values of δ_{max} and E_{max} are routinely published in standard handbooks. In Table II we reproduce representative values for some materials of interest in fusion devices; for a more complete listing and references to original publications, see Ref. [28]. The peak of the emission coefficient is generally rather broad, the precise identification of the maximum position is difficult, and there are some small variations between the published data sets. Figure 5 shows some experimental data for certain elemental materials and carbides scaled in this fashion, together with a plot of Eq. (7). Clearly, the data scale together well and all are in satisfactory agreement with the semi-empirical relation of Eq. (7).

The secondary electron emission yield increases with the angle of incidence Θ (measured from the surface normal) as follows (Ref. [29]):

$$\delta(\Theta) = \delta(\Theta = 0)/\cos^z \Theta \qquad (8)$$

where $\delta(\Theta = 0)$ is the value for normal incidence. The value of the power z is unity for all materials of high nuclear charge [29]. For the very light material Be, the value of z is closer to 1.3 [29], and for the lightest solid, condensed hydrogen, z is 1.5 [30].

There is no reliable method of estimating the values of δ_{max} or of E_{max}, and the application of the above scaling relations must generally be based on existing experimental data. Makarov and Petrov [31] did study how these factors varied with Z through the three long periods of the periodic table. The results of their analysis of a large number of published data sets are shown in Fig. 6, which illustrates δ measured at 2 keV and E_{max} as a function of target Z, arranged by atomic

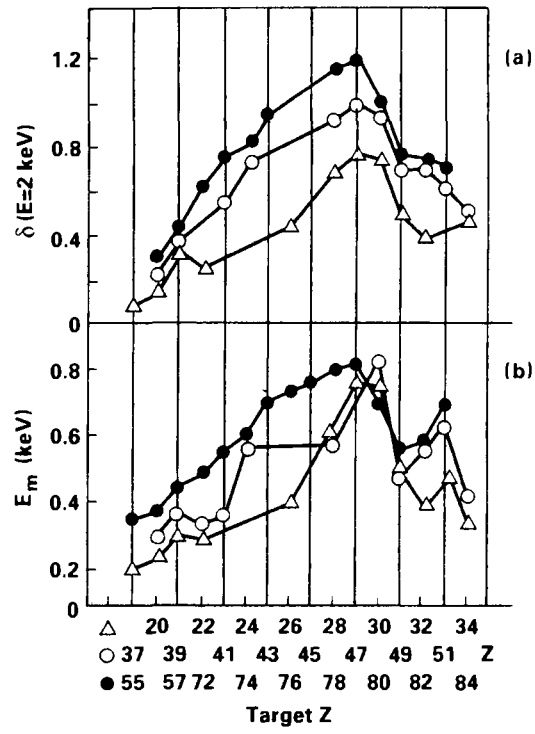

FIG. 6. Secondary electron emission coefficient δ (at 2 keV energy) and energy at which maximum δ occurs, E_m, as a function of target atomic number Z. From Makarov and Petrov [31].

shells. Clearly, for a partly filled shell the coefficient and energy of the maximum are small, they both increase as Z approaches a half filled shell and then generally decrease as the shell fills.

So far, the discussion has concentrated on elemental materials that are claimed, by the authors of the published data, to be clean and well defined. For technical materials that might find application in fusion devices we must be concerned with the precise nature of the surface and its physical condition. Texture and topography can play a major role in the secondary electron emission coefficient. Of rather direct interest are the studies by Woods et al. [32] of the secondary emission coefficient for a graphite limiter section removed from the JET device and for unexposed pocographite; the data are both for as-received materials and for materials cleaned by inert gas ion bombardment. Cleaned graphite limiter material had characteristics similar to those listed in Table I, with a maximum coefficient of about 0.9 at an energy of about 300 eV, while the unexposed pocographite had a maximum coefficient of 0.5 at about 300–500 eV. The energy location of the maximum changed with incidence angle for the limiter material (contrary to Eqs (7) and (8)), while it was almost invariant for the poco-

graphite. For both materials the coefficients decreased as a result of ion bombardment cleaning, by as much as 30% under some circumstances. Sputter texturing of pyrolitic graphite surfaces in various plasma environments leads to values ranging from 0.35 to 0.95 at 400 eV energy [26]. Carbon coated stainless steel surfaces exhibit variations of δ with the size of the grit utilized to polish the underlying steel surface [33]. Clearly, the precise topographical nature of the surface has a significant impact on the magnitude of δ. We should also not be surprised that δ varies with surface cleanliness; a study of TiN shows δ to decrease by 40% when an 'as-prepared' coating (on Nb) is sputter cleaned [34]. We must conclude that δ is very sensitive to surface conditions and topography; it is likely to change significantly during operation of a plasma device. Reliable values of δ can be obtained only by a study of the material in the condition found in the plasma device.

4. ION INDUCED ELECTRON EMISSION

Two distinct processes are recognized here. First, there are kinetic mechanisms, occurring for any incident projectile species, dependent on velocity, exhibiting a definite threshold, and generally similar to electron induced emission. The coefficient will be related to electronic stopping power and escape probability, generally in the terms of Eq. (1). Potential emission mechanisms take their energy from the vacancies in the projectile shell structure; therefore, potential emission occurs at any energy, generally decreases slowly with increasing energy (as the interaction time decreases) and is confined to projectiles which are excited or ionized. Kinetic emission will normally dominate, except at very low velocities or when the projectile is multiply ionized.

Somewhat arbitrarily, we divide our discussion into two parts. First we consider electron emission induced by impact of singly charged incident species. Here there is a considerable body of relevant data and the ejection process is primarily kinetic. Secondly we briefly review electron emission by multiply charged particles where the process is primarily governed by potential mechanisms. Here the data are sparse and not directly related to fusion applications; our discussion is designed to indicate the general behaviour of the phenomenon. We should note that the symbol normally used for electron emission induced by ion impact is γ rather than the symbol δ used for electron impact; this convention will be followed here.

4.1. Electron emission induced by singly charged species

Useful reviews of the subject have been provided by Krebs [35], by Baragiola et al. [36] by Hasselkamp [37] and much earlier by Medved and Strausser [38]. In Table III we list a selection of the data sources for this area. We find rather significant coverage of the light projectile impact, but very limited data on emission induced by impurity ions (C^+, N^+, O^+) or by the ions of metals that may find use as wall materials. For reference we also list in Table III data sources for rare gas impact cases; these are quite numerous and provide guidance on the general behaviour of the phenomenon. Table III concentrates on relatively recent data sources for which one expects proper attention to surface conditions and that the data are reliable. For earlier, but generally less reliable data, one might refer to the various reviews cited above and to our earlier paper [6]. One should also note the extensive work at energies above 100 keV by Hasselkamp et al. [52–55]. All data sources listed are for polycrystalline targets and generally involve normal incidence. We do not here review data for insulators and instead refer the reader to the review by Krebs [35].

A general indication of behaviour under proton bombardment is provided by Fig. 7, taken from Hasselkamp [37]. The coefficient is a maximum at around 100 keV H^+ energy and drops by a factor of five to keV energies. Some data are available for D^+ ions and are identical to those for H^+ on a velocity scale [42]. A very pleasing feature is that the data from different groups are generally in rather good agreement at overlapping energies. The extensive data sets of Zalm and Beckers [41] from 5 to 20 keV energies agree with those of Baragiola et al. [42] from 2 to 50 keV, to better than 10% in most cases; both publications give their data in convenient tabular form [41, 42]. Hippler et al. [39] have studied how the emission coefficient for H^+ impact varies with the atomic number of the target and find results very similar to those in Fig. 6 for the electron case; the coefficients are small for almost full or almost empty atomic shells and maximize for an approximately half filled shell.

Interestingly Schou [8] shows that the coefficients of Fig. 9 mirror rather well the electronic stopping power of these targets. This is expected from Eq. (1) because the factor D is proportional to stopping. The factor D of Eq. (1) does not vary much between targets. We suggests that, in the absence of a complete data set for δ, one could make a reasonable estimate by using the

TABLE III. DATA ON ION INDUCED ELECTRON EMISSION FOR SELECTED PROJECTILES AND TARGETS, FOR ENERGIES BELOW 100 keV ONLY

Target	Z	Projectile	Energy range (keV)	Refs
Be	4	H^+	100	[39]
C	6	H^+	30–100	[36, 39]
		H_2^+, H_3^+	40–100	[40]
		Ne^+, Ar^+, Kr^+, Xe^+	30–100	[36, 40]
		N^+, O^+	30–100	[36, 40]
		C^+	40–100	[40]
Al	13	H^+	2–100	[36, 39, 41, 42, 43, 44]
		H_2^+, H_3^+	2–100	[41, 42, 44]
		He^+	2–100	[41, 42, 43]
		Ne^+, Ar^+, Ke^+, Xe^+	2–100	[36, 41, 43]
		N^+, O^+	30	[36]
		Al^+	10–100	[43]
Ti	22	H^+	5–100	[39, 41]
		H_2^+, H_3^+	5–20	[41]
		He^+	5–20	[41]
		Ne^+, Ar^+, Kr^+, Xe^+	5–20	[41]
Fe	26	H^+	100	[39]
Ni	28	H^+	5–100	[39, 41]
		H_2^+, H_3^+	5–20	[41]
		He^+	5–20	[41]
		Ne^+, Ar^+, Kr^+, Xe^+	5–20	[41]
		Ni^+	8	[45]
Cu	29	H^+	2–100	[36, 39, 41, 42, 44, 46, 48]
		H_2^+, H_3^+	5–100	[41, 42, 43, 46]
		He^+	5–100	[41, 42, 46, 47, 48]
		Ne^+, Ar^+, Kr^+, Xe^+	2–100	[36, 41, 46, 47, 48]
		N^+, O^+	30	[36]
		Cu^+	10–100	[47, 48]
Mo	42	H^+	5–100	[36, 39, 41, 49]
		H_2^+, H_3^+	5–20	[41, 49]
		He^+	5–20	[41, 49]
		Ne^+, Ar^+, Kr^+, Xe^+	5–30	[36, 41]
		O^+, O_2^+, O^-, O_2^-, N^+, N_2^+	0.04–30	[36, 49, 50, 51]
		Mo^+	20–40	[67]
W	74	H^+	100	[39]
Au	79	H^+	5–100	[36, 39, 41]
		H_2^+, H_3^+	5–20	[41]
		He^+	5–20	[41]
		Ne^+, Ar^+, Kr^+, Xe^+	2–30	[36, 41]
		N^+, O^+	30	[36]

Notes: Certain of the work for H^+, H_2^+ and H_3^+ includes also data for D^+, D_2^+ and D_3^+.
Reference [48] contains excellent data as a function of incidence angle (Cu targets).

electron stopping power data of Andersen and Ziegler [58] to provide the energy dependence and normalizing to an available data point.

At high impact energies (>40 keV) it has been shown that the dependence of the emission coefficient on the angle of incidence Θ is given [48] by

$$\gamma(\Theta) = \gamma(\Theta = 0)/\cos^z \Theta \quad (9)$$

where the power z is unity for light ions (H^+, He^+) and between 1 and 1.2 for heavier species (Ne^+, Ar^+, Kr^+). These equations are valid to angles of about 80°, after which the coefficient falls rapidly. Note the similarity to Eq. (8), which is for electron impact.

Let us turn now to the question of electron emission induced by heavy ion impact. There are significant data for rare gas ion impact (see references in Table III) performed for the fundamental study of the emission phenomenon. The data from various sources are generally in good agreement, and useful tabulations over wide energy ranges can be found in the work of Zalm and Bekkers [41] and of Baragiola et al. [42]. Such data are, of course, of little direct value to the understanding of fusion situations and we will not discuss them in detail here. There is only sparse coverage of impurity ion (C^+, N^+, O^+ and metals) impact on metals and carbon. Useful indication of how the coefficient varies with projectile Z for various targets and with target Z for various projectiles is shown in Figs 8 and 9 from the work of Baragiola et al. [36]. Similar graphs for various projectiles on stainless steel [59, 60],

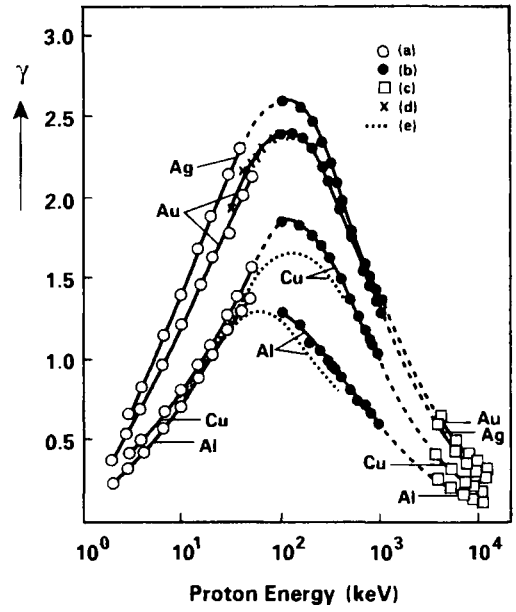

FIG. 7. Electron yield as a function of ion energy for H^+ impact on Al, Cu, Ag and Au; a compendium from Hasselkamp [37]. Data from (a) Baragiola et al. [42]; (b) Hasselkamp et al. [52]; (c) Koyama et al. [56]; (d) Veje [57]; (e) Svensson and Holmen [43] and Holmen et al. [47]. The dashed lines are interpolations to guide the eye.

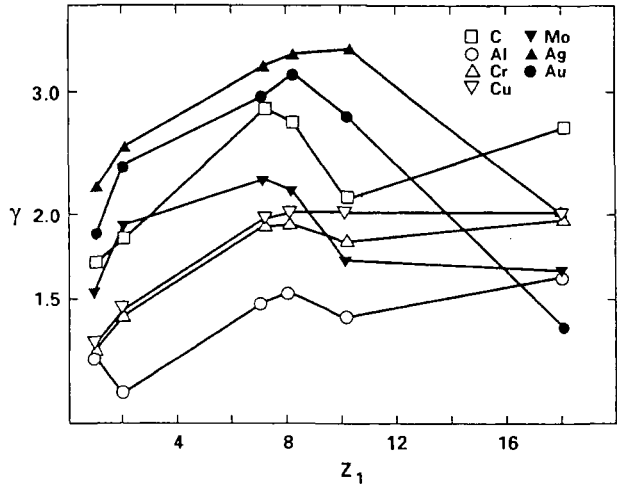

FIG. 8. Dependence of electron yield on projectile atomic number Z_1 for targets of C, Al, Cr, Cu, Mo, Ag and Au at a projectile energy of 30 keV. From Baragiola et al. [36].

on Al and on Ni [45] are also available, but the surfaces are likely to be covered with adsorbed gases. Regrettably, these are all at far too high an energy to be valuable in fusion situations and the coverage does not give a clear picture of the variation with shell structure. Figure 10 shows the variation with velocity for emission from Al bombarded by a wide variety of incident projectiles; this is perhaps the only recently published example of a broad ranging data set. The coefficients all increase generally linearly with the incident particle velocity. In Fig. 11 we have collected the data on emission induced by metallic and C^+ ions on the same material as a function of energy. The general picture is that the data are fragmentary and confined to energies of incidence far in excess of those anticipated in fusion devices. There is no systematic method for extrapolation to lower energies nor for interpolation to other combinations.

It may be valuable to note that there should be a distinct threshold for kinetic ejection processes. An estimate due to Baragiola et al. [42], based on the

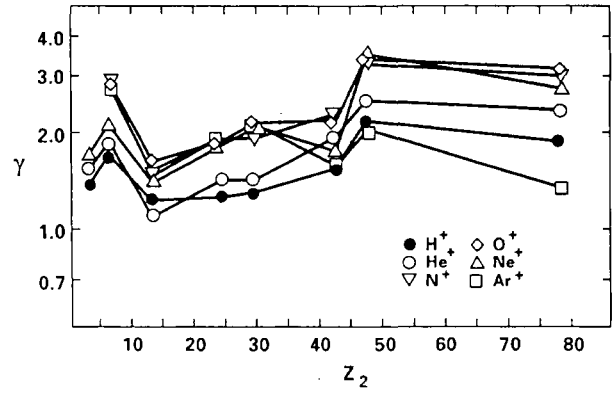

FIG. 9. Dependence of electron yield on target atomic number Z_2 for projectiles H^+, He^+, N^+, O^+, Ne^+, Ar^+ at a projectile energy of 30 keV. From Baragiola et al. [36].

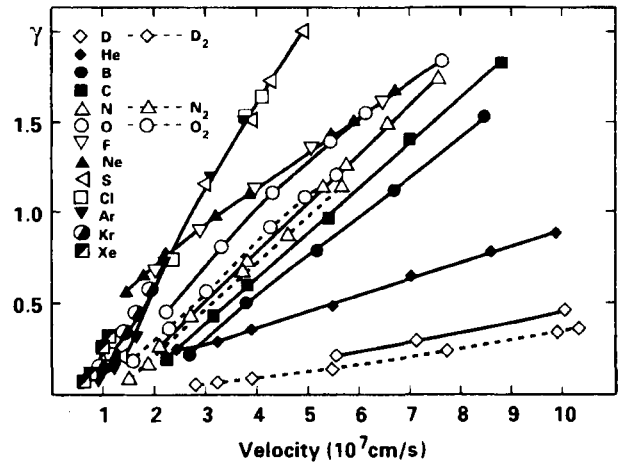

FIG. 10. Electron yield for various projectile ions, D^+, He^+, B^+, C^+, N^+, O^+, F^+, Ne^+, S^+, Cl^+, Ar^+, Kr^+, Xe^+, incident on Al, as a function of velocity (energies 1.2–50 keV). From Alonso et al. [61].

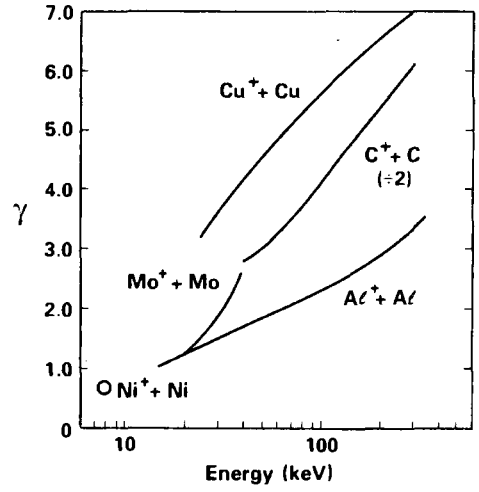

FIG. 11. Electron yield for C^+ and metallic ions on like materials; C^+ + C (shown divided by two) from Hasselkamp and Scharmann [40]; Al^+ + Al from Svensson and Holmen [43], Ni^+ + Ni from Fehn [45], Cu^+ + Cu from Holmen et al. [47] and Mo^+ + Mo from Telkovskij [67].

assumption that target electrons are free, sets the threshold at the incident velocity v_{th} where the maximum energy transfer (projectile to target electron) is equal to the work function ϕ:

$$v_{th} = \tfrac{1}{2} v_F \left[(1 + 2\phi/mv_F^2)^{1/2} - 1\right] \qquad (10)$$

where v_F is the velocity of electrons at the Fermi surface. For many materials this gives a threshold velocity of about 2×10^7 cm/s (or an energy of 200 eV for H^+). Extrapolation of the available data suggests that this may be approximately correct for light projectiles. For heavy particle impact, one might argue that fast target atom recoils may give rise to secondary emission and that this may result in a lower primary particle velocity threshold [61]. For heavy projectiles (e.g. Kr^+ and Xe^+ on Al) the recoil calculation gives a better estimate of an apparent threshold; for lighter species the estimates are the same. These prescriptions should be treated with caution since the model is oversimplified. Moreover, at the apparent threshold for kinetic emission there may remain a small but significant electron emission due to potential effects when the projectile is an ion. The potential emission yield for singly charged ions may be estimated by a theory of Kishinevskii [62]; representative estimates for a Cu surface are: for H^+ 0.05, for He^+ 0.32 and for Cu^+ zero (see Holmen et al. [47]); these values will slightly decrease with projectile energy and persist to zero impact energy.

4.2. Multiply charged ions

Electron emission by potential ejection processes will occur by impact of all ionized or excited atoms with a potential energy well above the surface work functions for multiply charged ions; at low energies, it will dominate. Figure 12, which shows the emission due to multiply charged nitrogen ions on W [63], is an illustrative example. The emission increases rapidly with charge state to a value of 7 to 9 electrons per incident ion for N^{6+}. Also plotted in Fig. 12 is an estimate of the kinetic emission contribution, which is believed to be largely independent of projectile charge. For the lowest ionization state, N^{4+}, the kinetic component produces an increasing coefficient with projectile energy and dominates at the highest velocities. The same kinetic emission will occur also for the other charge states and is responsible for the slight upturn to higher velocities seen on all the curves. The rapid decrease of coefficient with velocity for the higher

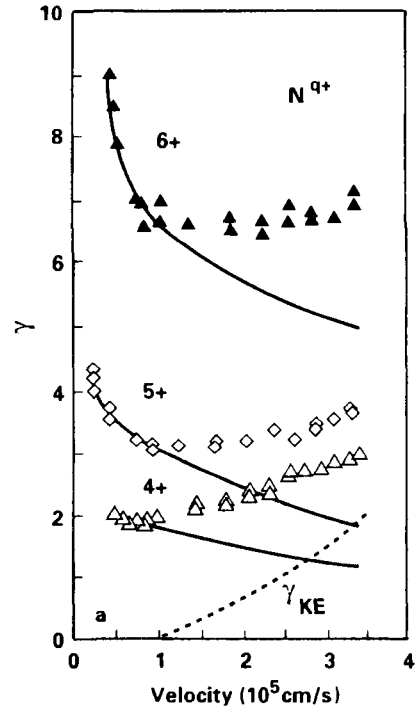

FIG. 12. Electron yield as a function of projectile velocity for N^{4+}, N^{5+} and N^{6+} incident on W. The dashed line gives an estimate of the kinetic emission coefficient and the solid lines provide an estimate of the potential emission alone. From Fehringer et al. [63].

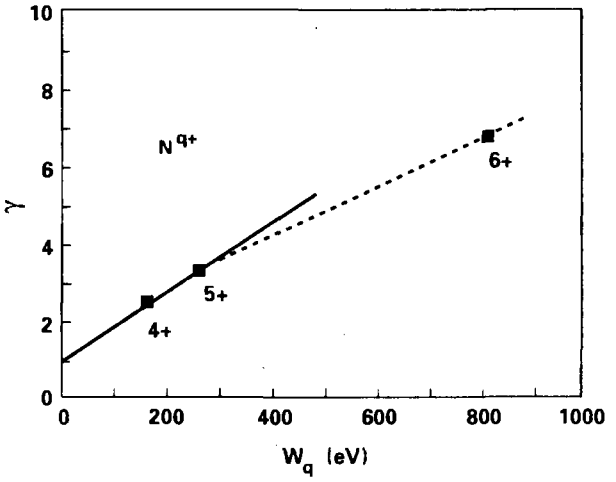

FIG. 13. Ion induced electron emission coefficient against potential energy of the projectile W_q. Data for N^{4+}, N^{5+}, and N^{6+} on W for a fixed velocity of 2.5 × 10^5 m/s [63].

charge states has been rationalized [64] in terms of the decreasing interaction time between projectiles and surface. A plot of the potential emission coefficient against the total potential energy of the ion at a fixed impact velocity is independent of the atomic number of the projectile [64]. Thus, one can use a plot such as Fig. 13 (which is for N on W [63]) to estimate coefficients for any other species (e.g. highly charged C and O ions) on the same target material. Deviations from linearity occur as the velocity is increased [64].

Data coverage in this field is rather sparse. There is reliable information on W targets, bombarded with ions of N, Ne, Ar and Kr, by Fehringer et al. [63] and Delaunay et al. [64]. Work by Oda et al. [65] on Ta and Au bombarded by Ar ions involves poorly defined surfaces, and the data by Decoste and Ripin [66] are for carbon ions on 'gassy' copper surfaces that have in no way been cleaned or defined; these data should be treated with great caution.

Active research in this area continues to add data sets, but coverage at the present time is minimal. There is as yet no clear indication whether fusion plasmas are significantly influenced by secondary emission resulting from the impact of multiply charged ions on wall surfaces.

5. CONCLUSION

Significant bodies of data exist on the subjects of electron induced secondary electron emission and electron reflection. From these data, one may often interpolate, sometimes with the assistance of semi-empirical formulas, to produce data for cases that have not been experimentally studied. Secondary emission is greatly influenced by surface conditions; reflection is less influenced. Data on ion induced electron emission at low energies are broadly available for the case of hydrogen and helium impact, with supporting data for rare gas ions. For the lighter projectiles, one may estimate the emission coefficients by relating to experimental data via stopping power information. For the heavier species likely to be found as impurities in plasma devices, the coverage is very sparse. For multiply charged species, the emission coefficients can be very high because of the dominance of the potential emission process. Information is again sparse. For none of these phenomena is there a reliable theoretical technique that can readily predict the emission coefficients.

ACKNOWLEDGEMENTS

The preparation of this paper was supported in part by the Chemical Sciences Division of the United States Department of Energy. Contributions by J. Schou and H. Winter are gratefully acknowledged.

REFERENCES

[1] HARBOUR, P.J., HARRISON, M.F.A., J. Nucl. Mater. **76&77** (1978) 513.
[2] FUCHS, G., NICOLAI, A., Nucl. Fusion **20** (1980) 1247.
[3] BROOKS, J.N., J. Nucl. Mater. **93&94** (1980) 437.
[4] MATTHEWS, G.F., McCRACKEN, G.M., SEWELL, P., WOODS, M., HOPKINS, B.J., J. Nucl. Mater. **145-147** (1987) 225.
[5] MANDREKAS, J., SINGER, C.E., RUZIC, D.N., J. Vac. Sci. Technol., A **5** (1987) 2315.
[6] THOMAS, E.W., Nucl. Fusion, Special Issue, Data Compendium for Plasma-Surface Interactions (1984) 94.
[7] ERTL, K., BEHRISCH, R., Physics of Plasma-Wall Interactions in Controlled Fusion (POST, D.E., BEHRISCH, R., Eds), NATO ASI Series, Plenum Press, New York (1986) 515.
[8] SCHOU, J., Scanning Microsc. **2** (1988) 607.
[9] ZANGWILL, A., Physics at Surfaces, Cambridge University Press, Cambridge (1988) 21.
[10] HAGSTRUM, H., Phys. Rev. **96** (1954) 336.
[11] BRONSHTEIN, I.M., SEGAL, R.B., Sov. Phys. — Solid State **1** (1959) 1142.
[12] KOLLATH, R., Handbuch der Physik (FLUGGE, S., Ed.), Vol. 21, Springer-Verlag, Berlin (1956) 232.
[13] DEKKER, A.J., Solid State Physics (SEITZ, F., TURNBULL, D., Eds), Vol. 6, Academic Press, New York (1958) 251.

[14] HACHENBERG, O., BRAUER, W., Adv. Electron. Electron Phys. **11** (1959) 413.
[15] HUNGER, H.J., KUCHLER, L., Phys. Status Solidi A **56** (1979) K45.
[16] ORESCHER, H., REIMER, L., SEIDEL, H., Z. Angew. Phys. **29** (1970) 331.
[17] DARLINGTON, E.H., J. Phys., D **8** (1975) 85.
[18] DARLINGTON, E.H., COSSLETT, V.E., J. Phys., D **5** (1972) 156.
[19] STERNGLASS, E.J., Phys. Rev. **95** (1954) 345.
[20] DARLINGTON, E.H., COSSLETT, V.E., J. Phys., D **5** (1972) 156.
[21] PALLUEL, P., C.R. Hebd. Séances Acad. Sci. **224** (1947) 1492.
[22] THOMAS, S., PATTISON, E.B., J. Phys., D **3** (1970) 349.
[23] THOMAS, J., PATTISON, E.B., J. Phys., D **2** (1969) 1539.
[24] BRONSHTEIN, I.M., ROSHCHIN, V.V., Sov. Phys. — Tech. Phys. **3** (1958) 2271.
[25] BRONSHTEIN, I.M., Bull. Acad. Sci. USSR **22** (1958) 442.
[26] WINTUCKY, E.G., CURREN, A.N., SOVEY, J.S., Thin Solid Films **84** (1981) 161.
[27] STERNGLASS, E., Westinghouse Res. Sci. (1954) paper 1772.
[28] Handbook of Chemistry and Physics, 67th edn, CRC Press, Boca Raton, FL (1986) E-366.
[29] BRONSHTEIN, I.M., DENISSOV, S.S., Sov. Phys. — Solid State **9** (1967) 731.
[30] SORENSEN, H., SCHOU, J., J. Nucl. Mater. **76&77** (1978) 634.
[31] MAKAROV, V.V., PETROV, N.N., Sov. Phys. — Solid State **23** (1981) 1028.
[32] WOODS, M.E., HOPKINS, B.J., McCRACKEN, G.M., Surf. Sci. **162** (1985) 928.
[33] RUZIC, D., MOORE, R., MANOS, D., COHEN, S., J. Vac. Sci. Technol. **20** (1982) 1313.
[34] PADAMSEE, H., JOSHI, A., J. Appl. Phys. **50** (1979) 1112.
[35] KREBS, K.H., Vacuum **33** (1983) 555.
[36] BARAGIOLA, R.A., ALONSO, E.V., FERRON, J., OLIVA-FLORIO, A., Surf. Sci. **90** (1979) 240.
[37] HASSELKAMP, D., Comments At. Mol. Phys. **21** (1988) 241.
[38] MEDVED, D.B., STRAUSSER, Y.E., Adv. Electron. Electron Phys. **21** (1965) 101.
[39] HIPPLER, S., HASSELKAMP, D., SCHARMANN, A., Nucl. Instrum. Methods Phys. Res., Sect. B **34** (1988) 518.
[40] HASSELKAMP, D., SCHARMANN, A., Phys. Status Solidi A **79** (1983) K197.
[41] ZALM, P.C., BECKERS, L.J., Philips J. Res. **39** (1984) 61.
[42] BARAGIOLA, R.A., ALONSO, E.V., OLIVA-FLORIO, A., Phys. Rev., B: Solid State **19** (1979) 121.
[43] SVENSSON, B., HOLMEN, G., J. Appl. Phys. **52** (1981) 6928.
[44] SVENSSON, B., HOLMEN, G., Phys. Rev., B: Solid State **25** (1982) 3056.
[45] FEHN, U., Int. J. Mass Spectrom. Ion Phys. **21** (1976) 1.
[46] ZALM, P.C., BECKERS, L.J., Surf. Sci. **152&153** (1985) 135.
[47] HOLMEN, G., SVENSSON, B., BUREN, A., Nucl. Instrum. Methods **185** (1981) 523.
[48] SVENSSON, B., HOLMEN, G., BUREN, A., Phys. Rev., B: Solid State **24** (1981) 3749.
[49] FERRON, J., ALONSO, E.V., BARAGIOLA, R.A., OLIVA-FLORIO, A., J. Phys., D **14** (1981) 1707.
[50] MAHADEVAN, P., MAGNUSON, G.D., LAYTON, J.K., CARLSON, C.E., Phys. Rev. **140** (1965) A1407.
[51] PERDRIX, M., PALETTO, S., GOUTTE, R., GUILLAUD, C., Br. J. Appl. Phys. **2** (1969) 441.
[52] HASSELKAMP, D., LANG, K.G., SCHARMANN, A., STILLER, N., Nucl. Instrum. Methods **180** (1981) 349.
[53] HASSELKAMP, D., SCHARMANN, A., Phys. Lett., A **96** (1983) 259.
[54] HASSELKAMP, D., HIPPLER, S., SCHARMANN, A., Nucl. Instrum. Methods Phys. Res., Sect. B **2** (1984) 475.
[55] HASSELKAMP, D., HIPPLER, S., SCHARMANN, A., Nucl. Instrum. Methods Phys. Res., Sect. B **18** (1987) 561.
[56] KOYAMA, A., SHIKATA, T., SAKAIRI, H., Jpn. J. Appl. Phys. **20** (1981) 65.
[57] VEJE, E., Nucl. Instrum. Methods **194** (1982) 433.
[58] ANDERSEN, H.H., ZIEGLER, J.F., Hydrogen Stopping Powers and Ranges in all Elements, Pergamon Press, New York (1977).
[59] STAUDENMAIER, G., HOFER, W.O., LIEBL, H., Int. J. Mass. Spectrom. Ion Phys. **11** (1976) 103.
[60] ROGASCHEWSKI, S., DUSTERHOFF, H., Phys. Status Solidi B **75** (1976) K173.
[61] ALONSO, E.V., BARAGIOLA, R.A., FERRON, J., JAKAS, M.M., OLIVA-FLORIO, A., Phys. Rev., B **22** (1980) 80.
[62] KISHINEVSKII, L.M., Radiat. Eff. **19** (1973) 23.
[63] FEHRINGER, M., DELAUNAY, M., GELLER, R., VARGA, P., WINTER, H., Nucl. Instrum. Methods Phys. Res., Sect. B **23** (1987) 245.
[64] DELAUNAY, M., FEHRINGER, M., GELLER, R., HITZ, D., VARGA, P., WINTER, H., Phys. Rev., B **35** (1987) 4232.
[65] ODA, K., ICHIMIYA, A., YAMADA, Y., YOSUE, T., Nucl. Instrum. Methods Phys. Res., Sect. B **33** (1988) 345.
[66] DECOSTE, R., RIPIN, R.H., J. Appl. Phys. **50** (1979) 1503.
[67] TELKOVSKIJ, V.G., Sov. Phys. Dokl. **1** (1956) 334.

ARCING IN MAGNETIC FUSION DEVICES

H. WOLFF
Central Institute of Electron Physics,
Berlin, Germany

ABSTRACT. Referring to the similarities with arc discharges in the cathode material vapour in vacuum environment the characteristics of arcing phenomena in magnetic fusion devices are reviewed. Attention is paid to the cathode phenomena of vacuum arcs, such as the motion of arc spots, the arc tracks produced, the erosion rate and the charged and neutral components of the emitted cathode material. It is pointed out that arc tracks found in fusion devices do not always come from 'unipolar arcs', but they may also originate from different types of bipolar arcs. In present-day devices, arcing can be suppressed successfully by proper surface conditioning and smooth plasma operation. So far, however, there are no real means to theoretically predict the occurrence of arcing in fusion devices.

1. INTRODUCTION

Arcing phenomena were already observed about 30 years ago in early fusion research installations [1, 2]. Post-operational inspection of the plasma facing surfaces of the discharge vessels and other inner structures revealed numerous erosion traces similar to the erosion pattern created by metal vapour discharges in vacuum. Already in the period from the late 1950s to the late 1970s, the problem of arcing attracted considerable attention because of the abundance of arcing tracks found in fusion devices and the amount of impurities that could be injected into discharges. Very similar arcing erosion patterns were found in most tokamaks and stellarators [3–17]. It was suspected that impurity injection caused by arcing might be predominant [10, 18–20] and might create a principal barrier that would prevent reaching fusion temperatures. There was also some apprehension that arcing could severely damage inner components of the discharge vessel, making frequent replacement necessary.

In the early 1980s, better cleaning procedures of the inner discharge vessel surfaces as well as much more stable operating conditions of tokamaks and longer pulses were achieved. Arcing became a rare event, and post-operational inspection of the vessel components showed that arcing traces were much less abundant; such traces were found mainly on the limiter or divertor structures and the antenna shields. At present, the vessel walls or the wall shields show almost no traces of arcing events. This is true in particular for the present generation of large tokamaks with long pulses. This may be the reason why systematic investigations of arcing in fusion devices were discontinued in the second half of this decade. Only a very limited number of new publications on this subject has appeared since the last review by Mioduszewski [21].

It is important to know the contribution of arcing to the plasma impurity content. Thus, the following points have to be considered: (1) It has to be found out whether arcing is an unavoidabe phenomenon in fusion devices or whether it is restricted to some critical phases of the discharge and can be circumvented. (2) The characteristics of the released impurities and the extent to which they penetrate into the plasma must be known.

Unfortunately, the first question cannot be answered satisfactorily so far. However, regarding the second point, the results of vacuum arc research form a useful basis. In particular, adequate data are available on the electrical characteristics of vacuum arcs, their duration and stability, on electrode erosion and on the materials emitted. However, there is considerable lack of data concerning materials for modern fusion devices, such as carbon, boron and beryllium, and their compounds, in particular at elevated temperatures.

The erosion traces found on the inner structural elements of magnetic fusion devices as well as the characteristic properties of the emitted material resemble those found in arcing discharges in cathode material vapour in a vacuum environment. The low density of the fusion plasma and the well known fact that the cathode spot mechanism does not appreciably depend on the conditions of the arc column and the anode may serve as a justification for treating the discharge mechanism responsible for the observed erosion traces in fusion devices as the cathode region of vacuum arcs. Although no direct analysis of material emitted by arcing in fusion devices is available, it seems to be reasonable to use the relevant results from vacuum arc investigations. Therefore, we consider vacuum arc discharges in more detail.

2. THE VACUUM ARC

Arc discharges burning in the vapour of cathode material in a low pressure or vacuum environment, the so-called vacuum arcs, have been investigated for a long time. Numerous industrial applications, primarily for vacuum circuit breakers, maintained the interest in the physics of this phenomenon, resulting in an extensive literature [22]. The understanding of the electrode phenomena and the properties of the inter-electrode plasma of vacuum arc discharges have been considered in numerous reviews [23–41]. Depending on the current range, the electrode distance, materials, magnetic fields, etc., vacuum arc discharges exhibit a wide variety of features. There is general agreement that the cathode mechanism is the most vital process of the vacuum arc discharge, since it generates the discharge medium, at least during the initiation of the discharge. With increasing discharge current, arc duration and electrode spacing, strongly evaporating spots on the anode may develop. In most cases, the inter-electrode plasma remains diffuse, with a low electron temperature. Only at high currents (more than tens of kiloamperes) can the arc column attain a more complex structure, composed of anode and cathode jets. This complex behaviour is shown in Fig. 1.

2.1. The cathode region of the vacuum arc

Numerous experimental and theoretical efforts have been made to explore the nature of the cathode mechanism. The extensive reviews cited above reflect the present knowledge. Nevertheless, important details of the cathode spot mechanism are still not well understood and there are considerable discrepancies between the different experimental results. Several crucial questions are controversial, for example the problems of the emission mechanism and the current density in the cathode spot, the time-scales of spot development and the surface erosion [26].

The reason for this is that almost no direct measurements can be carried out in a cathode spot. Even the extension of a cathode spot is not well defined. In numerous cases it is not possible to decide whether the spot is a single unity or whether there is a substructure [43].

The difficulties in resolving the basic mechanisms lie in the small volume of the spot (about 10^{-15} m^3), as well as the high power densities and steep gradients of most parameters. Additionally, the luminous spot exhibits rapid erratic movements, suggesting a highly transient nature of the cathode mechanism. The current transition at the cathode is concentrated in this spot area; it can assume various forms, depending on the surface conditions and the cathode temperature [40]. There is a general difference in the appearance of the erosion traces and in the spot mechanism between atomically clean metal surfaces and surfaces covered with layers of adsorbed gas, oxides, hyrdocarbons, etc. [32, 44]. It seems to be established that in the latter case the vacuum arc produces its discharge medium by removing these layers without significant erosion of the

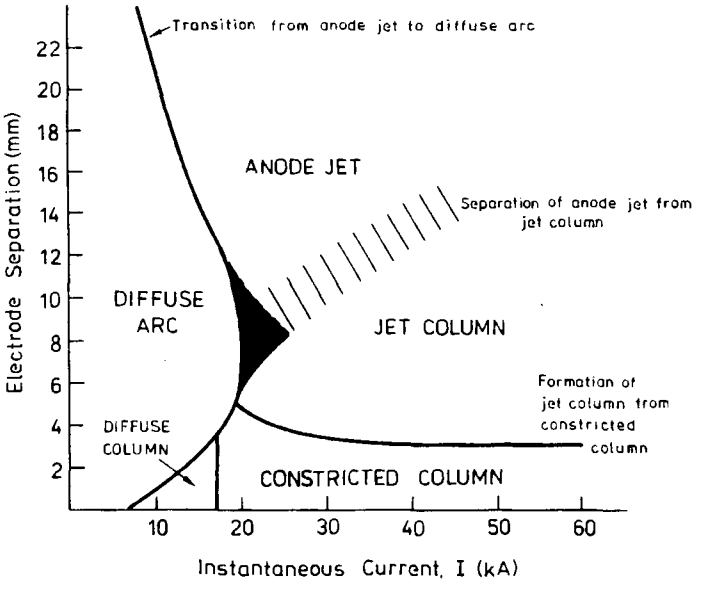

FIG. 1. Vacuum arc discharge modes as a function of current and gap length [42].

TABLE I. CATHODE SPOT PARAMETERS

Parameter		Value
Cathode drop voltage	U_c	10–30 V
Current density	j	10^{11}–10^{12} A·m^{-2}
Plasma density	n	10^{25} m^{-3}
Plasma pressure	p	10^{7} Pa
Current per spot	I	≤ 100 A
Cathode spot radius	r	10 μm
Debye length	λ_D	10^{-3} μm
Ionization length	ℓ_i	10^{-2} μm
Electric field strength	E	10^{10} V·m^{-1}
Average spot lifetime	τ	10 μs

underlying bulk metal cathode. Correspondingly, the erosion traces of 'type one' arcs [29, 32, 45] are very faint and blurred and are often hard to detect. By repeated arcing, these layers are removed, and a transition to 'type two' arcs takes place; this is associated with the production of well pronounced erosion traces consisting of numerous single craters which partially overlap.

Investigations using atomically clean surfaces shed more light on the cathode mechanism [46]. It was shown that a single spot never carries a current of more than about 100 A at a time. At higher currents, splitting of spots is observed. The physical extent of a spot can be established by the erosion craters left behind on the cathode surface (there is, however, some controversy about whether this is correct [47, 48]).

There is no general agreement on the processes by which the craters are formed — either by resistance heating [27] or by ion impact heating and by the action of the ion pressure [36, 49]. Heating and excavation of the crater may be accelerated by successive melting and expulsion of thin (<0.1 μm thick) molten layers [23, 50].

On the other hand, a certain minimum current, I_c, is required for an arc spot [37, 51]. This minimum current is closely connected with the melting points and the vapour pressure characteristics of the cathode material [31]. Surface cleanliness, dielectric inclusions and also circuit parameters affect the arc stability at the lower current limits.

Table I summarizes typical parameters of the cathode spot plasma of a diffuse (low current) vacuum arc on atomically clean metal surfaces; this can be taken as an 'order-of-magnitude' guidance [26, 34]. We summarize here only the main aspects of the cathode mechanism, giving preference to those aspects which are of relevance to material erosion and emission.

2.1.1. Crater size

Microscopic studies of the erosion traces produced by vacuum arcs on clean metal surfaces reveal a crater structure. Chains of craters, some partially overlapping, with a crater size of several micrometres, are observed. Also, larger crater structures, of 10–50 μm diameter, can be found; these are interpreted as a superposition of several craters. The size of a single crater depends on the cathode material, its overall temperature and the arc current. The crater radius increases with arc current [27, 46, 52] and with the bulk temperature of the cathode [40, 50]. At room temperature, this dependence can be approximated by the empirical formula

$$r_c = r_{mat} \exp I/I_{mat} \quad (1)$$

with r_{mat} and I_{mat} being characteristic for different materials, as shown in Table II.

The influence of the bulk cathode temperature T(K) on the crater size was found to obey approximately the formula (see Ref. [27]):

$$r(T)/r(300) = \lambda(300)/\lambda(T)\ [\arccos(300/T_m) \arccos(T/T_m)] \quad (2)$$

where $\lambda(300)$ is the heat conductivity at room temperature and $\lambda(T)$ is that at temperature T. T_m is the melting temperature. Additionally, an empirical temperature dependent factor was introduced [40], allowing for the non-stationary nature of crater formation.

Experimental investigations [40] revealed that even at very high cathode temperatures craters are produced; for example, on tungsten craters were observed at 2500 K. The transition to spotless pure thermionic arcs seems to be possible (if at all) only at still higher temperatures and is probably not relevant for arcing

TABLE II. CHARACTERISTIC CRATER RADII

Cathode material	I (A)	r (μm)
Copper	83	1.7
Molybdenum	33	1.2
Stainless steel	46	3.8

processes in fusion devices. Thus the development of erosion tracks consisting of crater structures can be considered to be a reliable sign of arcing combined with significant erosion. Further data on the temperature dependence of the crater size for different materials are required. At higher bulk cathode temperatures or higher surface loads, enhanced erosion associated with ejection of large droplets should be expected according to Ref. [53].

2.1.2. *Motion of arc spots*

As pointed out above, the cathode mechanism of a discharge in vacuum is a highly non-stationary process. The arc spot has a short lifetime τ. The quasi-stationary arc discharge consists of a sequence of spot formations and extinctions. The spots move at random in elementary steps of the crater radius r, with time constants τ of the order of 10 ns. Surface irregularities, contamination or particles may produce jumps over longer distances. A qualitative picture of the crater development with time was given by Jüttner [46]. First, there is an explosion of a field emitting micropoint, then the formation of a plasma cloud and the development of a crater and, finally, the extinction of the crater with the formation of new microprotrusions which may serve as the starting point of a new spot sequence.

On the basis of this model the spot movement can be treated as a random walk with steps r in time intervals τ [50, 51, 54], resulting in a diffusion-like movement with $\langle r^2 \rangle / \tau \simeq 10^{-3}$ m^2/s, which, averaged over several milliseconds, corresponds to an apparent velocity of about 1 m/s.

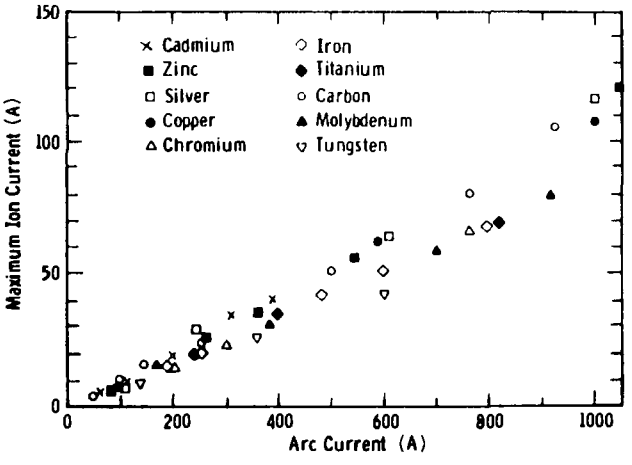

FIG. 2. Maximum ion current from the cathode spot on Cd, Zn, Ag, Cr, Fe, Ti, C, Mo and W electrodes versus the DC arc current (no anode spot present) [83].

Transverse magnetic fields align the spot path and produce velocities of between 10 and 100 m/s. The motion is mostly directed oppositely to $\vec{J} \times \vec{B}$. This so-called retrograde motion has been studied for a long time, and many attempts to explain this phenomenon were made without reaching a general consensus [55–69]. Unfortunately, most of the experimental work was carried out at low magnetic field strengths ($\ll 1$ T). It is not clear whether these results can be applied directly to high magnetic fields (> 1 T), which usually exist in fusion devices, since there are indications that the direction of spot motion (according to or opposite to $\vec{J} \times \vec{B}$) may change with increasing field strength [69]. Arcing tracks found in tokamaks clearly show that the motion of spots is in the retrograde direction [10, 18, 21, 70].

2.1.3. *Arc ignition*

Explosive emission processes are widely assumed to initiate arc discharges [71–74]. Under the influence of locally enhanced electric fields, local plasma density increases and the development of hot spots by focused energetic beams, protruding surface microstructures may receive a sudden energy input which cannot be balanced by thermal conduction to the bulk of the cathode or by evaporation cooling. The surface structure (or emission site) becomes overheated, which leads to explosive ejection of matter, partially in an ionized state [36, 39, 73, 74]. Once a high enough electromotive force is available with a low inner circuit resistance, more power is fed into the plasma cloud until the spot mechanism is fully developed [36]. Discharge initiation depends sensitively on the surface conditions, in particular on the surface microstructure, on contamination layers and dielectric inclusions. Continuous discharges or other cleaning processes may substantially change the surface conditions, leading to an increase of the breakdown voltage by up to an order of magnitude [44, 75, 76]. This explosive emission process is assumed to be responsible not only for gap breakdown and arc development but also for the elementary steps of spot movement (Section 2.1.2).

2.1.4. *Erosion rate, emission of cathode material*

Closely connected with the crater formation is the problem of cathode material ejection. The erosion rate is defined as the ratio of the net mass loss of cathode material to the charge transfer by the discharge. A certain part of the material removed from the craters remains on the cathode surface, forming crater rims

TABLE III. PARAMETERS OF THE MEAN ION FLUX EMITTED FROM THE CATHODE [87][a]

Material	Refs	Arc voltage (V)	Mean ion flux			Ion charge fraction f_i (%)					Ion erosion rate (μg/C)
			Charge (e)	Potential (V)	Energy (eV)	$Z_1 = 1$	$Z_2 = 2$	$Z_3 = 3$	$Z_4 = 4$	$Z_5 = 5$	
Pb	[84]	10.3		(20)		*	*				215
Cd	[84]	10.8	1.003	(16)	(15.8)	99.7	0.3				117-130
Zn	[84]	12.0		(20)		*	*				68-76
Ca	[81]	13	1.47	28	41	53	47	T			
Mg	[84]	14.2	1.50	(33)	(49)	50	50				17-25
C	[81]	16	1.04	27	28	96	4				13-17
Ag	[84]	16.5		(42)		*	*	*			78-108
	[81]	16.5	1.36	44.5	61	65	34	1			
Ni	[84]	18	1.37	(43)	(59)	65	33	2			44
	[81]	18.5	1.54	34.5	53	48	48	3	T		
Fe	[89]	19	1.47	72	106	54	46	0.5			40-50
Cr	[89]	19.5	2.02	38	76	16	68	14	2		22-27
Al	[84]	20	1.42	(46)	(66)	60	38	2			19-25
	[81]	20	1.58	39	62	49	44	7			
Ti	[89]	20	1.79	42	76	27	67	6			45-52
Cu	[81]	20.5	1.85	48	89	30	54	15	0.4		35-40
	[89]	22	1.70	48	82	38	55	7	0.5		
Zr	[81]	21.5	2.17	46	100	14	60	21	5	T	48
Tn	[81]	24	2.72	65	178	13	35	28	13	10	65-72
Mo	[81]	25.5	1.99	78	156	16	69	13	1.5		47-52
	[89]	28	2.86	53	152	3	33	42	19	3	

* — ions detected; T — traces (<0.1%).

[a] Ion erosion rate from Ref. [27]. The mean ion potential V_i, the mean ion energy E_i and the mean ion flux charge Z are connected by the following relations: $Z = \sum_i Z_i f_i/100$ and $V_i = E_i/Z$.

and flow patterns, while the other part is emitted in the form of ions, neutral vapour, molten droplets and solid particles. Particles or droplets may also carry a charge, but their integral charge transfer is much smaller than the charge transported by ions and even more by electrons. The components emitted by cathode spots, their angular and velocity distribution and the overall mass loss of the cathode were studied in detail by several groups [27, 37, 77-86]. It was found [80] that the ion mass loss per Coulomb charge transfer can be regarded as a constant value for a certain metal, while the neutral mass loss per Coulomb (vapour and particles) is a function of different parameters, such as arc current, arc duration, melting temperature of the cathode material and arc spot movement. From these dependences it was concluded that ions and neutral components are produced at different places and by different mechanisms: the ions by electron collision ionization in the dense plasma of the spot, and the neutrals and particles by evaporation and ejection of the molten crater surfaces.

2.1.4.1. The ion component

For each material the dependence of the ion current component on geometrical factors such as electrode spacing and anode area indicates that the ions are produced in the cathode spot region by ionization of cathode material vapour and are subsequently ejected in almost isotropic free flight from this region. Comparison of the erosion rate with the ion current and the particle flux shows that the evaporated atoms are nearly fully ionized within the cathode spot plasma. These

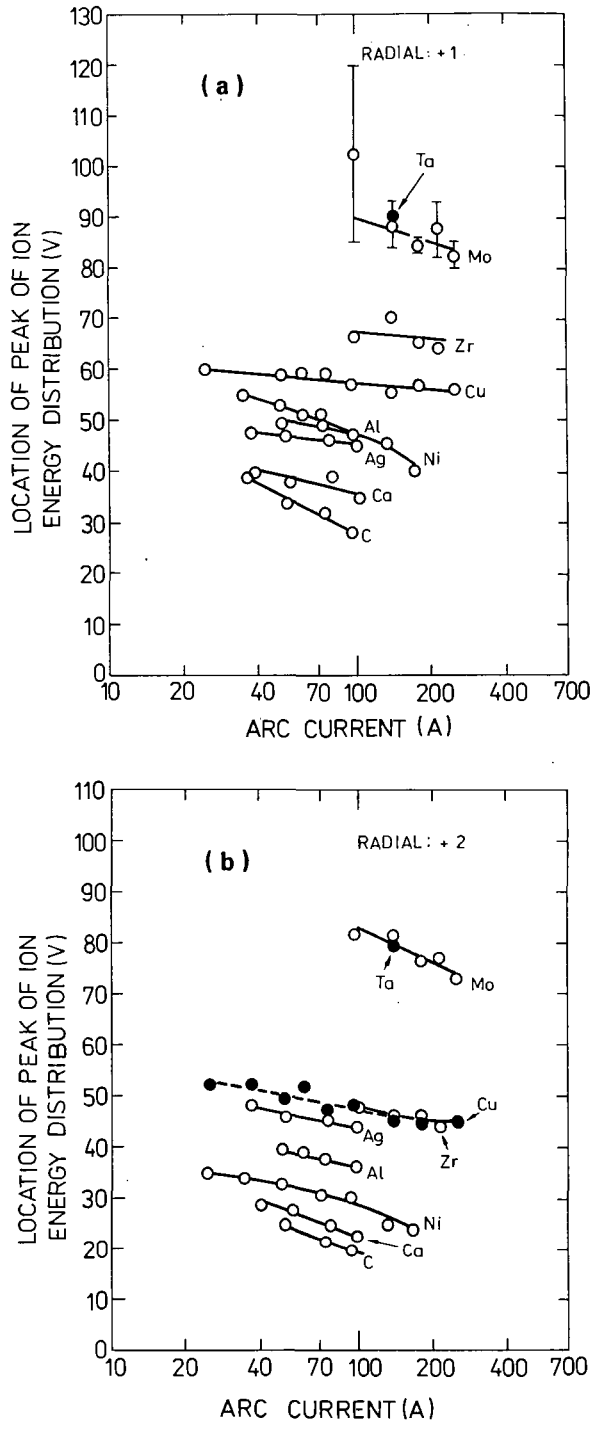

FIG. 3. Location of the peaks of the energy distribution of (a) single charged and (b) double charged ions emitted radially from the cathode spot as a function of arc current [81].

directly measurable ion currents represent about 7–10% of the arc current for metal cathodes with a wide span of boiling temperatures (Fig. 2).

The average charge state of the emitted ions is generally higher for high-Z elements and for materials with a high boiling point, while the arc current has little influence. For example, cathode spots on tungsten emit ions with charge states up to 5, those of chromium and iron are up to 3, and carbon and lithium emit only singly charged ions. Charge state distributions have been measured by several groups [77, 78, 81, 84, 87–89]. There are some discrepancies between the results obtained by these groups. These differences may be due to different experimental conditions and various discharge currents, and to whether the electrical or the particle currents are given. Generally, most of the measured quantities in this field suffer from relatively large margins of error; this is due to the numerous but difficult to define factors influencing the experimental results, such as the material chosen, the geometry of the arrangement and the method of arc ignition. Table III summarizes the charge state fractions and the mean charge of the emitted ions measured by different groups as well as the energy and the calculated accelerating potential [87].

Measurements [81, 84, 88–90] revealed that the ions are emitted with a directed energy considerably exceeding the arc voltage (Fig. 3). The origin of the ion energy was studied with the assumption of different mechanisms, such as a potential hump [81] in the immediate vicinity of the cathode surface, ambipolar drag by the electron component or hydrodynamic acceleration [87, 91]. There are suggestions that the ion acceleration is due to the non-stationariness of the arc cathode mechanism. However, a convincing explanation is still missing.

2.1.4.2. The neutral component

The overall erosion rate, which can be determined, for example, by weight loss evaluation, is at least as high as the ion erosion rate, but it may attain considerably higher values because of the emission of particles (clusters of atoms) and vapour [27, 84, 92]. The integral erosion rate is a function of charge transfer by the arc, and the minimum value that can be determined is close to the ion erosion rate. Figure 4 illustrates the dependence of the total erosion rate on the transported charge for several metals. It has been established that the emission rate of the neutral component depends on the local surface temperature (in relation to the melting temperature) at the arc spot and in its vicinity, so that the energy input per unit area of the cathode and the heat conduction loss into the bulk of the cathode are determining factors. The relative contributions of vapour and particles to the total neutral mass loss cannot be specified exactly. Several authors [79, 80, 86, 92] have

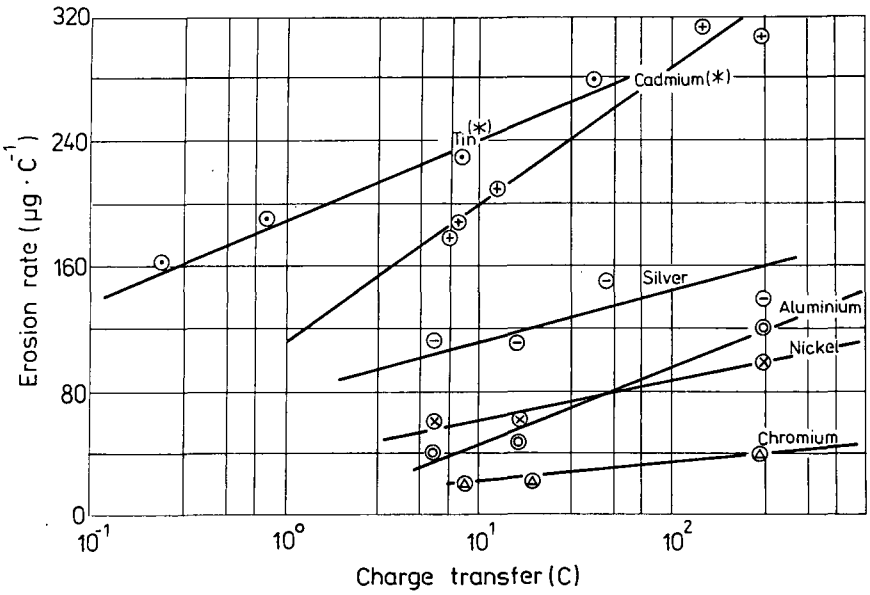

*FIG. 4. Dependence of the total erosion rate on the number of Coulombs transported by a vacuum arc [27, 79, 83, 84, 97]. * for tin: multiply ordinate values by four. * for cadmium: multiply ordinate values by two. (The minimum erosion rate due to ion emission is to be identified with the left hand starting point of the lines.)*

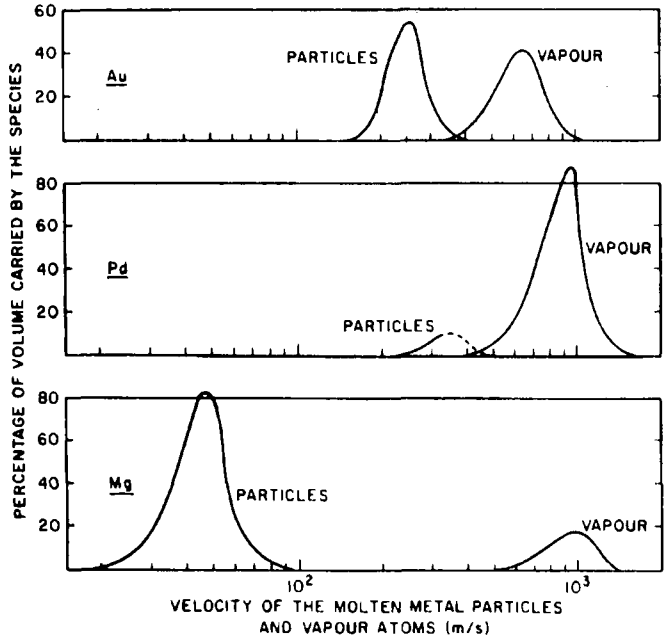

FIG. 5. Velocity distribution of molten metal particles and metal vapour atoms emitted by vacuum arcs [86].

investigated the neutral components and found that the particle emission is dominant. It is estimated that the maximum contribution of mass lost in form of vapour does not exceed about 10% of the total erosion. The size and the velocity distribution of the molten particles emitted have been investigated by several authors [80, 85, 86] for some metals, mainly at low currents. In this range, the largest part of the volume carried by particles is due to particle sizes from 2 to 6 μm; at higher cathode temperatures, the contribution of larger particles increases according to the growing size of the crater [40].

The particles are emitted with velocities in the range of several ten m/s to several hundred m/s, depending

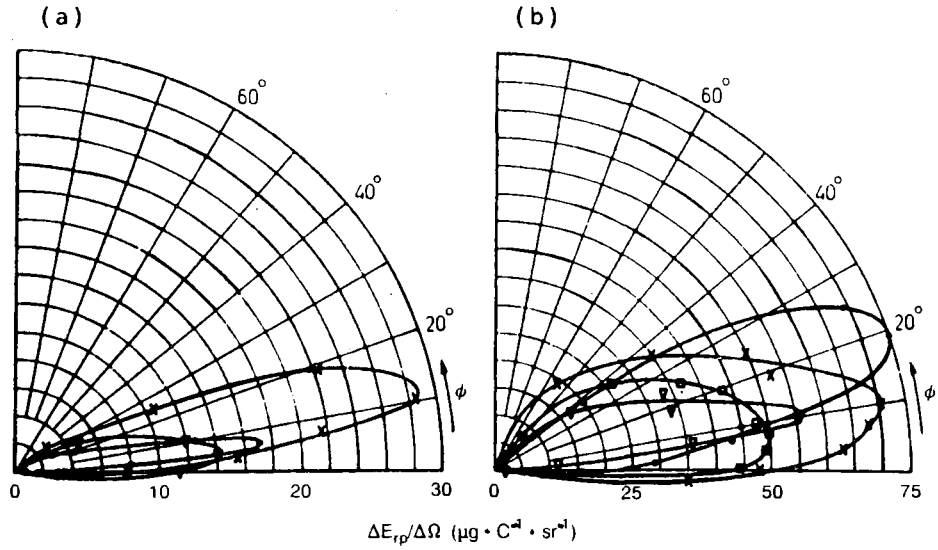

FIG. 6. Angular distribution of the particle mass in a vacuum arc. Particle erosion rate per solid angle as viewed from the spot centre [27, 80].
(a) Cu for various amounts of charge transfer: q = 2.4 C; D = 20.8 C; x = 200 C.
(b) Cd for various amounts of charge transfer: q = 0.2 C; D = 0.47 C; p = 45 C; x = 135 C.

on the cathode material, while the velocity of the vapour is in approximate accordance with the temperature of the crater pool (Fig. 5). There are indications that a considerable part of the vapour is generated by particles evaporating during their flight [93, 94].

The expected mechanisms causing droplet emission are the ion pressure acting on the molten crater pool and elastic readjustment after extinction of the spot. A model [95] based on the mechanical properties of the liquid cathode material gives the ejection velocity in dependence on the droplet radius.

Particles may carry a negative charge, which can be estimated by considering the ambipolar flow to an isolated particle. This charge may be compensated by thermal electron emission [93, 96].

The angular distribution of emitted particles of different size has been investigated thoroughly [80, 84, 97]. Typical angular distributions of particles for Cu and Cd as a function of the charge transfer are given in Fig. 6. Larger particles are emitted at small angles, while smaller particles predominate at larger angles to the cathode plane. With increased charge transfer, large particles are shifted to larger angles.

3. ARCING IN FUSION DEVICES

The phenomenology of arcing traces in fusion devices is described in numerous papers and reviews [10, 18, 21, 70]. Judging from arc erosion traces found in experimental fusion devices and the results of direct observations of arcing in tokamaks, mainly low current diffuse arcs seem to develop in previous and present-day devices. There may be some exceptional cases of arc discharges in tokamaks constricted to high currents, since some spots of local heavy erosion (melting, evaporation and generation of droplets and splashes which cannot be associated with runaway electron effects) indicate the possible existence of fixed constricted arc modes.

Most arc erosion traces found in magnetic fusion devices show that the cathodic arc spots appear to move in the retrograde direction (i.e. opposite to the electromotive force $\vec{J} \times \vec{B}$) [55–59]. The microscopic structure of the erosion traces shows varieties very similar to those of vacuum arcs in strong magnetic fields. With the surface normal to the direction of the magnetic field, and depending on the material and the cleanliness of the surface, straight chains of well pronounced overlapping craters are observed, with diameters of 1–10 μm by order of magnitude, or chains of numerous craters with diameters smaller than 1 μm, or fern-like structures with a barely resolvable microstructure. When the surface normal is oriented along the direction of the magnetic field, the traces bear witness of the random motion of the cathode spot, exhibiting a crater structure similar to that discussed above (see Ref. [10]).

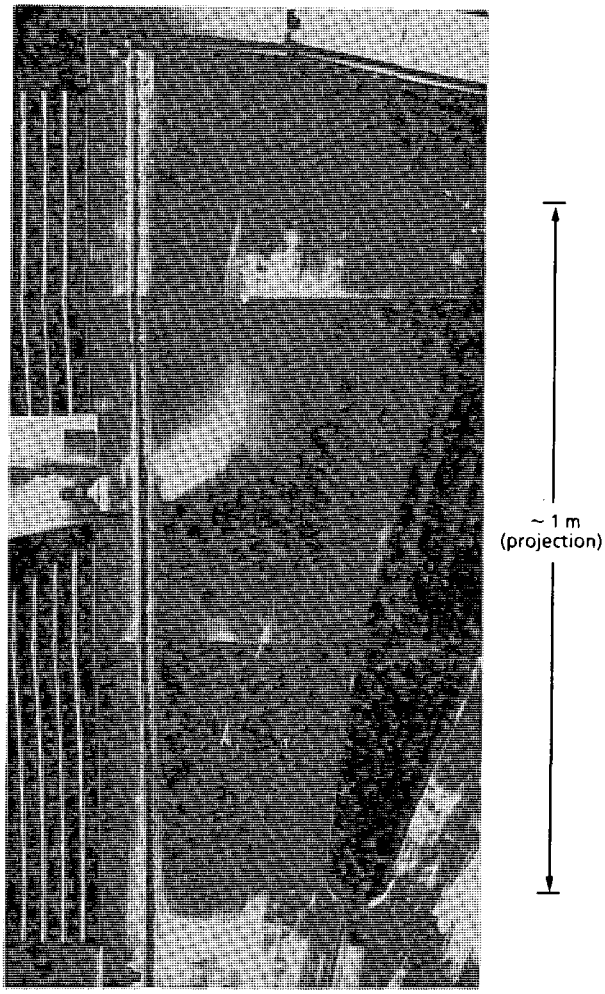

FIG. 7. Arc tracks on the vessel surface of T-15 after DC glow discharge cleaning in He and H with short pressure excursions of up to 5–8 Pa.

The appearance of the different features of the erosion traces depends strongly on the material as well as on the surface topography and on the surface conditions, i.e. on whether the surface is covered by adsorbed gases or condensed layers.

It seems to be appropriate to identify different kinds of arcing in fusion devices, which are sometimes difficult to distinguish, judging only by the erosion tracks left behind. The different kinds of arc discharges are discussed below.

(1) Multipactor discharges on antenna structures during high power RF heating: This type of arc discharge has been observed on ICRF antennas, preferentially when materials with high secondary electron emission yields are used, for example aluminium. At the present power levels, these multipactor discharges can be avoided by a proper choice of the antenna and shield design and of the materials used. Regardless of the problems which could arise from multipactor discharges at more elevated power levels, they are excluded from consideration in this paper.

(2) Glow discharge cleaning (for example DC with about 5–10 A and 300–500 V) of the (cathode) surfaces of the discharge vessel may produce arc-like tracks. This kind of erosion tracks has been identified recently in T-15 (Fig. 7, unpublished) and may be attributed to a glow discharge cleaning regime at elevated gas pressure (>1 Pa). The strongly abnormal glow discharge coupled with a high local current density on a contaminated surface may produce instabilities which lead to arc ignition. This type of (bipolar) arcing should be avoided during the conditioning process, since considerable amounts of eroded material may be redistributed in an undesirable manner throughout the whole vessel surface.

(3) There is some apprehension that because of the high energy stored in the plasma and the longer disruption decay time in future large tokamaks, high induced currents may arise in passive torus circuits, leading to bipolar constricted arc discharges across gaps, followed by severe local damage of vessel structure components [98]. There should be special design provisions to suppress this electromagnetically induced arcing during rapid changes in the plasma taking place, for example, at startup, shutdown, plasma position control and disruption. Bipolar discharges, in particular with arc constriction, should be clearly distinguishable from the low current diffuse unipolar arcs by the appearance of erosion traces and their movement properties, and possibly by the existence of associated anode spot traces. In present-day devices, this type of bipolar arc-like discharges has not been identified unambigously.

(4) Arc discharges supported by a plasma induced electromotive force. Previous reviews were devoted mostly to this more common type of arcing, often called unipolar arcing, the cathode mechanism of which is equivalent to the low current diffuse mode of the vacuum arc discharge. The necessary energy supply and the anodic backflow required by charge conservation are realized by the plasma body and the surrounding wall structure, respectively, without anodic spots.

Usually, arc discharges are fed by external electromotive forces applied by means of two electrodes: the anode and the cathode. In contrast, unintended arcing phenomena in fusion devices operate without such external electromotive forces. Clearly identifiable is only the cathodic arc spot — a bright, fast moving spot

of microscopic extension. Unfortunately, direct optical observations of arcing processes in fusion devices are very rare because the place and the instant of arc ignition cannot be predicted. In some experimental work, ignition of arcs at specially prepared biased probes in tokamaks has been observed [99–101]; this has given some information on the arcing probability in dependence of tokamak operation and surface conditions of the probe.

The problems connected with an understanding of this kind of discharge in fusion devices are due to the difficulties in tracing the sources of the electromotive force driving the discharges and in locating the discharge channels. The only source for the potential differences necessary to support arc discharges is the fusion plasma itself. Sufficiently high potential differences may be induced by steep gradients of density and temperature as well as by transient electromagnetic fields within the plasma body or they may be produced by space charge fields between plasma and wall. A systematic theoretical approach to evaluate these fields is extremely complicated because two very different kinds of plasma must be considered together: the diluted high temperature plasma in strong magnetic fields and the high density arc spot plasma. The generation of an electromotive force, the anodic backflow and the energy supply for the dissipative effects in the cathode and the arc column have to be included [20, 102–104].

Even more difficult are the ignition conditions. There are some attempts of a theoretical treatment of arcs induced by non-stationary plasmas [102–104]. At present, only simple models are available which make plausible the existence of arcing phenomena in magnetic fusion devices. Numerous experimental investigations of arcing in fusion devices have been summarized in different reviews [10, 18, 21, 70, 105] and it seems unnecessary to describe them here. Also, various simulation experiments have been performed to study the conditions of the initiation and sustainment of arcs in gas discharge plasmas generated in different ways, such as DC and pulsed discharges, RF discharges, electrically or hydrodynamically driven shock tubes and lasers [18, 63, 64, 106–115]. These simulations have confirmed, in principle, the possibility of ignition and sustainment of arcing without the application of external electromotive forces, but it is not clear whether the results can be directly applied to the case of arcing in magnetic fusion devices. In particular, the specific sources of electromotive forces in a fusion device, the discharge channels and the ignition conditions cannot be predicted on the basis of these results. At present, it is only possible to give some rather general rules concerning the possible mechanisms of arcing and the conditions for the development of arcs in fusion devices.

Several conditions must be fulfilled for ignition and sustainment of an arc discharge in a low pressure environment:

(a) The driving voltage U must be higher than, or at least equal to, the cathode drop of the potential U_c or of the arc voltage U_{arc}, the latter being somewhat higher than U_c (Table III): $U > U_{arc} > U_c \simeq 10$–$30$ V.

(b) The current available per arc spot must exceed a minimum value I_c, depending on the material.

(c) Ignition of arcs requires voltages that are considerably higher than U_c, in particular when ignition occurs by breakdown phenomena without contacting electrodes.

3.1. The sheath model of unipolar arcs

Robson and Thonemann [115] coined the term 'unipolar arc' for the phenomenon of discharges with only one determinable electrode (with cathode functions) and proposed a first model. They considered the space charge sheath between the plasma and the solid surface of a conducting wall as the source of the electromotive force required to sustain unipolar arcs. Because of the higher velocities of the electrons relative to the ions, the wall becomes negatively charged, creating a space charge layer with a potential difference approximately equal to

$$eU_f = -kT_e\,(2.84 + 0.5 \ln m_i/m_p) \qquad (3)$$

assuming $n_e = n_i$ and $T_e = T_i$; m_p and m_i denote the proton and the ion mass, respectively. Remembering that an arc needs a minimum voltage U_{arc} (of the order of 10–30 V for most metallic wall materials), an arc can be sustained if $U_f > U_{arc}$. Therefore, with hydrogen ($m_i = m_p$) an electron temperature of approximately 3–10 eV would be necessary to sustain an arc, i.e. typical tokamak edge plasmas would be able to sustain arcs. According to Ref. [115], the unipolar arc current flow is closed in the neighbourhood of the cathode arc spot. The sheath potential difference drops in the immediate vicinity of the cathode spot to U_c according to the current drawn by the arc. This current has to be transported by the surrounding plasma, causing a disturbed annular zone with a sheath potential difference lower than U_f; this leads to an increased electron current to the wall in this annular 'anode' zone A. A minimum area condition of the anode zone can be estimated for

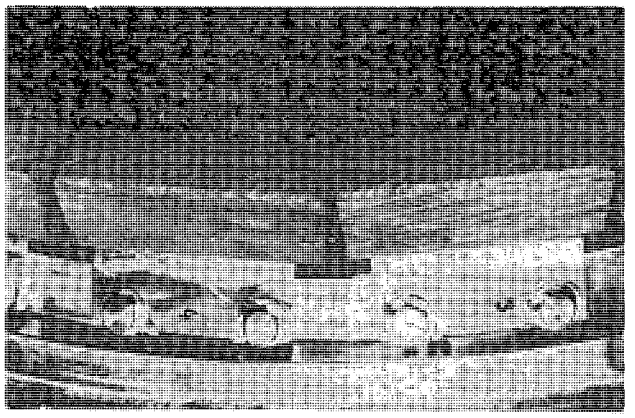

FIG. 8. Arc tracks influenced by the action of the magnetic field on graphite tiles of the T-15 fixed poloidal aperture limiter.

the minimum current I_c required to sustain a metal vapour arc on the given material:

$$A \geq I_c/\{ne\,(kT_e/2\pi m_e)^{1/2} \times [\exp(-eU_c/kT_e) - \exp(-eU_f/kT_e)]\} \quad (4)$$

3.1.1. *Influence of the magnetic field*

The action of the strong magnetic field in fusion devices with magnetic confinement must also be taken into account:

(a) The spot plasma itself is not affected by the magnetic field because of its high density and because its dimensions are smaller than the electron Larmor radius [82, 116].

(b) The movement of the spot as a whole is controlled by the magnetic field [55, 58, 63, 64, 66, 68, 69, 117]. The direction of arc spot movement in magnetic fields can be considered to consist of two components: the retrograde movement and the Robson drift [117], which cause differently shaped erosion track curves, depending on the field direction and the cathode geometry [66] (Fig. 8).

(c) The plasma in the anode zone is strongly influenced by the magnetic field. At least the anode zone becomes elongated in the direction of the magnetic field [102].

(d) In magnetic fields the arc spot plasma is prevented from free expansion. The plasma is confined along field lines as soon as the electron gyration frequency exceeds the collision frequency. The ions are coupled to the electrons by electric fields [82].

The latter statement is of special importance for arcing phenomena in magnetic fusion devices since the confined column may become considerably long, up to several turns around the torus [13, 101, 118, 119]. The existence of a filamentary structure of the arc column was experimentally confirmed by measurements of its inductance and its voltage drop [18, 101, 119]. The diameter of the confined current channel was estimated to be typically less than 10 mm. Depending on the inner geometry of the torus and the placement of limiters, antennas and so forth as well as on the q values, the connection lengths of the channel may be very different. Two limiting cases should be distinguished: (1) An isolated zone (the anode area) which collects the return currents is connected by a relatively short current channel (less than a few turns around the torus). In this case the current is limited by the electron saturation current from the surrounding plasma to the collecting structure. (2) There is no connecting 'anode area', so that the arc current is limited by cross-field diffusion from the plasma into the arc column filament.

The arc voltage as a function of the field strength of an axial magnetic field B[T] and the column length z[m] were established empirically [116] for copper and molybdenum. An additional voltage drop ΔV over the arc column was found:

$$\Delta V_{Cu}(z)\ [V] = (8.85\sqrt{B} + 0.47)\ \ln z/z_0 \quad (5)$$

$$\text{for } z_0 = 1 \times 10^{-4}\ \text{m}$$

$$\Delta V_{Mo}(z)\ [V] = (6.95\sqrt{B} + 2.11)\ \ln z/z_0 \quad (6)$$

$$\text{for } z_0 = 3.5 \times 10^{-4}\ \text{m}$$

No data are available for other materials. For a given material, z_0 characterizes a critical semi-sphere radius around the spot centre inside which the magnetic field has no influence. Whether this empirical relation can be extended to very long arc channels in strongly magnetized plasma remains to be verified.

3.1.2. *Other models of unipolar arcs*

There are some attempts to supplement the sheath model by taking into account any peculiarities due to the action of the magnetic field [118, 120, 121]. The case of arcing on surfaces perpendicular to the magnetic field, for example on limiter structures intersecting magnetic field lines, was treated in various ways: Nedospasov and Petrov [118, 121] drew attention to

the development of a potential difference between flux tubes ending on an active arc spot and neighbouring ones, giving rise to a transverse current which transfers hot electron energy to the arc. Mirnov [120] considered the energy accumulated in flux tubes. If such a flux tube is intercepted by a limiter because of changes of the q values or because of disruptions, a high overvoltage arises at the limiter surface which may cause ignition of an arc. Maeno et al. [8] and Yamamoto et al. [122] discussed the possible role of runaway electrons in the formation of arcing. A more general approach including the main plasma body was proposed by Ecker et al. [103, 104] and Hantzsche [102]. The problem is extremely complex, especially if non-stationariness is included. So far, only a few basic features of the general problem have been treated, for example in a stationary model concerned with the details of the current backflow to the wall in a plasma with electromotive forces in the sheath only [104], and a study of the generation and dissipation of electromotive forces in the plasma body [103].

The complexity of the whole problem is clearly demonstrated in the comprehensive review of Ecker [20]. According to this review, there are at present no real means to theoretically predict the occurrence of arcing in fusion devices.

4. CONCLUSIONS

Numerous experimental investigations on arcing in fusion devices and in simulation installations have been performed which are summarized in reviews [10, 18, 20, 21, 70, 123]. From these, some general rules concerning the arcing phenomena can be given:

(1) The ignition conditions of arcs in fusion devices can be considered by analogy with arc ignition and breakdown in vacuum [36, 39, 71–74]. The starting point is the production of an initial plasma of sufficient density to allow arc development under the action of a low impedance source with a voltage higher than the arc voltage. The initial plasma may be produced by explosive emission from surface protrusions [39, 73, 74]. Dielectric surface inclusions and impurity layers strongly enhance ignition [9, 44, 75, 76, 124–126]. This was demonstrated convincingly by a series of experiments in tokamaks [99, 127, 128] as well as in simulation devices [107, 108, 110, 111]. Both types of experiment show an increase of the onset voltage for arcing with the number of arcs from a few tens of volts to more than 500 V. This effect is attributed to the self-cleaning process by arcing, which is well known in vacuum discharges, as mentioned above. A certain dependence on the material and the surface temperature has been established. Consequently, several tokamak relevant materials have been investigated with regard to this problem [1, 63, 64, 129–134]. The relevance of this kind of results is questionable since erosion and deposition processes during tokamak operation may substantially change the surface conditions. Moreover, specific effects of tokamak discharges (instabilities, runaway electrons, etc.) may create locally favourable conditions for arc ignition which surpass any conditions originating from the choice of materials or the state of the surface.

(2) By observations with probes, spectroscopy and light detection it has been found that arcing in fusion devices occurs almost exclusively during the startup and end phases of the discharge, particularly in the case of disruptive terminations and during MHD instabilities (mainly if rational values of q near surfaces are passed) [5, 6, 10, 18, 135]. This result is closely connected with the ignition problem. According to Hantzsche [136] the occurrence of arcing in fusion devices depends much less on the conditions required for the existence of arcs than on the ignition conditions.

(3) An arc spot emits ions, neutral vapour and particles with widely differing energies. As regards impurity injection, particles are most dangerous since they carry the greater part of eroded material at higher energies compared with the vapour component. The majority of the latter is ionized outside the last closed magnetic flux surface (inside the scrape-off layer) and is caught by limiters or divertor plates in the same way as the ion component.

(4) Judging from the erosion traces produced by usual low current diffuse arcs, it is almost impossible to determine the nature of an arc and whether it is truly unipolar or bipolar, and to identify the anticipated current channel or the anode zone. Bipolar constricted high current arcs should be discernible by the heavy erosion and possibly by anode erosion traces. The impurity production by arcing can be estimated fairly well by evaluation of the arc tracks. In present-day fusion devices, arcing can be largely suppressed by smooth plasma operation. The amount of impurities attributable to arcing is considerably smaller than that from other sources. In future large devices provision should be made to rule out the generation of induced high current discharges across gaps in the first wall structure [98].

REFERENCES

[1] CRASTON, J.L., HANCOX, R., ROBSON, A.E., et al., in Peaceful Uses of Atomic Energy (Proc. 2nd Int. Conf. Geneva, 1958), Vol. 32, UN, New York (1958) 414.

[2] SIMONOV, V.A., SVILKIN, B.I., KUTUKOV, G.P., in Plasma Physics and Controlled Nuclear Fusion Research (Proc. Int. Conf. Salzburg, 1961), Nucl. Fusion Supplement — Part 1, IAEA, Vienna (1962) 320.

[3] CLAUSING, R.E., EMERSON, L.C., HEATHERLY, L., J. Nucl. Mater. **93&94** (1980) 150.

[4] GOODALL, D.H.J., CONLON, T.W., SOFIELD, C., McCRACKEN, G.M., J. Nucl. Mater. **76&77** (1978) 492.

[5] GOODALL, D.H.J., McCRACKEN, G.M., Nucl. Fusion **19** (1979) 1396.

[6] GOODALL, D.H.J., J. Nucl. Mater. **93&94** (1980) 154.

[7] JÜTTNER, B., LAUX, M., LINGERTAT, J., et al., Nucl. Fusion **20** (1980) 497.

[8] MAENO, M., OHTSUKA, H., YAMAMOTO, S., YAMAMOTO, T., et al., Nucl. Fusion **20** (1980) 1415.

[9] MASKREY, J.T., DUGDALE, D.A., J. Nucl. Mater. **10** (1963) 233.

[10] McCRACKEN, G.M., J. Nucl. Mater. **93&94** (1980) 3.

[11] MIODUSZEWSKI, P., CLAUSING, R.E., HEATHERLY, L., J. Nucl. Mater. **85&86** (1979) 963.

[12] McCRACKEN, G.M., GOODALL, D.H.J., Arcing and Surface Damage in DITE, Rep. CLM-R167, Culham Laboratory, Abingdon, Oxfordshire (1977); McCRACKEN, G.M., GOODALL, D.H.J., Nucl. Fusion **18** (1978) 537.

[13] ZYKOVA, N.M., IVANOV, R.S., KABANOV, V.N., et al., in Controlled Fusion and Plasma Physics (Proc. 10th Eur. Conf. Moscow, 1981), Vol. 1, European Physical Society (1981) paper J-4.

[14] OHTSUKA, H., OGIWARA, N., MAENO, M., J. Nucl. Mater. **93&94** (1980) 161.

[15] DUAN, W., CHEN, J., YANG, S., J. Nucl. Mater. **111&112** (1982) 502.

[16] COHEN, S.A., DYLLA, H.F., ROSSNAGEL, S.M., et al., J. Nucl. Mater. **76&77** (1978) 459.

[17] HILDEBRANDT, D., LAUX, M., LINGERTAT, J., et al., Beitr. Plasmaphys. **20** (1980) 314.

[18] LANGLEY, R. (Ed.), Arcing Phenomena in Fusion Devices (Proc. Workshop Oak Ridge, 1979), Spec. edn, Oak Ridge National Laboratory, TN (1979).

[19] ECKER, G., in Plasma-Wall Interactions (Proc. Int. Symp. Jülich, 1976), Pergamon Press, Oxford (1977) 245.

[20] ECKER, G., in Phenomena in Ionized Gases (Proc. 16th Int. Conf. Düsseldorf, 1983), Vol. Invited Papers, published by the Organizing Committee (1983) 9–23.

[21] MIODUSZEWSKI, P., in Data Compendium for Plasma-Surface Interactions, Nucl. Fusion Special Issue 1984 (1984) 105.

[22] MILLER, H.C., A Bibliography and Author Index for Electrical Discharges in Vacuum, Techn. Inf. Series, GEPP-TIS-366e UC13, General Electric Co. (1988).

[23] JÜTTNER, B., in Phenomena in Ionized Gases (Proc. 17th Int. Conf. Budapest, 1985), Vol. Invited Papers, published by the Organizing Committee (1985) 262.

[24] GUILE, A.E., IEEE Proc. A **131** (1984) 450.

[25] ECKER, G., in Vacuum Arcs, Wiley, New York (1980) 228.

[26] HARRIS, L.P., ibid., p. 120.

[27] DAALDER, J.E., Cathode erosion of metal vapour arcs in vacuum, PhD thesis, Univ. of Technology, Eindhoven (1978).

[28] ECKER, G., Ergeb. exakt. Naturwiss. **33** (1961) 1.

[29] RAKHOVSKIJ, V.I., Physical Bases of the Commutation of Electrical Current in Vacuum, Nauka, Moscow (1970) (in Russian).

[30] KIMBLIN, C.W., IEEE Trans. Plasma Sci. **PS-10** (1982) 322.

[31] KESAEV, I.G., Cathode Processes in Electric Arcs, Nauka, Moscow (1968) (in Russian).

[32] LYUBIMOV, G.A., RAKHOVSKIJ, V.I., Sov. Phys. - Usp. **21** (1979) 693.

[33] KIMBLIN, C.W., Arcing Phenomena in Fusion Devices (Proc. Workshop Oak Ridge, 1979), Spec. edn, Oak Ridge National Laboratory (1979).

[34] HARRIS, L.P., ibid.

[35] KIMBLIN, C.W., in Phenomena in Ionized Gases (Proc. 15th Int. Conf. Minsk, 1979), published by the Organizing Committee (1981) 202.

[36] HANTZSCHE, E., Beitr. Plasmaphys. **23** (1983) 77.

[37] FARRALL, G.A., Proc. IEEE **61** (1973) 1113.

[38] MITCHELL, G.R., Proc. Inst. Electr. Eng. (London) **117** (1970) 2315.

[39] LITVINOV, E.A., MESYATS, G.A., PROSKUROVSKIJ, D.I., Sov. Phys. - Usp. **26** (1983) 138.

[40] JÜTTNER, B., Physica C **114** (1982) 255.

[41] MILLER, H.C., IEEE Trans. Plasma Sci. **PS-13** (1985) 242.

[42] HEBERLEIN, J.V.R., GORMAN, J.G., IEEE Trans. Plasma Sci. **PS-8** (1980) 283.

[43] DJAKOV, B.E., HOLMES, R., J. Phys., D **7** (1974) 569.

[44] ACHERT, J., ALTRICHTER, B., JÜTTNER, B., et al., Beitr. Plasmaphys. **17** (1977) 419.

[45] GUILE, A.F., JÜTTNER, B., IEEE Trans. Plasma Sci. **PS-8** (1980) 259.

[46] JÜTTNER, B., Beitr. Plasmaphys. **19** (1979) 25.

[47] RAKHOVSKIJ, V.I., IEEE Trans. Plasma Sci. **PS-12** (1984) 199.

[48] RAKHOVSKIJ, V.I., in Discharges and Electrical Insulation in Vacuum (Proc. 13th Int. Symp. Paris, 1988), Vol. 1, Les éditions de physique, Les Ulis (1988) 142.

[49] HANTZSCHE, E., JÜTTNER, B., PUCHKAROV, V.F., et al., J. Phys., D **9** (1976) 1771.

[50] JÜTTNER, B., J. Phys., D **14** (1981) 1265.

[51] FARRALL, G.A., in Vacuum Arcs, Wiley, New York (1980) 184.

[52] DAALDER, J.E., IEEE Trans. Power Appar. Syst. **PAS-93** (1974) 1747.

[53] DAALDER, J.E., Physica C **104** (1981) 91.

[54] DAALDER, J.E., J. Phys., D **16** (1983) 17.

[55] SCHRADE, H.O., in Discharges and Electrical Insulation in Vacuum (Proc. 13th Int. Symp. Paris, 1988), Vol. 1, Les éditions de physique, Les Ulis (1988) 172.

[56] SCHRADE, H.O., AUWETER-KURTZ, M., KURTZ, H.L., IEEE Trans. Plasma Sci. **PS-11** (1983) 103.

[57] NEMTSCHINSKIJ, S.A., Sov. Phys. - Tech. Phys. **28** (1983) 150.
[58] DROUET, M.G., IEEE Trans. Plasma Sci. **PS-13** (1985) 235.
[59] AUWETER-MING, M., SCHRADE, H.O., J. Nucl. Mater. **93&94** (1980) 799.
[60] AGARWAL, M.S., HOLMES, R., J. Phys., D **17** (1984) 743.
[61] ZHUKOV, V.M., AKSENOV, M.S., FURSEY, G.N., Sov. Phys. - Tech. Phys. **28** (1983) 1588.
[62] NÜRNBERG, A.W., FANG, D.Y., BAUDER, U.H., et al., J. Nucl. Mater. **103&104** (1981) 305.
[63] FANG, D.Y., NÜRNBERG, A., BAUDER, U.H., BEHRISCH, R., J. Nucl. Mater. **111&112** (1982) 791.
[64] FANG, D.Y., IEEE Trans. Plasma Sci. **PS-11** (1983) 110.
[65] HARRIS, L.P., IEEE Trans. Plasma Sci. **PS-11** (1983) 94.
[66] HINTZE, W., LAUX, M., Beitr. Plasmaphys. **21** (1981) 247.
[67] YUKHIMCHUK, S.A., SVIDERSKAYA, O.M., Sov. Phys. - Tech. Phys. **27** (1982) 1393.
[68] SETHURAMAN, S.K., BARRAULT, M.R., J. Nucl. Mater. **93&94** (1980) 791.
[69] ROBSON. E.A., J. Phys., D **11** (1978) 1917.
[70] MIODUSZEWSKI, P., Comments Plasma Phys. Controll. Fusion **6** (1980) 7.
[71] FURSEY, G.N., IEEE Trans. Electr. Insul. **EI-20** (1985) 659.
[72] FARRALL, G.A., IEEE Trans. Electr. Insul. **EI-20** (1985) 815.
[73] BUGAEV, S.P., LITVINOV, E.A., MESYATS, G.A., et al., Sov. Phys. - Usp. **18** (1975) 51.
[74] MESYATS, G.A., PROSKUROVSKIJ, D.I., Impulsive Electrical Discharges in Vacuum, Nauka, Novosibirsk (1984) (in Russian).
[75] PROSKUROVSKIJ, D.I., PUCHKAREV, V.F., J. Phys. (Les Ulis) **40** (1979) 411.
[76] HALBRITTER, J., IEEE Trans. Electr. Insul. **EI-20** (1985) 671.
[77] BROWN, I.G., GALVIN, J.E., in Discharges and Electrical Insulation in Vacuum (Proc. 13th Int. Symp. Paris, 1988), Vol. 1, Les éditions de physique, Les Ulis (1988) 214.
[78] BROWN, I.G., FEINBERG, B., GALVIN, J.E., J. Appl. Phys. **63** (1988) 4889.
[79] DAALDER, J.E., J. Phys., D **8** (1975) 1647.
[80] DAALDER, J.E., J. Phys., D **9** (1976) 2379.
[81] DAVIS, W.D., MILLER, H.C., J. Appl. Phys. **40** (1969) 2212.
[82] KIMBLIN, C.W., Proc. IEEE **59** (1971) 546.
[83] KIMBLIN, C.W., J. Appl. Phys. **44** (1973) 3074.
[84] PLYUTTO, A.A., RYZHKOV, V.M., KAPIN, A.T., Sov. Phys. - JETP **20** (1965) 328.
[85] TUMA, D.T., CHEN, C.L., DAVIES, D.K., J. Appl. Phys. **49** (1978) 3821.
[86] UTSUMI, T., ENGLISH, J.H., J. Appl. Phys. **46** (1975) 126.
[87] KUTZNER, J., MILLER, C.H., in Discharges and Electrical Insulation in Vacuum (Proc. 13th Int. Symp. Paris, 1988), Vol. 1, Les éditions de physique, Les Ulis (1988) 226.
[88] LUNEV, V.I., OVCHARENKO, V.D., KHOROSHIKH, V.M., Sov. Phys. - Tech. Phys. **22** (1977) 855.
[89] LUNEV, V.M., PADALKA, V.G., KHOROSHIKH, V.M., Sov. Phys. - Tech. Phys. **22** (1977) 858.
[90] MILLER, H.C., J. Appl. Phys. **52** (1981) 23.
[91] HANTZSCHE, E., Zesz. Nauk. Politech. Poznan **38** (1989) 9.
[92] UDRIS, Ya.Ya., Radio Eng. Electron. Phys. **8** (1963) 1050.
[93] BOXMAN, R.L., GOLDSMITH, S., J. Appl. Phys. **52** (1981) 151.
[94] HAYESS, E., JÜTTNER, B., LIEDER, G., et al., in Discharges and Electrical Insulation in Vacuum (Proc. 13th Int. Symp. Paris, 1988), Vol. 1, Les éditions de physique, Les Ulis (1988) 138.
[95] HANTZSCHE, E., in Discharges and Electrical Insulation in Vacuum (Proc. 7th Int. Symp. Novosibirsk, 1976), USSR Acad. Sci., Novosibirsk (1976) 324.
[96] HILDEBRANDT, D., JÜTTNER, B., PURSCH, H., et al., Nucl. Fusion **29** (1989) 305.
[97] KUTZNER, J., ZALUCKI, Z., in Gas Discharges (Proc. Int. Conf. London, 1990), IEEE Conf. Publ. No. 70 (1970) 87.
[98] MURRAY, J.G., GORKER, G.E., Fusion Technol. **8** (1985) 664.
[99] ERTL, E., ASDEX Team, JÜTTNER, B., Nucl. Fusion **25** (1985) 1413.
[100] HILDEBRANDT, D., JÜTTNER, B., PURSCH, H., in Plasma Physics and Technology (Proc. 14th Seminar Liblice, 1987), Inst. of Plasma Physics, Czechoslovak Acad. Sci., Prague (1987).
[101] JAKUBKA, K., JÜTTNER, B., LAUX, M., SIEMROTH, P., Sov. J. Plasma Phys. **12** (1986) 152.
[102] HANTZSCHE, E., Beitr. Plasmaphys. **20** (1980) 329.
[103] ECKER, G., RIEMANN, K.-U., WIECKERT, C., Beitr. Plasmaphys. **22** (1982) 463.
[104] WIECKERT, C., J. Nucl. Mater. **76&77** (1978) 499.
[105] BEHRISCH, R., Physics of Plasma-Wall Interaction, Plenum Press, New York (1986).
[106] STAMPA, A., KRÜGER, H., J. Phys., D **16** (1983) 2135.
[107] EHRICH, H., KARLAU, J., MÜLLER, K.G., J. Nucl. Mater. **111&112** (1982) 526.
[108] EHRICH, H., KARLAU, J., MÜLLER, K.G., IEEE Trans. Plasma Sci. **PS-14** (1986) 603.
[109] ROGOFF, G.L., LOWRY, J.F., PINSKER, R.I., J. Appl. Phys. **54** (1983) 1289.
[110] HOETHKER, K., BIEGER, W., HARTWIG, H., et al., J. Nucl. Mater. **93&94** (1980) 785.
[111] MIODUSZEWSKI, P., CLAUSING, R.E., HEATHERLY, L., J. Nucl. Mater. **91** (1980) 297.
[112] MIODUSZEWSKI, P., CLAUSING, R.E., HEATHERLY, L., in Arcing Phenomena in Fusion Devices (Proc. Workshop Oak Ridge, 1979), Spec. edn, Oak Ridge National Laboratory, TN (1979).
[113] NÜRNBERG, A.W., BAUDER, U.H., MOOSER, C., et al., Beitr. Plasmaphys. **21** (1981) 127.
[114] SCHWIRZKE, F., TAYLOR, R.J., J. Nucl. Mater. **93&94** (1980) 780.
[115] ROBSON, A.E., THONEMANN, P.C., Proc. Phys. Soc. **73** (1959) 508.

[116] GUNDLACH, H.C.W., in Discharges and Electrical Insulation in Vacuum (Proc. 8th Int. Symp. Albuquerque, 1978), Sandia National Labs, Albuquerque, NM (1978) A2.1.
[117] ROBSON, A.E., in Phenomena in Ionized Gases (Proc. 4th Int. Conf. Uppsala, 1959), Vol. 1, North-Holland, Amsterdam (1960) IIB/376.
[118] NEDOSPASOV, V.A., PETROV, V.G., J. Nucl. Mater. **93&94** (1980) 775.
[119] SIEMROTH, P., JÜTTNER, B., JAKUBKA, K., SAKHAROV, N.V., IEEE Trans. Plasma Sci. **PS-13** (1985) 300.
[120] MIRNIV, S.V., Sov. J. Plasma Phys. **7** (1981) 376.
[121] NEDOSPASOV, A.V., PETROV, V.G., Nucl. Fusion **21** (1981) 413.
[122] YAMAMOTO, S., SHIMOMURA, Y., OHASA, K., et al., J. Phys. Soc. Jpn. **48** (1980) 1053.
[123] McCRACKEN, G.M., STOTT, P.E., Nucl. Fusion **19** (1979) 889.
[124] BARENGOLZ, Yu.A., Sov. Tech. Phys. Lett. **11** (1985) 563.
[125] HANCOX, R., Br. J. Appl. Phys. **11** (1960) 468.
[126] MASKREY, J.T., DUGDALE, R.A., Br. J. Appl. Phys. **17** (1966) 1025.
[127] JAKUBKA, K., JÜTTNER, B., J. Nucl. Mater. **102** (1981) 259.
[128] ERTL, K., BEHRISCH, R., ASDEX Team, JÜTTNER, B., in Controlled Fusion and Plasma Physics (Proc. 11th Eur. Conf. Aachen, 1983), Vol. 7D, Part II, European Physical Society (1983) 385.
[129] WHITLEY, J.B., MATTOX, D.M., in Arcing Phenomena in Fusion Devices (Proc. Workshop Oak Ridge, 1979), Spec. edn, Oak Ridge National Laboratory, TN (1979).
[130] JÜTTNER, B., PURSCH, H., SHILOV, V.A., J. Phys., D **17** (1984) 31.
[131] KOCH, A.W., NÜRNBERG, A.W., J. Nucl. Mater. **122&123** (1984) 1437.
[132] LANGLEY, R.A., EMERSON, L.C., WHITLEY, J.B., MULLENDORE, A.W., J. Nucl. Mater. **93&94** (1980) 479.
[133] SCHWIRZKE, F., BUNSHAH, R.F., TAYLOR, R.J., Thin Solid Films **83** (1981) 117.
[134] ZOBOV, E.A., SOKOLOV, V.G., et al., J. Appl. Mech. Tech. Phys. **21** (1980) 147.
[135] ALEXANDER, K.F., CHICHEROV, V.M., HINTZE, W., et al., in Plasma Physics (Proc. Int. Conf. Göteborg, 1982), Chalmers University of Technology, Göteborg (1982) 391.
[136] HANTZSCHE, E., in Phenomena in Ionized Gases (Proc. 15th Int. Conf. Minsk, 1981), published by the Organizing Committee (1981) 184.

PULSE HEATING AND EFFECTS OF DISRUPTIONS AND RUNAWAY ELECTRONS ON FIRST WALLS AND DIVERTORS

J.B. WHITLEY, W.B. GAUSTER,
R.D. WATSON, J.A. KOSKI, A.J. RUSSO
Sandia National Laboratories,
Albuquerque, New Mexico,
United States of America

ABSTRACT. The thermal response of plasma facing components is often a critical performance limiting issue. The effect of these materials on the plasma (for example by impurity injection) is often directly tied to the component temperature, and the severe thermal stresses and melting/evaporation that may occur strongly influence the component lifetime. As machines move to long pulse operation, the issues relating to heat removal by coolants such as water will also become critical. Disruptions and creation of runaway electrons are difficult to avoid and, while efforts to circumvent them are being made, components must still be designed to withstand these events. Finally, the effects of neutron irradiation of the thermal properties of materials could become a major issue for future devices.

1. INTRODUCTION

The performance of plasma facing components (PFCs) in magnetic fusion devices will be dictated to a large degree by their response to the thermal loads generated by interactions with the plasma. Since the interior components are directly coupled to the plasma, their successful performance is mandatory to maintain the plasma at the required purity levels. Their location inside the vacuum boundary means that replacement or repair requires entering the torus — an activity which is difficult, time consuming and costly. The thermal performance of PFCs is one of the critical technologies that limits the ultimate power level and availability of the device and, as such, is a technology that will play an important role in determining the economic viability of fusion as an energy producing source (see, for example, Refs [1–12]).

The thermal loads on PFCs are commonly divided into 'normal' loads and 'off-normal' loads. Normal loads are the power fluxes incident on the components during a typical discharge. These loads range from the order of 0.1 MW/m^2 for first wall panels to 10–30 MW/m^2 for divertor plates. The pulse lengths will be long, maybe hundreds or even thousands of seconds, and the components will reach thermal equilibrium during the pulse. In many cases, active cooling with a flowing coolant (typically water, helium or a molten salt) will be required to remove the incident energy. The basic design parameter needed for the thermal design of these components is the incident power flux. Measurements of the power flow in the plasma edge of existing tokamaks are used to validate and calibrate the edge models used for these designs. At present, our ability to predict power flows is very crude, with large uncertainties involved as we scale the calculations up to an ITER size machine [13].

Off-normal events are characterized as those events that deliver power loads greater than twice the normal loads for any time period. Examples of off-normal events are edge localized modes (ELMs), plasma disruptions and runaway electrons. These events are usually random, unanticipated occurrences caused by either a hardware failure or unexplained plasma events. ELMs are often observed during high-confinement (H-mode) operation and present themselves as either frequent, low intensity events or less frequent, more severe thermal events. Disruptions and runaway electrons are much more serious excursions. Disruptions deliver thermal loads of the order of 10 MJ/m^2 over times of about 0.1 ms and also generate severe eddy currents in components which lead to large mechanical forces. Runaway electrons can be generated during low density plasma discharges, during radiofrequency (RF) heating and during disruptions. These electrons can be accelerated to energies greater than 100 MeV and are very intense beams. Models to predict the occurrence of thermal loads from these events are relatively crude and the scaling laws to predict ITER conditions are very uncertain. It is clear that the occurrence of these off-normal events must be minimized and that the phenomena must receive much more attention in the future if reliable machine operation is expected.

Once the thermal environment has been defined, the next step is to predict the component response to this environment. The desired response is to have the

component absorb and transfer the incident energy to the coolant for the total number of machine cycles, while not contaminating or otherwise negatively impacting the plasma. In reality, the component can fail, for example by evaporation or sublimation, by thermal shock causing fracture, by thermal fatigue generated cracking or by exceeding the coolant heat transfer limits. Component fabrication often produces residual stresses that interact with the operational stresses to cause fracture. Finite element modelling is used to predict these temperature and stress states, but a great deal more data on the behaviour of components under these conditions must be generated, and work on the development of lifetime codes needs to be emphasized.

The final environmental effect that will start playing a critical role in ITER components is that of neutron damage. ITER and other power producing devices will produce sufficient fluxes of high energy neutrons to substantially alter the material properties of all PFCs. These changes include a reduction in thermal conductivity, an increase in strength, a reduction in density and volume changes (densification or swelling). These changes will alter both the stress state and the surface temperature of the component and will most likely shorten its expected service life. Data on these effects are just starting to be generated and will require substantial investments in fission reactor space for irradiation, and in the development of specialized test equipment and 14 MeV neutron sources to determine the response of irradiated components to the pulsed thermal environment.

2. SELECTION OF PLASMA FACING MATERIALS

The selection of materials that are in contact with the plasma either as limiters and first walls or in the divertor regions of magnetic confinement fusion devices represents a key problem area. In the large plasma physics experiments that have been performed so far, the understanding and control of plasma–material interactions have been essential elements in the attainment of favourable plasma parameters. An important example of this was given by the neutral beam heating experiments on the PLT tokamak in 1978, reviewed by Hosea et al. [14]. When tungsten limiters were used initially, strong, centrally peaked radiation was observed. The electron temperatures decreased during beam injection, a density rise greater than the influx of particles was observed, and the ion temperatures were limited to 2 keV. After the tungsten limiters were replaced by carbon and gettering by titanium on the walls was done between discharges, the radiation attributable to impurities was greatly reduced. The density rise during injection became comparable to the ion influx, and a record central ion temperature of 7 keV was achieved.

A more recent example is given by the attainment of enhanced confinement discharges in the Tokamak Fusion Test Reactor (TFTR) and the role played by conditioning of the graphite wall [15]. After a helium conditioning procedure was used, the hydrogen recycling coefficients during gas fuelled Ohmic discharges dropped from about one to values as low as 0.5; the target plasmas with relatively low densities and low recycling coefficients achieved in this way were necessary for the attainment of neutral beam heated plasmas with high confinement ('supershots') in which ion temperatures up to 30 keV were measured in 1987 [16].

In the Joint European Torus (JET) experiment, more than 50% of the inner surface of the vessel has been covered with fine grain graphite or fibre reinforced carbon tiles [17]. The introduction of graphite has led to pumping effects that were used to advantage during neutral beam heating [18]. Beryllium as a wall and limiter material has also been studied in JET. First results from experiments done after beryllium was evaporated over the interior of the vacuum vessel to an initial average thickness of 100 Å showed a distinct improvement of the plasma properties [19]. The parameter space attained in terms of effective charge, dilution density and temperature was expanded considerably, and an equivalent D–T fusion Q of 0.5–0.7 was achieved.

The JT-60 tokamak has provided experience with both metal (molybdenum coated with titanium carbide) and carbon (fine grain graphites) walls [20]. With metal walls, impurity control by the divertor was achieved during high power neutral beam heating. The reduction of surface–wall interactions led to effective atomic numbers in the plasma between 1.5 and 2, with only 10% of the input power radiated. As with the other large tokamaks, extensive wall conditioning was needed before operation with graphite walls. In the outboard divertor configuration, some high performance (H-mode) discharges were produced.

In addition to this large physics database on the effect of PFC material choices on the plasma performance, there is also considerable experience on the mechanical behaviour of these components. The most extensive experience is, of course, with graphite

[21-23]. Both isotropic, nuclear grade graphites and carbon fibre composites have been used. In regions of high heat fluxes (>10 MW/m^2) there has been evidence of thermal fracture of the isotropic graphite. Most of these regions have been replaced by carbon fibre composites, and these have performed quite well mechanically with no sign of fracture. Metallic components often suffer from localized melting due either to disruption events or to power overloading during normal pulses. Many examples of surface melting and gross deformation from disruption induced eddy current forces exist. There have also been several studies of the power flow from the plasma edge [24, 25]. These studies are in general agreement with the exponential model that has been developed and show a very well defined edge that is very sensitive to component alignment. There is now a consensus that components must be aligned to an accuracy of better than ± 1 mm to avoid local heating problems.

3. PFC ENGINEERING

Figure 1 shows a schematic representation of a generic, actively cooled PFC, identifying the many considerations involved. Surface effects such as sputtering and hydrogen recycling have the most direct impact on plasma performance and for that reason generally receive the most attention. Bulk effects such as crack growth can cause component failure, and bulk property damage brought on by the intense neutron environment of D-T devices may dictate the component lifetimes. Next generation and future machines will operate with long pulses, which will require active cooling and hence consideration of the many coolant issues such as burnout and erosion/corrosion. Most designs proposed consist of a structure/armour arrangement which introduces an interface that can affect the component response in many ways. Finally, there are many component issues such as fabricability and cost that may ultimately decide what options are feasible and practical.

Given the importance of the plasma facing material to plasma operation, it is clear that this must be a dominating concern when engineering a PFC. However, there are many material properties that dictate the component response and usefulness, and all of these properties must be considered. Desirable properties include: high thermal conductivity, low Z, good thermal shock resistance, low sputtering, low coefficient of thermal expansion (CTE), low elastic modulus, high melting point, high strength, high toughness, low outgassing, low tritium inventory, low neutron activation, good oxidation resistance, low toxicity, low swelling and embrittlement, low cost, etc. The selection of materials is a particularly challenging task because no single material can simultaneously satisfy all of the requirements. Hence, an armour material that is intended to face the plasma and give the desired plasma properties is bonded to a substrate used to provide support and cooling. Promising candidates for armour materials are isotropic graphite, carbon/carbon

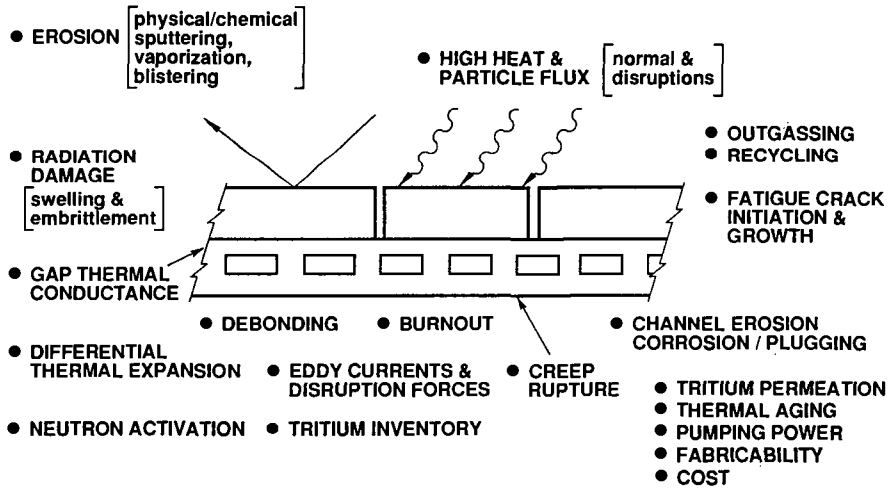

FIG. 1. Schematic representation of an armoured PFC, showing many of the considerations going into the design decision.

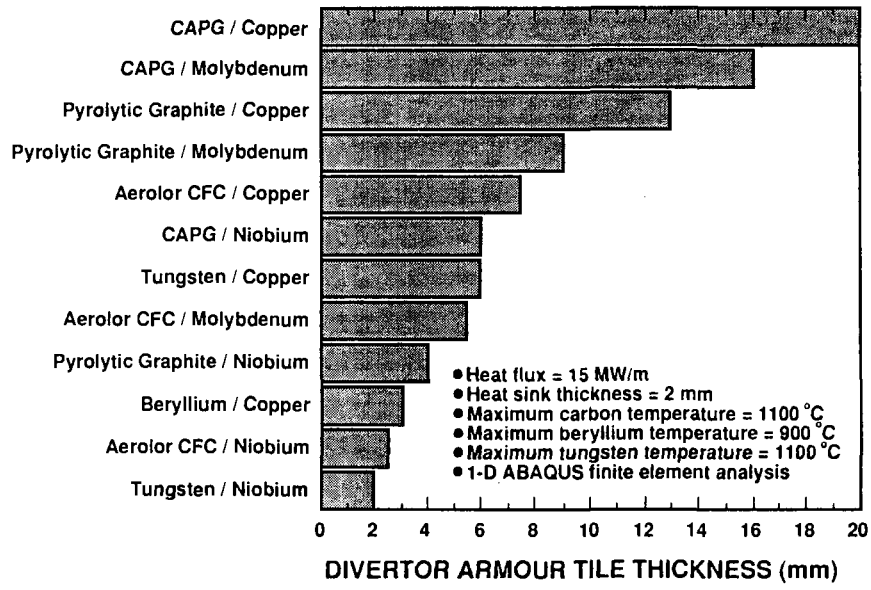

FIG. 2. Bar chart showing the calculated maximum tile thickness allowed for a divertor element with an incident heat flux of 15 MW/m^2 and a surface temperature limit of 1100°C for carbon and tungsten and 900°C for beryllium.

composites, pyrolytic graphite (PG), compression annealed pyrolytic graphite (CAPG), beryllium and tungsten. Bonding techniques for armour tiles include brazing, diffusion bonding and plasma spray coating.

Thermal conductivity is an especially critical property because the armour tiles must be sufficiently thick to withstand erosion from sputtering and repeated plasma disruptions, as well as protect the heat sink from runaway electrons. Figure 2 shows 1-D ABAQUS [26] finite element results for the maximum tile thickness at a heat flux of 15 MW/m^2, assuming an allowed (steady state) surface temperature of 1100°C for carbon and tungsten, and 900°C for beryllium. A large range of thicknesses is evident, from 2.0 mm for tungsten brazed to niobium, to 20 mm for CAPG brazed to copper.

3.1. Thermohydraulics

High velocity, highly subcooled water is the preferred coolant for high heat flux components because it provides a larger heat transfer coefficient than either helium gas or liquid metals [27–29]. The efficiency of heat transfer is increased by allowing subcooled nucleate boiling, which occurs at fluxes greater than about 10 MW/m^2. In this regime, no net water vapour is generated because the microbubbles collapse in the subcooled bulk fluid, thereby creating a highly turbulent boundary layer which enhances heat transfer. Figure 3 traces the heat transfer performance of the different flow regimes. The abscissa represents the difference between the temperature of the heated wall and the bulk or average temperature of the fluid, while the ordinate represents the heat flux supported

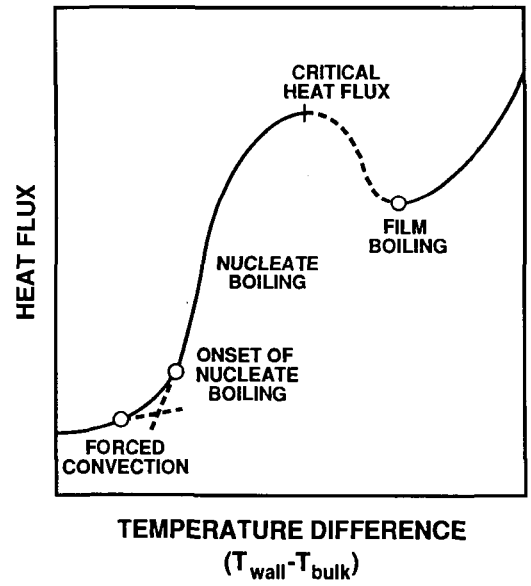

FIG. 3. Schematic representation of the different heat transfer regimes that exist in a water cooled element. Plotted is the heat flux into the water versus the temperature difference between the inner wall of the channel and the bulk average of the water.

by that temperature difference. For the lower left part of the curve, heat transfer with fully developed turbulent flow can be predicted with the well known Dittus-Boelter [30] or Colburn [31] correlations. Corrections to these correlations for heat fluxes primarily on one side of the cooling channel have also been reported [32]. As the wall temperature and thus $T_w - T_b$ is increased, the liquid near the wall exceeds its saturation temperature and, if wall surface conditions permit, vapour bubbles are nucleated at the wall. Because the average fluid temperature T_b is still below the saturation temperature, the bubbles which are formed at the wall collapse after mixing with the cooler fluid at the centre of the channel. One effect of this bubble nucleation, mixing and collapse is a significant increase in the heat flux which can be passed to the liquid.

Correlations predicting the onset of nucleate boiling for water in simple geometries are available [33], but effects such as wall surface conditions and dissolved gases in the water can affect the accuracy of the predictions. Correlations predicting the heat fluxes supported in this region of highly subcooled flow boiling are sparse [34, 35] for the geometries of interest in fusion power applications.

As the wall temperatures continue to rise, nucleate boiling activity continues to increase. If the heat flux at the cooling channel wall is too high, the mixing of the bubbles with the central core of even a highly subcooled fluid is not rapid enough and vapour accumulates on the wall. If the vapour, with its poorer heat transfer properties, blankets a significant portion of the wall, heat transfer is significantly reduced and a phenomenon known as critical heat flux (CHF) occurs; in this case the wall temperatures must be substantially increased to maintain the previously supported heat flux through the vapour blanket. If this temperature rise is sufficient to melt the thin walled tube, then 'burnout' and failure can occur at the location of CHF. Prediction of this phenomenon, represented as the peak heat flux in Fig. 3, has been the subject of considerable research.

At the upper right of the curve in Fig. 3 the steady state film boiling regime is entered. Here a blanket of vapour at the cooling channel wall passes the heat flux to a central core of liquid. Because of the extremely high wall temperatures required, this mode of operation is generally avoided. The relative simplicity of film boiling compared to nucleate boiling does permit a more complete analysis of this flow regime [36].

2-D and 3-D finite element computer codes have been used to model the heat transfer in high heat flux components [13]. However, numerical instabilities are often encountered when working in the boiling regime. Some finite element codes have been modified to permit calculation of the non-linear boiling film coefficient in a self-consistent manner with stable solutions. These codes predict that internal heat flux magnification can be as high as 1.8 for circular cooling channels because of geometric focusing. On the other hand, use of copper internal fins can reduce the internal heat flux by as much as 50% because of the extended area in contact with the water.

A significant number of correlations have been used to predict CHF limits for uniform heating, including: Tong (W-2), Gunther, Gambill, Katto, Bowring, Knoebel, Macbeth, Griffel and Weisman [37]. These correlations agree only within a factor of ten because they require extrapolations to conditions (one-sided heating, high subcooling, etc.) outside the range of experimental data. Nevertheless, good agreement has been found with the Tong correlation for electron beam (one-sided) test data [38]. Using a twisted tape insert can increase the CHF limit by a factor of 1.8, to 60 MW/m^2 at 10 m/s with a 10 mm diameter tube. More experiments are needed to study the effects of heated length, inlet temperature, velocity, pressure, internal fins, porous coatings and twist ratio.

3.2. Thermal stress and fatigue

The thermal stresses that develop when materials are exposed to high, steady state heat fluxes are very severe loads. Temperature gradients during the steady state removal of a heat flux of 10 MW/m^2 range from approximately 25°C per millimetre for copper to values of $>$ 500°C per millimetre for stainless steel. If the component has constraints that resist the expansion of the heated area, then thermal stresses will develop, with the stresses during the heating cycle being compressive in the near surface region and tensile in the bulk region [39].

A figure of merit describing the stress response of a material to an incident steady state heat flux can be derived in a straightforward manner. Since the temperature gradient produces the thermal stress, the first step will be to develop a relationship for the temperature profile during surface heating which can be derived from Fourier's law of heat conduction [40]. For the case of a steady state solution with an applied constraint that allows expansion but no bending, the stress profile will be linear, passing through zero near the centre. If the thermal stress is now set equal to the yield strength σ_y of the material and the equation is

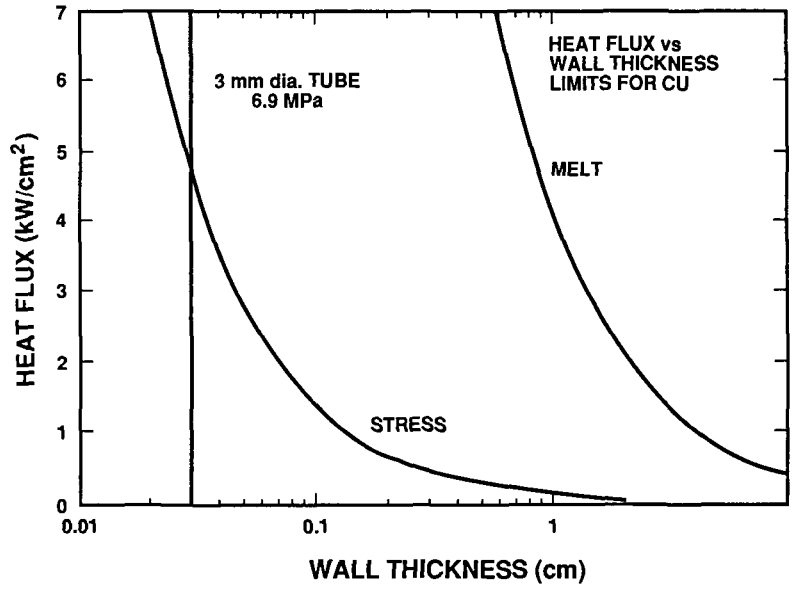

FIG. 4. Plot of the calculated surface thermal stress limit for copper. Also shown is the surface melting limit and the minimum tube thickness required for 6.9 MPa coolant pressure.

then solved for F (the incident heat flux), the thermal stress heat flux limit is derived:

$$F_0^{stress} = 2\sigma_y (1 - \nu)k/d\alpha E \quad (1)$$

where α is the coefficient of thermal expansion, E is Young's modulus, ν is Poisson's ratio, k is the thermal conductivity, d is the thickness and σ_y is the yield strength. This limit is plotted as a function of d for copper in Fig. 4. For copper, this maximum stress limit for a 1 cm thick structure corresponds to a heat flux of less than 10 MW/m^2. The limits for a large number of different materials are compared in Fig. 5. The values for the copper alloys are high owing to their high thermal conductivities and relatively high strengths, while the high value for graphite is due to its high strength and low thermal expansion. The low value for stainless steel is due mainly to its very low thermal conductivity.

If the heat flux limit given by Eq. (1) is not exceeded, then the component deformation from the heat pulse will be primarily elastic. The fatigue resistance of most materials under these conditions is adequate and will probably not be life limiting. It is quite common, however, for high heat flux components to be designed to operate under conditions that cause the thermal stress limit to be exceeded. In such a case, a portion of the surface of the material will be plastically deformed by thermal cycling. As an example, a finite element calculation for a beryllium limiter exposed to a surface heat flux of 2.5 MW/m^2 for a pulse length of 15 s is shown in Fig. 6. Note that a purely elastic analysis predicts surface stresses well in excess of the material's yield strength. Since the yield strength is temperature dependent, it decreases in the near surface region where the temperature is rapidly increasing. The zone of plastic deformation extends to a depth of about 2–3 cm. The plastic deformation that

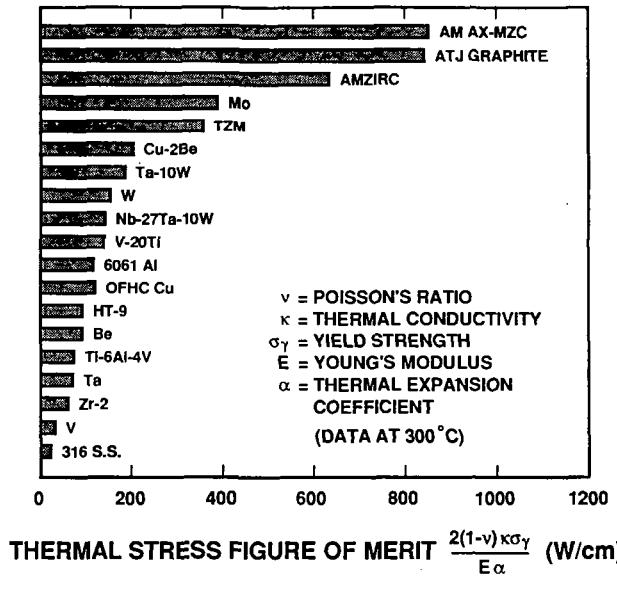

FIG. 5. Comparison of the calculated surface thermal stress limits for a number of materials.

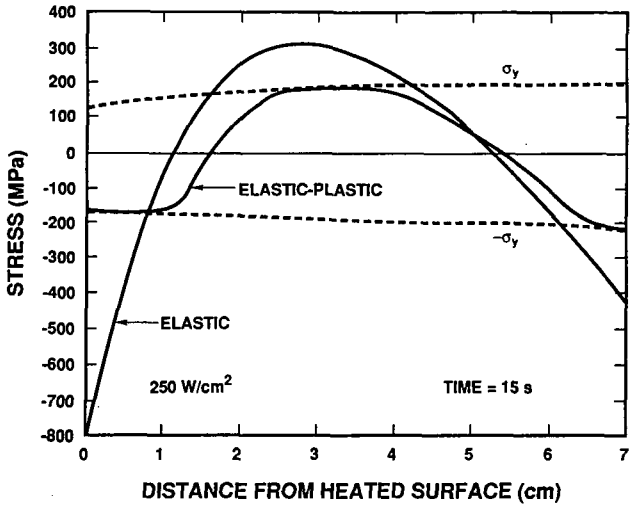

FIG. 6. Finite element calculation of the thermal stress profile generated in a 7 cm thick beryllium tile exposed to a heat flux of 2.5 MW/m². Both the purely elastic and the elastic-plastic analysis are shown.

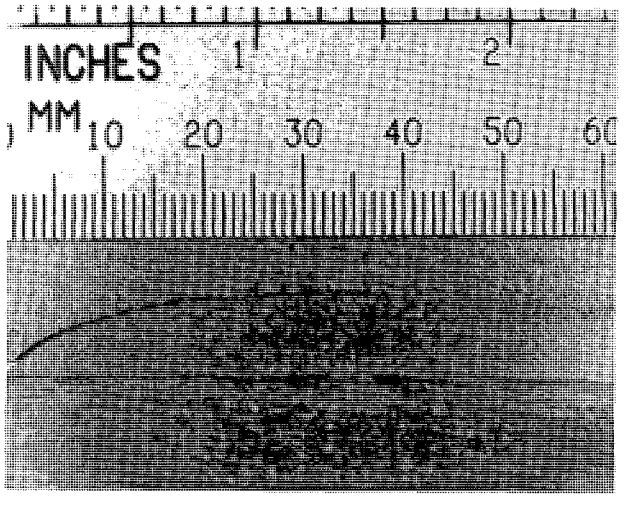

FIG. 7. Braze joint between a pyrolytic graphite tile and OFHC copper. Note the large crack in the graphite that initiated at the free edge during furnace cool-down due to residual braze stresses.

occurred during the heating phase leads to a residual tensile stress in the surface region during cooling. This complex stress/strain history is one reason why extensive thermal testing of a component subjected to repeated thermal loading will be required before lifetimes can be reliably predicted.

Residual braze stresses can fracture graphite tiles that are brazed to metal substrates because of the large mismatch in the coefficient of thermal expansion [41, 42]. Figure 7 shows examples of fractured graphite to metal braze joints. The fracture almost always initiates at the interface near the free edge corner where a stress singularity exists [43]. A variety of techniques can reduce these stresses. One approach is to choose substrate metals which have a low yield strength, such as annealed OFHC copper, so that the stress singularity is bounded. Another method is to use long hold times during the furnace cooldown to allow the substrate to creep and relax out residual stresses. Metal substrates with high yield strengths and high creep resistance (Inconel, molybdenum, copper alloys, etc.) often crack brazed graphite tiles.

Soft, pliable interlayers, such as plasma sprayed OFHC copper and copper felt/metal meshes, have successfully been used to braze pyrolytic graphite to high strength copper alloys. Heat transfer through the felt/metal mesh is limited because of its porosity. Carbon fibre reinforced copper matrix composite interlayers have been used [44], and wrapping copper tubes with either tungsten or carbon fibres is another method being studied. Stress analyses have shown that reducing the angle between the free edge and the interface to less than 70° eliminates the stress singularity for ceramic/metal joints [45]. Slots machined in the soft copper interlayer leave thin connecting webs that can also deform and reduce the stress concentration. Graded plasma sprayed coatings have been successfully used to make thick coatings, such as SiC and aluminium [46].

High heat flux testing of beryllium tiles and OFHC copper heat sinks demonstrated that very long fatigue

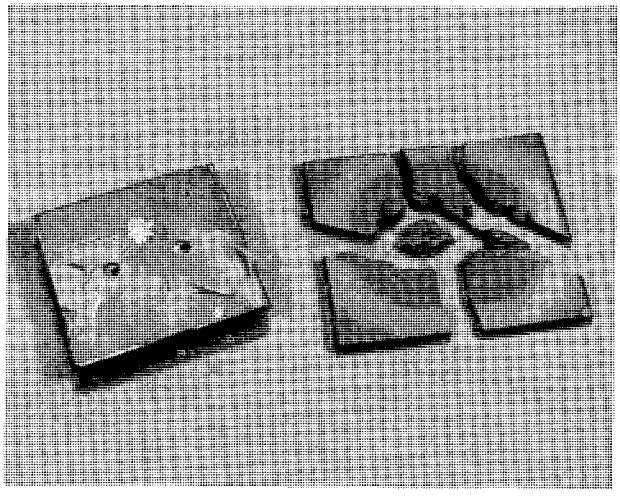

FIG. 8. Example of a thermal stress fracture in a sample of graphite brazed onto Inconel, after exposure to a heat flux of 0.5 MW/m² for 3.5 s.

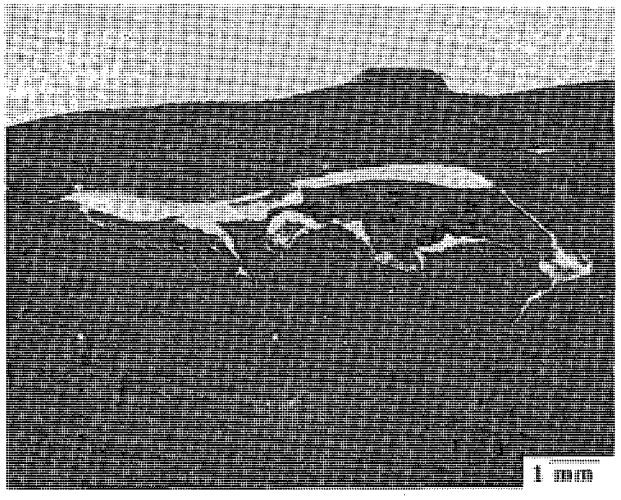

FIG. 9. Dramatic cyclic fatigue failure in a sample of vanadium explosively bonded to copper, exposed to a heat flux of 20 MW/m^2 for 1.5 s for a total of 1000 cycles.

lifetimes can be achieved even at heat fluxes that cause elastic stresses which exceed the yield stress, because the cyclic plastic strains were small (< 1%) [47]. An OFHC copper neutral beam dump was operated at 50 MW/m^2 for over 25 000 cycles with 5 s pulses without a water leak [48]. Another OFHC beam dump was operated at 40 MW/m^2 for 10 000 cycles with 20 s pulses without failure [49]. Slotting of the plasma facing surface has been successfully used on both the ISX-B and the JET beryllium limiter tiles to delay the initiation of thermal fatigue cracking. High cycle fatigue tests are needed for the less ductile metals such as molybdenum alloys.

The thermomechanical performance of duplex structures with brazed tiles depends on both the quality of the braze bond and the degree of mismatch in the coefficient of thermal expansion (CTE). Thermal stresses are superimposed on the residual braze stresses and can exceed the ultimate strength of brittle materials. Figure 8 shows the remains of a D-III armour tile, consisting of a 2 cm thick POCO AXF-5Q graphite tile brazed to a 2 cm thick Inconel substrate with a thin molybdenum interlayer after an explosive thermal stress fracture at a heat flux of 0.5 MW/m^2 applied for 3.5 s [50]. In this case, however, the graphite is still well bonded to the substrate. High heat flux testing of a 5 mm thick tungsten tile at 20–30 MW/m^2 for 1 s pulses caused interface fracture and tile melting after only 360 cycles [51]. In another test, a 2 mm thick plasma sprayed tungsten coating on a copper–beryllium alloy tested at 2.5 MW/m^2 for 20 s pulses fractured after 5000 cycles [52, 53].

A poorly studied but perhaps important thermal fatigue issue for future devices could be the effects due to the joining of dissimilar metals. Under some thermal cycling conditions, an unstable thermal ratcheting could be encountered which would lead to a very early component failure. An example of a vanadium/copper system exhibiting this behaviour is shown in Fig. 9, where the mismatch in thermal expansion and strength of the two materials, coupled with the cyclic high heat flux applied, lead to a dramatic, early failure of the composite structure [54]. Careful analysis and extensive testing must be done on all components of this type proposed for future devices.

4. DISRUPTIONS AND RUNAWAY ELECTRONS

Tokamak disruptions are plasma instabilities which result in rapid loss of confinement and termination of plasma current (for an additional discussion of this subject, see Ref. [55]). They cause high heat loads and electromechanical shocks to the plasma facing components. Among the known causes of disruptions are plasma densities that are too high, excessive plasma current (low q), excess plasma pressure (beta limit), transition phases (turn on of neutral beam, etc.), impurity buildup, strong ELMs and control circuit instability. In present tokamaks, about 25% of all discharges terminate in disruptions.

The type of disruption which has been studied most is that due to operating near the density limit. These disruptions may be characterized by four phases:

(1) *Pre-precursor:* A slow shrinking of the current channel, accompanied by increased radiation which approaches or exceeds the power input level (duration < 1 s). This phase is not always seen.

(2) *Precursor:* MHD precursors are seen before many, but not all, disruptions (duration ~ 100 ms, mostly the (m,n) = (2,1) or (1,1) modes). The mode rotation is often damped by interaction with vacuum vessel currents and, shortly after it locks, the energy quench occurs. The nature of this phase seems to be a strong function of the type of machine.

(3) *Energy quench:* In a short time (about 1 ms), much of the plasma thermal energy (approximately 80%) is lost to the PFCs. The mechanisms for this rapid dissipation are not well understood. There is usually a small displacement of the plasma, but the particle loss does not seem to match the energy loss.

(4) *Current quench:* Following the energy quench, the plasma current rises momentarily owing to a current redistribution and a reduction of the internal inductance, and then decays at a rate that varies both with the machine considered and from shot to shot. The time varies from 5 ms to 100 ms, and during this period the plasma magnetic energy is deposited on the walls or transferred to runaway electrons which ultimately deposit it on or in the walls.

Present attempts at disruption control (aside from restricting the operating range of the discharge) seem to be centred on trying to sense and cancel the MHD precursors that are often present before the disruption.

Runaway electrons can be generated in a tokamak at startup, during normal operation and during a plasma disruption. Proper selection of the current ramp-up rate and gas fill rate at the start, and maintenance of a low loop voltage during normal operation can limit the number and energy of runaways generated at those times to low values which can usually be tolerated in a tokamak. Disruption generated runaways, on the other hand, can attain both high energy and large number densities; thus they can damage vessel walls or PFCs [21–23, 56].

Runaway electrons are generated during a disruption as follows. At the start of a disruption there is a rapid cooling of the plasma. During this period there is a redistribution of current in the plasma which usually flattens the profile and reduces the plasma internal inductance. This leads to a slight increase in current [57] and a short lived negtive spike in the external loop voltage. The drop in temperature causes the plasma resistance to rise; the plasma loop voltage, which is the current times the resistance, also rises to high values (up to kilovolts) from its normal value of less than one volt. This causes the current to fall, and the collapsing poloidal magnetic field inductively sustains the high loop voltage. The collisional friction forces acting on an electron vary as $1/\text{energy}^{3/2}$; therefore, electrons in the tail of the velocity distribution which are above a critical velocity can accelerate to higher energies in the electric field direction [58]. An electron circling the machine gains energy approximately equal to the loop voltage during each cycle and speeds up very quickly.

Once an electron has started this process, the only things that limit its acquiring even more energy are radiation by the electron, which removes energy at higher rates as the electron energy increases, impact with a solid barrier as its orbit changes, or some instability or resonant interaction which increases its energy perpendicular to the magnetic field to the point where it can be trapped in a magnetic well. If a sufficient number of electrons run away, the high energy, low resistance portion of the current can approach the total current, and the loop voltage will fall as the current stabilizes at a plateau which is some fraction of its initial value. This effect can also limit the maximum attainable energy of an electron.

The thermal energy deposited during either plasma disruptions or runaway electron events can cause melting and/or vaporization of the surface and, in addition, can introduce thermal stress cracks. For metals, thermal fatigue effects are not expected to be as important as the material loss by vaporization and possibly by melting. For ceramics and other brittle materials such as graphite, cracking and spalling are serious concerns and adequate testing is required to characterize the material response to this load. Measurements indicate that typical disruption conditions are an energy deposition of 5–10 MJ/m^2 in times of 0.1–1.0 ms. While the amount of material lost by evaporation can be estimated using relatively simple models, more recent calculations have been performed which carry out a detailed energy balance including surface cooling by evaporation and radiation. These computer codes solve this problem of two moving boundaries (i.e. the liquid–vapour interface and the solid–liquid interface) and predict the surface temperature rise, the melt layer depth and the amount of material lost by vaporization [59, 60]. The actual heat flux delivered when evaporation is occurring will usually not be a simple function of the plasma power incident on the surface but will be reduced by the shielding that occurs when a vapour cloud forms [61]. Measurements of vaporization and melting also show that convective mixing in the melt plays a major role in determining the melt layer thickness and the amount of vaporization [60, 62].

One area of uncertainty in these calculations is the stability of the melt layer. As can be seen from the results in Fig. 10, the depth of melted material resulting from a single disruption can be quite large. If the melt layer resolidifies without significant movement, then the problem of material loss from disruption heat loads seems manageable. If, however, the molten material is redistributed by the eddy current forces before it solidifies, then the use of most metals is questionable unless the expected disruption frequency can be significantly reduced.

The thermal effects from runaway electrons are more severe even though the affected area is much smaller. The energy densities deposited by runaway electrons have been estimated to be as high as

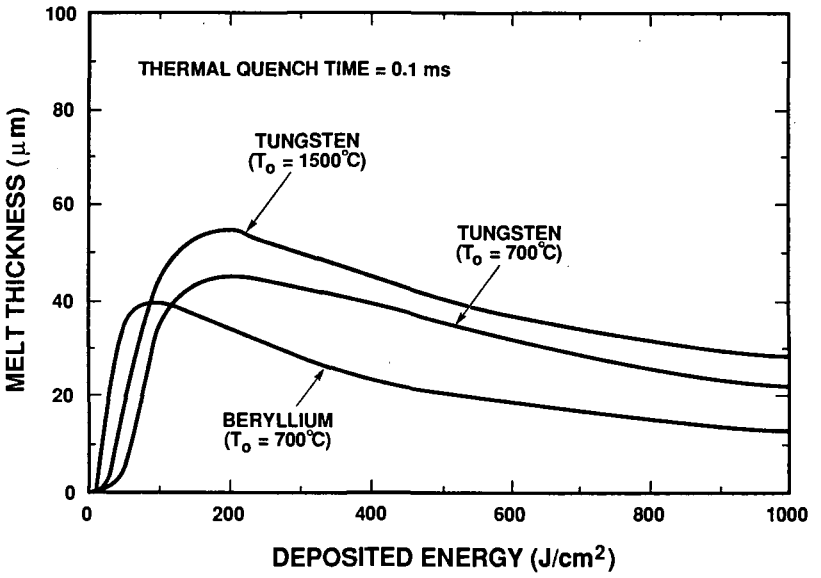

FIG. 10. Calculated values of the depth of material melted as a function of energy deposited during a 0.1 ms plasma disruption.

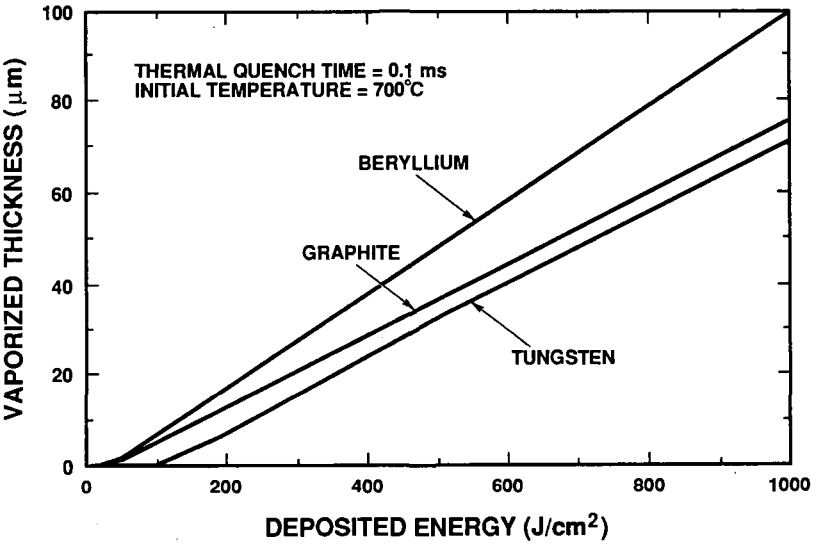

FIG. 11. Calculated amounts of total material vaporized as a function of energy deposited during a 0.1 ms plasma disruption.

80 MJ/cm^2 over areas of a few square centimetres [63]. Energy densities of this magnitude will cause severe melting and vaporization in all metals and can lead to surface spallation. Graphite is more capable of withstanding these events and, if discharges containing significant runaways cannot be avoided, then it may be necessary to povide a graphite armour for those regions where runaways could strike, even if the rest of the interior is covered with metal surfaces.

Figure 11 shows the calculated vaporization for carbon, beryllium and tungsten from a plasma disruption thermal quench on the divertor [38]. Threshold damage energies are 1–3 MJ/m^2 for short pulses. Carbon vaporizes less than tungsten, and tungsten vaporization is lower than beryllium vaporization, with the amount vaporized not very sensitive to the deposition time over the range 0.1–3 ms. Large differences exist between theory and measurements.

In simulation experiments using both laser and electron beam irradiations it was found that the measured weight losses for carbon exceed the calculated values by factors of 3–6, possibly owing to cluster emission of carbon particles [64, 65]. In this case, with 10 MJ/m^2 and 0.1 ms deposition, the erosion would increase to 0.5 mm per disruption. Conversely, theoretical models of vapour shielding predict a reduction in the absorbed heat flux by factors of 2–10 (which agree well with some experiments [66]). In a third experiment with longer pulse lengths (200–500 ms) it was found that the measured weight loss agreed very closely with predictions, without having to rely on any vapour shielding effect [67]. Remember that, in all calculations, convective mixing was not included and that its inclusion could be expected to alter the relative rankings.

For beryllium and tungsten, the melting thicknesses depend strongly on the deposition time, but not so much on energy above 10 MJ/m^2. In Fig. 10, the 1-D calculation shows that tungsten has twice the melt layer thickness of beryllium, despite its high melting point. At 12 MJ/m^2 and 3.0 ms pulse length, the tungsten melt layer is 0.02 mm thick. At higher energies, the melt layer thickness decreases as more energy goes into sublimation. If the melt layer is lost because of surface instabilities, plasma 'wind' or electromagnetic forces, then the total disruption erosion is nominally the same for beryllium and tungsten since beryllium vaporizes roughly 40% more material than tungsten.

Runaway electrons generated during the current quench phase (20–200 ms) of a disruption in tokamaks have been observed to cause severe damage to PFCs, including melting, sublimation and fractures [56]. For ITER, the maximum electron energy was calculated to be 35–120 MeV with a flux of 100 MJ/m^2, which is sufficient to penetrate deep into the structure [13]. 1-D and 2-D Monte Carlo codes have been used to predict the energy deposition in multilayered structures [55, 68]. The energy threshold needed to damage the heat sink is roughly 20 MJ/m^2 for copper with 10 mm of carbon armour, at a 5° angle of incidence. The damage thresholds are correspondingly higher for materials with higher melting points such as molybdenum and niobium. The use of tungsten as a plasma facing material can provide substantial protection to the water cooled heat sink against runaway electrons. With carbon or beryllium it is difficult to envision how high heat flux components will survive the high energy runaway electrons that are predicted for ITER.

5. NEUTRON IRRADIATION EFFECTS

All plasma interactive components will be subjected to high energy neutron irradiation. The material property changes induced by this environment are similar to those encountered by other structural materials and have been discussed in detail in Ref. [69]. Briefly, the property changes believed to be most critical and potentially life limiting are reductions in thermal conductivity, void swelling and embrittlement. Graphite has been observed to have a significant reduction in thermal shock resistance after neutron irradiation in studies for fission [70]. Beryllium may be particularly susceptible to swelling due to the Be(n, 2n)^{2}He reaction producing large quantities of helium. The refractory metals such as tungsten and molybdenum generally experience increases in their ductile to brittle transition temperatures, which limits their lifetimes. A further complication for plasma interactive components is the use of designs that consist of two materials joined intimately by brazing or other bonding techniques. In these cases, small differences in their response to neutron irradiation could lead to severe problems if, for example, their neutron induced swelling thresholds occur at different fluences. It seems to be particularly imperative that all composite structures be thoroughly tested before installation to identify and avoid these types of problems.

6. TEST FACILITIES

Because of the critical nature of PFCs and the complex nature of the thermal stress response, it has been necessary to test the proposed materials and components in relevant high heat flux environments in various types of laboratory facilities. These devices are used to study 'normal heat load' conditions and 'off-normal' (disruption or runaway electron) conditions, and include electron beam sources, ion beam sources, lasers, plasma guns and radiant heaters. The list of operating high heat flux test facilities is quite long and is becoming longer (a few facilities are discussed in Refs [71–79]). Major facilities include electron beam systems in the USA (30 kW), Japan (200 kW), the EC (several at 30–60 kW, one under assembly at 200 kW) and the USSR (30 kW). Major neutral beam type ion sources exist in the USA (800 kW), Japan (6 MW) and the EC (5 MW and 2 MW). A large laser system (5 kW) is used by the

EC for disruption simulation, and plasma gun systems used in the USA (10 kJ) and the USSR (100 kJ) are being developed for disruption studies. High energy electron accelerators have been used to study runaway electron energy deposition in Japan, and high energy electrons generated by the ATF stellarator will be studied in the USA. Electron beam test facilities located in radiation hot cells are under construction in both the USA (30 kW) and the EC (30 kW); these will permit thermal shock testing of neutron irradiated plasma facing components and materials. Neutron irradiation studies are being performed in fission reactors in the USA (HFIR, FFTF) and the EC (Petten). In addition, numerous fabrication development laboratories and physical property measurement laboratories are in use worldwide.

As a group, these facilities cover an extremely wide range of operating conditions and have been used extensively to qualify materials and components for fusion. This area is one where international collaboration has been quite active and has allowed the sharing of unique resources.

7. SUMMARY

The restrictions placed on the plasma facing materials by the physics of the plasma, the harsh environment that exists in the plasma edge and the complex nature of the components all combine to make the thermal response of these structures to pulse heating one of the major issues to be addressed in future devices. Further experiments to understand and build the relevant databases for issues such as critical heat flux and thermal fatigue must continue, and models must be developed and benchmarked. Further studies to characterize the plasma edge and especially the edge power flow in operating devices must be emphasized and models for extrapolation to next generation devices developed. The characterization of disruptions and subsequent runaway electron generation is a critical issue, since these events could be life limiting for ITER and beyond. Further laboratory studies to determine the response of materials to these events must continue. Finally, new materials and fabrication methods must be explored and tested to identify the optimum design for future devices.

For tokamak designers, these thermal issues are often the lifetime limiting issues. Unfortunately, the uncertainties in the plasma edge conditions and disruption conditions make it very difficult to design components capable of high performance over all conceivable operating parameters. In addition, safety issues related to toxic and/or radioactive dust (such as beryllium, graphite or activated tungsten) further restrict the operating limits of the device. The one issue that will not change is that high performance, reliable and maintainable PFCs must be developed for fusion to be taken to a power reactor phase.

ACKNOWLEDGEMENT

This work was supported by the United States Department of Energy under Contract No. DE-AC04-76DP00789.

REFERENCES

[1] SMITH, D.L., J. Nucl. Mater. **103&104** (1981) 19.
[2] NYGREN, R.E., J. Nucl. Mater. **103&104** (1981) 31.
[3] BEHRISCH, R., J. Nucl. Mater. **85&86** (1979) 1047.
[4] US FED-INTOR Activity and US Contribution to the International Tokamak Reactor Phase-2A Workshop: Critical Issues, Vols 1 and 2, USA FED-INTOR/82-1 (Oct. 1982).
[5] MATTAS, R.F., SMITH, D.L., ABDOU, M.A., J. Nucl. Mater. **122&123** (1984) 66.
[6] CARROLL, M.C., Technical Assessment of Plasma-Interactive Options for Claddings and Attachments for Steady State, Rep. PPG-1085 UCLA-ENG-87-26, School of Engineering and Applied Science, California Univ., Los Angeles (1986).
[7] CONN, R.W., J. Nucl. Mater. **103&104** (1981) 7.
[8] GAUSTER, W.B., KOSKI, J.A., WATSON, R.D., J. Nucl. Mater. **122&123** (1984) 80.
[9] WHITLEY, J.B., J. Nucl. Mater. **133&134** (1985) 39.
[10] TAKATSU, H., ANDO, T., YAMAMOTO, M., et al., J. Nucl. Mater. **155–157** (1988) 27.
[11] MIYAHARA, A., TANABE, T., J. Nucl. Mater. **155–157** (1988) 49.
[12] WHITLEY, J.B., WILSON, K.L., BUCHENAUER, D.A., J. Nucl. Mater. **155–157** (1988) 82.
[13] WATSON, R.D. (Ed.), ITER Divertor Engineering Design, ITER Rep. TN-PC-8-9-1, Max-Planck-Institut für Plasmaphysik, Garching (1989).
[14] HOSEA, J.C., GOLDSTON, R.J., COLESTOCK, P.L., Nucl. Fusion **25** (1985) 1155.
[15] DYLLA, H.F., ULRICKSON, M., BELL, M.G., et al., J. Nucl. Mater. **162–164** (1989) 128.
[16] WAMPLER, W.R., DOYLE, B.L., J. Nucl. Mater. **162–164** (1989) 1025.
[17] REBUT, P.H., DIETZ, K.J., LALLIA, P.P., J. Nucl. Mater. **162–164** (1989) 172.
[18] EHRENBERG, J., J. Nucl. Mater. **162–164** (1989) 63.
[19] DIETZ, K.J., PICK, M.A., PEACOCK, A.T., et al., in Fusion Engineering (Proc. 13th Symp. Knoxville, TN, 1989), IEEE, New York (1990) 512.
[20] JT-60 Team, presented by HOSOGANE, N., J. Nucl. Mater. **162–164** (1989) 93.

[21] DIETZ, K.J., J. Nucl. Mater. **155–157** (1988) 8.
[22] DYLLA, H.F., ULRICKSON, M.A., OWENS, D.K., et al., J. Nucl. Mater. **155–157** (1988) 15.
[23] YAMASHINA, T., GAUSTER, W.B. (Eds), High Heat Flux (Proc. Japan–US Workshop P134, 1989), Hokkaido University (1989). See also other proceedings from this series.
[24] Papers in J. Nucl. Mater. **162–164** (1989) and other Plasma–Surface Interaction Conferences.
[25] McGRATH, R.T., Thermal Loads on Tokamak Plasma Facing Components During Normal Operation and Disruptions, Rep. SAND89-2064, Sandia National Laboratories, Albuquerque, NM (1990).
[26] ABAQUS, Users Manual, Version 4.6, May 1987, Hibbit, Karlsson and Sorensen, Inc., Providence, RI (1987).
[27] BOYD, R.D., Fus. Technol. **7** (1985) 7.
[28] GAMBIL, W.R., BUDNY, R.D., WANSBROUGH, R.W., J. Chem. Eng. Prog. **57** 32 (1961) 127.
[29] BOYD, R.D., WONG, C.P.C., CHA, Y.S., Technical Assessment of Thermal-Hydraulics for High Heat Flux Fusion Components, Rep. SAND84-0159, Sandia National Laboratories, Albuquerque, NM (1985).
[30] DITTUS, F.W., BOELTER, L.M.K., Heat Transfer in Automobile Radiators of the Tubular Type, Univ. of Calif. Publ. Eng. **2** (1930) 443.
[31] COLBURN, A.P., Trans. Am. Inst. Chem. Eng. **29** (1933) 174.
[32] KAYS, W.M., Convective Heat and Mass Transfer, McGraw-Hill, New York (1966) 174.
[33] BERGLES, A.E., ROHSENOW, W.M., "The determination of forced convection surface boiling heat transfer," Paper 63-HT-22, presented at 6th National Heat Transfer Conference of ASME/AIChE, Boston, 11–14 Aug. 1963.
[34] JENS, W.H., LOTTES, P.A., Analysis of Heat Transfer Burnout, Pressure Drop and Density Data for High Pressure Water, Rep. ANL-4624, Argonne National Laboratory, Argonne, IL (1951).
[35] THOM, J.R.S., WALKER, W.M., FALLON, T.A., REISING, G.F.S., "Boiling in sub-cooled water during flow up heated tubes or annuli", Paper No. 6, Presented at Symp. on Boiling Heat Transfer in Steam Generating Units and Heat Exchangers, Manchester, 15–16 Sep. 1965, Institute of Mechanical Engineers, London.
[36] BERENSON, P.J., ASME J. Heat Transfer **83** (1951) 351.
[37] KOSKI, J.A., BEATTIE, A.G., WHITLEY, J.B., CROESSMANN, C.D., Experimental Verification of Subcooled Flow Boiling for Tokamak Pump Limiter Designs, ASME Rep. No. 87-HT-45, American Society of Mechanical Engineers, New York, NY (1987).
[38] SMITH, D., WATSON, R.D., US Contribution to the ITER Plasma Facing Components Engineering Homework Task, Rep. TN-PC-1-9-U-1, Max-Planck-Institut für Plasmaphysik, Garching (1989).
[39] SCHIVELL, J.F., GROVE, D.J., J. Nucl. Mater. **53** (1974) 107.
[40] CHAPMAN, A.J., Heat Transfer, MacMillan, New York (1984).
[41] DALGLEISH, B.J., LU, M.C., EVANS, A.G., J. Acta Metall. **36** 8 (1988) 2029.
[42] BLANCHARD, J.P., WATSON, R.D., Nucl. Eng. Des./Fusion **4** (1986) 61.
[43] BLANCHARD, J.P., GHONIEM, N.M., J. Thermal Stresses **12** (1989) 501.
[44] GOTOH, Y., OKAMURA, H., ITOH, S., et al., Fusion Eng. Des. **9** (1989) 295.
[45] IANCU, O.T., J. Comput. Struct. **33** 3 (1989) 873.
[46] SMITH, M.F., WHITLEY, J.B., McDONALD, J.M., J. Thin Film Solids **118** (1984) 23.
[47] WATSON, R.D., WHITLEY, J.B., Nucl. Eng. Des./Fusion **4** (1986) 49.
[48] MILORA, S.L., COMBS, S.K., FOSTER, C.A., Nucl. Eng. Des./Fusion **3** (1986) 301.
[49] WHITLEY, J.B., MULLENDORE, A.W., WATSON, R.D., et al., J. Nucl. Mater. **111&112** (1982) 866.
[50] WATKINS, J.G., WHITLEY, J.B., LUTZ, T.L., McDONALD, J.M., J. Fusion Eng. Des. **9** (1989) 225.
[51] SEKI, M., in Proc. US-Japan Workshop 111-112, La Jolla, CA, 1990, Rep. SAND90-1478C, Sandia National Laboratories, Albuquerque, NM (1990).
[52] SEKI, M., OGAWA, M., MINATO, A., et al., J. Fusion Eng. Des. **5** (1987) 205.
[53] OGAWA, M., SEKI, M., FUKAYA, K., et al., J. Fusion Eng. Des. **9** (1989) 227.
[54] MULLENDORE, A.W., WHITLEY, J.B., MATTOX, D.M., Thin Solid Films **83** (1981) 79.
[55] BOLT, H., MIYAHARA, A., Runaway-Electron-Materials Interaction Studies, Rep. NIFS-TECH-1, ISSN 0915-6356, National Institute for Fusion Science, Nagoya (1990).
[56] HOVEN, H., KOIZLIK, K., LINKE, J., NICKEL, H., WALLURA, E., KOHLHAAS, W., J. Nucl. Mater. **162–164** (1989) 970.
[57] WESSON, J.A., GILL, R.D., HUGON, M., et al., Nucl. Fusion **29** (1989) 641.
[58] COHEN, R.H., Phys. Fluids **19** (1976) 239.
[59] HASSANEIN, A.M., KULCINSKI, G.L., WOLFER, W.G., Nucl. Eng. Des./Fusion **1** (1984) 307.
[60] CROESSMANN, C.D., KULCINSKI, G.L., WHITLEY, J.B., J. Nucl. Mater. **128&129** (1984) 816.
[61] GILLIGAN, J., HAHN, D., MOHANTI, R., J. Nucl. Mater. **162–164** (1989) 957.
[62] SCHILLER, P., BROSSA, F., CAMBINI, M., QUATAERT, D., RIGON, G., Fusion Eng. Des. **6** (1988) 131.
[63] WHITLEY, J.B., KOSKI, J.A., AYMAR, R., in Fusion Technology (Proc. 14th Symp. Avignon, 1986), Pergamon Press, Oxford (1987) 627.
[64] BOLT, H., MIYAHARA, A., KURODA, T., et al., J. Fusion Eng. Des. **9** (1989) 33.
[65] VAN DER LAAN, J.G., J. Nucl. Mater. **162–164** (1989) 964.
[66] GILLIGAN, J., HAHN, D., MOHANTI, R., J. Nucl. Mater. **162–164** (1989) 957.
[67] CROESSMANN, C.D., KULCINSKI, G.L., WHITLEY, J.B., J. Nucl. Mater. **141–143** (1986) 108.
[68] NIEMER, K.A., CROESSMANN, C.D., GILLIGAN, J.G., BOLT, H.H., Modeling of Runaway Electron Damage for the Design of Tokamak Plasma Facing Components,

Rep. SAND89-2405, Sandia National Laboratories, Albuquerque, NM (1990).
[69] WHITLEY, J.B., WILSON, K.L., CLINARD, F.W. (Eds), J. Nucl. Mater. **122&123** (1984).
[70] SATO, S., KAWAMATA, K., KURUMADA, A., UGACHI, H., AWAJI, H., ISHIDA, R., J. Nucl. Sci. Technol. **24** (1987) 547.
[71] CROESSMANN, C.D., GILBERTSON, N.B., McDONALD, J.M., WHITLEY, J.B., Electron Beam Test System High Intensity/Short Pulse Mode, Rep. SAND86-2408, Sandia National Laboratories, Albuquerque, NM (1987).
[72] De CONINCK, R., SNYKERS, M., J. Nucl. Mater. **76&77** (1978) 629.
[73] SEKI, M., YAMAZAKI, S., MINATO, A., HORIE, T., TANAKA, Y., TONE, T., Fusion Eng. Des. **5** (1987) 215.
[74] RIGON, G., MORETTO, P., BROSSA, F., Fusion Eng. Des. **5** (1987) 299.
[75] NAKAMURA, K., YAMADA, R., SAIDOH, M., MURAKAMI, Y., J. Nucl. Mater. **111&112** (1982) 852.
[76] FUJITSUKA, M., SHIKAMA, T., YAMAUCHI, Y., SHINNO, H., OKADA, M., J. Nucl. Mater. **152** (1988) 163.
[77] VAN DER LAAN, J.G., J. Nucl. Mater. **162–164** (1989) 964.
[78] KOIZLIK, K., BOLT, H., HOVEN, H., LINKE, J., NICKEL, H., WALLURA, E., J. Nucl. Mater. **155–157** (1988) 398.
[79] YANAGI, H., SUKEGAWA, T., KOBAYASHI, K., MADARAME, H., HASHIZUME, H., MIYA, K., J. Nucl. Mater. **155–157** (1988) 402.

PLASMA-MATERIAL INTERACTION ISSUES IN FUSION REACTOR DESIGN AND STATUS OF THE DATABASE

R.K. JANEV
Division of Physical and Chemical Sciences,
International Atomic Energy Agency,
Vienna

A. MIYAHARA
National Institute for Fusion Science,
Nagoya, Japan

ABSTRACT. A general overview of the plasma-material interaction issues in fusion reactor design is presented. Emphasis is put on thoses processes of particle-surface interaction and high heat material response which play a critical role in the plasma performance and in reactor technology related design areas. The data status and needs for these processes are also briefly discussed.

1. INTRODUCTION

The programmatic objectives of next step fusion devices (ITER, NET, FER, OTR, etc.) are to demonstrate the scientific and technological feasibility of fusion and to provide an adequate physics and engineering database for the design of demonstration fusion reactors. These programmatic objectives translate into a set of basic technical objectives related to the reactor's plasma performance (high power multiplication factor Q, long pulse (or steady state) self-sustained burn), nuclear performance (neutron wall loads of around 1 MW/m^2 and fluences of ~ 1 $MW \cdot a/m^2$, provision for an extended nuclear technology testing programme), engineering integrity and long operation time (several thousand hours of operation over several calendar years), remote maintenance and safety. During the conceptual design, the technical objectives of the fusion device are translated into basic machine and plasma parameters, as well as performance specifications of the main device subsystems. Optimization of the operational domain in the parametric space of the ractor and the component performance specifications represents a complex iterative process in which a balance between many conflicting requirements must be found and in which the technical objectives are confronted with the existing knowledge and technological possibilities. A compromise is usually made through selecting the basic mission of the device, by reliable extrapolations of the existing physics knowledge and by accepting design flexibility to allow for incorporation of the expected results from ongoing research in the final engineering design phase. Such an approach has been adopted in the ITER Conceptual Design [1].

The attainment of long pulse ignited and high Q plasmas implies a high confinement capability of the device, which requires large plasma dimensions, high values of the plasma current (I) and magnetic field (B), and a reasonably large plasma elongation. The values of these parameters for the reference ITER design [2] are: major radius R = 6.0 m, minor radius a = 2.15 m, elongation $\kappa \simeq 2$, I $\simeq$ 22 MA, B = 4.85 T, with an edge safety factor of $q_\psi(95\%) \gtrsim 3.0$. Assuming that the energy confinement time (τ_E) scalings, derived from experience on existing large tokamaks, can be extrapolated to an ITER size machine, the confinement time obtained for ITER ($\tau_E \simeq$ 4–5 s) is sufficient for ignition of its plasma (with nominal average densities around 10^{20} m^{-3} and ion temperatures in the range of 10–20 keV). With an operating point sufficiently far from the disruptive density and beta limits (i.e. operating with $\langle n \rangle \simeq (0.7\text{–}1.5) \times 10^{20}$ m^{-3}, $\beta(\%) = gI/(aB)$, with $g \simeq 2.5$ and thus $\beta \simeq 5.3\%$), the nominal fusion power P_f of ITER is about 1 GW. The parametric space for stable operation allows ITER to operate with plasma currents of up to 25 MA and a Troyon factor $g \simeq 3$, which increases the attainable fusion power ($P_f \sim \beta^2$) to about 2 GW. The power and particle exhaust capabilities of the machine, however, limit the power output to about 1 GW.

Present reactor design work, based on the tokamak concept, faces a lack of firmly established databases in several design areas. As exemplified by the ITER conceptual design, these 'critical' areas [2–4] include: plasma performance (including confinement physics, plasma burn physics, operational limits), power and particle exhaust, characterization and control of disruptions, plasma heating, fuelling and burn control, and certain technological areas (magnets, plasma facing components and blanket). Because of the functional integrity of the device, most of the database problems in the above areas are interrelated. Thus, the plasma energy balance, impurity control, power and particle exhaust, tritium inventory and thermomechanical performance of plasma facing components are all connected through the effects of plasma–material interactions. In Section 2 we describe briefly the impact of these effects on the fusion reactor design. In Sections 3 and 4 we present the status of the databases for the underlying physical and thermomechanical processes.

2. PLASMA PERFORMANCE AND REACTOR TECHNOLOGY ISSUES RELATED TO PLASMA–MATERIAL INTERACTIONS

2.1. General considerations

The critical role that plasma–material interactions play in the achievement of the technical objectives of a reactor level fusion device can be understood from the fact that the effects of these interactions define the boundary conditions for both the plasma dynamics inside the torus and the thermal processes in the surrounding material structures. The plasma (particle)–surface interaction processes are a source of impurities in the plasma which through their powerful radiation become an essential factor in the plasma energy balance. The plasma–wall interaction processes, together with the gas phase atomic processes between plasma particles and released impurities, define the parameters of the boundary plasma (outside the separatrix, the last closed magnetic flux surface). The edge plasma, through its dynamical coupling with the main plasma (inside the separatrix), has a strong influence on the plasma transport processes and thereby on the gross energy confinement time [5]. Moreoever, the plasma edge conditions play an essential role in the transition from the low (L−) to the enhanced (H−) plasma confinement regime [6]. Furthermore, the most dangerous, disruptive plasma instabilities develop at the singular magnetic flux surfaces at the plasma periphery, where also most of the neoclassical and anomalous transport is generated [7]. Impurity radiation and hydrogen recycling in the plasma edge, together with the strong parallel (to the magnetic field lines) plasma flow in the scrape-off layer (SOL), are the major factors which determine the plasma parameters in this region.

On the other hand, the material plasma boundaries have to receive the entire thermal power and to conduct it to the background heat sink structures and coolants. The thermomechanical response of plasma facing components to plasma particle and heat fluxes defines not only the structural and functional integrity (lifetime) of these components but also the heat transport and heat extraction processes [8]. The surface heating and temperature gradients in the plasma facing materials define the initial conditions for the thermal stress behaviour of the components and their thermomechanical and thermohydrodynamic compatibility with the supporting structures and the coolants [8]. Plasma–material interactions have an impact on the reactor safety because of problems connected with the tritium inventory.

2.2. Impurity shielding

The most important effects of plasma–material interactions on the reactor performance are: impurity generation, erosion of plasma facing materials and thermal action on the plasma facing components. Impurities are generated by a number of processes induced by particle impact (physical sputtering, radiation enhanced sublimation, desorption, chemical erosion), by thermal processes (thermal sublimation, desorption, evaporation), as well as by electrical phenomena in the plasma–wall system, such as unipolar arching. Diffusion of impurities into the central plasma region may lead to intolerable radiation losses and prevent ignition. The most powerful radiation processes in the hot ($T \sim 15$–20 keV) central plasma region are line emission, bremsstrahlung and dielectronic recombination (if the impurity ion is not fully stripped). The radiative power losses due to these processes are proportional to q, q^2 and q^4, respectively, where q is the impurity ion charge, which for highly stripped ions is close to the atomic number Z. High-Z impurities ($Z \gtrsim 40$) can prevent ignition already at concentration levels of 10^{-5} to 10^{-4} of plasma density. By increasing the Z_{eff} parameter of the plasma, the high-Z impurities also introduce an effective dilution of fuel density and thus impair the fulfilment of the ignition criterion.

On the other hand, the impurities obey neoclassical transport dynamics and tend to accumulate in the central plasma region. All these properties lead to the preference of using low-Z plasma facing materials.

Minimization of impurity influxes from the walls is particularly important for long pulse (or steady state) operation regimes (because of the impurity accumulation effect), and efficient shielding of the plasma from impurities is an important design issue. An approach to this problem which is currently adopted in most tokamak reactor designs (including ITER, NET and FER) is the use of a poloidal divertor. Strong temperature gradients in the region outside the last closed magnetic flux surface divert the radially diffusing plasma into a rapid conductive longitudinal flow towards the divertor chamber, where it intercepts the divertor plates. The plasma particle and heat fluxes on the vessel wall are thereby significantly reduced. The parallel plasma flow in the scrape-off region also entrains the ionized wall impurities towards the divertor, thus providing a shield for the main plasma. However, the diverted particle and power fluxes striking the divertor plates induce very intense plasma-material interaction. Still, the divertor concept for impurity control is attractive since it localizes the problem. Moreover, this concept offers also a way for resolving the thermal power and particle exhaust problem.

The degree of aggravation of the plasma–material interaction conditions on divertor plates can be appreciated if one takes into account the magnitude of particle and thermal power fluxes, Γ_n and Γ_E, traversing the separatrix (for ITER: $\Gamma_n = 4 \times 10^{21}$ s^{-1}, $\Gamma_E =$ 117 MW [1, 9]) and the divertor plate area on which they are deposited. Because of the parallel plasma flow in the scrape-off region, the particle and power fluxes experience an exponential decay in the direction perpendicular to the magnetic field, characterized by the following decay lengths (see Ref. [10]):

$$\lambda_n = \left(\frac{D_a L}{C_s}\right)^{1/2}$$

$$\lambda_E = \left(\frac{\chi_a L}{\gamma_s C_s}\right)^{1/2} \qquad (1)$$

where D_a and χ_a ($\simeq 1.5$–$2\ D_a$) are respectively the cross-field plasma particle diffusion and heat conductivity coefficients, C_s is the ion acoustic velocity, L is the connection length and γ_s ($\simeq 7$–10) is a constant characterizing the amount of energy deposited on the divertor plate surface by each electron–ion pair. For ITER plasma parameters ($L \simeq 55.5$ m, $C_s \simeq 10^6$ m/s, $D_a \simeq 2$ m^2/s, $\chi_a \simeq 1$–4 m^2/s, $\gamma_s \simeq 8$), the predicted values of SOL widths are $\lambda_n \simeq 1$ cm and $\lambda_E \simeq$ 0.25–0.5 cm. (The adopted values for D_a and χ_a are extrapolations from experience on present large tokamaks.) The small values of λ_n and λ_E indicate that the fluxes flowing towards divertor plates will be deposited on relatively small areas, thus imposing severe requirements on the plate materials. The situation is somewhat eased because of the radiation losses taking place in the scrape-off and divertor regions and the hydrogen and impurity recycling in the divertor. Gas recycling in front of the divertor plates is particularly beneficial since it provides an intense plasma cooling mechanism by which the near-plate plasma temperature can be kept below the threshold for physical sputtering of most candidate materials ($T_e \lesssim 20$ eV). Additional gas puffing in the divertor can enhance the recycling. While reducing the energy of plasma particles impinging on the plates, the recycling process may greatly increase their flux on the plates (up to 4.4×10^{24} s^{-1} for ITER). This, however, has a positive consequence in that it increases the neutral particle density in the divertor and thus facilitates the gas pumping from the divertor. Other methods for reducing the particle and power loads on divertor plates rely on their delocalization, which can be achieved by magnetic sweeping of the separatrix and an increase of the width of the SOL by ergodization of the magnetic field near the separatrix (local enhancement of D_a and χ_a in Eqs (1)) and/or an increase of the connection length L. The increase of the separation between the X-point of the separatrix and the divertor plates, apart from increasing L (i.e. λ_n and λ_E), also reduces the probability of impurity penetration from the divertor into the main plasma region.

2.3. Erosion rates

Material erosion of plasma facing components is a serious design issue regarding not only plasma contamination but also the lifetime of these components. Excessive erosion rates may require frequent replacement of plasma facing components (particularly the divertor plates), which has an impact on the reactor engineering, the effective operation time and the cost. Under normal operating conditions, the main erosion mechanisms are physical sputtering, thermal sublimation, radiation enhanced sublimation (for carbon based materials only) and chemical sputtering (for materials chemically active with hydrogen, such as carbon based materials and metal oxides). During off-normal events,

such as plasma disruptions and runaway electrons, the main erosion mechanisms are evaporation and cluster emission.

The efficiency of the erosion mechanisms during normal reactor operation depends on the incident particle energy and the temperature of the material. Physical sputtering requires an energy threshold E_{th} which for low-Z materials bombarded by hydrogenic ions is below ~ 20 eV (for carbon, $E_{th} \simeq 10$ eV), for medium-Z material is 50–80 eV ($E_{th}(Fe) \simeq 64$ eV) and for high-Z materials is above 150 eV ($E_{th}(Mo) = 164$ eV, $E_{th}(W) \simeq 400$ eV) [11]. The sputtering yield in the threshold region is a very steep function of the impact energy, reaching rapidly its maximum value. Therefore, in view of impurity generation and erosion, it is important to keep the plasma temperature in front of the plasma facing components below the sputtering threshold. (The particle impact energy is determined by the sheath potential, $E \simeq 2\ T_i + 3.5\ q\ T_e$, where T_i and T_e are the plasma ion and electron temperatures and q is the ionic charge.) Physical sputtering induced by self-ions has much lower threshold value (which decreases with increasing Z) and its yield may become greater than one. This is certainly the case for multiply charged impurity self-ions which may be accelerated by the sheath potential to high energies.

For carbon based materials at elevated temperatures (400–700°C), bombarded by hydrogenic ions with an energy of 100–200 eV, chemical sputtering becomes a dominant erosion mechanism [12]. At still higher material temperatures (above 1200°C), radiation enhanced sublimation greatly dominates the erosion of graphites [13]. The observed 'carbon bloom' or 'carbon catastrophe' phenomena in fully carbonized tokamaks with substantial plasma power (JET, TFTR), leading to rapid radiation collapse of the discharge [14, 15], are associated with this erosion mechanism. Therefore, radiation enhanced sublimation limits the working temperature of carbon based materials in reactor plasma facing components to 1000–1200°C. Doping of these materials by B, Si and Ti usually results in significant reduction of the erosion rates induced by chemical sputtering and radiation enhanced sublimation. (However, it should be noted that metal doping of graphites leads to a significant reduction of their thermal conductivity under high neutron irradiation, see Section 4.2.)

The net erosion rates of plasma facing materials can also be reduced by the process of redeposition of eroded material. Because of high neutral densities near divertor plates, the mean free path of sputtered atoms is small (< 1 mm for ITER conditions), and, when ionized, they are diverted back to the surface and redeposited. If the plasma temperature is low, the energy gained by these ions from the sheath potential will not be so high as to cause significant self-sputtering. The redeposition effect may reduce the net erosion rate for graphite by a factor of about 200. Under ITER conditions, the total peak gross erosion of graphite at 1000°C would be ≈ 3 m per burn year [1], while inclusion of the redeposition effect reduces this value to an acceptable level of 4–13 cm per burn year [9]. Since the thickness of divertor plate and first wall tiles is primarily determined by thermomechanical considerations (e.g. thermal stress resistance requires smaller thickness, see Ref. [16]), it appears that replacement of the carbon based divertor plate tiles would be necessary for ITER [17].

The material erosion during the thermal quench phase of plasma disruptions, which is due to the impact of relativistic (~ 100–200 MeV) runaway electrons generated in the last, current quench phase of the disruptions, is very high and represents a lifetime limiting factor. The typical duration of the thermal quench phase is 0.1–3 ms, with a peak energy deposition of 5–10 MJ/m^2 (in the worst cases up to 20 MJ/m^2) on divertor plates and about 2–2.5 MJ/m^2 on the first wall. The typical current quench time of a disruption is 5–50 ms, with an energy deposition by runaway electrons in the range 50–500 MJ/m^2 usually over small (several cm^2) areas. Surface material melting and intense evaporation are associated with the rapid energy deposition during these violent events, which also induce additional thermal and electromechanical stresses in the material. For a worst-case 20 MJ/m^2 disruption, the calculated graphite erosion during disruption [17] is about 0.1–0.2 mm, limiting the lifetime of a 10 mm divertor tile to 50–100 disruptions. Disruption simulation experiments on graphite, using both laser and electron beams [18, 19], show about five times greater erosion (possibly associated with cluster emission that was not included in the calculations), which leads to an unacceptably low plate lifetime.

The thermomechanical effects of plasma disruptions are also significant; they are discussed in detail in Ref. [16].

2.4. Power and particle exhaust

The thermal power and helium ash exhaust from the reacting plasma volume is one of the most serious reactor design issues. The plasma power consists of fusion alpha particle heating power (20% of the total

TABLE I. ITER PLASMA PARAMETERS AND POWER LOADS [1, 9]

Parameter	Physics Phase	Technology Phase	
		Long pulse	Steady state
Plasma current (MA)	22	15.4	18.9
$\langle n_e \rangle$ (10^{20} m^{-3})	1.22	1.06	0.64
$n_e(a)$ (10^{20} m^{-3})	0.35	0.30	0.18
Pulse length (s)	400	2500	Steady state
Fusion power (MW)	1080	860	750
Current drive power (MW)	0	110	113
Plasma power (MW)	218	283	263
Power radiated in the core plasma (MW)	102	185	76
Power into SOL (MW)	116	98	187
Power load to first wall:			
average (MW/m^2)	0.1–0.2	0.1–0.2	0.1–0.2
peak value (MW/m^2)	~0.6	~0.6	~0.6
Power load to divertor plates:			
average (MW/m^2)	~8	~6	~17
peak value (MW/m^2) (with separatrix sweeping)	17; 20[a]	11; 14	83; 75
T_e at plate (eV)	5; 12–17	6.6; 10–20	160; 100–220
T_i at plate (eV)	5; 6–10	6; 7–9	20; 30–40

[a] Inner plate; outer plate.

fusion power), auxiliary heating power, associated with non-inductive current drive, and Ohmic heating power. ITER has been designed to operate in two significantly different regimes: an ignition regime ($Q = \infty$), for performing studies on the reactor plasma performance and the physics of burning plasma (Physics Phase), and a sub-ignited, long pulse regime ($Q \simeq 6$–10), for nuclear technology and engineering options testing (Technology Phase). The basic plasma parameters, the plasma power content and, consequently, the heat loads on the plasma facing components in these two regimes are significantly different. The corresponding values for ITER are given in Table I [1, 9]. In this table, two scenarios are given for ITER operation in the Technology Phase: a 'hybrid' operation scenario, in which the plasma current is driven by inductive, non-inductive and bootstrap drives (contributing roughly equally to the total current), and a steady state scenario, in which the current is driven non-inductively and by the neoclassical bootstrap effect (contributing about 30%). We note that the hybrid scenario requires impurity seeding (0.1% Fe) to increase the plasma resistance (i.e. Z_{eff}). The values for the power loads in Table I are obtained by assuming that about 40% of the plasma power is radiated inside the core plasma region, that the divertor operates in a high recycling regime, and that a $\pm$ 3 cm sweeping of the separatrix null-point is applied. The main design concern related to the thermal power exhaust are the high power loads on divertor plates. The divertor plate material should withstand such loads preferably for the entire integrated operation time (more than one year in the Technology Phase) and be able to efficiently transmit the received power to the background structures. Therefore, these materials should have adequate thermomechanical properties (high thermal conductivity, low thermal expansion coefficient, good thermal shock resistance, high yield strength and toughness, low elastic moduli, long fatigue lifetime) and thermophysical characteristics (high melting point, high evaporation heat, low erosion and low tritium inventory). The off-normal plasma events, discussed in Section 2.3, impose even higher requirements on the thermophysical and thermomechanical properties of the plate (as well as the first wall) materials. Obviously, it is difficult to expect that a single material possesses

all the above mentioned favourable characteristics, to which one should also add a set of requirements related to the neutron irradiation effects (good neutron damage resistance, low helium production, swelling and embrittlement) and safety requirements (low neutron activation). Thus, the thermal power exhaust problem strongly influences several reactor design aspects (impurity control, material selection, safety) and has an impact on the reactor engineering.

To reduce the power loads to divertor plates, it would be beneficial to enhance the plasma radiation losses in both the scrape-off and divertor regions. In the present large tokamak experiments, about 50–60% of the total thermal power entering the scrape-off region can be radiated out without terminating the discharge by a radiation collapse. Under normal reactor operating conditions, the impurity content must be kept to levels allowing radiative power exhaust in the edge of 20–30% only. Increase of these losses to 40–50% of the SOL plasma power would significantly reduce the thermal load on plasma facing materials. The old 'cold plasma mantle' concept [20] (a deliberate injection of controllable amounts of impurities with $Z \sim 10$ in the scrape-off region to increase radiation) has recently received renewed attention after obtaining stable 'detached' plasmas [21] with a radiation profile peaked inboard the separatrix. If it proves to be stable at reactor level powers, the detached mode plasma operation can provide an efficient radiative exhaust mechanism for the thermal power.

Because of the strong field-parallel plasma flow in the SOL, the parameters of the plasma near divertor plates and the power loads to the plates are strongly related with the plasma parameters at the separatrix [22]. Within a simplified one-dimensional collision model of the edge plasma, the plasma electron temperature at the plate (T_p) and the plasma power load on the plate (W_p) are given (up to an unessential factor) [23] by

$$T_p \sim \frac{(W_n F_n)^{20/9}}{n_s^{28/9}} \frac{\chi_\parallel^{8/9}}{\chi_\perp^{10/9}} \tag{2}$$

$$W_p \sim \frac{(W_n F_n)^{14/9}}{n_s^{7/9}} \frac{\chi_\parallel^{2/9}}{\chi_\perp^{7/9}} \tag{3}$$

where W_n is the neutron wall load, n_s is the electron density near the separatrix, $\chi_\parallel$ and $\chi_\perp$ are the thermal conductivities in the direction parallel and perpendicular to the magnetic field, and

$$F_n \sim (1 - f_\alpha)(1 + P_{CD}/P_\alpha) \tag{4}$$

where P_{CD} and P_α are the current drive and alpha powers, respectively, and f_α is the radiated fraction of P_α. Equations (2) and (3) show that T_p and W_p can be reduced non-linearly by increasing the scrape-off radiation losses and the plasma density near the separatrix. Impurity seeding in the ITER 'hybrid' operation scenario for the Technology Phase helps significantly in this respect. An increase of n_s would have a considerable effect on decreasing T_p. However, this possibility cannot be used too far, since low plasma densities are required in the outer main plasma region for achieving efficient heating of this region by lower hybrid radiofrequency waves (envisaged in all heating scenarios for ITER). Increase of the perpendicular thermal conductivity (e.g. by ergodization of the magnetic field in the near-separatrix region) would also be beneficial for decreasing T_p and W_p, but would probably worsen the conditions on the first wall.

The plasma–material interaction processes have an indirect effect on the helium exhaust problem, mainly through the hydrogen recycling in the divertor region. The hydrogen recycling coefficient is determined, among other factors, by the particle reflection from the surface, hydrogen trapping and detrapping processes, particle impact induced desorption and other surface chemistry phenomena. An efficient helium removal from the divertor region requires that the fraction C_{He} of helium ions in the D–T flux coming to the divertor plate be relatively high. The pumping efficiency ϵ_{He} of the divertor pump [23] is proportional to

$$\epsilon_{He} \sim C_{He} \frac{W_n^{20/9} F_n^{11/9}}{n_s^{28/9}} \frac{\chi_\parallel^{8/9}}{\chi_\perp^{10/9}} \tag{5}$$

and can be increased by reducing n_s and increasing the radiation losses in the SOL and the divertor (i.e. decreasing F_n). For the ITER plasma parameters, the estimated value of C_{He} is 2–2.5% [9], which gives $\epsilon_{He} \sim (2\text{–}3) \times 10^{-2}$. This translates into a required pumping speed of 300–350 m^3/s in the Physics and Technology Phases (with the long pulse 'hybrid' operation scenario) and a pumping speed of about 1100 m^3/s for a steady state operation scenario. Values of the pumping speed above 700 m^3/s would pose serious technological and engineering problems for the design.

2.5. Selection criteria for plasma facing materials

The plasma–material interaction processes together with the safety issues impose the most stringent criteria

TABLE II. SELECTION CRITERIA FOR MATERIALS OF PLASMA FACING COMPONENTS

Criterion	General qualification	Materials[a]	
		Favoured	Unfavoured
A. Plasma facing materials			
(1) Potential for radiation losses	Low Z	Be, B, CBM	W, Mo, Ta, SS
(2) Erosion properties:			
— physical sputtering	Low	W, Mo, Ta, Nb, and	CBM
— chemical sputtering	Low	Be, B, Si, Ti doped CBM	—
(3) Disruption resistance:			
— thermal erosion	Low	High melting point	
— crack formation	Low	Ta, Mo, CFC	CAPG, PS, SS
(4) Thermomechanical properties:			
— thermoconductivity	High	CAPG, PG, CFC, W	IG, SS
— thermal stress resistance	High	CFC, W, Mo	IG, SS
— fatigue lifetime	Long	Mo	—
— fracture toughness	High	SS, Ti, Al, CBM	—
— creep strength	High	Mo, V, Ti, SS	—
(5) Irradiation influence:			
— changes of physical properties	Low	W, Ta, Mo, SS	CBM
— swelling	Low	W, Mo, Ta	CBM
— changes of mechanical properties	Low	CFC, Ta	W, Mo
— neutron activation	Low	CBM, Be, V, Ti, Al	W, Mo, Ta
— helium production	Low	W, Mo, CBM, Nb, V	Be
— reduction of thermoconductivity	Low	—	CBM (?)
(6) Tritium retention	Low	W, Mo, Be, Ti, Nb	CBM
(7) Availability	High	All metals, CBM except CFC	
B. Heat sink and structural materials			
(1) Thermomechanical properties:			
— thermal stress resistance	High	DS Cu, Cu, Mo	SS, V
— fatigue lifetime	High	DS Cu, Mo	—
— creep strength	High	Mo, DS Cu	—
— fracture toughness	High	SS, DS Cu, Cu, Nb	Mo
(2) Irradiation influence:			
— changes of physical properties	Low	SS, Mo, DS Cu, Cu, Nb	—
— swelling	Low	DS Cu, Nb	SS, Cu, Mo
— changes of mechanical properties	Low	DS Cu, Nb	Mo, SS
— neutron activation	Low	LASS	Mo, Cu, Nb, SS
(3) Tritium retention/permeation	Low	—	—
(4) Compatibility with coolants			
— critical heat flux	High	Cu, DS Cu, Mo, Nb	SS
— erosion/corrosion	Low	DS Cu, SS, Mo, Nb	—
— ICSC	Low	Mo, DS Cu	SS
— hydrid formation	Low	Mo, Cu, DS Cu	Nb
(5) Availability	High	All materials	
(6) Fabricability:			
— welding	High	SS, Cu, Nb	Mo, DS Cu
— joining with PFM	High	Mo, Nb, Cu	DS Cu, SS

[a] CBM — carbon based materials
CFC — carbon fibre composite
CAPG — compression annealed pyrolytic graphite
PG — pyrolytic graphite
IG — isotropic graphite
SS — stainless steel
DS Cu — dispersion strengthened Cu alloys
LASS — low activation stainless steel
PFM — plasma facing materials

TABLE III. MATERIALS OF PLASMA FACING COMPONENTS CONSIDERED FOR ITER

Component	Physics Phase		Technology Phase			
			First option		Alternative	
	PFM	Substrate	PFM	Substrate	PFM	Substrate
Fist wall	C-C (doped)	SS	C-C (doped)	SS	W (coating) (backup: SS)	SS
Divertor plates	C-C (doped) $T_{DP} < 1000°C$	Cu, Mo alloy	C-C (doped)	Cu, Mo alloy $T_{eP} \leq 50$ eV	W	Mo, Nb, Cu alloy $T_{eP} \leq 20$ eV (backup: Be)

on the selection of plasma facing materials. These criteria can be divided into several groups, as shown in Table II. Some of the currently favoured (and unfavoured) materials according to each of these criteria are also given in Table II.

The specific material selection during the design process is based on a compromise, guided by the predicted (calculated) effects of a particular choice of material (or a combintion of materials) on the overall reactor performance, as well as by considerations related to the available database for material properties, technological experience and engineering requirements. Taking into account all these considerations, the currently favoured plasma facing reactor materials are: carbon–carbon (C–C) composites, possibly doped with B, Si, Ti, etc., carbon fibre composites (also possibly doped with B, Si, Ti), Be and refractory metal (W, Mo, Nb, Ta) alloys and graphites (fine grained, pyrolytic). A particular choice among these candidates is subject to the fulfilment of certain specific conditions to avoid phenomena which could deteriorate the plasma performance or the component lifetime (e.g. low near-plate plasma temperture for W and Mo, working temperature below $\sim 1000°C$ for carbon composites, etc.). For the structures of plasma facing components, the following materials are currently the favoured ones: SS 316, low activation stainless steels, Ni, Cu, Mo, Nb, Re and Ti alloys, Be and ceramics (as isolators).

The materials selected for the ITER plasma facing components (armour and background structure) in the Physics and Technology Phases of operation are given in Table III [3, 4, 24]. The considered alternatives and backup choices for the Technology Phase are also given in the table.

The choice of carbon composites (C–C) for plasma facing materials in ITER is based on their good thermomechanical performance. If doped with B, Ti or Si, their high erosion rates are also significantly reduced. Critical issues related to C–C as plasma facing materials are high retention of tritium (particularly in the co-deposited eroded carbon) and effects of neutron irradiation damage (degradation of their thermal conductivity, etc.). It is predicted that the C–C tiles on the first wall could last for the entire operation time of ITER, but several replacements of the C–C divertor plates would be necessary. If the near-plate temperature can be kept below 20 eV (by intense recycling), tungsten (bonded on a Nb, Mo or Cu alloy) would be a better alternative to the C–C divertor plate armour for the Technology Phase because of its adequate thermal properties. However, the strong neutron activation of tungsten remains an important concern. Tungsten is also considered as a material for coating of the first wall stainless steel armour for the Technology Phase, with radiation cooled C–C tiles on the expected high heat spot areas.

3. STATUS OF THE DATABASE FOR PARTICLE-MATERIAL INTERACTION PROCESSES

The plasma-material interaction phenomena originate from particle impact induced processes and from collective (material response) processes, induced by

thermal energy deposition in the material. Most of the processes induced by particle impact are associated with the atomic plasma particles (electrons, plasma ions, hydrogen neutrals, impurity ions), and their most important effect is the release of material impurities into the plasma (apart from the reflection and trapping of the incident particles). These processes usually do not induce significant large scale microstructural changes in the material and consequently do not change its thermomechanical properties.

Here, we review briefly the status of the database for particle–solid interaction processes, excluding the neutron irradiation processes. The effects of the latter on thermomechanical properties are significant; they are discussed in Section 4, together with the database for heat flux and material response. Since for most of these processes the database is discussed in detail in the preceding articles in this issue, our analysis will be confined mainly to the identification of the deficiencies in the database with respect to the reactor design needs and of the research problems connected with the establishment of the required database for plasma–material interaction.

3.1. Particle and energy reflection

A sufficiently energetic plasma ion colliding with a solid surface may enter the substrate, undergo a sequence of energy and momentum transfer collisions with the substrate atoms and, as a result, may either come to rest in the substrate after exhausting its energy or be returned ('backscattered') to the plasma region with reduced energy and altered momentum. It is obvious that the reflected particle fraction and the associated kinetic energy are important elements in the overall particle and energy balance in the plasma, and that they have a particularly important role in the (hydrogen and impurity) recycling process in the plasma edge. Hydrogen recycling has also an important impact on reactor fuelling.

The reflection is characterized by total particle and energy reflection coefficients, which are functions of incident particle energy and angle, and by the angular and energy distribution of reflected particles. The available database for particle and energy reflection is comprehensively discussed in Refs [25, 26]. For the fusion plasma ions (H, D, T, ^{4}He) colliding with elemental monatomic materials of fusion interest (Be, B, C, Al, Si, Ti, Fe, Ni, Cu, Nb, Mo, Ta, W) and with some composite materials (SS, TiC, TiH_2, TiD_2, TiB_2, TiN, SiN_3, WO_3) the database on particle and energy reflection coefficients for normal ion incidence is well documented, except in the low energy (several eV) region. Similar data information is available also for the self-ions [26, 27].

Most of the recent information has been generated by numerical simulation Monte Carlo type codes (see Ref. [26] for details). A comprehensive set of reflection data for the H, D, T, ^{3}He and ^{4}He ions colliding with the above mentioned elemental materials has recently been generated by using a numerical solution of the approximated ion transport equation (bipartition model) [28]. This set of data includes a wide range of incidence angles (between 0° and 90°) as well as information on energy and angular distribution of reflected particles.

The available information permits an analytic representation of the data in the form of generalized, analytic fit expressions containing the atomic and collision parameters of the system [27, 29]. While describing with adequate accuracy all the existing data, these expressions also permit extrapolations and interpolations in the parametric space (energy range, projectile–target mass ratio, surface binding energy). The numerical simulation codes, such as MARLOWE and TRIM, can also provide particle reflection data for any projectile–target combination at energies above about 10 eV, provided the surface binding energy of the particle (close to its sublimation energy) is accurately known. Data below this energy are, however, both scarce and difficult to obtain because of experimental difficulties and because of the inapplicability of existing numerical codes (all being based on the classical binary collision dynamics) to the description of the collision process in this energy region. Since the collision energy is of the order of the typical energy for inelastic electron transitions (several eV), the quantum effects should play a prominent role in the collision dynamics of low energy ion–surface collisions. These effects are not included in the existing numerical codes. A major uncertainty present in the reflection data, which is again particularly pronounced at low collision energies, comes from the surface roughness and, in general, the state of the surface (surface temperature, adsorption layers and their hemical composition, etc.). The surface state is an ill defined dynamical parameter which may change during the discharge pulse and which may significantly affect the particle reflection process.

Another important piece of information lacking in the available reflection database is the charge and quantum state of reflected particles. The collision processes of reflected particles entering the edge plasma region depend crucially on the charge and

quantum state of these particles, and successful plasma edge modelling ultimately requires this information. For instance, it is important to know what fraction of reflected hydrogen, especially in the low energy part of its energy distribution, enters the plasma in ionic, neutral or molecular form and what is the excited state (electronic, vibrational) distribution of neutral species. This information significantly influences the neutral transport kinetics and the energy balance in the plasma edge.

3.2. Particle trapping and release

The non-reflected plasma particles that come to rest in the material substrate become subject to a thermal diffusion which can lead either to their permanent trapping in the lattice vacancies and intrinsic defects or to their release by thermal desorption after reaching the surface. The particle trapping and release are significant factors in the recycling process and determine the inventory of hydrogen isotopes and helium in the plasma facing materials. The tritium inventory is an important safety concern, while excessive helium trapping may cause massive erosion by blister exfoliation [30].

The process of thermally activated diffusion of implanted particles in a solid depends critically on the lattice characteristics, the particle–lattice interactions and the substrate temperature. All of these dependences can be expressed by two temperature dependent parameters: the particle diffusivity and the particle solubility for the corresponding gas in a given material. These two parameters enter the set of coupled differential transport equations describing the particle diffusion in solids [31]. However, the experimental or theoretical determination of particle diffusivity and solubility is fraught with significant difficulties; this leads to uncertainties in the estimates of particle trapping and release. Particle release also depends critically on the boundary conditions at the surface (the value of the molecular recombination rate), which are strongly affected by the level of surface impurities. The available experimental and theoretical data for hydrogen and helium trapping and release in various materials of fusion interest are reviewed in Refs [31, 32]. Information, although not always self-consistent, is most abundant for carbon based materials and is rather sparse for Be and refreactory metals (Mo and W). The results of experimental measurements and theoretical calculations show a strong sensitivity to the structural and surface characteristics of the material, which, in their turn, may also depend on the particle bombardment conditions (impact energy, fluence, etc.). Theoretical investigations of particle trapping and release are impaired by the complexity of a plethora of dynamical processes that are interrelated with particle diffusion. Since thermally activated diffusion usually starts already during the process of particle bombardment, the diffusion process as well as particle trapping and release evolve simultaneously with other processes induced by particle impact, such as vacancy creation, sputtering cascades, detrapping (and retrapping) and surface erosion. A self-consistent description of all of these strongly correlated processes is required in order to arrive at reliable results. However, neither the dynamics nor some basic input parameters (such as solubility, diffusivity, boundary conditions, characteristic times) are sufficiently well known to perform such complex calculations. Still, because of the variability of a large number of parameters and conditions on which the particle trapping and release depend, the theoretical modelling apporoach, supplemented by certain experimentally determined input parameters, is the most promising method of establishing the database for these processes.

3.3. Particle induced desorption

The first wall of present fusion devices is usually covered by a few adsorbate layers formed by the residual gas at the plasma edge (O_2, CO, H_2O, etc.), by neutral edge plasma hydrogen molecules and by impurity segregation on the surface at elevated temperatures. The molecules adsorbed in these layers have binding energies in the range of 0.5 eV to several electronvolts and can be desorbed in interactions either with the lattice phonons (thermal desorption) or with the plasma photons, electrons, ions and charge exchange neutrals. The highest desorption yield induced by particle impact is due to the ion (or neutral) impact. Particle induced desorption can obviously be an important factor in hydrogen recycling and impurity generation. Under long pulse reactor plasma operation, desorption takes place in the earlier stage of the discharge and its effects on hydrogen recycling can be considered to be transitory. However, surface impurity segregation at elevated material temperatures may continue to be an operative adsorption mechanism. The subsequent particle induced desorption may, therefore, still contribute to the impurity fluxes in a reactor plasma.

The database for particle induced desorption is not adequate for most of the adsorbents and surfaces of

fusion interest [33]. The experimental data are usually strongly dependent on the surface conditions. Although three basic desorption mechanisms have been identified (direct knock-off of adsorbed particles by the incident particles, and desorption due to the collision cascades of reflected and sputtered particles), detailed information on their dynamics, particularly at low impact energies, is still lacking. Specifically, information on the energy and angular distribution of desorbed particles, on their charge and their quantum state, and on their chemical composition (atomic or molecular form) is rather sparse. There are only a limited number of theoretical models for desorption, and none of them adequately describes the quantum, surface chemistry and temperature effects. Since most of the desorbed particles leave the surface with relatively small energies (below 10 eV), it is evident that all these effects should play a dominant role in the desorption dynamics.

3.4. Erosion processes

As discussed in Section 2.3, erosion of the plasma facing materials is one of the most important design issues, with regard to both plasma contamination and, even more, the lifetime of divertor plates. The most important erosion mechanism induced by particle impact is physical sputtering [11, 34], consisting of a cascade of energy and momentum transfer binary collisions of the substrate atoms, initiated by the bombarding plasma or by impurity ions, which ends with a release of surface material into the plasma. Physical sputtering is characterized by an energy threshold (related to the surface binding energy) and by a sharp increase of the yield in the threshold region. The database for the total sputtering yield of materials of fusion interest, bombarded by hydrogen isotopes, helium and self-ions, is fairly well documented [11, 34, 35], except for the threshold energy region. The threshold energy itself is a parameter that is not well defined and the value of which may strongly depend on the chemical composition of surface layers. This uncertainty is particularly pronounced in the case of self-sputtering and for chemically active projectile–target systems. The existing theoretical knowledge of the process and the available experimental database, complemented by Monte Carlo type simulation calculations (see Ref. [11]), allow unified analytic fit expressions for the total sputtering yield to be constructed [34, 36]. These expressions contain only two or three fitting parameters. By establishing approximate semi-empirical relations of these parameters with the collision and interaction parameters of the projectile–target system [36], the analytic fit expressions are generalized in a form that can be used for predictive purposes.

The physical sputtering database is less documented with regard to the energy and angular distributions of sputtered particles. This information is required for modelling of impurity transport in the plasma edge. Information on the charge and quantum state distributions of sputtered particles is also sparse. The effects of the surface roughness on the sputtering yield and the angular distribution of sputtered particles are expected to be significant at low impact energies [11], but they have been very little investigated. Since under realistic plasma conditions the material surfaces are simultaneously bombarded by various types of particles, information on synergistic effects of sputtering is required. Only a limited amount of such information is presently available [11].

As mentioned in Section 2.3, important erosion mechanisms for carbon based materials are also chemical sputtering and radiation enhanced sublimation. Chemical sputtering of graphite is the dominant erosion mechanism at energies below the threshold for physical sputtering ($\simeq 15$ eV, for carbon); at high impact energies it shows a strong temperature dependence (with a maximum in the range 700–1000 K) [12]. The basic mechanism for chemical sputtering is thermal desorption of surface molecules formed by interactions of implanted particles with substrate material. However, the specific mechanisms of molecule formation and the detailed dynamics of their desorption are still not well understood. (Some of the existing models of chemical sputtering are discussed in Ref. [13].) The available database for the chemical erosion yields of graphite and other carbon based materials due to bombardment by hydrogen and other ions is thoroughly reviewed in Refs [12] and [13]. Semi-empirical analytic fit expressions for the sputtering yield are also provided in these references for certain ranges of the projectile energy, target temperature and particle flux. The extension of validity of these expressions to conditions typical for a reactor remains uncertain. The energy and angular distributions of chemically sputtered particles are also not adequately documented.

Radiation enhanced sublimation (RES) by light ion impact has been observed (up to now) only for carbon materials at temperatures above a certain threshold value, which for H(D) and He ions is about 1200 K and 1000 K, respectively. Above the threshold, the erosion yield due to this process increases exponentially, and at a certain temperature (~ 2000 K for He) it reaches values greater than one. The process is

described in terms of diffusion of vacancy interstitial (Frenkel) pairs (created in collisions of bombarding particles with substrate atoms) and their sublimation at the surface. This model adequately explains the projectile mass and temperature dependence of the RES erosion but gives a stronger (inverse) dependence on the particle flux than observed. The existing database for the RES erosion of carbon materials by light ions, oxygen and carbon ions is reviewed in Ref. [13]. The dependence of the erosion yield on the projectile mass, target temperature and particle flux has been fitted to a simple analytic expression, but its extension to fusion relevant fluxes (above 10^{18} $cm^{-2} \cdot s^{-1}$) is somewhat uncertain.

Because of the characteristic signatures of the process (temperature threshold, rise of the exponential yield with temperature, isotropic angular distribution of eroded (predominantly atomic) particles, energy distribution equivalent to the surface temperature), the RES erosion can easily be identified and its yield experimentally measured. The most relevant parameters to be determined are, however, the threshold temperature and the increment of the yield growth, since the initiation of this erosion process should certainly be avoided in fusion devices, at least on a large scale. It should be mentioned that the erosion rates due to both chemical sputtering and RES can be significantly reduced by doping the carbon materials with B, Si and Ti. The available erosion data of doped graphites are also discussed in Ref. [13].

Another important erosion mechanism, mainly related to helium trapping, is blister exfoliation. Blistering in plasma facing metallic materials depends on the energy spectrum and the angle of incidence of bombarding helium ions and becomes a serious erosion mechanism only when a critical concentration ($\simeq 0.4$ He/metal) is reached in the lattice and when the peak of this concentration is at least about 10 nm below the surface [30]. A narrow energy spectrum is more likely to produce blistering. Blistering may occur also in a repetitive way if the material temperature is (at least locally) in the range of 0.2-0.4 T_m, where T_m is the melting temperature. Because of the higher permeability of hydrogen in most of the fusion relevant materials, hydrogen trapping is not expected to lead to serious blistering. The database on this erosion mechanism is discussed in Ref. [30], and not much new information has become available since then.

A general remark should be made regarding the database for all the erosion processes discussed. Most of the erosion data have been produced under well defined beam experiment conditions. In a real plasma environment, particularly for long discharge pulses and high plasma ion and neutron fluxes, both the surface conditions and the material structural characteristics may continuously undergo significant changes. The resulting erosion rates may be considerably different from those determined under well defined experimental conditions. Although there are some data for materials that have been exposed to plasma action and from fusion plasma simulators such as PISCES (see Refs [13, 26]), more data of this type and information on their correlation with beam–surface data are required.

To make our discussion on the database for material erosion processes complete, we should also mention the erosion mechanisms which are not initiated by particle bombardment but rather by excessive heat loads. Such conditions exist during plasma disruptions and, as discussed in Section 2.3, they are characterized by energy depositions of 5–10 MJ/m^2 during a period of 0.1–3 ms. Material melting and evaporation resulting from this fast energy deposition and temperature rise lead to massive surface erosion. Computer modelling of melting and evaporation processes requires, besides the energy deposition rate, a number of parameters related to the thermophysical properties of the material (density, melting point, heat of fusion and sublimation, heat of evaporation, specific heat, thermal conductivity, vapour pressure — the last three parameters as functions of temperature). The values of these parameters for a number of fusion related materials (Be, Al, Ti, TiC, SS 304, Mo, W) are collected and evaluated in Ref. [37].

Material evaporation occurs also during the current quench phase of the disruption, when energies of the order of 50–500 MJ/m^2 are deposited over small areas for a period of 5–50 ms. As discussed in Section 2.3, this energy is deposited in the material by runaway electrons (with energies in the range 200–300 MeV). High energy runaway electrons are generated also during other types of high MHD activities, as well as during the current rise and current ramp-down phases of the discharge, when the plasma loop voltage undergoes significant changes. In all these cases, the enhanced electron flow from the plasma to the walls creates conditions necessary for ignition of unipolar arcs, which are accompanied by local material overheating and evaporation [38, 39]. The erosion rates induced by unipolar arcs for selected materials of fusion interest (C, Al, Ti, Cr, Fe, Ni, Cu, Mo, W) are given in Ref. [38]. On average, one surface atom is released for every 20–30 electron charge units of the arc current. During the quiescent phase of the dis-

charge, arcing is not probable, and it is expected that in a fusion reactor this erosion mechanism will either be of a transitory nature or constitute a minor component of the disruption erosion.

3.5. Particle induced electron emission

The plasma sheath potential adjacent to the boundary materials is an important parameter influencing both plasma–material interaction processes (by providing additional energy to the ions) and plasma and impurity transport in the edge (by changing the ambipolar plasma flow and the plasma collisionality). Electron emission from the surfaces reduces the sheath potential, which is beneficial from the point of view of the above effects. Electron emission from surfaces can be induced either by plasma particle impact (including photons) or by electric fields (generated, for instance, during arcing). Under quiescent plasma operating conditions, the most efficient electron emission mechanism is by plasma electron impact. The secondary electron production coefficient for this mechanism for most materials of fusion interest becomes greater than one already in the impact energy range 100–250 eV. This coefficient has a broad maximum in the range 300–600 eV (for fusion relevant materials) and then slowly decreases.

Material bombardment by plasma ions and low charged impurity ions can also induce secondary electron emission with significant production coefficients in the region of several tens of keV. The underlying physical mechanism for the process is excitation of valence band electrons (by energy transfer from the projectile) and their escape from the potential well of the solid (with a broad energy distribution, peaked typically at a few eV). The escape stage of the process is evidently dependent on the surface potential (or effective work function), i.e. on the surface conditions.

A broad database is available for both electron induced and light ion induced electron emission from clean surfaces. The part of this database relevant to fusion has been reviewed in Refs [40, 41]. For the plasma impurity ions, even in low charge states, the database is very limited. In general, data on particle induced electron emission for realistic plasma machine surfaces is rather sparse. There is evidence that slow, multiply charged ions can induce copious electron production from metal surfaces via the potential electron emission (Auger) mechanism. Information on the electron emission coefficient for ions and surfaces of fusion interest is not yet available. However, highly charged impurity ions have been observed in the periphery plasmas of currently operating tokamaks [42].

4. DATABASE FOR THERMOMECHANICAL MATERIAL PROPERTIES

The thermomechanical behaviour of plasma facing materials and components during both normal operation and off-normal events is an important reactor design issue. The basic requirements for these materials and components are that they must be able to withstand the thermal loads and associated thermomechanical stresses without significant deterioration of their structural and functional integrity, and to absorb and transmit the plasma heat fluxes to the background supporting structures and coolants, and that they must have an adequate response to high flux neutron irradiation effects.

4.1. Thermomechanical response to high heat fluxes

Under normal plasma operating conditions the high heat plasma fluxes are located only on divertor plates and on isolated hot spots on first wall armour tiles. During off-normal events, however, both the first wall and the divertor plates are subject to high heat loads. The most relevant material properties with respect to withstanding high heat loads are the thermal conductivity, thermal fracture toughness, thermal shock resistance, and the overall response parameters such as the thermal stress heat flux limit and the fatigue lifetime. The thermal conductivity of the material is a particularly critical property since, through the thermal stress heat flux limit, it defines the thickness of the protecting first wall tiles and divertor plates (related to their erosion lifetime), the efficiency of heat transfer (and the corresponding critical heat flux and material operating temperature), and some other component response parameters. Other important thermophysical and mechanical properties relevant for the thermomechanical response of materials to high heat fluxes are the specific heat capacity, coefficient of thermal expansion, melting point, boiling point, evaporation heat, heat of fusion (sublimation), elastic moduli, Poisson's ratio, shear modulus, material strengths (tensile, compressive, flexural, shear), elongation, creep and fatigue cracks growth, phase stability, etc. The influence of these properties on various thermomechanical response parameters is discussed in Refs [8, 16]. The most comprehensive database on

thermophysical and thermomechanical properties of fusion related materials is contained in Refs [43–45]. Because of their good thermal properties (high thermal conductivity, high temperature strength, good thermal shock resistance, high vaporization temperature), carbon based materials (isotropic and pyrolytic graphites, C–C composites, carbon-fibre composites) are presently considered as adequate materials for the first wall protecting tiles of next generation fusion machines. As mentioned earlier, the carbon-fibre composites, as well as all B, Si or Ti doped carbon materials have significantly improved erosion characteristics. However, the dopant may significantly reduce the thermal conductivity (e.g. by 50% in the case of doping with 3% B). The technological development and the search for new types of carbon based composite materials with improved characteristics, particularly with respect to the neutron damage effects, is currently pursued vigorously (see Ref. [16]). Detailed information on the thermomechanical properties of carbon composites is collected in Refs [43–47]. The database for these materials is, however, rather incomplete in the region of elevated temperatures and higher levels of neutron radiation damage. This remark also holds for the other candidate plasma facing materials (Be, W, Mo, Nb, and Al and SiC cermets).

The higher temperatures and radiation fluences may lead to significant reduction of thermal conductivity and to degradation of the thermomechanical properties of other materials. Data on thermomechanical properties for the structural materials of plasma facing components (SS 316, low activation steels, Ti-, Ni- and Cu-alloys, Be, Mo-, Nb- and Re-alloys) are also available [43–45, 47, 48], but data for elevated material temperatures and high neutron fluences are sparse. The required data information for the design of next step fusion devices is specified in Refs [47, 49, 50].

4.2. Neutron damage effects

Neutron irradiation produces point defects, interstitials and vacancies in the material which may agglomerate, forming dislocation loops and vacancy clusters. The major effects of these internal defects on the thermomechanical properties of materials are reduction of thermal conductivity and thermal shock resistance, and initiation of void swelling and embrittlement. The significance of these effects evidently depends on the irradiation dose, neutron energy spectrum, material structure and temperature. For pyrolytic graphite, for instance, neutron doses at a level of 0.1 dpa reduce the thermal conductivity by a factor of 100 at temperatures around 150°C, but only by a factor of two at temperatures around 450°C. For carbon–fibre composites the effect is, however, not so dramatic, but for large fluences it may still be significant.

The dimensional changes caused by neutron induced swelling (and usually associated with in-plane shrinkage) may be quite large for high irradiation doses and may become critical for the structural integrity of plasma facing components. For multi-material plasma facing components, the neutron irradiation induced dimensional and thermal conductivity changes may be different for each of their structural constituents, which can induce additional thermomechanical stresses in the components.

Because of the absence of suitable 14 MeV neutron sources with fusion relevant characteristics (energy spectrum, flux) it is not possible to perform systematic investigations of the neutron irradiation effects on fusion reactor materials. Such studies are, however, indispensable for characterization of the thermomechanical response of plasma facing materials to plasma particle and heat fluxes under realistic reactor conditions. The available information regarding neutron induced effects on thermomechanical properties of fusion relevant materials is reviewed in Refs [51, 52].

5. CONCLUDING REMARKS

Plasma–material interactions in fusion reactor plasmas have a decisive impact on the overall plasma performance and impose stringent limitations on the reactor operation scenario. The effects of these interactions define the acceptable design options in several critical reactor design areas, such as impurity control, power and particle exhaust and selection of plasma facing materials.

The establishment of a comprehensive and credible database for plasma–material interaction effects and material response parameters is an essential prerequisite for the selection of plasma facing reactor materials. The diversity of design requirements for these materials and the incompleteness of the existing database (particularly at elevated temperatures and high neutron fluences) make this choice difficult. For a better characterization of the present candidate materials or the development of new materials with improved properties, a certain degree of focusing of the research on plasma–material interaction is required. International co-operation could also significantly enhance the efficiency of these efforts [49, 50, 53, 54].

ACKNOWLEDGEMENTS

The authors are indepted to Drs. M.F.A. Harrison, W.B. Gauster and V.R. Barabash for useful comments.

REFERENCES

[1] ITER Concept Definition, Vol. 2, ITER Documentation Series, No. 3, IAEA, Vienna (1989).
[2] POST, D.E., "ITER: Physics basis", Plasma Physics and Controlled Nuclear Fusion Research 1990 (Proc. 13th Int. Conf. Washington, 1990), Vol. 3, IAEA, Vienna (1991), paper IAEA-CN-53/F-I-3.
[3] TOSCHI, R., "ITER: Design overview", ibid., paper IAEA-CN-53/F-I-2.
[4] SALPIETRO, E., "ITER: Engineering basis", ibid., paper IAEA-CN-53/F-I-4.
[5] STANGEBY, P.C., McCRACKEN, G.M., Nucl. Fusion **30** (1990) 1225.
[6] KEILHACKER, M., Plasma Phys. Control. Fusion **29** (1987) 1401.
[7] ROSENBLUTH, M.N., RUTHERFORD, P.H., "Tokamak plasma stability", Fusion, Vol. 1, Part A (TELLER, E., Ed.) , Academic Press, New York (1981) 31.
[8] CONN, R.W., "Magnetic fusion reactors", ibid., Part B, p. 194.
[9] COHEN, S.A., BRAAMS, B.J., BROOKS, J., et al., "Power and particle control for ITER", Plasma Physics and Controlled Nuclear Fusion Research 1990 (Proc. 13th Int. Conf. Washington, 1990), Vol. 3, IAEA, Vienna (1991) paper IAEA-CN-53/F-III-3.
[10] STANGEBY, P.C., in Physics of Plasma-Wall Interactions in Controlled Fusion" (POST, D.E., BEHRISCH, R., Eds), Plenum Press, New York (1986) 41.
[11] ECKSTEIN, W., BOHDANSKY, J., ROTH, J., this issue, p. 51.
[12] ROTH, J., in Data Compendium for Plasma-Surface Interactions, Special Issue 1984, Nucl. Fusion (1984) 72.
[13] ROTH, J., VIETZKE, E., HAASZ, A.A., this issue, p. 63.
[14] PITCHER, C.S., McCRACKEN, G.M., STANGEBY, P.C., et al., in Controlled Fusion and Plasma Physics (Proc. 16th Eur. Conf. Venice, 1989), Vol. 13B, Part III, European Physical Society (1989) 879.
[15] ULRICKSON, M., BELL, M.G., BUDNY, R., et al., in Plasma Physics and Controlled Nuclear Fusion Research 1988 (Proc. 12th Int. Conf Nice, 1988), Vol. 3, IAEA, Vienna (1989) 889.
[16] WHITLEY, J.B., GAUSTER, W.B., WATSON, R.D., KOSKI, J.A., RUSSO, A.J., this issue, p. 109.
[17] BAKER, C., "ITER: Nuclear engineering", Plasma Physics and Controlled Nuclear Fusion Research 1990 (Proc. 13th Int. Conf. Washington, 1990), Vol. 3, IAEA, Vienna (1991), paper IAEA-CN-53/F-II-2.
[18] BOLT, H., MIYAHARA, A., Runaway Electron-Materials Interaction, Res. Rep. NIFS-TECH-1, National Institute for Fusion Science, Nagoya (1990).
[19] VAN DER LAAN, J.G., J. Nucl. Mater. **162–164** (1989) 964.
[20] GIBSON, A., WATKINS, M.L., in Controlled Fusion and Plasma Physics (Proc. 8th Eur. Conf. Prague, 1977), Vol. 1, Czechoslovak Academy of Sciences, Prague (1977) 31.
[21] McCRACKEN, G.M., ALLEN, J., AXON, K., et al., J. Nucl. Mater. **145–147** (1987) 181; STRACHAN, J.D., BOODY, F.P., BUSH, C.E., et al., J. Nucl. Mater. **145–147** (1987) 186.
[22] MAHDAVI, M.A., DeBOO, J.C., HSIEH, C.L., et al., Phys. Rev. Lett. **47** (1981) 1602.
[23] HARRISON, M.F.A. (Culham Laboratory, Abingdon), personal communication, 1990.
[24] VIEIDER, G., AKIBA, M., ANTIPENKOV, A., et al., in Plasma Physics and Controlled Nuclear Fusion Research 1990 (Proc. 13th Int. Conf. Washington, 1990), Vol. 3, IAEA, Vienna (1991), paper IAEA-CN-53/F-III-12.
[25] ECKSTEIN, W., VERBEEK, H., in Data Compendium for Plasma–Surface Interactions, Special Issue 1984, Nucl. Fusion (1984) 12.
[26] ECKSTEIN, W., this issue, p. 17.
[27] ITO, R., TABATA, T., ITOH, N., et al., Data on the Backscattering Coefficients of Light Ions from Solids (A Revision), Rep. IPPJ-AM41, Institute of Plasma Physics, Nagoya (1985).
[28] LUO, Zhengming, WU, Wenfeng, ZHON, Yong, Reflection of H^+, D^+, T^+, $^3He^+$ and $^4He^+$ from a Surface of Solids, Rep. INST-8, Institute of Nuclear Science and Technology, University of Sichuan (1991).
[29] THOMAS, E.W., JANEV, R.K., SMITH, J.J., Particle Reflection from Surfaces — A Recommended Database, Rep. IAEA(NDS), IAEA, Vienna (1991).
[30] WILSON, K.L., in Data Compendium for Plasma–Surface Interactions, Special Issue 1984, Nucl. Fusion (1984) 28.
[31] WILSON, K.L., ibid., p. 85.
[32] WILSON, K.L., BASTASZ, R., CAUSEY, R.A., et al., this issue, p. 31.
[33] TAGLAUER, E., in Data Compendium for Plasma-Surface Interactions, Special Issue 1984, Nucl. Fusion (1984) 43.
[34] BOHDANSKY, J., ibid., p. 61.
[35] ROTH, J., BOHDANSKY, J., OTTENBERGER, W., Data on Low-Energy Light Ion Sputtering, Rep. IPP-9126, Max-Planck-Institut für Plasmaphysik, Garching (1979).
[36] JANEV, R.K., THOMAS, E.W., QIU Yanghui, Physical Sputtering of Solids by Light Ion Impact. An Evaluated Database, Rep. IAEA(NDS), IAEA, Vienna (1991).
[37] LANGLEY, R.A., in Data Compendium for Plasma–Surface Interactions, Special Issue 1984, Nucl. Fusion (1984) 55.
[38] MIODUSZEWSKI, P., ibid., p. 105.
[39] WOLFF, H., this issue, p. 93.
[40] THOMAS, E.W., in Data Compendium for Plasma–Surface Interactions, Special Issue 1984, Nucl. Fusion (1984) 94.
[41] THOMAS, E.W., this issue, p. 79.
[42] RICE, J.E., MARMAR, E.S., KAELNE, E., KAELNE, J., Phys. Rev. A **35** (1987) 3033.
[43] DAVIS, J.W. (Co-ordinator), Materials Handbook for Fusion Energy Systems (publication packages 1 to 11 from 1980 to 1986), McDonnell Douglas Astronautics Co., Richland, WA (1980–1986).
[44] DAVIS, J.W. (Co-ordinator), International Fusion Material Handbook, Status Report, September 1990, International Energy Agency, Paris (1990).

[45] ZOLTI, E., NET Material Data for Predesign Analysis of In-Vessel Components, NET Rep. N/I/3300 5/A, Max-Planck-Institut für Plasmaphysik, Garching (1990).

[46] ROTH, E.P., WATSON, W.D., MOSS, M., DROTNING, W.D., Thermo Physical Properties of Advanced Carbon Materials for Tokamak Limiters, SAND88-2057, Sandia National Laboratories, Albuquerque, NM (1989).

[47] SMITH, D., ALTOVSKY, I.V., BARABASH, V.R., et al., ITER Blanket and Shield Conceptual Design and ITER Material Evaluation and Database. Part B (Summary Report of ITER Specialists Meetings on Material Database, Garching, June 1988 and February 1990), Max-Planck-Institut für Plasmaphysik, Garching (1990).

[48] WHITLEY, J.W., J. Nucl. Eng. Des./Fusion **4** (1986) 49.

[49] WHITLEY, J.B., MIYAHARA, A. (Eds), Plasma-Material Interaction/High Heat Flux Data Needs for the Next Step and Steady State Devices (Proc. US-Japan Workshop Q86, March 1988), Rep. SAND 88-1072, Sandia National Laboratories, Albuquerque, NM (1988).

[50] JANEV, R.K. (Ed.), IAEA Consultants Meeting on Thermal Response of Plasma Facing Materials and Components, Summary Report, Rep. INDC(NDS)-237/M6, IAEA, Vienna (1990).

[51] WHITLEY, J.B., WILSON, K.L., CLINARD, F.W. (Eds), J. Nucl. Mater. **122-123** (1984).

[52] KELLY, B.T., BROCKLEHURST, J.E., in Proc. Tenth Biennial Conference on Carbon, Bethlehem, PA, 1971.

[53] JANEV, R.K., MIYAHARA, A. (Eds), IAEA Advisory Group Meeting on Particle-Surface Interaction Data for Fusion, Summary Report, Rep. INDC(NDS)-226/MA, IAEA, Vienna (1989).

[54] ULRICKSON, M., BARABASH, V.R., MATERA, R., et al., Report from the IAEA Consultants Meeting on Evaluation of Thermo-Mechanical Properties Data of Carbon-Based Plasma Facing Materials, Rep. INDC(NDS)-246/MO, IAEA, Vienna (1991).

HOW TO ORDER IAEA PUBLICATIONS

An exclusive sales agent for IAEA publications, to whom all orders and inquiries should be addressed, has been appointed for the following countries:

CANADA UNITED STATES OF AMERICA	UNIPUB, 4611-F Assembly Drive, Lanham, MD 20706-4391

In the following countries IAEA publications may be purchased from the sales agents or booksellers listed or through major local booksellers. Payment can be made in local currency or with UNESCO coupons.

ARGENTINA	Comisión Nacional de Energía Atómica, Avenida del Libertador 8250, RA-1429 Buenos Aires
AUSTRALIA	Hunter Publications, 58 A Gipps Street, Collingwood, Victoria 3066
BELGIUM	Service Courrier UNESCO, 202, Avenue du Roi, B-1060 Brussels
CHILE	Comisión Chilena de Energía Nuclear, Venta de Publicaciones, Amunategui 95, Casilla 188-D, Santiago
CHINA	IAEA Publications in Chinese: China Nuclear Energy Industry Corporation, Translation Section, P.O. Box 2103, Beijing IAEA Publications other than in Chinese: China National Publications Import & Export Corporation, Deutsche Abteilung, P.O. Box 88, Beijing
CZECHOSLOVAKIA	S.N.T.L., Mikulandska 4, CS-116 86 Prague 1 Alfa, Publishers, Hurbanovo námestie 3, CS-815 89 Bratislava
FRANCE	Office International de Documentation et Librairie, 48, rue Gay-Lussac, F-75240 Paris Cedex 05
HUNGARY	Kultura, Hungarian Foreign Trading Company, P.O. Box 149, H-1389 Budapest 62
INDIA	Oxford Book and Stationery Co., 17, Park Street, Calcutta-700 016 Oxford Book and Stationery Co., Scindia House, New Delhi-110 001
ISRAEL	Heiliger & Co. Ltd. 23 Keren Hayesod Street, Jerusalem 94188
ITALY	Libreria Scientifica, Dott. Lucio de Biasio "aeiou", Via Meravigli 16, I-20123 Milan
JAPAN	Maruzen Company, Ltd, P.O. Box 5050, 100-31 Tokyo International
PAKISTAN	Mirza Book Agency, 65, Shahrah Quaid-e-Azam, P.O. Box 729, Lahore 3
POLAND	Ars Polona-Ruch, Centrala Handlu Zagranicznego, Krakowskie Przedmiescie 7, PL-00-068 Warsaw
ROMANIA	Ilexim, P O. Box 136-137, Bucharest
SOUTH AFRICA	Van Schaik Bookstore (Pty) Ltd, P.O. Box 724, Pretoria 0001
SPAIN	Díaz de Santos, Lagasca 95, E-28006 Madrid Díaz de Santos, Balmes 417, E-08022 Barcelona
SWEDEN	AB Fritzes Kungl. Hovbokhandel, Fredsgatan 2, P.O. Box 16356, S-103 27 Stockholm
UNITED KINGDOM	HMSO, Publications Centre, Agency Section, 51 Nine Elms Lane, London SW8 5DR
USSR	Mezhdunarodnaya Kniga, Smolenskaya-Sennaya 32-34, Moscow G-200
YUGOSLAVIA	Jugoslovenska Knjiga, Terazije 27, P.O. Box 36, YU-11001 Belgrade

---

Orders from countries where sales agents have not yet been appointed and requests for information should be addressed directly to:

Division of Publications
International Atomic Energy Agency
Wagramerstrasse 5, P.O. Box 100, A-1400 Vienna, Austria

INFORMATION FOR AUTHORS

General

NUCLEAR FUSION (NF) publishes papers, letters and critical reviews on theoretical and experimental aspects of controlled thermonuclear fusion research and comments on these contributions. Appropriate scientific summaries of major international conferences and workshops are also considered for publication.

Manuscripts, which may be submitted in Chinese, English, French, Russian or Spanish, will be published in English. For a manuscript submitted in a language other than English, a translation into English of technical terms should be provided. Manuscripts must be submitted in triplicate and typewritten double spaced on good quality standard size paper. All copies should include the main text, an abstract, tables, references, figures, captions and appendices, as appropriate. One set of glossy prints or reproducible transparencies of the figures should also be provided. *Final manuscript versions may be submitted in camera-ready form or on diskettes (see NF's Note for Authors, available on request from the NF Office).*

Every manuscript submitted must be accompanied by a disclaimer stating that the paper has not been published and is not being considered for publication elsewhere. If no copyright is claimed by the authors, the IAEA automatically owns the copyright of the paper.

Authors will receive proofs of the text of accepted manuscripts. Proofs of figures are sent only if requested. Rejected manuscripts will not be returned unless this is expressly requested within six weeks of rejection.

Fifty reprints are provided free of charge; additional reprints may be ordered at the time the author returns the proofs. Manuscripts and correspondence should be addressed to: The Editor, NUCLEAR FUSION, International Atomic Energy Agency, Wagramerstrasse 5, P.O. Box 100, A-1400 Vienna, Austria.

Manuscript preparation

Authors are referred to any recent issue of NF for examples of *format* and *style*.

All submitted articles should be *concise* and written in a *clear style*. The description of the methods used, either theoretical or experimental, should be given in detail only when such methods are new. Exhaustive description of previous or related work is not appropriate. If a laboratory report is used as the basis for a manuscript, it should be checked and rewritten for journal presentation.

Titles should be as concise as possible but sufficiently informative to describe the subject of the paper.

Abstracts must briefly summarize the contents of the article. They should state the principal objectives, mention the methodology employed, summarize the results (emphasizing the new findings) and present the main conclusions. They should be concise and self-contained so that they can be used by the International Nuclear Information System (INIS) and other abstracting systems without changes. General, well known information should be avoided in the abstract and accommodated in the introduction.

Letters to NF are either short communications of new approaches and developments or research notes. As a rule, they should be no longer than ten typewritten double spaced standard pages, including references and figures.

Guidelines for *bibliographical citations* can be found in issues 2, 3 and 4 of NF **28** (1988). In short, references should be accurately described in sufficient detail for easy identification. In the text, they should be indicated consecutively by Arabic numerals in square brackets. All references should be listed on a separate page at the end of the text. In this list, the names of all authors (or, if there are more than six, of the first three authors plus 'et al.') or else the corporate author (e.g. TFR GROUP) should be given. All unpublished material, e.g. laboratory reports, doctoral theses or papers in proceedings that have not yet been published, should be cited with full titles, place and year; citations of reports should also contain laboratory prefix and number, date of issue, etc. References to periodicals should contain the name of the journal, volume number, page number and year of publication; the title of the article is not needed. References to books should contain the full title of the book, names of editors (if any), name and location of the publisher, year of publication and page number (if appropriate). References to personal communications should be avoided if possible. For journal citations use the list of abbreviations given in "IAEA-INIS-11, INIS: Authority List for Journal Titles". Russian names should be transliterated according to "IAEA-INIS-10, INIS: Transliteration Rules for Selected Non-Roman Characters". Examples of the style followed by NF for references are:

REFERENCES

[1] KAYE, S.M., GOLDSTON, R.J., Nucl. Fusion **25** (1985) 65.

[2] MIODUSZEWSKI, P.K., SIMPKINS, J.E., EDMONDS, P.H., et al., J. Nucl. Mater. **128 & 129** (1984) 884.

[3] TRUBNIKOV, B.A., in Problems of Plasma Theory, Vol. 1 (LEONTOVICH, M.A., Ed.), Gosatomizdat, Moscow (1963) 98 (in Russian). [English translation: Reviews of Plasma Physics, Vol. 1, Consultants Bureau, New York (1965) 105.]

[4] UCKAN, N.A., SHEFFIELD, J., in Tokamak Startup (KNOEPFEL, H., Ed.), Plenum Press, New York (1986) 45.

[5] JT-60 TEAM: ABE, T., AIKAWA, H., AKAOKA, H., et al., in Plasma Physics and Controlled Nuclear Fusion Research 1986 (Proc. 11th Int. Conf. Kyoto, 1986), Vol. 1, IAEA, Vienna (1987) 11.

[6] TFR GROUP, in Controlled Fusion and Plasma Physics (Proc. 11th Eur. Conf. Aachen, 1983), Vol. 7D, Part II, European Physical Society (1983) 493.

[7] KOVRIZHNYKH, L.M., Transport Processes in Toroidal Magnetic Traps, Internal Rep. IC/70/86, International Centre for Theoretical Physics, Trieste (1970).

[8] MARKLIN, G., MHD Stability of the Spheromak, PhD Thesis, Univ. of Maryland, College Park (1983).

[9] TUBBING, B.J.D., LOPES CARDOZO, N.J., VAN DER WIEL, M.J., Tokamak heat transport, A study of heat pulse propagation in JET, submitted to Nucl. Fusion.

[10] YAMADA, H., KUSANO, K., KAMADA, Y., UTSUMI, M., YOSHIDA, Z., INOUE, N., Observation of ultra-low q equilibrium, to be published in Nucl. Fusion.

All *figures* should be on separate sheets and numbered consecutively with Arabic numerals, e.g. Fig. 1. A separate list of captions must be provided (see also *General* above).

Tables must carry a heading and be numbered consecutively with Roman numerals in the order in which they are mentioned in the text, e.g. Table II. Footnotes to tables should be indicated by raised letters (not numbers or asterisks) and set immediately below the table itself. Tables should be typed clearly for possible direct reproduction.

Footnotes to the text should be numbered consecutively with raised Arabic numerals; excessive use of footnotes should be avoided.

All *equations* should be typed as carefully as possible, with unavailable Greek letters and other symbols clearly inserted by hand so that formulas may be reproduced without retyping. Specifically:

(1) To eliminate confusion between symbols with similar appearance (e.g. between ones, ells and primes), make them as distinct as possible, if necessary marking them clearly by hand. In manuscripts with hand-written formulas, all further sources of confusion (such as n's and u's, u's and v's, e's and l's, J's and I's) should also be marked.

(2) Indicate a vector by an arrow on top rather than by bold face lettering.

(3) Tensors of second rank should bear two arrows on top; if higher rank tensors are required, choose an appropriate symbol and explain it.

(4) Indicate the normal algebraic product by simple juxtaposition of symbols, i.e. without multiplication sign (×).

(5) Write scalar products of vectors with a raised point, e.g. $\vec{A} \cdot \vec{B}$.

(6) Use the multiplication sign (×) solely to designate: (i) a vector product, (ii) an algebraic (but not a scalar) product in the case where an equation has to be split over two lines, and (iii) in expressions like 3 cm × 3 cm or 2×10^6 cm.

(7) The nabla operator (∇) does not carry an arrow.

(8) When equations are split over two or more lines, place operational signs only at the beginning of each new line, not at the end of the preceding line (except at the end of a page). For direct reproduction of an equation, the length of the lines should not exceed 9 cm.

(9) Where it is impossible to split long fractions over two lines, use negative exponents; similarly, replace root signs by fractional exponents where appropriate.

(10) Do not use symbols, abbreviations and formulations that are recognizable only in a particular language.

Use *SI units* as far as possible; where this is not possible, please give the appropriate conversion factor.

INTERNATIONAL
ATOMIC ENERGY AGENCY
VIENNA, 1991